



**UNIVERSIDADE ESTADUAL DE CAMPINAS
INSTITUTO DE QUÍMICA**

Gabriel de Biasi Báfero

**Evaluation of molybdenum-based catalysts for the hydrodeoxygenation of
biomass-derived model compounds**

**Avaliação de catalisadores de molibdênio para a hidrodesoxigenação de
compostos modelo derivados da biomassa**

**CAMPINAS
2024**

Gabriel de Biasi Báfero

Evaluation of molybdenum-based catalysts for the hydrodeoxygenation of biomass-derived model compounds

Avaliação de catalisadores de molibdênio para a hidrodesoxigenação de compostos modelo derivados da biomassa

Tese de Doutorado apresentada ao Instituto de Química da Universidade Estadual de Campinas como parte dos requisitos exigidos para a obtenção do título de Doutor em Ciências.

Doctor's Thesis presented to the Institute of Chemistry of the University of Campinas as part of the requirements to obtain the title of Doctor in Sciences.

Supervisor: Dr. Daniela Zanchet

O arquivo digital corresponde à versão final da Tese defendida pelo aluno Gabriel de Biasi Báfero e orientada pela Profa. Dra. Daniela Zanchet.

**CAMPINAS
2024**

Ficha catalográfica
Universidade Estadual de Campinas (UNICAMP)
Biblioteca do Instituto de Química
Simone Luiz Alves - CRB 8/9094

B145e Báfero, Gabriel de Biasi, 1996-
Evaluation of molybdenum-based catalysts for the hydrodeoxygenation of biomass-derived model compounds / Gabriel de Biasi Báfero. – Campinas, SP : [s.n.], 2024.

Orientador: Daniela Zanchet.
Tese (doutorado) – Universidade Estadual de Campinas (UNICAMP), Instituto de Química.

1. Catálise heterogênea. 2. Conversão de biomassa. 3. Hidrodesoxigenação. 4. Acetona. 5. Molibdênio. I. Zanchet, Daniela, 1972-. II. Universidade Estadual de Campinas (UNICAMP). Instituto de Química. III. Título.

Informações Complementares

Título em outro idioma: Avaliação de catalisadores de molibdênio para a hidrodesoxigenação de compostos modelo derivados da biomassa

Palavras-chave em inglês:

Heterogeneous catalysis

Biomass conversion

Hydrodeoxygenation

Acetone

Molybdenum

Área de concentração: Química Inorgânica

Títuloção: Doutor em Ciências

Banca examinadora:

Daniela Zanchet [Orientador]

Camila Alves de Rezende

Cristiane Barbieri Rodella

Leandro Pierroni Martins

Luiz Henrique Vieira

Data de defesa: 16-05-2024

Programa de Pós-Graduação: Química

Identificação e informações acadêmicas do(a) aluno(a)

- ORCID do autor: <https://orcid.org/0000-0001-9920-0632>

- Currículo Lattes do autor: <http://lattes.cnpq.br/9410174410733202>

BANCA EXAMINADORA

Profa. Dra. Daniela Zanchet (Orientadora)

Profa. Dra. Camila Alves de Rezende (IQ/UNICAMP)

Dra. Cristiane Barbieri Rodella (LNLS/CNPEM)

Prof. Dr. Leandro Pierroni Martins (IQ/UNESP)

Prof. Dr. Luiz Henrique Vieira (IQSC/USP)

A Ata da defesa assinada pelos membros da Comissão Examinadora, consta no SIGA/Sistema de Fluxo de Dissertação/Tese e na Secretaria do Programa da Unidade.

Este exemplar corresponde à redação final da Tese de Doutorado defendida pelo aluno **Gabriel de Biasi Báfero**, aprovada pela Comissão Julgadora em 16 de maio de 2024.

Dedicatória

À minha amada família, em especial
às grandes mulheres da minha vida:
minha mãe, Ana Lúcia, e minhas
avós, Lidia e Nydia.

Agradecimentos

Felizmente, tenho muitos a quem agradecer pela conclusão deste trabalho.

Em primeiro lugar, agradeço a todas as agências de fomento do nosso país, cujo auxílio tem sido fundamental para o bom desenvolvimento da educação, ciência e tecnologia no Brasil. Em especial, ao Conselho Nacional de Desenvolvimento Científico e Tecnológico (CNPq), que financiou a bolsa de doutorado da qual fui beneficiário nos últimos 4 anos (140849/2020-3) e ao Fundo de Apoio ao Ensino, Pesquisa e Extensão (FAEPEX) pelo auxílio ponte concedido (63520-24). Também, à agência britânica *Newton Mobility Grants*, que financiou meu estágio de 3 meses na *Cardiff University*, no País de Gales, entre fevereiro e maio de 2023 (R1/191179).

Ao Instituto de Química (IQ) e à Universidade Estadual de Campinas (UNICAMP) por serem minha segunda casa e palco do meu crescimento profissional na última década. Agradeço por todas as oportunidades oferecidas, seja na forma de funcionários, docentes, infraestrutura ou da variedade de auxílios dos quais usufrui.

À Profa. Daniela Zanchet, pela recepção no seu Grupo de Catálise e Nanomateriais (GCN) e por aceitar o desafio compartilhado de concluirmos um doutorado em menos de 2 anos. Nesse tempo, tem sido uma orientadora atenta e humana. Agradeço pelas oportunidades, conselhos e conhecimentos partilhados. Acredito ter evoluído a passos largos e, principalmente, aprendi a pensar mais “fora da caixa”. Espero poder contar sempre com a sua amizade e colaboração.

Aos queridos Davi Leite, Guilherme Strapasson e Leonardo Sousa, que me receberam calorosamente no GCN, logo se tornando importantes colaboradores científicos e, mais importante, amigos amados e indispensáveis. Vocês têm grande parte neste trabalho e a isso serei sempre grato.

À Larissa Ferreira, ao Marcelo Brasil, ao Pedro Nunes e, mais uma vez, ao Davi Leite e ao Guilherme Strapasson, por colaborarem com a revisão bibliográfica e parte introdutória deste trabalho. Foram essenciais na reta final.

A todos os demais membros do GCN, passados e presentes, que se mostraram bons amigos e colegas de trabalho. Sem repetir nomes, ao Renan Guerra, Natália Ladeira, Natália Oliveira, Breno Artuzi, Mateus Duenha e Felippo Locatelli, além dos técnicos Laura Novais e Rafael Godoi. A vocês, o meu muito obrigado.

À Profa. Heloise Pastore, a Lolly, por todos os anos de formação e orientação no seu Grupo de Peneiras Moleculares Micro e Mesoporosas (GPM³). Foram muitas oportunidades e projetos desde a iniciação científica até o começo do doutorado, e que tiveram forte impacto no meu crescimento profissional. Aproveito para agradecer aos membros do GPM³ com os quais convivi. Também foram bons colegas de trabalho e muitos se converteram em amigos para uma vida toda.

À Erica Munsignatti, pelos inúmeros conhecimentos compartilhados e por ter sido minha “coorientadora” durante os meus anos de GPM³. Hoje, minha grande amiga.

À Mariana Rodrigues, colaboradora científica constante desde os meus anos de GPM³. Hoje, também minha grande amiga.

Aos alunos de iniciação científica que orientei e auxiliei: Caio Fava, Camila Kubota, Celso Soares, Breno Artuzi, Mateus Duenha e Pedro Nunes. A vocês, agradeço pela oportunidade de partilhar e trocar conhecimentos. Me ajudaram a ter mais certeza da profissão que escolhi. Nesse mesmo caminho, às centenas de alunos de graduação que tive o privilégio de acompanhar através do Programa de Auxílio à Docência (PAD) e do Programa de Estágio Docente (PED). Foram incontáveis semestres atuando em diferentes disciplinas de química geral e química inorgânica e que muito contribuíram para a minha formação.

Aos professores do IQ e da UNICAMP, pela competência, dedicação e por tudo que puderam me ensinar. Em especial, à querida Profa. Regina Buffon, que têm me acompanhado de perto desde o princípio. Hoje, mais uma boa amiga.

Aos técnicos e funcionários do IQ e da Unicamp, por sua atenção, gentileza e prontidão em auxiliar. Em particular, à Deborah Simoni, à Karen Goraieb, à Sonia Fanelli e à Raquel Miller, agradeço pela amizade e pelo carinho.

Aos amigos que colecionei ao longo dos muitos anos de IQ e de UNICAMP, tanto àqueles que mantive, quanto àqueles que acabaram ficando no passado. Com vocês foi muito mais prazerosa essa jornada.

Aos colegas do Grupo *Chemistry and Photophysics of Luminescent Nanomaterials* (CPLn), coordenado pelo Prof. Paulo César de Sousa Filho, o PC, e do Laboratório de Nanotecnologia e Energia Solar (LNES), coordenado pela Profa. Ana Flávia Nogueira, agradeço pela convivência saudável nos últimos dois anos. Em especial, à Tamires Oliveira, minha querida amiga.

Ao Dr. Jonathan Bartley, pesquisador do *Cardiff Catalysis Institute* (CCI), no País de Gales, pela orientação e recepção no seu grupo de pesquisa, chefiado pelo Prof. Graham Hutchings, durante meu estágio na *Cardiff University*. Aproveito para agradecer a todos os funcionários e pesquisadores do CCI, especialmente aos Drs. James Hayward e David Morgan, que me auxiliaram na preparação e caracterização dos catalisadores propostos e que compõem parte substancial deste trabalho.

Também à Profa. Camila Rezende (IQ/UNICAMP), à Dra. Cristiane Rodella (LNLS/CNPEN), ao Prof. Leandro Martins (IQ/UNESP), e ao Prof. Luiz Henrique Vieira (IQSC/USP), por aceitarem participar da banca examinadora deste trabalho e pelas valiosas contribuições.

Aos amigos, funcionários e professores do colégio Educap, onde tive toda a minha formação inicial, desde a educação infantil até o ensino médio. Ainda hoje se interessam pela minha felicidade e pelo meu sucesso.

Finalmente, à minha amada família e a tudo que dela deriva.

Tenho a felicidade de ter uma família grande e acolhedora, que me cercou de muito amor e carinho e que me apoiou e me aplaudiu a cada nova etapa. Meus pais sempre zelaram por uma convivência intensa e saudável não apenas com os meus avós, tios e primos, mas também com uma família estendida muito presente e amorosa. A isso serei eternamente grato.

À minha mãe, Ana Lúcia, que me deu e continua me dando vida. Minha companheira e amiga. Muito do que nos une e nos fortalece são as preocupações e sonhos comuns. “Te amo infinitamente”, e amo mais ainda essa expressão que é nossa e só nossa, mas que começou com a Tia Maria.

Ao meu pai, Marco Túlio, que sempre me deu espaço e liberdade para que fosse exatamente como sou. Me proporcionou muitas oportunidades e muitos momentos de lazer e descontração.

Às minhas avós, Lidia e Nydia, que, mesmo donas de personalidades opostas, foram capazes de me dar todo o amor e ternura do mundo. Agradeço todos os dias pela nossa proximidade e cumplicidade. À vó “Lidinha” pelo afeto simples, mas poderoso, e por sempre ter sido a minha maior admiradora. À vó Nydia por ser nada menos que constante, por seu espírito inabalável e por ter me ensinado a amar essa maravilha de família que partilhamos.

Aos meus avôs, João e Pádua, também tão diferentes, mas igualmente capazes do amor. Ao vô João pela constante preocupação com o nosso bem-estar pessoal e material, e também pela alegria simples e descontraída. Ao vô Pádua por ainda ser um dos meus maiores e mais importantes interlocutores e, mais ainda, por ter me ensinado a criar e amar os cavalos.

Ao meu irmão, Miguel, dono de uma personalidade e de um intelecto ímpares. Meu grande amigo. À minha irmã, Izadora, a mais meiga e, por hora, a mais “adolescente”.

Aos meus amados tios, primos e parentes, difíceis de enumerar, sempre tão interessados na minha felicidade e importantes para mim. Em especial às queridas tias Maria Inês e Carla. Também às minhas tias-avós Maria, Lúcia, Maria Isabel e Ana Maria. Às minhas bisavós Maria, Adelina, Lélia e Zuleika. Às “tias”, com laço sanguíneo ou não, Viviane, Liliam, Daniela, Mariana, Elisabete, Marlene, Odila e Lourdes. À maravilhosa Zenaide. À querida Dona Amabile. Às primas Laura, Izabel, Lia e Alice. Ao tio Mário, ao padrinho Márcio e ao primo Joaquim. E a tantos outros que peço o perdão de não mencionar.

Resumo

Os óxidos metálicos têm ganhado atenção como catalisadores para diversas reações de redução e oxidação devido à sua abundância, disponibilidade, custo-benefício e ao potencial de integrar diversos sítios catalíticos num único material; sítios ácido-base, redox e vacâncias de oxigênio. Trabalhos anteriores têm corroborado a viabilidade dos óxidos metálicos como candidatos promissores para reações de hidredesoxigenação (HDO), um processo destinado a valorizar produtos derivados da biomassa através da diminuição do seu teor de oxigênio. Na primeira parte deste estudo, o óxido de molibdênio (MoO_3) *bulk* foi submetido à reação de HDO da acetona, fornecendo novas perspectivas sobre a formação *in situ* de oxicarbeto de molibdênio (MoO_xC_y) e suas propriedades catalíticas. As características da fase MoO_xC_y se mostraram dependentes da temperatura e do tempo de reação, influenciando o equilíbrio de diversos sítios catalíticos e a subsequente distribuição de produtos finais. A correlação intrínseca entre os sítios ativos - principalmente sítios ácidos de Brønsted/Lewis e sítios de hidrogenação/hidrogenólise - e os mecanismos de reação foram discutidas em detalhes. Uma vez que as propriedades das fases MoO_3 e MoO_xC_y estavam mais bem estabelecidas, outros catalisadores de Mo, tanto *bulk* quanto suportados, também foram investigados utilizando a reação de HDO da acetona. As propriedades resultantes da combinação de Mo com outros metais da primeira série de transição (Mn, Fe, Co, Cu, Zn) foram investigadas por meio da avaliação de molibdatos metálicos (MMo), uma classe especial de óxidos metálicos mistos *bulk*. Como catalisadores, eles também passaram por transições de fase severas sob condições de HDO da acetona, mas, diferentemente de MoO_3 , produziram misturas de fases dependentes do metal da primeira série de transição, geralmente envolvendo fases de óxido (MoO_2) e de carbeto ($\alpha\text{-MoC}_{1-x}$) de molibdênio de baixa coordenação. CuMo apresentou resultados promissores no contexto de HDO. Finalmente, com o objetivo de ampliar a acessibilidade de Mo e outros metais da primeira série de transição (Fe, Co, Ni, Cu), além de combiná-los com funcionalidades ácidas, foram preparados catalisadores suportados em zeólita, também avaliados na reação de HDO da acetona. Zeólitas ZSM-5 com diferentes razões molares Si/Al e, portanto, diferentes concentrações de sítios ácidos, foram testadas preliminarmente. Resultados interessantes foram observados, consolidando os catalisadores de Cu juntamente aos de Mo como promissores no contexto de HDO.

Abstract

Metal oxides have gained attention as catalysts for diverse reduction and oxidation reactions due to their abundance, availability, cost-effectiveness, and the potential to integrate various catalytic sites, such as acid-base, redox, and oxygen vacancy sites. Previous findings have substantiated the viability of metal oxides as promising candidates for hydrodeoxygenation (HDO) reactions, a pivotal process aimed at valuing biomass-derived products by diminishing their oxygen content. In the first part of this study, bulk molybdenum oxide (MoO_3) was subject to acetone HDO reaction, yielding new insights into the *in situ* formation of molybdenum oxycarbides (MoO_xC_y) and elucidating their catalytic properties. The characteristics of the MoO_xC_y phase were contingent upon temperature and time on stream, influencing the balance of diverse catalytic sites and the ensuing distribution of final products. The intrinsic correlation among the active sites – mainly Brønsted/Lewis acid sites and hydrogenation/ hydrogenolysis sites – and the reaction pathways were discussed in detail. Once the properties of MoO_3 and MoO_xC_y phases were better addressed, other Mo-based catalysts, both bulk and supported, were also investigated in the context of the acetone HDO reaction. The properties resulting from the combination of Mo with other abundant first-row transition metals (Mn, Fe, Co, Cu, Zn) were assessed through the evaluation of metal molybdates (MMo), a special class of bulk mixed metal oxides. As catalysts, they also went through severe phase transitions under acetone HDO conditions but, differently from MoO_3 , they produced phase mixtures that were dependent on the first-row transition metal, usually involving lower coordinated molybdenum oxide (MoO_2) and carbide ($\alpha\text{-MoC}_{1-x}$). CuMo presented exciting results towards efficient HDO. Finally, in order to broaden the accessibility of Mo and other first-row transition metals (Fe, Co, Ni, Cu), in addition to combining them with acid functionalities, zeolite supported catalysts were prepared and evaluated on the acetone HDO reaction. ZSM-5 zeolites with different Si/Al molar ratios and, therefore, concentration of acid sites, were primarily tested. Interesting results arose, consolidating Cu-based materials together with Mo-based ones as promising HDO catalysts.

List of Figures

Figure 1. Representation of lignocellulose structure and main compounds: cellulose, hemicellulose, and lignin. Adapted from [5].	24
Figure 2. Biorefinery structure and the different routes for lignocellulosic biomass upgrading. Adapted from [2].	25
Figure 3. Main oxygenated components found in lignin bio-oils. Adapted from [4].	27
Figure 4. Different processes for bio-oil valorization. Adapted from [9].	28
Figure 5. Representation of the main reaction mechanisms involved in HDO processes. Adapted from [2].	30
Figure 6. Statistics for “molybdenum” AND “hydrodeoxygenation” keywords search in Web of Science®, generating a total of 161 entries.	32
Figure 7. Structural models of (a) orthorhombic α -MoO ₃ , highlighting its layered nature, (b) monoclinic β -MoO ₃ , (c) monoclinic β -MoO ₂ and (d) tetragonal t-MoO ₂ .	35
Figure 8. Representative high resolution TEM images of the three different types of MoO ₂ samples at different magnifications. A, D, and G show the amorphous type samples; B, E, and H show the nanostructured samples; and C, F, and I show the crystalline samples. Images C, F, H, and I were collected with samples aligned along the [001] zone axis. Extracted from [83].	36
Figure 9. Reaction coordinate for acetone deoxygenation to propylene on α -MoO ₃ (010) surface with a single terminal oxygen vacancy. Mo, O, C, and H are shown in green, red, blue, and white, respectively. All energies are in eV. Extracted from [67].	39

Figure 10. (a) Comparison of the homolytic bond dissociation energies (BDEs) of lignin-derived model compounds at 320 °C in gas phase. (b) Normalized XRD patterns of the spent MoO ₃ catalysts after m-cresol HDO (in comparison with fresh MoO ₃ , MoO ₂ , Mo ₂ C and MoO _x C _y H _y samples). The symbol (*) and (+) indicates the peak assignment corresponding to MoO _x C _y H _y and MoO ₂ phases, respectively. (c) XPS of the Mo (3d) energy region of the fresh and spent MoO ₃ samples after m-cresol HDO. The numbers in parentheses are the corresponding oxidation state percentages of Mo ⁶⁺ , Mo ⁵⁺ and Mo ⁴⁺ , respectively. Adapted from [64].	42
Figure 11. Main reaction pathways arising from guaiacol HDO conversion. Adapted from [130].	44
Figure 12. a–e) HRTEM images and FFT patterns of MoC at various temperatures (refer to each image). The scale bars are 5 nm for all images. f) Scheme showing the preferential facet changes with temperature increase. Extracted from [160].	47
Figure 13. Schematic representation of the evolution of Mo ₂ C functionality with increasing oxygen content. Extracted from [172].	49
Figure 14. Schematic representation of the <i>in situ</i> oxidation of Mo ₂ C and its impact on anisole HDO activity. Adapted from [65].	51
Figure 15. Reaction network for acetone HDO over Mo-based catalysts. Extracted from [107].	64
Figure 16. Products' distribution (colored) and conversion (black triangles) for acetone HDO reaction over MoO ₃ _comm: (A) 300→400, from 300 to 400 °C, and (B) 400→300, from 400 to 300 °C. total TOS: 18 h (0.1 °C min ⁻¹). WHSV = 7.32 g _{acetone} g _{catalyst} ⁻¹ h ⁻¹ . Feed: 2.4 mL min ⁻¹ acetone, 51 mL min ⁻¹ H ₂ , balance He. Total flow: 100 mL min ⁻¹ .	67

Figure 17. Products' distribution (colored bars) and conversion (black triangles) of acetone HDO reactions for MoO₃_comm (A, B) and MoO₂_comm (C, D): 350C, isothermal at 350 °C (A, C), and 400C, isothermal at 400 °C (B, D). TOS: 6 h. WHSV = 7.14 g_{acetone} g_{catalyst}⁻¹ h⁻¹. Feed: 2.4 mL min⁻¹ acetone, 51 mL min⁻¹ H₂, balance He. Total flow: 100 mL min⁻¹.69

Figure 18. (A) XRD patterns and (B) XPS spectra of Mo 3d region of post-reaction samples: MoO₃_comm (as received) and 350C1h, 350C6h, 400C1h, and 400C6h catalysts after acetone HDO reaction. The spin-orbit splitting of 3.1 eV was considered for each Mo species. Reaction conditions of pre-treated samples: WHSV = 7.14 g_{acetone} g_{catalyst}⁻¹ h⁻¹. Feed: 2.4 mL min⁻¹ acetone, 51 mL min⁻¹ H₂, balance He. Total flow: 100 mL min⁻¹.70

Figure 19. ³¹P NMR spectra of adsorbed TMPO on (bottom) MoO₃_comm (as received) and (middle) 350C6h and (top) 400C1h catalysts. Reaction conditions of pre-treated samples: WHSV = 7.14 g_{acetone} g_{catalyst}⁻¹ h⁻¹. Feed: 2.4 mL min⁻¹ acetone, 51 mL min⁻¹ H₂, balance He. Total flow: 100 mL min⁻¹. Phys. - physisorbed TMPO, L - LAS, B1 to B4 - BAS, where the higher the number, the stronger the site.74

Figure 20. Acetone-TPD curves of (A) MoO₃_comm, (B) 350C6h, and (C) 400C1h catalysts after acetone HDO reaction. Acetone, propene, methane, and carbon dioxide were monitored from room temperature to 500 °C. Reaction conditions of pre-treated samples: WHSV = 7.14 g_{acetone} g_{catalyst}⁻¹ h⁻¹. Feed: 2.4 mL min⁻¹ acetone, 51 mL min⁻¹ H₂, balance He. Total flow: 100 mL min⁻¹.76

Figure 21. Yields of (A) C₆O, (B) C_n, (C) C₃A, (D) IPA, and (E) C₃E of acetone HDO reactions for MoO₃_comm and MoO₂_comm: 350C, isothermal at 350 °C, and 400C, isothermal at 400 °C. TOS: 6 h. WHSV = 7.14 g_{acetone} g_{catalyst}⁻¹ h⁻¹. Feed: 2.4 mL min⁻¹ acetone, 51 mL min⁻¹ H₂, balance He. Total flow: 100 mL min⁻¹. In (B), C_n was not detected for MoO₂_comm at both temperatures.80

Figure 22. Active sites and related reaction pathways showed by the ordered and amorphous oxycarbide phases, both formed during acetone HDO reaction over MoO₃ catalyst at 350 and 400 °C, respectively.83

Figure 23. Reaction network for acetone HDO over MMo catalysts. Adapted from [107].87

Figure 24. XRD patterns of the first-row transition metal molybdate catalysts (MMo): MnMo, FeMo, CoMo, CuMo, and ZnMo.88

Figure 25. SEM images of the first-row transition metal molybdate catalysts (MMo): (A) MnMo, (B) FeMo, (C) CoMo, (D) CuMo, and (E) ZnMo.89

Figure 26. Products' distribution (colored) and conversion (black triangles) for acetone HDO reaction over MoO₃_comm (A) and first-row transition metal molybdate catalysts (MMo): MnMo (B), FeMo (C), CoMo (D), CuMo (E), and ZnMo (F). 300→400 tests were carried out from 300 to 400 °C, isothermal every 20 °C, total TOS: 3 h. WHSV = 7.32 g_{acetone} g_{catalyst}⁻¹ h⁻¹. Feed: 2.4 mL min⁻¹ acetone, 51 mL min⁻¹ H₂, balance He. Total flow: 100 mL min⁻¹.91

Figure 27. Products' distribution (colored) and conversion (black triangles) for acetone HDO reaction over MoO₃ (A) and first-row transition metal molybdate catalysts (MMo): MnMo (B), FeMo (C), CoMo (D), CuMo (E), and ZnMo (F). 400C tests were carried out at 400 °C, isothermal, TOS: 6 h. WHSV = 7.32 g_{acetone} g_{catalyst}⁻¹ h⁻¹. Feed: 2.4 mL min⁻¹ acetone, 51 mL min⁻¹ H₂, balance He. Total flow: 100 mL min⁻¹.94

Figure 28. Products' distribution (colored) and conversion (black triangles) for acetone HDO reaction over CuMo (A) and related catalysts: MoO₃_comm (B), CuO (C), Cu₂O (D), CuO/MoO₃ – PM (physical mixture) (E), CuO@MoO₃ 10 wt.% (impregnated) (F). The 100→300 tests were carried out from 100 to 300 °C, isothermal every 50 °C, total TOS: 2.5 h. WHSV = 7.32 g_{acetone} g_{catalyst}⁻¹ h⁻¹. Feed: 2.4 mL min⁻¹ acetone, 51 mL min⁻¹ H₂, balance He. Total flow: 100 mL min⁻¹.97

Figure 29. Reaction network for acetone HDO over metal/zeolite catalysts. Adapted from [107].107

Figure 30. Products' distribution (colored) and conversion (black triangles) for acetone HDO reaction over pristine ZSM-5 zeolites (Z11.5, Z40, and Z140) at (A) 200 °C, (B) 300 °C, and (C) 400 °C. 200→400 tests were carried out from 200 to 400 °C, isothermal every 100 °C, total TOS: 1.5 h. WHSV = $7.32 \text{ g}_{\text{acetone}} \text{ g}_{\text{catalyst}}^{-1} \text{ h}^{-1}$. Feed: 2.4 mL min^{-1} acetone, $51 \text{ mL min}^{-1} \text{ H}_2$, balance He. Total flow: 100 mL min^{-1}109

Figure 31. Products' distribution (colored) and conversion (black triangles) for acetone HDO reaction over pristine ZSM-5 zeolites: (A) Z11.5, (B) Z40, (C) and Z140, isothermal at 400 °C, TOS: 3 h. WHSV = $7.32 \text{ g}_{\text{acetone}} \text{ g}_{\text{catalyst}}^{-1} \text{ h}^{-1}$. Feed: 2.4 mL min^{-1} acetone, $51 \text{ mL min}^{-1} \text{ H}_2$, balance He. Total flow: 100 mL min^{-1}111

Figure 32. SEM images of the metal/zeolite catalysts: (A) Z140, (B) Mo/Z140, (C) Fe/Z140, (D) Co/Z140, (E) Ni/Z140, (F) Cu/Z140.114

Figure 33. Products' distribution (colored) and conversion (black triangles) for acetone HDO reaction over Z140 and metal/zeolite catalysts (Mo/Z140, Fe/Z140, Co/Z140, Ni/Z140, and Cu/Z140) at (A) 200 °C, (B) 300 °C, and (C) 400 °C. 200→400 tests were carried out from 200 to 400 °C, isothermal every 100 °C, total TOS: 1.5 h. WHSV = $7.32 \text{ g}_{\text{acetone}} \text{ g}_{\text{catalyst}}^{-1} \text{ h}^{-1}$. Feed: 2.4 mL min^{-1} acetone, $51 \text{ mL min}^{-1} \text{ H}_2$, balance He. Total flow: 100 mL min^{-1}115

List of Tables

Table 1. Mass fraction of oxygenated compounds in some bio-oils obtained from the pyrolysis of different biomass sources. Adapted from [22].	27
Table 2. Relevant structural properties of main molybdenum oxide structures.	34
Table 3. Relevant structural properties of main molybdenum carbide structures.	46
Table 4. Structural formula of acetone and main products obtained through acetone HDO reaction.	60
Table 5. Summary of the catalytic data obtained for acetone HDO reaction as a function of temperature (300→400 and 400→300 tests) and under isothermal conditions (350C and 400C tests) for the MoO _x catalysts.	66
Table 6. Acid and textural data of: MoO ₃ _comm, 350C6h and 400C1h catalysts after acetone HDO reaction. Reaction conditions of pre-treated samples: WHSV = 7.14 g _{acetone} g _{catalyst} ⁻¹ h ⁻¹ . Feed: 2.4 mL min ⁻¹ acetone, 51 mL min ⁻¹ H ₂ , balance He. Total flow: 100 mL min ⁻¹ .	74
Table 7. Nominal and experimental atomic ratios (Mo/M, where M = Mn, Fe, Co, Cu, Zn) of the first-row transition metal molybdate catalysts (MMo). The experimental data was obtained through SEM-EDX and XPS measurements.	90
Table 8. Summary of the catalytic data obtained for acetone HDO reaction as a function of temperature (300→400 tests) for the first-row transition metal molybdate catalysts (MMo): MnMo, FeMo, CoMo, CuMo, and ZnMo. Also, MoO ₃ for comparison purposes.	92
Table 9. Summary of the catalytic data obtained under acetone HDO isothermal conditions (400C tests) for the first-row transition metal molybdate catalysts (MMo): MnMo, FeMo, CoMo, CuMo, and ZnMo. Also, MoO ₃ is shown.	95

Table 10. Summary of the catalytic data obtained for acetone HDO reaction as a function of temperature (100→300 tests), at 300 °C, for CuMo and related catalysts: MoO₃_comm, CuO, Cu₂O, CuO/MoO₃ – PM (physical mixture), CuO@MoO₃ 10 wt.% (impregnated).98

Table 11. Summary of the catalytic data obtained for acetone HDO reaction as a function of temperature (200→400 tests), for pristine ZSM-5 zeolites (Z11.5, Z40, and Z140) at 200 °C, 300 °C, and 400 °C.110

Table 12. Summary of the catalytic data obtained for acetone HDO reaction as a function of TOS (isothermal tests), for pristine ZSM-5 zeolites (Z11.5, Z40, and Z140) at 400 °C.112

Table 13. Summary of the catalytic data obtained for acetone HDO reaction as a function of temperature (200→400 tests), for Z140 and metal/zeolite catalysts (Mo/Z140, Fe/Z140, Co/Z140, Ni/Z140, and Cu/Z140) at 200 °C, 300 °C, and 400 °C.116

List of Abbreviations, Acronyms, and Symbols

Al _{Oh}	aluminum atoms octahedrally coordinated
Al _{Td}	aluminum atoms tetrahedrally coordinated
AS	acid sites
BAS	Brønsted acid sites
BE	binding-energy
BET	Brunauer–Emmett–Teller model
BTX	benzene, toluene, and xylenes – aromatics
C ₁	methane
C ₂	ethane/ethene
C ₂ HO	acetaldehyde
C ₃ A	propane
C ₃ E	propene
C ₄	isobutane/isobutene and isomers
C ₆	hexane/hexene and isomers
C ₆ O	methyl isobutyl ketone and isomers
C ₉	nonane/nonene and isomers
C ₉ O	diisobutyl ketone and isomers
CDP	coupling deoxygenated products
DDP	direct deoxygenation products
DTBP	2,6-di-tert-butylpyridine
EDX	energy dispersive X-ray analysis
FFT	fast Fourier transform
FID	flame ionization detector
FTIR	Fourier transformed infrared spectroscopy
FTO	fluorine dopped tin oxide

FWHM	full width at half maximum
GC	gas chromatography analysis
HDO	hydrodeoxygenation reaction
HHP	hydrogenation/hydrogenolysis products
HPDEC	high-power decoupling (related to solid state NMR analysis)
HS	hydrogenation/hydrogenolysis sites
ICP-OES	inductively coupled plasma optical emission spectrometry
IPA	isopropanol
IZA	International Zeolite Association
LAS	Lewis acid sites
LEIS	low energy ion scattering analysis
MAS	magic angle spinning (related to solid state NMR analysis)
MFI	mordenite framework inverted (zeolite family)
MMo	metal molybdate samples, where M = Mn, Fe, Co, Cu, and Zn
Mo ^{δ+}	intermediary molybdenum oxidation states (close to 5+)
MTO	methanol-to-olefins reaction
M/Z140	supported metal/zeolite samples, where M = Mo, Fe, Co, Ni, and Cu, and Z140 refers to ZSM-5 zeolite with Si/Al molar ratio of 140
NAP-XPS	near ambient pressure X-ray photoelectron spectroscopy
NMR	nuclear magnetic resonance
OP	oxygenated products
OVS	oxygen vacancy sites
PM	physical mixture
Py	pyridine
SDA	structure directing agent
SEM	scanning electron microscopy
SSA	specific surface area

TCD	thermal conductivity detector
TEM	transmission electron microscopy
TGA	thermogravimetric analysis
TMPO	trimethylphosphine oxide
TOS	time on stream
TPD	thermoprogrammed desorption analysis
TPR	thermoprogrammed reduction analysis
XPS	X-ray photoelectron spectroscopy
XRD	X-ray diffractometry analysis
XRF	X-ray fluorescence analysis
ZSM-5	Zeolite Socony Mobil 5 (other name for the MFI zeolite family)
ZX	ZSM-5 zeolite samples, where X refers to different Si/Al molar ratios: 11.5, 40, and 140

Summary

Chapter 1. Introduction	24
1.1. Biomass upgrading	24
1.2. Bio-oil and its valorization routes	26
1.3. Hydrodeoxygenation reaction and biomass-derived compounds	29
1.4. Commonly employed catalysts for hydrodeoxygenation processes	31
1.5. Mo-based catalysts for hydrodeoxygenation processes	33
1.5.1. Molybdenum oxides	33
1.5.2. Molybdenum carbides	45
Chapter 2. Motivation and proposal	53
Chapter 3. Experimental section	54
3.1. Materials	54
3.2. Methods	54
3.2.1 Bulk Mo-based catalysts	54
3.2.2 Supported Mo/zeolite and M/zeolite catalysts	55
3.3. Characterization	55
3.4. Catalytic Evaluation	58
3.4.1. Acetone HDO set up and main products	58
3.4.2. Effect of diffusive transport phenomena	60
Chapter 4. MoO_x properties evaluated during acetone HDO reaction: The impact of strong Brønsted acid sites and Mo⁵⁺ species generated on stream	63
4.1. Contextualization	63
4.2. Results	66
4.3. Discussion	76
4.4. Considerations	82
Chapter 5. First-row transition metal molybdates (MMo) as candidates for acetone HDO reaction: Promoting C-C coupling products and high deoxygenation degrees	84
5.1. Contextualization	84

5.2. Results	87
5.3. Discussion	99
5.4. Considerations	104
 Chapter 6. Evaluating Mo/zeolite and M/zeolite catalysts over acetone HDO reaction: The effect of combining zeolites acidity and abundant metals	105
6.1. Contextualization	105
6.2. Results	108
6.3. Discussion	118
6.4. Considerations	122
 Chapter 7. Final considerations	123
 Chapter 8. Perspectives	125
 Chapter 9. References	126
 Chapter 10. Appendix	144
10.1. Effect of mass and heat transport phenomena	144
10.2. Supporting information	147
10.3. Permissions	162
10.3.1. Enhanced Brønsted Acidity and Hydrogenating Sites Generated on MoO₃ during Acetone Hydrodeoxygenation	162

Chapter 1. Introduction

1.1. Biomass upgrading

With the projected increase in global population, energy consumption is expected to soar to approximately 16 billion tons of oil equivalents by 2040 [1]. However, this demand continues to rely heavily on fossil fuels, driving significant efforts to transition towards sustainable energy models [2]. Lignocellulosic biomass is an attractive renewable source derived from living or recently living organisms (essentially plants) and abundantly available in nature [3]. The products of lignocellulosic biomass upgrading present great potential for various applications, including energy storage, biofuel and chemical production, and heat and electricity generation [4]. Moreover, beyond providing a sustainable alternative to fossil fuels, lignocellulosic biomass derivatives could play a crucial role in agricultural and forest waste management.

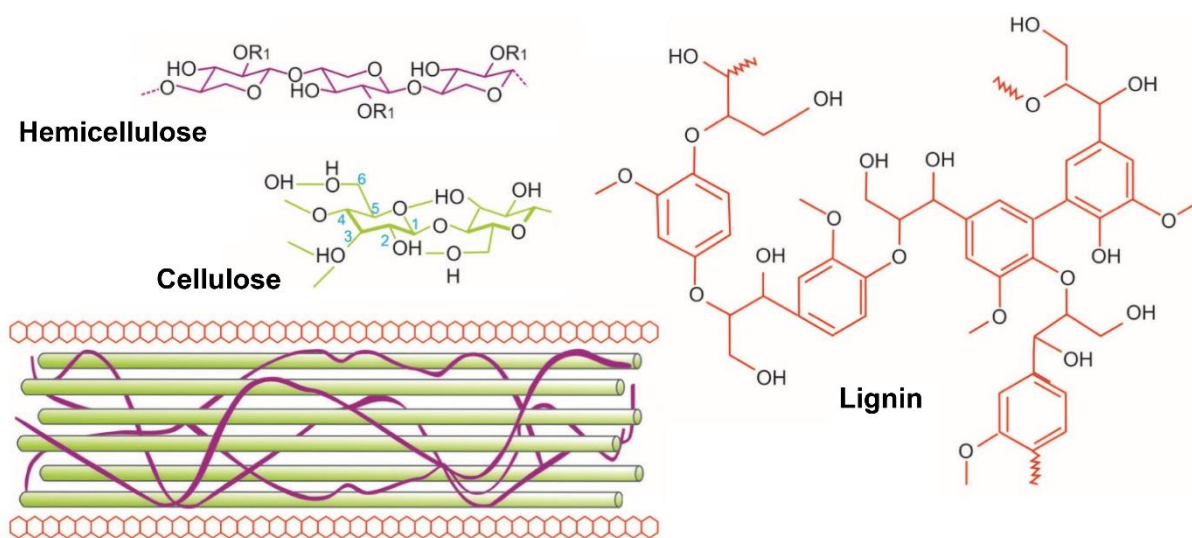


Figure 1. Representation of lignocellulose structure and main compounds: cellulose, hemicellulose, and lignin. Adapted from [5].

Lignocellulosic biomass is primarily constituted of cellulose, hemicellulose, and lignin [6], depicted in Figure 1, alongside proteins and extractives like tannins, resins, fatty acids, and inorganic salts [7]. Cellulose, comprising a significant portion of lignocellulosic biomass (35–40 %), consists of long linear chains of β-(1,4)-glycosidically linked D-glucose units [8]. Following, there is hemicellulose (25–40 %), a complex heterogeneous polysaccharide that serves as a connecting element

between cellulose and lignin within the cell wall [7]. The third component, lignin (10–20 %) accumulates in the secondary cell wall, presenting itself as a complex three-dimensional amorphous natural polymer [9]. Various upgrading processes, such as chemical, biochemical, and thermochemical routes, are able to maximize lignocellulosic biomass utilization, producing a number of high value-added products and paving the way for potential biorefineries, as illustrated in Figure 2.

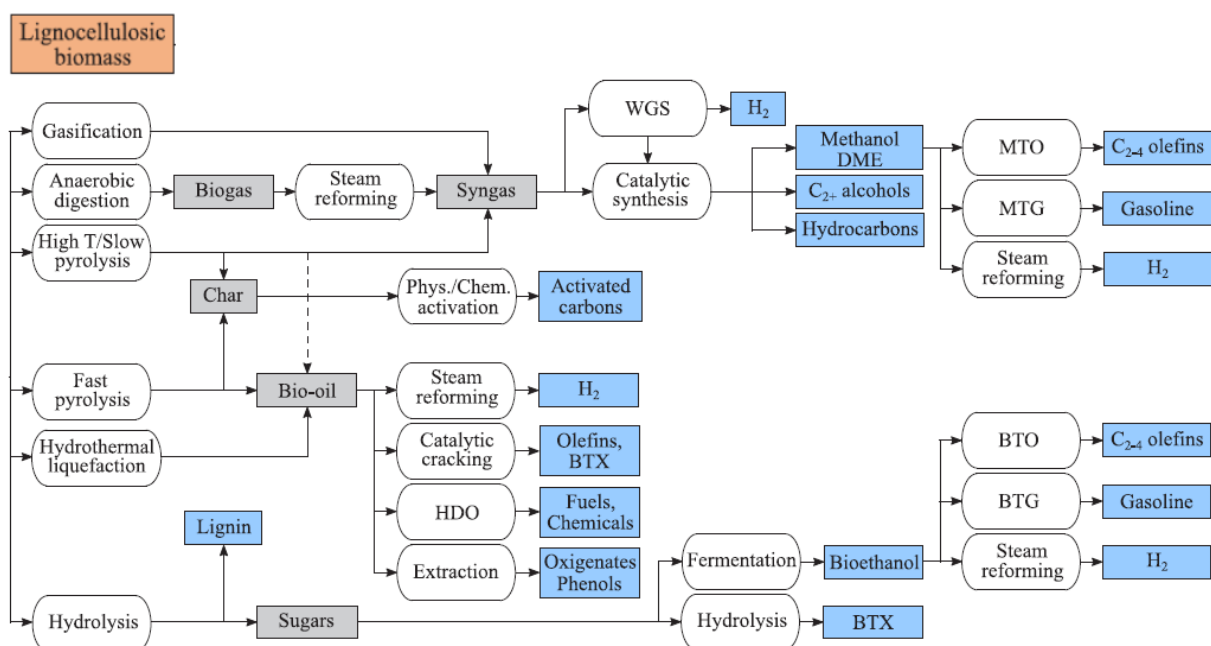


Figure 2. Biorefinery structure and the different routes for lignocellulosic biomass upgrading. Adapted from [2].

Chemical valorization primarily involves hydrolysis reactions, promoting the depolymerization of the three lignocellulosic biomass components, whereas biochemical pathways utilize microorganisms in fermentation processes, yielding products such as biogas and bioethanol [2]. In turn, thermochemical methods utilize thermal catalytic conversion to obtain a number of interesting products [2]. Fast pyrolysis stands out as one of the most efficient thermochemical methods for lignocellulosic biomass valorization due to the potential of its liquid product, the bio-oil, also yielding a solid waste, known as char, and noncondensable gases (Figure 2). The proportion of each product depends on pyrolysis conditions and process parameters [10]. Pyrolysis conditions can be easily adjusted to maximize char yield, a process referred to as carbonization, typically involving slow heating rates [11]. Activated carbons, valuable for adsorption, catalysis, and electrochemical applications, can be

prepared using this method [12]. However, the economic feasibility of biomass pyrolysis primarily hinges on bio-oil utilization.

Fast pyrolysis technology has seen significant development, with high bio-oil yields achieved at considerably low temperatures (450–550 °C) and high heating rates (10^3 – 10^4 °C s⁻¹) [13]. Generally, fast pyrolysis is conducted in relatively simple units, using various reactor configurations, with lower production costs compared to other thermochemical technologies [14–16]. Fast pyrolysis also offers promising environmental benefits, with limited emissions due to the lower temperatures [17]. The possibility of implementing geographically dispersed pyrolysis units is another advantage of this approach, allowing bio-oil production near biomass sources and large-scale valorization in existing refinery units [18,19]. Given the interest in sustainable energy and chemical production, bio-oil valorization has been extensively studied, particularly focusing on the hydrodeoxygenation (HDO) route.

1.2. Bio-oil and its valorization routes

Pyrolysis bio-oils typically display an opaque brown-black appearance, accompanied by a viscous texture and a distinct pungent odor. The predominant constituent is water (usually 20–30 %), primarily sourced from the moisture content in the raw material and generated through biomass condensation during pyrolysis. Influenced by factors such as biomass precursors and pyrolysis conditions, the chemical composition of bio-oil varies, commonly featuring high concentrations of carbon, oxygen, and hydrogen, alongside minor levels of nitrogen and sulfur [20]. Figure 3 depicts the main oxygenated components found in bio-oils, which are primarily phenolic compounds, but other functionalities can be found, including carboxylic acids, aldehydes, alcohols, esters, and ketones [21]. Table 1 details the composition of the oxygenated fraction in some bio-oils obtained from the pyrolysis of different biomass sources.

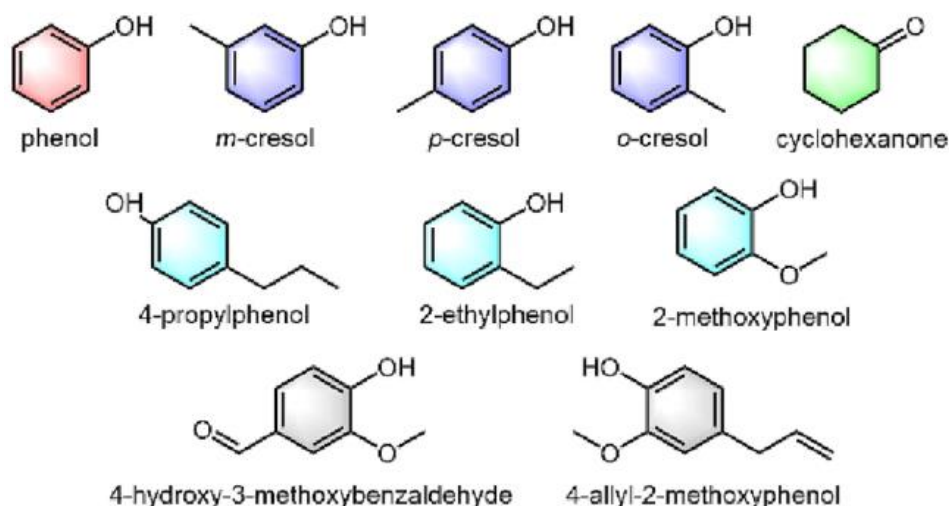


Figure 3. Main oxygenated components found in lignin bio-oils. Adapted from [4].

Table 1. Mass fraction of oxygenated compounds in some bio-oils obtained from the pyrolysis of different biomass sources. Adapted from [22].

Raw material	Mass fraction (%)						
	Ketones/ Aldehydes	Acids	Phenols	Furans	Alcohols	Esters	Others
Rice husk	21.0	33.2	18.9	2.8	-	6.9	17.4
Pine sawdust	11.1	20.5	25.9	13.4	2.3	6.5	20.4
Pine + Spruce	18.3	10.9	-	-	6.6	-	45.4
Palm tree	21.8	19.2	5.0	-	6.9	-	45.1

It is worth noting that the high oxygen content of bio-oils contributes to their corrosiveness (pH, 2.1–4.0), owing to the abundance of carboxylic acids, and also to their relatively low heating value (HHV, 16–19 MJ kg⁻¹) and viscosity (40–100 cP) [23]. Due to these characteristics, bio-oils' thermal and chemical stability is inferior to that of traditional petroleum oils [24]. Therefore, ensuring bio-oil stability is crucial for safe storage and transportation. Stability assessments involve monitoring changes in viscosity, water content, and average molecular weight. An extensively proposed method involves separating its aqueous and organic fractions [25]. This separation allows for independent valorization of each fraction, yielding an easily manageable aqueous fraction and an organic fraction with a notably higher calorific value [26]. Another approach to stabilize bio-oil is through aging leading to significant physicochemical alterations [27]. Other common pretreatments involve physical

methods such as ash and char removal, solvent or antioxidant addition, and bio-oil emulsification [28]. Accordingly, several physical and chemical technologies have been developed for bio-oil valorization, as displayed in Figure 4. Catalytic upgrading pathways include cracking, HDO, and steam reforming



Figure 4. Different processes for bio-oil valorization. Adapted from [9].

Catalytic cracking of bio-oil essentially generates hydrocarbons (Figure 2). Studies involving the catalytic cracking of various model compounds found in bio-oil, including alcohols and phenols, identified three primary pathways for deoxygenation: dehydration, decarbonylation, and decarboxylation [29,30]. Alcohols were found to be the most reactive, producing alkenes directly through dehydration. However, phenol exhibited high stability at moderate temperatures. Catalytic pyrolysis offers a similar approach to catalytic cracking, enabling cracking reactions during bio-oil production or as a subsequent stage, treating pyrolysis volatiles before condensation [31,32].

Steam reforming is a prominent method for producing H_2 from biomass (Figure 2) due to catalyst advancements and process flexibility [33]. Water content is not a limiting factor in bio-oil steam reforming, as the aqueous and distilled fractions contain sufficient water for the process [34]. However, the challenge lies in the rapid deactivation by coke at high reaction temperatures (around $700^\circ C$), hindering the direct reforming of raw bio-oil [35]. To address this, in-line reforming of pyrolysis volatiles has been proposed, utilizing reactors such as fluidized beds for the pyrolysis and for the reforming step [36].

The already mentioned HDO pathway offers a versatile approach for the stabilization and/or valorization of raw bio-oil. By adjusting reaction conditions and

catalysts, the severity of hydrogenation steps can be tailored. HDO stands out as an effective technology for carbon economy [37], unlocking the potential of bio-oil as a fuel, feedstock for refineries, or source of high-quality products like phenolics and aromatics [2]. While HDO offers significant advantages, some challenges include high H_2 consumption and safety considerations due to harsh operating conditions. Unlike cracking, HDO provides more flexibility and can yield either fuel or partially deoxygenated bio-oil [38]. Research on HDO encompasses a wide range of operating conditions, with studies often conducted using model compounds due to bio-oil instability [22].

1.3. Hydrodeoxygenation reaction and biomass-derived compounds

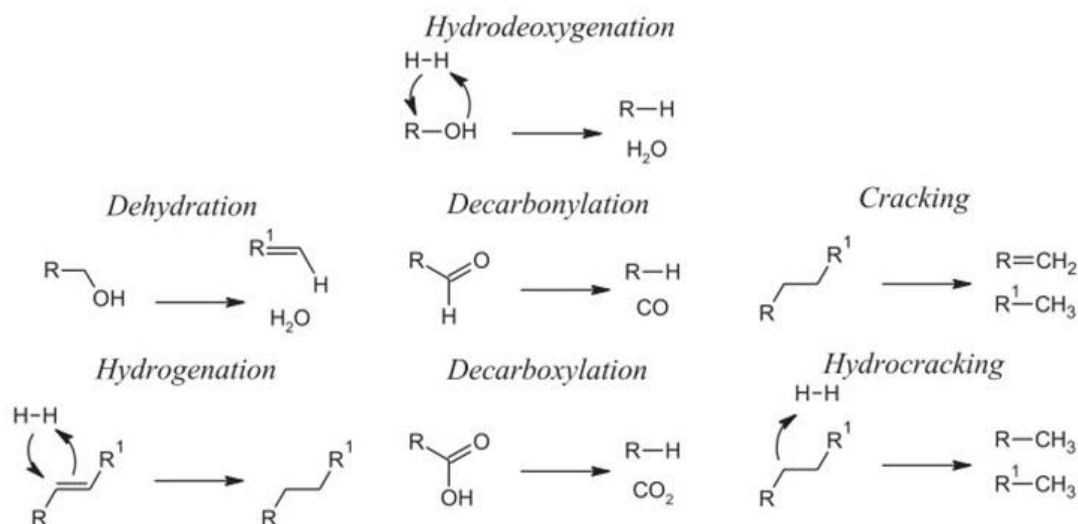
Bio-oils can be processed through hydrotreating reactions, promoting similar products to those obtained from fossil fuels, although the heteroatom compositions may change. In both cases, the hydrotreating units serve to hydrogenate unsaturated hydrocarbons and to remove heteroatoms. In bio-oils, the main heteroatom present is oxygen (nitrogen and sulfur are in negligible amounts), so the HDO reaction is critical to upgrade it. The HDO reaction involves combining a solid catalyst with a hydrogen-rich atmosphere to reduce the high oxygen content present in bio-oils and their derived compounds. The selective cleavage of C–O bonds over C=C hydrogenation and C–C cleavage is a milestone, targeting hydrocarbons as main products.

Most studies for the HDO reaction of biomass-derived compounds are carried out in liquid phase batch reactors. These, however, employ high temperatures and pressures, posing possible safety problems [2], besides the necessity of using solvents. In the gas phase, however, the reaction has been carried out satisfactorily under mild conditions for biomass-derived compounds, that is, pressures in the order of 1 atm and temperatures not greater than 500 °C [39,40].

The mechanism of typical HDO processes involves a series of complex and key reactions, including C–O bond hydrogenolysis, dehydration, decarboxylation, hydrogenation of unsaturated compounds, and hydrocracking through a carbocation mechanism. Bifunctional catalysts increase the variety of involved pathways, with different steps favored depending on reaction conditions, such as temperature, pressure, and H_2 partial pressure. While the ideal pathway effectively removes oxygen as water without altering the carbon chain, side reactions compete, reducing overall

carbon efficiency. Dehydration becomes prominent in the absence or very low partial pressure of hydrogen, but olefins presence is disfavored due to their hydrogenation to paraffins.

Figure 5. Representation of the main reaction mechanisms involved in HDO processes. Adapted from [2].



Moreover, hydrogenation, cracking, and hydrocracking reactions involving hydrocarbons occur concurrently with oxygen removal pathways, each mechanism schematically represented in Figure 5. The nature of oxygenated compounds significantly influences the mechanism, with aromatic carbon bonds displaying higher bond dissociation energies compared to aliphatic carbon bonds. This implies that oxygen removal from phenols and aromatic ethers is more difficult than from alcohols and aliphatic ethers. Thermodynamic studies of C-O bond cleavage have been elucidating these aspects, emphasizing the importance of selected operation conditions depending on the feedstock.

The HDO mechanisms and fundamentals have been primarily studied using model compounds due to the complexity of raw bio-oil conversion, which involves numerous side reactions and interactions between reactants. Various pathways have been proposed for the HDO of representative oxygenates found in bio-oil, such as ketones, common phenolics, furanics, guaiacol, and anisole. Given its reactivity, different pathways have been discussed for acetone HDO, most importantly the selective C-O bond cleavage leading to propene [41]. Phenolics, like phenol and cresols, represent a widely studied group of model compounds. Phenol HDO usually follows a two-step pathway with initial hydrogenation to cyclohexanol followed by

deoxygenation to cyclohexane. Furans, prevalent compounds in bio-oil, commonly undergo HDO toward pentane *via* decyclization-hydrogenation pathways [42]. The guaiacol HDO mechanism is usually intricate, encompassing diverse pathways like dehydroxylation, methoxy group elimination, and methyl shift reactions [2]. Anisole HDO mechanisms exhibit similar complexity [2]. Therefore, different model compounds are able to provide valuable insights into HDO mechanisms and pathways, shedding light on the efficient conversion of bio-oil constituents.

1.4. Commonly employed catalysts for hydrodeoxygenation processes

Catalysts play a pivotal role in the efficiency and selectivity of HDO processes. There are significant differences between the performance of noble metal-based catalysts and abundant metal-based catalysts, bulk or supported [2]. Noble metals such as Pt [43,44], Pd [45,46], Ru [47], and Rh [48] exhibit higher activity for hydroprocessing when compared to abundant metals, allowing milder operating conditions and promoting highly hydrogenated final products. However, noble metals are expensive, and their activity, in many cases, depends on the properties of the support used and the metal content, which may compromise economic viability. On the other hand, abundant metal-based catalysts, such as Ni [46,47], Co [41], Mo [49], and W [50], offer a more affordable alternative to noble metals. They usually present lower hydrogenation/hydrogenolysis activity, avoiding extensive saturation and C-C bond breaking.

The choice of the support plays a crucial role for the catalysts efficiency and stability during HDO reactions. “Neutral” supports, such as α -Al₂O₃ [51] and SiO₂ [52], usually promote good metal particles dispersion. On the other hand, acidic supports, such as γ -Al₂O₃ [53] and zeolites [54], are critical for the deoxygenation of the most refractory compounds in bio-oil, especially phenolics, due to simultaneous methyl transfer and hydrodeoxygenation reactions. However, these acidic supports may increase coke formation associated with acid catalyzed condensation reactions [2].

Among the best candidates, Mo-based catalysts have attracted great attention given the chemical versatility of molybdenum in both bulk and supported systems [55–60]. Within the commonly employed HDO reaction conditions, molybdenum can exhibit oxidation states spanning from +6 to +2, which allows for unique electronic properties for these catalysts [61,62]. Statistically, studies on Mo-based catalysts in the HDO reaction have significantly increased in recent years, as shown in Figure 6. A simple search on the Web of Science platform using "molybdenum" AND "hydrodeoxygenation" as keywords (title and abstract) revealed that about half of the verified works (161 entries) were published in the last 5 years. Approximately half of these reports focused on bulk catalysts, while the other half focused on supported catalysts. Among the bulk Mo systems, there was a preference for carbides, followed by oxides, sulfides, nitrides, and phosphides. Supported catalysts employed Mo in the form of these same materials, as well as mono- and bimetallic nanoparticles. The most commonly used supports were carbon, silica, alumina, and titania.

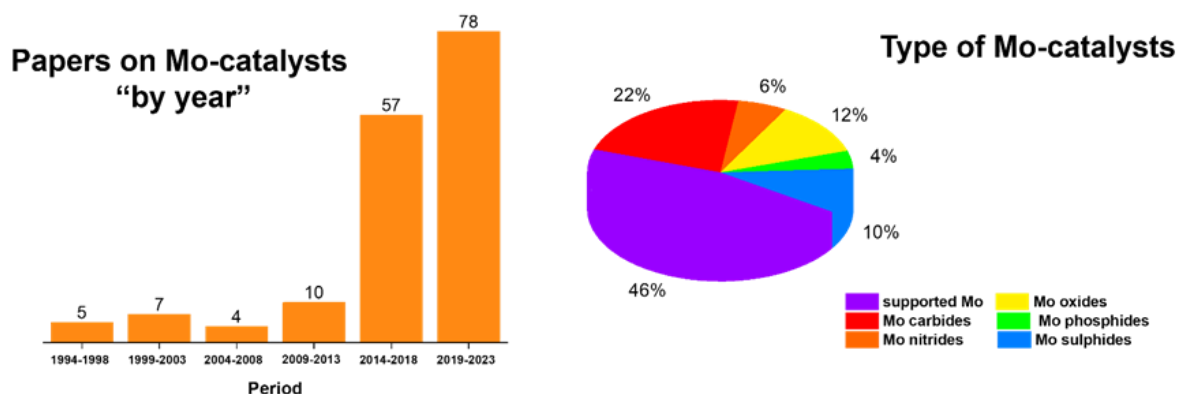


Figure 6. Statistics for "molybdenum" AND "hydrodeoxygenation" keywords search in Web of Science®, generating a total of 161 entries.

Each of these systems has its own characteristics, especially regarding the role of $\text{Mo}^{\delta+}$ species in the main and side reactions that make up the intricate network of HDO. Special attention should be given to molybdenum carbide and oxide catalysts, as under the reducing/carburizing HDO atmosphere, the formation of oxycarbide phases invariably occurs at determinate temperatures [63], leading to an extensive debate among prestigious research groups about which phases would be truly active in these cases, motivating numerous works in this direction [39,58,64–68].

1.5. Mo-based catalysts for hydrodeoxygenation processes

Mo-based compounds are versatile materials due to their unique structural and electronic properties. As stated, molybdenum can span through a wide range of oxidation states (0, +2, +3, +4, +5, and +6), allowing the formation of a variety of materials with different properties (e.g. composition, band structure, crystalline domain, electronic environment, catalytic activity, etc.).

Promoted and unpromoted MoS₂ catalysts are traditionally employed as hydrodesulfurization (HDS) catalysts in petroleum refining industries. They represent one of the earliest catalysts studied for the HDO of bio-oil and its derivatives [69–71]. Since then, a spectrum of molybdenum compounds, such as nitrides and phosphides, and particularly oxides, carbides, and mixed oxycarbide phases, has been under intense scrutiny for their potential as efficient HDO catalysts [71].

1.5.1. Molybdenum oxides

Oxides are the most common configuration for molybdenum compounds, in which [MoO₆] octahedra are the fundamental building blocks, comprising fully oxidized polymorphs (e.g., α -MoO₃, β -MoO₃, and h-MoO₃), and more reduced counterparts (e.g., MoO₂, Mo₂O₃, and MoO). Table 2 summarizes the most relevant structural properties of some of the main molybdenum oxide structures.

MoO₃ polymorphs present a rich variety of crystal structures, including monoclinic, orthorhombic, and hexagonal systems. Each of these systems is composed of [MoO₆] octahedra units arranged in distinct configurations, with α -MoO₃ and β -MoO₃ being the most common phases. The orthorhombic phase (i.e., α -MoO₃) is the most thermodynamically stable polymorph at room temperature and ambient pressure. It presents a layered structure of distorted [MoO₆] octahedra units arranged through edge-sharing zigzag rows along the (001) direction and corner-sharing rows along the (100) direction (Figure 7), while weak van der Waals interactions are responsible for their stacking [72–75]. The monoclinic system (i.e., β -MoO₃) is a metastable polymorph composed of distorted [MoO₆] octahedra arranged in a three-dimensional network through corner-sharing connections. The hexagonal system (i.e., h-MoO₃) is a metastable polymorph composed of [MoO₆] zigzag chains connected by corner-sharing units along the c-axis, giving rise to one-dimensional tunnels capable

of intercalating different cations [76,77]. The phase transition from β -MoO₃ to α -MoO₃, and h-MoO₃ to α -MoO₃ polymorphs can be induced by thermal treatments at temperatures above 320 °C and 440 °C, respectively [78–80].

Table 2. Relevant structural properties of main molybdenum oxide structures.

	α -MoO ₃	β -MoO ₃	h-MoO ₃	β -MoO ₂	t-MoO ₂
collCode	35076	80577	135008	152316	71194
Geometry	Orthorhombic	Monoclinic	Hexagonal	Monoclinic	Tetragonal
Space Group	Pbnm	P21m	P63m	P21c	P42mm
Mo site	Mo ⁶⁺ at O _h	Mo ⁶⁺ at O _h	Mo ⁶⁺ at O _h	Mo ⁴⁺ at T _d	Mo ⁴⁺ at T _d
Mo-Mo distance	3.43 Å	a) 3.67 Å b) 3.84 Å	3.32 Å	a) 3.13 Å b) 3.73 Å	4.85 Å
O-O distance*	2.66 Å	2.71 Å	3.50 Å	2.70 Å	2.71 Å
Mo-O distance	a) 1.67 Å b) 1.73 Å c) 1.95 Å d) 2.33 Å	a) 1.72 Å b) 1.87 Å c) 2.20 Å d) 2.27 Å	a) 1.72 Å b) 1.96 Å c) 2.19 Å	a) 1.77 Å b) 2.03 Å c) 2.18 Å	2.07 Å
Lattice Parameter	a=3.96 Å b=13.86 Å c=3.70 Å	a=7.18 Å b=7.61 Å c=10.50 Å	a=10.59 Å b=10.59 Å c=3.72 Å	a=5.61 Å b=4.86 Å c=5.62 Å	a=4.85 Å b=4.85 Å c=2.81 Å
No. of atoms/cell	4 Mo ⁶⁺ 12 O ²⁻	2 Mo ⁶⁺ 6 O ²⁻	2 Mo ⁶⁺ 6 O ²⁻	4 Mo ⁴⁺ 8 O ²⁻	2 Mo ⁴⁺ 4 O ²⁻

* closest distance

MoO₂ is an unusual transition metal oxide owing to its semi-metallic nature [73,81]. Monoclinic β -MoO₂ crystallizes in a distorted rutile structure, in which the [MoO₆] octahedra units are arranged in corner-sharing sheets in the *bc*-plane, and form chains of edge-sharing octahedra along *a* [73,81]. The semi-metallic nature of β -MoO₂ originates from the short Mo-Mo distances (c.a., 2.5 Å) caused by the distortions of the octahedra in the chains along *a* [73,81,82]. MoO₂ can also crystallize in its tetragonal polymorph (t-MoO₂), arranged through edge- and corner-sharing [MoO₆] octahedra. Representations of the MoO_x polymorphs are depicted in Figure 7.

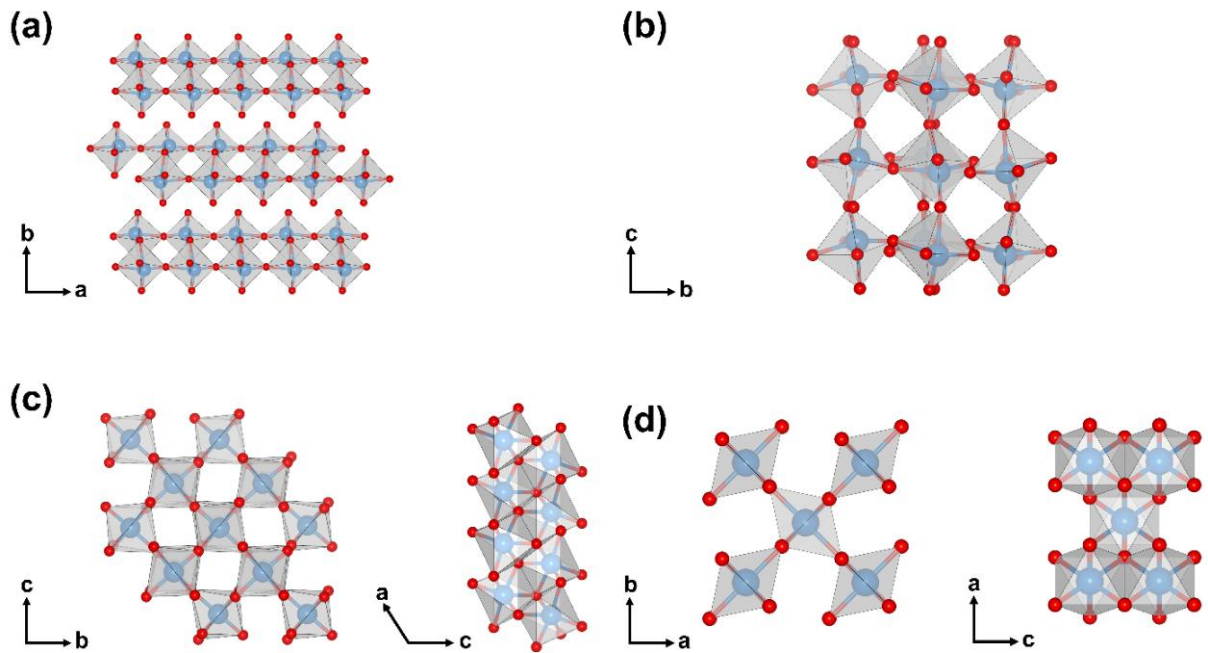


Figure 7. Structural models of (a) orthorhombic α - MoO_3 , highlighting its layered nature, (b) monoclinic β - MoO_3 , (c) monoclinic β - MoO_2 and (d) tetragonal t - MoO_2 .

It is important to highlight that nanosized domains of molybdenum oxides can lead to crystal structures that differ from the expected bulk counterparts. An elegant example was reported by Christiansen *et al.* [83], through the investigation of the relationship between structure, size, and properties of MoO_2 materials employing detailed atomic pair distribution function analysis combined with high-resolution electron microscopy. MoO_2 nanostructures were synthesized with different degrees of crystallinity: amorphous, nanosized, and bulk crystalline domains. They were able to demonstrate the presence of a high concentration of defects in domains of 3-5 nm, associated with extended defects, while the average bulk crystalline domains retained a disordered rutile structure. Representative high-resolution TEM images are illustrated in Figure 8 for amorphous, nanostructured, and bulk crystalline domains, depicting the different degrees of crystallinity of nanostructured MoO_2 particles.

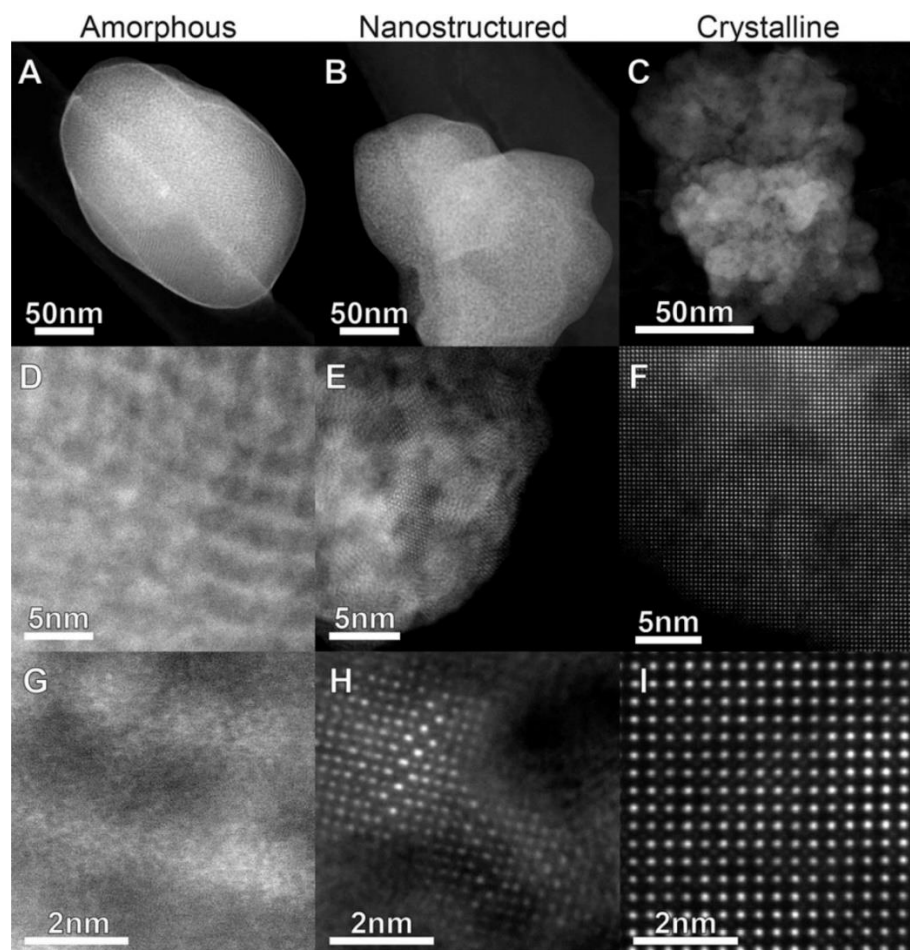


Figure 8. Representative high resolution TEM images of the three different types of MoO_2 samples at different magnifications. A, D, and G show the amorphous type samples; B, E, and H show the nanostructured samples; and C, F, and I show the crystalline samples. Images C, F, H, and I were collected with samples aligned along the $[001]$ zone axis. Extracted from [83].

According to the Wulff construction [84], a particle's morphology is directly related to its crystal structure and the surface tension of the exposed crystal facets. Thus, exploring different morphologies of molybdenum oxides, such as nanoparticles [83], nanorods [85], nanobelts [77], and two-dimensional sheets [86], can be beneficial to expose preferential facets and enhance the material's performance. Trzciński *et al.* [87] employed pulsed laser deposition to grow preferentially oriented MoO_3 crystalline films onto FTO substrates. The electrochemical properties of the substrates preferentially oriented in the (011) and (102) facets were enhanced due to the facilitated intercalation of cations into the structural gaps; while when (00k) facets were exposed, improvements in the hydrogen evolution were observed. Zhang *et al.* [88]

prepared layers of MoO₂ with primarily exposed (010) facets through the carbothermic reduction of MoO₃. They demonstrated that the high availability of (010) facets enhanced the oxygen reduction reaction by facilitating the access of oxygen to the surface of the catalyst and decreasing the energy barriers of the reactional mechanism. The coupling of experimental data and DFT calculations supported their hypothesis. In a last example, Zhang *et al.* [89] combined experimental evidence and DFT calculations to demonstrate that Fe-doping can regulate the crystal facets of MoO₃, reducing the energy barrier of the reaction pathway, and accelerating the oxygen evolution reaction kinetics by the modulation of the electronic structure and improvement of the conductivity of the material.

Oxygen vacancy defects, [MoO₆] octahedra distortions and conformation, and stacking faults also play a significant role in shaping the properties of molybdenum oxides [90–93]. These structural features can directly impact the electronic properties, surface reactivity, and catalytic performance, and their control and design can provide opportunities for tailoring material for targeted applications. Oxygen vacancies are among the most common defects in molybdenum oxides and are frequently associated with the enhancement in the materials' performance [90,91,94]. For catalysis, in special for bio-oil upgrading reactions, these vacancies play a pivotal role in the redox properties of the material, being responsible for enhancing the catalytic performance towards deoxygenation through the reverse Mars-van-Krevelen mechanism [94].

In summary, molybdenum oxide's structural complexity, morphology, polymorphism, and defects yield both challenges and opportunities for materials design and engineering. Understanding its structural and electronic properties is crucial for enhancing its performance and play a pivotal role in the design of tailored catalysts.

As stated, oxides represent the most stable form of molybdenum compounds. Among them, the crystalline α -MoO₃ stands out as the most common and stable molybdenum oxide phase. Consequently, it is predominantly referred to when simply using the MoO₃ formula. MoO₃ has been widely employed in the oxidation of hydrocarbons [95], hydrocracking [96] and desulfurization [97]. It is suggested that the Mo-O bond strength plays a key role in the C-O bond formation during selective oxidation of hydrocarbons [98]. Compared with other reducible metal oxides, the Mo-O bond in MoO₃ is relatively strong, and significantly stronger than the majority of C-O bonds present on oxygenated compounds [99,100]. Hence, the potential of MoO₃ as a

HDO catalyst has been the subject of investigation for a long time, particularly in its ability to selectively remove oxygen atoms from oxygenates without affecting C-C or C=C bonds, through the already mentioned reverse Mars-van-Krevelen mechanism on oxygen vacancies [94,101].

While numerous theoretical studies have explored the MoO_3 electronic structure and also the formation of hydrogen molybdenum bronzes (H_xMoO_3) [73,102,103], there is a scarcity of reports regarding the catalytic reactivity of MoO_3 . In a pivotal study [104], the acrolein HDO mechanism on a Mo_3O_9 cluster was investigated using a theoretical approach. Under H_2 atmosphere, water formation generated an oxygen defect site on the Mo_3O_9 cluster, enhancing acrolein adsorption and further transformation. Despite multiple thermodynamically favorable pathways, allyl alcohol predominated due to its lower formation barrier compared to the ideal HDO pathway.

In another work [67], the elementary steps for acetone HDO to propylene over MoO_3 surface have been investigated. The analysis also showed the preferential creation of an oxygen vacancy, making the MoO_3 surface approach metallic behavior. The most favorable pathway for deoxygenation involves a surface-mediated two-step process, starting with the adsorption of acetone onto a single oxygen vacancy, leading to the formation of chemisorbed propylene, as illustrated in Figure 9. This mechanism involves the dissociative chemisorption of H_2 on adjacent surface oxygen atoms, followed by an H transfer to form a water molecule. Subsequently, acetone adsorption on the oxygen-deficient unsaturated $\text{Mo}^{\delta+}$ site results in a Mo-O bond, leading to the formation of acetone enolate. Finally, propylene is released into the gas phase while oxidizing the surface back to a pristine MoO_3 surface.

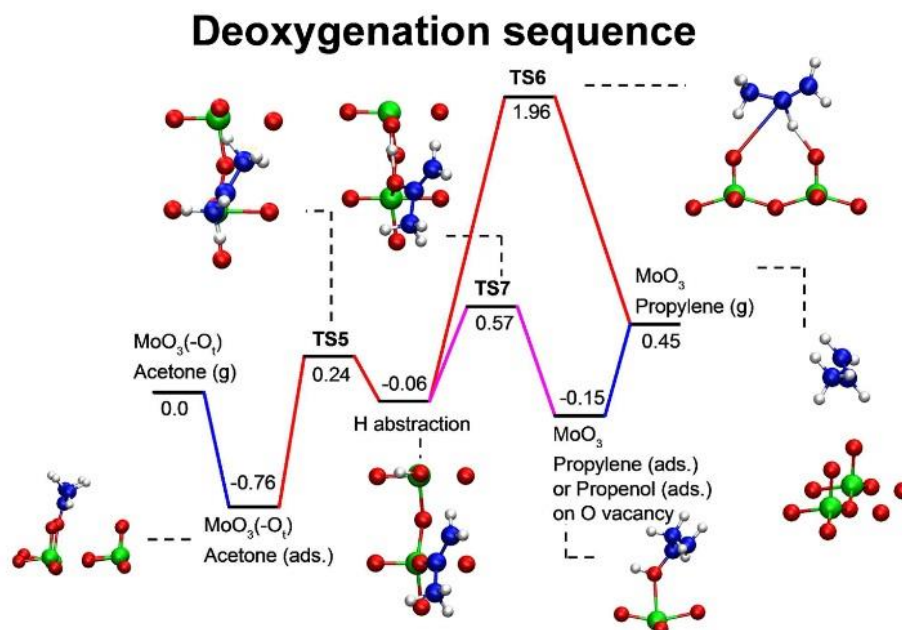


Figure 9. Reaction coordinate for acetone deoxygenation to propylene on α - MoO_3 (010) surface with a single terminal oxygen vacancy. Mo, O, C, and H are shown in green, red, blue, and white, respectively. All energies are in eV. Extracted from [67].

From another perspective, reduced molybdenum oxide surfaces (MoO_3 and MoO_2) were theoretically examined for anisole HDO [105]. It was found that Mo^{4+} on MoO_2 should exhibit the highest activity in removing oxygen from oxygenated compounds. Additionally, the study revealed H_2 chemisorption lower activation barriers for MoO_2 when compared to MoO_3 . On the other hand, analysis on anisole dissociation indicated strong binding for MoO_2 , which may contribute to its significant low activity during anisole HDO experiments, consistent with Sabatier's principle.

These findings underscore the significance of oxygen vacancy sites in molybdenum oxides (MoO_x), which play a crucial role in both the adsorption and direct deoxygenation of oxygenated compounds. Additionally, they emphasize the importance of H_2 chemisorption and dissociation, which are essential components for efficient HDO activity. However, under typical HDO reaction conditions, whether starting from bio-oils or their derivatives, with elevated temperatures (300-500 °C) and reducing/carburizing streams (H_2 /oxygenated substrate), MoO_3 undergoes significant structural changes. Initially, MoO_3 is partially reduced, leading to the generation of randomly distributed oxygen vacancies across the surface. As oxygen is removed, atomic rearrangement occurs to eliminate these vacancies through local collapses. Eventually, the structure of MoO_3 , composed of double lamellae of side-sharing

octahedra, undergoes a condensation process that results in the concurrent formation of monoclinic MoO_2 and oxycarbide phases [64,106,107]. In this way, the active HDO phases ultimately encompass more than just MoO_3 .

Furthermore, other active sites can also occur on the MoO_x surface, particularly acid sites, whose properties are determined and vary according to the reaction conditions, directly impacting the HDO catalytic outcome [70]. As previously stated, the initial chemisorption step is expected to occur at the oxygen vacancies. These vacancies facilitate Lewis acid/base interactions with the substrate, as the lone pair of oxygen in the target molecule is attracted to the unsaturated metal site. Thus, the reactivity of the system is partly influenced by the availability and strength of the Lewis acid sites on the catalyst. Research on the relative concentration of Lewis acid sites on various oxides suggests the following order: $\text{Cr}_2\text{O}_3 > \text{WO}_3 > \text{Nb}_2\text{O}_5 > \text{Ta}_2\text{O}_5 > \text{V}_2\text{O}_5 \approx \text{MoO}_3$ [108]. Naturally, the reduction of the MoO_3 surface should promote the formation of more Lewis functionalities. Another perspective highlights the relative strength of Lewis acid sites among different oxides: $\text{WO}_3 > \text{MoO}_3 > \text{Cr}_2\text{O}_3$ [109]. Following the reaction advancement, the subsequent step in the mechanism involves proton donation, relying on the presence of hydrogen available on the catalyst, typically in the form of hydroxyl groups for most oxides. For the catalyst to have proton-donating capabilities, Brønsted acid hydroxyl groups must be present on its surface. The relative Brønsted hydroxyl acidity among different oxides follows: $\text{WO}_3 > \text{MoO}_3 > \text{V}_2\text{O}_5 > \text{Nb}_2\text{O}_5$ [110]. In this context, the HDO activity of MoO_x is expected to depend on Lewis-type undercoordinated $\text{Mo}^{\delta+}$ sites and related oxygen vacancies, as well as Brønsted acid sites, represented by surface hydroxyl groups, which are further promoted under HDO reaction conditions.

Even before their structural, electronic, and surface properties became relevant within the context of bio-oil upgrading, supported MoO_x catalysts garnered interest for various hydrotreating reactions [111–113]. In the 1990s, alongside MoS_2 , Al_2O_3 based CoMo/NiMo catalysts were already commercially employed for gas-oil HDS [114]. In the subsequent years, bio-oils derived from biomass pyrolysis, and consequently, HDO valorization pathways gained prominence due to their numerous environmental advantages over fossil fuels. As a result, many studies followed, primarily focusing on investigating the HDO of model compounds, given the complexity of raw bio-oil conversion. Parallely, numerous studies employing MoO_x catalysts for direct oil valorization processes were undertaken [115–122], but the extensive promotion of side

reactions and unwanted interactions among reagents hindered more fundamental correlations between reaction mechanisms and catalysts' properties.

The investigation of model compounds HDO using MoO_x catalysts was mainly motivated by a pivotal study that screened several reducible metal oxides for their HDO ability: V_2O_5 , Fe_2O_3 , CuO , WO_3 , and MoO_3 [39]. Using acetone HDO as a probe reaction, MoO_3 presented the highest activity and selectivity to deoxygenated products. The MoO_x catalysts, bulk and supported, were then extended for use with other biomass-derived compounds, mainly phenol, m-cresol, anisole, guaiacol, dibenzofuran, among others.

Still regarding acetone, which is the simplest ketone representative, the acetone HDO reaction network proved to be extensive due to acetone high reactivity, leading to different products according to the nature of the catalytic sites [41,107,123]. Under acetone HDO reaction conditions, MoO_3 underwent partial carburization to a mixture of MoO_2 and, depending on the temperature, 350 or 400 °C, crystalline or amorphous oxycarbides, respectively [107]. These phases presented strong Brønsted acidity and were able to stabilize undercoordinated Mo^{5+} species with high hydrogenation/hydrogenolysis capability, promoting mainly propylene and propane [107].

When evaluated for the HDO of lignin-derived compounds, known to be less reactive than smaller molecules like acetone, MoO_x catalysts proved to be highly effective. A pioneering study demonstrated that MoO_3 could selectively convert various model compounds (phenol, m-cresol, anisole, guaiacol, and diphenyl ether) into aromatic hydrocarbons under atmospheric H_2 pressures [64]. Bond-dissociation energy (BDE) calculations suggest that the strength of each C–O bond type is influenced by the additional substituents in the ring (Figure 10 A) [124]. The trend of BDEs follows the order $\text{Ph-OH} > \text{Ph-OMe} > \text{Ph-O-Ph} > \text{PhO-Me}$, indicating that a $\text{C}_{(\text{etheric})}\text{-O}$ bond is generally more reactive than a $\text{C}_{(\text{aromatic})}\text{-O}$ bond. Although diphenyl ether exhibits the highest reactivity among all model compounds tested, MoO_3 preferentially cleaves phenolic Ph-OMe bonds over the weaker aliphatic PhO-Me bonds. The outcomes of m-cresol HDO revealed good stability at 320 °C, during which MoO_3 underwent partial surface carburization, leading to the formation of MoO_2 and crystalline Mo-oxycarbide (Figure 10 B) [125]. At 400 °C, MoO_2 was obtained (Figure 10 B), and the catalyst experienced significant deactivation. As seen for acetone HDO, the partially carburized catalyst may play a role in stabilizing undercoordinated Mo^{5+}

species on the surface, thereby slowing down the over-reduction into the MoO_2 phase (Figure 10 C) [126,127]. Given the lower *m*-cresol reactivity, here the oxygen vacancies associated with these undercoordination sites become essential for the selective cleavage of C-O bonds leading to toluene.

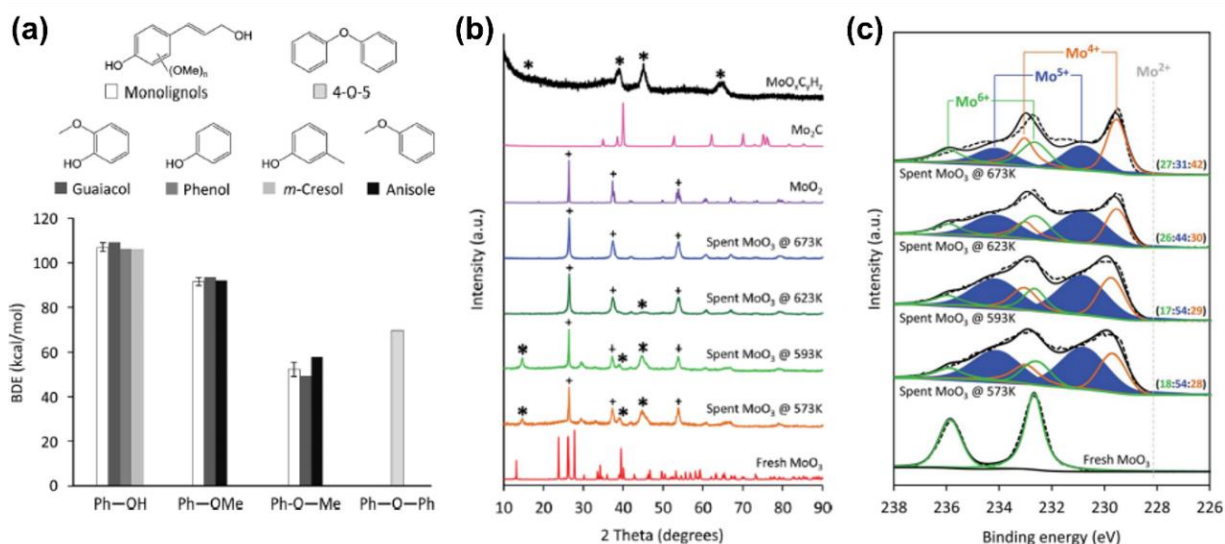


Figure 10. (a) Comparison of the homolytic bond dissociation energies (BDEs) of lignin-derived model compounds at 320 °C in gas phase. (b) Normalized XRD patterns of the spent MoO_3 catalysts after *m*-cresol HDO (in comparison with fresh MoO_3 , MoO_2 , Mo_2C and $\text{MoO}_x\text{C}_y\text{H}_z$ samples). The symbol (*) and (+) indicates the peak assignment corresponding to $\text{MoO}_x\text{C}_y\text{H}_z$ and MoO_2 phases, respectively. (c) XPS of the Mo (3d) energy region of the fresh and spent MoO_3 samples after *m*-cresol HDO. The numbers in parentheses are the corresponding oxidation state percentages of Mo^{6+} , Mo^{5+} and Mo^{4+} , respectively. Adapted from [64].

The activity of MoO_x in *m*-cresol HDO was further examined by investigating the impact of different metal oxide supports (SiO_2 , Al_2O_3 , TiO_2 , ZrO_2 , and CeO_2) on its redox behavior and reactivity [58]. All catalysts exhibit high toluene selectivity at 320 °C and using low H_2 pressures. The catalytic performance in HDO was strongly influenced by the reducibility of surface MoO_x species and the electronegativity of the support cation, except for CeO_2 . Data indicated that TiO_2 and ZrO_2 were the optimal supports, promoting high conversion and enhanced stability. As confirmed by electronic characterization, these supports played a crucial role in stabilizing intermediate Mo^{5+} states, consistently associated with elevated reaction rates and selectivity towards toluene. It is important to highlight that MoO_x species were

predominantly present as oligomeric domains on all supports, and there was no evidence of sintering under reaction conditions, nor the formation of MoO_2 and/or crystalline oxycarbide phases. This is a common trend for supported MoO_x catalysts, which usually exhibit good dispersions, even at higher loadings, until reaching the monolayer, only then forming crystalline particles [128].

Other studies have advanced in the investigation of bulk and supported MoO_x catalysts for the HDO of phenolic compounds [57,129–132], always relying on oxygen vacancy-driven mechanisms for selective C–O cleavage, usually associating it with the catalyst evolution promoting unsaturated Mo^{5+} sites. Furthermore, subsequent steps involving hydrogenation have also been explored for the production of saturated hydrocarbons through the combination of MoO_x with metal promoters. Platinum, nickel, and copper nanoparticles were uniformly dispersed on the surface of $\text{MoO}_3/\text{TiO}_2$ systems for p-cresol HDO [132]. The catalysts showed high conversions at 300 °C, following the order: Pt- > Ni- > Cu- $\text{MoO}_3/\text{TiO}_2$. The experimental data combined with DFT calculations show that all the metals behave as effective promoters for H_2 dissociation. These free H atoms then spillover accelerating the oxygen vacancies formation on MoO_3 , which are the active sites for the direct deoxygenation mechanism producing toluene. The low metal loadings were responsible for further obtention of methyl cyclohexane, without extensive methanation.

Within the HDO context, conventional phenolic compounds feature less reactive Ph–OH bonds for C–O cleavage, while anisole presents the etheric Ph–OMe bond, and guaiacol possesses both. The clear correlation between these structures implies that, for example, anisole and phenol are a natural part of the guaiacol HDO reaction pathways, as shown in Figure 11 [130]. Studies involving MoO_x , both bulk and supported, have shown a preferential conversion of guaiacol to phenol, with oxygen vacancies cleaving only the more reactive –OMe group [64,133]. On the other hand, the addition of other functionalities to the system, such as Ni nanoparticles, reportedly increases side reactions, leading not only to the –OH group cleavage yielding benzene but also to hydrogenation steps promoting cyclohexane [134]. For anisole HDO, most studies employing MoO_x catalysts deal with selectivity issues [59,68,135–137]. Anisole deoxygenation to benzene only occurred as a secondary reaction preceded by unwanted methyl transfer reactions yielding phenol and cresol (Figure 11). Catalysts with more pronounced metallic characteristics have shown better outcomes regarding selectivity [138–141].

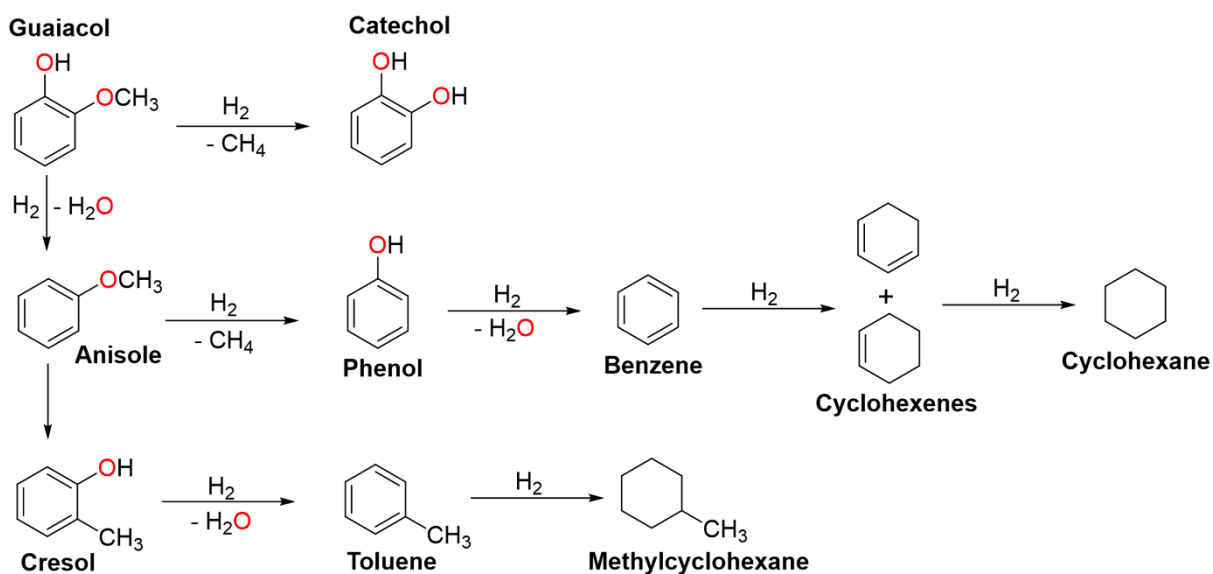


Figure 11. Main reaction pathways arising from guaiacol HDO conversion. Adapted from [130].

Non-phenolic model compounds, featuring different functional groups, were also evaluated for the HDO reaction over MoO_x catalysts. Fatty acids present long carbon chains and a terminal carboxylate group, $-COOH$, making them difficult to be fully deoxygenated. Many studies explored palmitic acid HDO and supported MoO_x catalysts, highlighting the role of oxygen vacancies and unsaturated Mo^{5+} sites [142–145]. Al_2O_3 , SiO_2 , and TiO_2 supports usually led to mixed results, promoting alkanes/alkenes, but mainly aldehydes [142–144]. The combination of MoO_x properties with zeolites acidity and microporous structure revealed good C-O cleavage rates, however smaller alkanes produced *via* hydrocracking predominate [145].

The HDO of polyols using MoO_x catalysts have shown only partial deoxygenation. Using Pd-modified MoO_3 catalyst, glycerol and erythritol, which present 3 and 4 -OH groups, yielded 1-propanol and 1,2-butanediol, respectively [146]. In turn, the HDO of furanics usually present high deoxygenation rates. Pt-modified MoO_3/MgO catalyst was 100 % selective for dibenzofuran HDO to phenylbenzene [147]. In both cases, further characterization indicated the formation of partially reduced MoO_x centers, in which unsaturated $Mo^{\delta+}$ sites should be responsible for C-O cleavage.

Furthermore, more comprehensive HDO investigations have been conducted using MoO_x catalysts to establish fundamental correlations with various substrates. An

insightful study focused on bulk MoO₃ for the HDO of 1-butanol, butanal, butyric acid, 2-butanol, 2-butanone, and THF [56]. The C₄ compounds typically produced a mixture of butene isomers and butane, with observed reactions including hydrogenation and dehydrogenation of carbonyl and hydroxyl groups, respectively, as well as deoxygenation to hydrocarbons. The overall reactivity towards C-O cleavage was found to follow the order C–OH > C=O > C–O–C; reiterating the results obtained through phenolic compounds.

1.5.2. Molybdenum carbides

Molybdenum carbides are composed of simultaneous contributions of metallic, covalent, and ionic bonds, giving rise to unique structural and electronic characteristics. The metallic, covalent, and ionic contributions are associated with the Mo-Mo bonds, Mo-C bonds, and charge transfer between molybdenum and carbon, respectively [148–150]. Due to these unique properties, molybdenum carbides are widely employed for various catalytic reactions [151].

Catalytically active molybdenum carbides are commonly composed of cubic (i.e., δ -MoC), hexagonal (i.e., α -MoC), and orthorhombic (i.e., β -Mo₂C) systems, with Mo atoms composing the lattice sites and C atoms residing in the interstitial sites between Mo atoms [148,152,153]. The δ -MoC phase presents a face-centered cubic arrangement, with each molybdenum atom surrounded by six carbon atoms; the α -MoC phase presents a hexagonal close-packed arrangement, with alternating molybdenum and carbon layers; while the β -Mo₂C phase is composed of an orthorhombic structure, with carbon atoms occupying half octahedral interstitial sites available in one layer, and half interstitial sites of the upcoming layer, in such a way that each molybdenum possesses three almost planar carbon neighbors, while each carbon atom coordinates with six molybdenum atoms within the structure [154,155]. Moreover, a d-band center analysis using DFT calculations indicated that, among these carbides, β -Mo₂C is the one with the stronger metallic character [152]. Table 3 summarizes the most relevant structural properties of these molybdenum carbide phases.

Table 3. Relevant structural properties of main molybdenum carbide structures.

	β -Mo ₂ C	h-Mo ₂ C	α -MoC	h-MoC
collCode	246146	197655	77157	44987
Geometry	Orthorhombic	Hexagonal	Cubic	Orthorhombic
Space Group	Pbcm	P63mmc	Fm-3m	P65mmc
Mo-Mo distance	a) 3.00 Å b) 2.92 Å c) 4.21 Å	2.93 Å	3.02 Å	a) 2.01 Å b) 3.01 Å
C-C distance*	3.06 Å	2.36 Å	3.50 Å	3.01 Å
Mo-C distance	2.06 Å	2.09 Å	2.14 Å	2.12 Å
Lattice Parameter	a=4.75 Å b=6.01 Å c=5.21 Å	a=3.00 Å b=3.00 Å c=4.72 Å	a=4.27 Å b=4.27 Å c=4.27 Å	a=3.01 Å b=3.01 Å c=14.61 Å
No. of atoms/cell	8 Mo ²⁺ 4 C ⁴⁻	2 Mo ²⁺ 1 C ²⁻	4 Mo ⁴⁺ 4 C ⁴⁻	6 Mo ⁴⁺ 6 C ⁴⁻

* closest distance

Molybdenum carbides are frequently obtained through thermal solid-gas reactions employing molybdenum oxides (e.g., MoO₃, MoO₂) as precursors in combination with simultaneous reducing and carburizing atmospheres [156,157]. The carburization process occurs through the output of oxygen from the metal oxide sublattice by the reducing environment and concomitant carbon insertion into the interstitial sites between molybdenum lattice sites. Alternative synthesis methodologies were also reported, such as carbothermal hydrogen reduction employing carbon nanotubes [158]; microwave-assisted carburization of MoO₃ and carbon black [62]; and a sol-gel like route employing urea [159]. It is important to highlight that additional molybdenum oxyhydride (MoO_xH_y) and oxycarbohydride (MoO_xC_yH_z) phases can also be formed [61,106].

The phase- and facet-dependent reactivity and performance of molybdenum carbides is also a crucial point for the development of catalysts. *In situ* HR-TEM measurements on the formation and annealing of molybdenum carbides using different carbon sources shed light on important features for the design and engineering of

carbide phases of molybdenum [160]. It was found out that the carburization of MoO_3 using an amorphous carbon film produced a hexagonal Mo_2C phase, on the other hand, when sucrose was employed the MoC phase was obtained. They suggested that the decomposition of sucrose led to a high portion of sp^3 and crosslinked carbon atoms with high reactivity, leading to the formation of cubic $\delta\text{-MoC}$ (interstitial sites fully occupied by C atoms). In contrast, when an amorphous carbon film was employed, the formation of hexagonal Mo_2C suggests that Mo atoms were just partially occupied by C, which could be associated with a lower reactivity of the carbon source. The growth evolution and restructuration of $\delta\text{-MoC}$ was also evaluated, from 500 to 1100 °C. It was possible to observe (111) to (100) facet changes with the increase in temperature, in which the (111) facet formed at low temperatures (<700 °C) had Mo- or C-terminated surfaces, with higher surface energy and reactivity; while (100) facets transitioned to (111) facets when heated above 900 °C, presenting a homogeneous C/Mo surface ratio, associated with enhanced stability. HR-TEM images and FFT patterns of the structural reconstruction of $\delta\text{-MoC}$ as a function of temperature are presented in Figure 12a-e, and a schematic representation of the facets evolution is presented in Figure 12f. Understanding how to control the phases and facets of molybdenum carbides allows the tuning of structural, electronic, and surface properties, helping in the development of new promising catalysts.

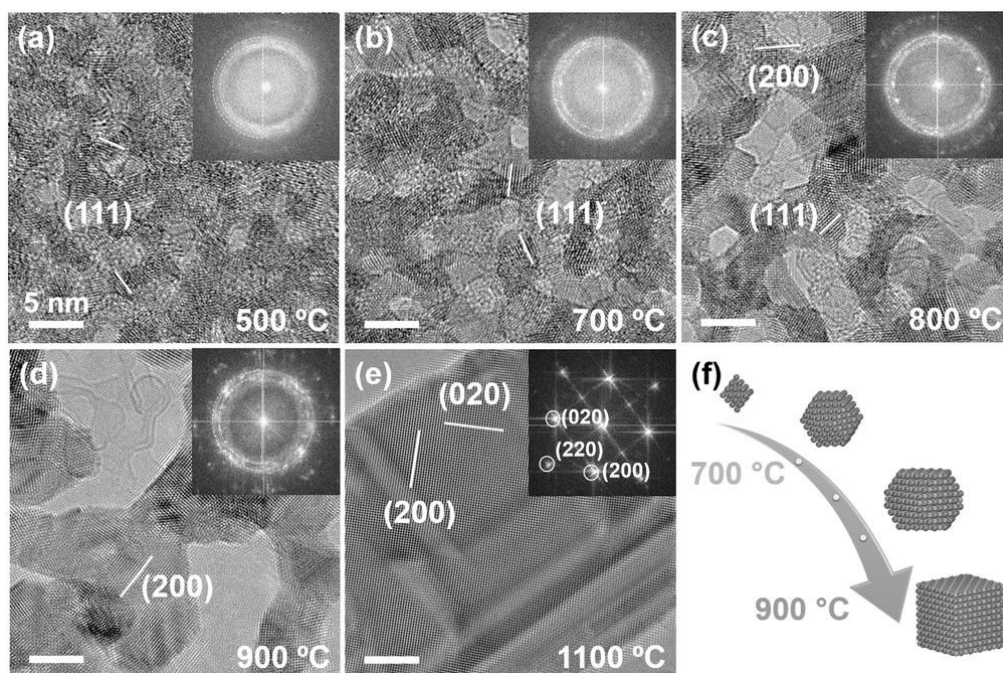


Figure 12. a–e) HRTEM images and FFT patterns of MoC at various temperatures (refer to each image). The scale bars are 5 nm for all images. f) Scheme showing the preferential facet changes with temperature increase. Extracted from [160].

Due to their unique structural and electronic characteristics, molybdenum carbides have been widely employed for various catalytic reactions: Fischer-Tropsch synthesis [161], hydrocarbon dehydrogenation [162], methanol reforming [163], hydrotreatment processes [164–166], among others.

Particularly, Mo_2C has demonstrated exceptional catalytic activity and selectivity in hydrogen-mediated reactions, typically facilitated by noble metals. Its preference arises from its resilience to CO and sulfur poisoning, as well as its superior resistance to sintering compared to noble metals [151]. As mentioned, it has been suggested that the incorporation of carbon atoms into the interstitial sites of molybdenum framework alters the electronic characteristics of molybdenum atoms, rendering Mo_2C more akin to metallic behavior in terms of activity [167], making it more prone to hydrogenation and hydrogenolysis reactions. At the same time, Mo_2C exhibits a strong oxophilic activity able to remove oxygen atoms effectively, which has been widely explored for the selective C–O bond cleavage required in HDO processes [168,169].

A theoretical study on the HDO of furfural, furfuryl alcohol, 2-methylfuran, and furan over a Mo_2C (101) surface proposes a mechanism involving two distinct sites for effective vapor-phase reaction [170]. Considering a surface with molybdenum and carbon exposed terminations, furanics adsorption is expected to occur on surface unsaturated molybdenum sites, while H_2 dissociative adsorption prefers surface unsaturated carbon atoms. Another theoretical study involving the same Mo_2C (101) surface for butyric acid HDO confirmed these findings [171]. It was shown that the more exposed molybdenum and carbon atoms are coordinatively unsaturated and present negative H_2 adsorption energies, while the less exposed molybdenum and carbon atoms are coordinatively saturated and present positive H_2 adsorption energies, rendering them inactive for H_2 adsorption. Furthermore, the rapid and stronger adsorption of H_2 on the more exposed surface carbon atoms promotes butyric acid adsorption on more exposed surface molybdenum atoms.

Nevertheless, the presence of oxygen in the reactant mixture is known to modify the Mo_2C properties [172,173]. The surface oxidation reduces the metallic character of Mo_2C , while concurrently enhancing its acidic nature, resulting in the formation of oxycarbides with bifunctional catalytic capabilities [172,174]. Figure 13 provides a representation of the transformation in Mo_2C functionality corresponding to varying oxygen content [172]. It is important to highlight that the presence of acid sites on Mo_2C

is dependent on several factors, including carburization conditions, passivation treatment, and the introduction of oxygen co-feed or other oxygenates during reaction. The titration of 2,6-di-tert-butylpyridine during reaction revealed that Brønsted acid sites were responsible for the dehydration of isopropanol to propylene over an oxygen-modified Mo_2C [175]. Furthermore, it was further reported that the proportion of acid sites can be adjusted by the phase/composition of Mo_2C , and the acid strength can be tuned by the carbide particle size [176]. In essence, acid sites may either exist inherently on Mo_2C or be formed during pretreatment or over the reaction. However, similarly to MoO_x catalysts, the importance of these acid sites in controlling reactivity varies depending on the reaction conditions.

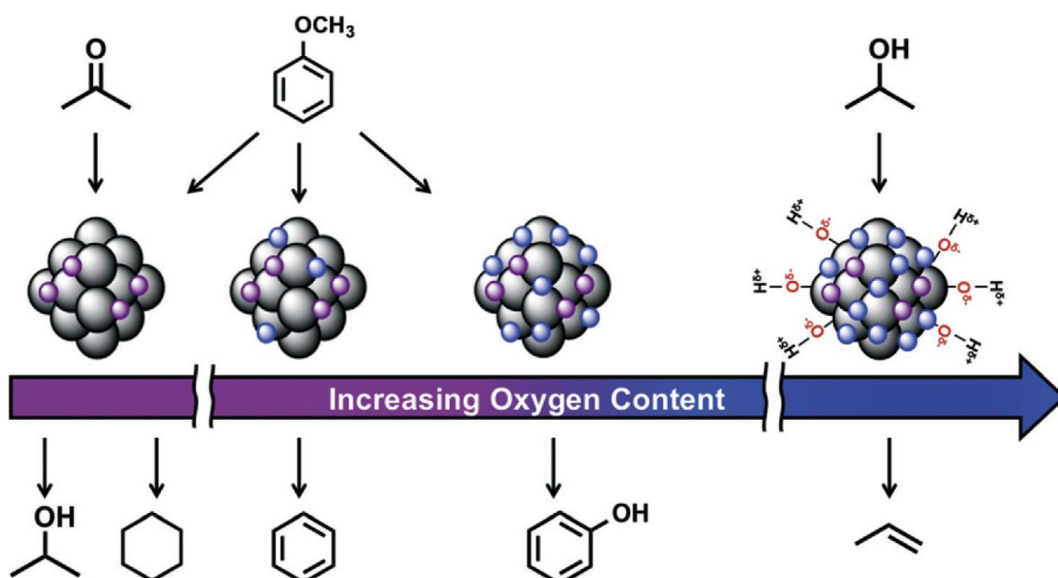


Figure 13. Schematic representation of the evolution of Mo_2C functionality with increasing oxygen content. Extracted from [172].

The impact of oxygen on the HDO activity of Mo_2C catalysts also extends to its electronic properties, as shown by operando near atmospheric pressure X-ray photoelectron spectroscopy (XPS) experiments [63]. During such experiments, MoO_3 and Mo_2C catalysts were tested for anisole HDO at 300 °C and low H_2 pressures (~1 mbar). The analysis indicated that the surface of fresh Mo_2C remains predominantly carbidic (~85 % Mo^{2+}) throughout the reaction, but undergoes a notable transformation acquiring a significant oxidic character (~15% of Mo^{4+} , Mo^{5+} , and Mo^{6+}). This modification suggests that the elevated HDO selectivity of Mo_2C may also stem from the presence of oxycarbide phases on its surface, leading to a preferential formation of benzene from anisole.

Similarly to what happened with MoO_x catalysts, Mo_2C primarily gained interest for hydrotreating reactions [177,178], given the extensive use of Mo_2S as a HDS catalyst in the 1990s [114]. Since then, with the increasing search for alternatives to fossil sources and the emergence of biomass as an abundant and renewable feedstock, many studies have dedicated themselves on the investigation of Mo_2C , both bulk and supported, for the valorization of bio-oils and their derived model compounds, mainly phenol, m-cresol, anisole, guaiacol, furfural, dibenzofuran, glycerol, among others [179,180]. Once again, numerous studies have utilized Mo_2C catalysts for direct oil valorization processes [181–187]. However, due to the complexity of raw bio-oils, these studies have encountered extensive promotion of side reactions and unwanted interactions among reagents, which have hindered the establishment of more fundamental correlations between reaction mechanisms and catalysts' properties.

As already shown in Figure 11, the model phenolic compounds studied for HDO present structural correlation and many common reaction pathways [130]. Conventional phenolic compounds like phenol and m-cresol feature less reactive Ph–OH bonds for C–O cleavage, while anisole presents the etheric Ph–OMe bond, and guaiacol possesses both.

There are numerous reports on guaiacol HDO using carbon-supported Mo_2C catalysts [188–194]. A parenthesis should be made here to emphasize that, among the many methods for preparing Mo_2C , the carbothermal reduction has been widely employed [180]. Through this synthetic route, molybdenum compounds react with carbon-supports under hydrogen flow and temperature, undergoing nucleation, growth, and facet development stages leading to well-defined particles [195]. The many variables involved lead to carbon-supported Mo_2C catalysts with different properties, from degree of carburization to Mo_2C particle size, which directly affect HDO activity. As expected, most guaiacol HDO studies using such catalysts reported preferential conversion of guaiacol to phenol, cleaving only the more reactive –OMe group. Additionally, the formation of catechols has been extensively observed, suggesting that the generation of phenol may involve the demethylation of guaiacol followed by the dehydroxylation of catechol [190]. Other studies focused on different supports. Pt/ Mo_2C supported on SBA-15 led to efficient guaiacol HDO producing mainly phenol, benzene and cyclohexane, through the combination of Pt metallic character and Mo_2C acidic properties generated on stream [196]. Mo_2C supported on

a bimetallic zeolitic imidazolate framework (ZIF), containing zinc and cobalt, preferentially converted guaiacol into phenol, but also cyclohexane [197].

For anisole HDO, most studies employing Mo_2C catalysts have shown high deoxygenation levels, resulting in the production of benzene without further hydrogenation to cyclohexane [65,198–200]. In contrast to guaiacol and other phenolics, which typically involve breaking less reactive Ph-OH bonds, anisole presents only the Ph-OMe bond for cleavage. Despite the well-known tendency of Mo_2C surface to be oxidized under typical HDO reaction conditions, an insightful study using CO titration highlighted the importance of oxygen in suppressing the metallic character of Mo_2C , thereby preventing extensive subsequent hydrogenation during anisole HDO, as depicted in Figure 14 [65]. An interesting strategy was employed by encapsulating Mo_2C nanoparticles inside a zeolite cavity [199]. In addition to high benzene yield, the close proximity of the zeolite Brønsted acid sites around the Mo_2C metallic sites was found to be the key factor for enabling high and stable anisole conversion and selectivity.

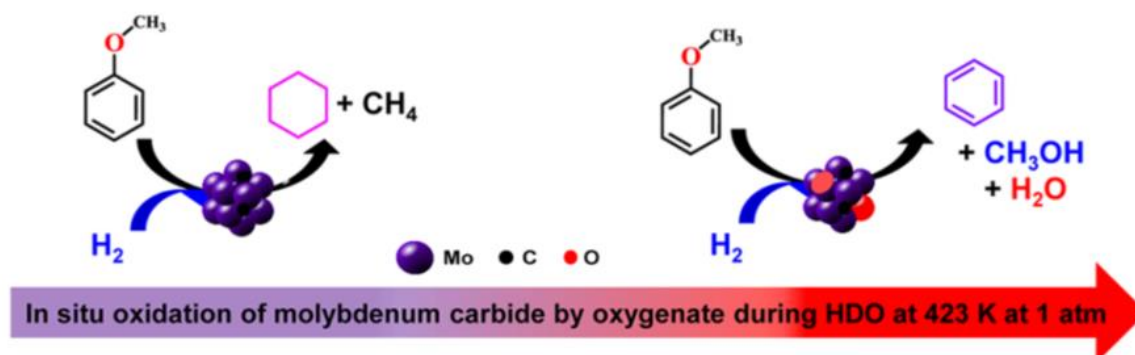


Figure 14. Schematic representation of the *in situ* oxidation of Mo_2C and its impact on anisole HDO activity. Adapted from [65].

Simpler phenolics, such as phenol and m-cresol, can undergo selective conversion to the corresponding deoxygenated aromatics, benzene and toluene, respectively, presenting high yields [201–205]. Despite the lower reactivity of Ph-OH bonds when compared to Ph-OMe bonds, unlike guaiacol, these simpler phenolics do not present adsorption competitiveness between such functionalities. An interesting insight was obtained through the *in situ* methanol and/or water titration during benzene/toluene hydrogenation reactions [202]. The data suggest that the inhibition of the aromatic hydrogenation function on Mo_2C during phenolic HDO reactions is a result of *in situ* surface modification by oxygenates.

Non-phenolic model compounds, featuring different functional groups, were also evaluated for the HDO reaction over Mo_2C catalysts. For furfural HDO, most studies showed good selectivity toward the carbonyl cleavage, however preserving the furanic structure [206–208]. On the other hand, for dibenzofuran HDO, totally deoxygenated products were mainly obtained [209]. Pure Mo_2C promoted biphenyl, while Ni-modified Mo_2C led to cyclohexylbenzene and bicyclohexane, as expected due to nickel enhanced metallic character [209,210].

Carboxylic acids HDO was also evaluated using Mo_2C catalysts. Oleic acid was mainly converted into paraffins when a carbon-supported Mo_2C catalyst was employed [210]. Substituting Mo_2C for W_2C , the selectivity shifts towards olefins, highlighting the hydrogenation capability of well dispersed Mo_2C . For acrylic acid HDO, Mo_2C promoted propane, showing that the reaction predominantly occurs by a dehydration/hydrogenation route [211]. Contrarily to what happens when using MoS_2 and noble metals, Mo_2C suppresses decarbonylation and decarboxylation routes, which would lead mainly to ethane.

Chapter 2. Motivation and proposal

Once we placed our interest in the HDO reaction of model molecules as a tool for fundamental studies over potential catalysts within the biomass valorization context, the starting motivations of this work involved the investigation of the high activity reported for MoO_x catalysts in HDO reactions; the invariable formation of MoO_xC_y phases under reducing/carburizing conditions; and the catalytic properties of these phases in relation to the $\text{MoO}_3/\text{Mo}_2\text{C}$ duality.

In this sense, the first part of this study aimed to provide new insights into the properties of active sites formed when MoO_3 nanopowder is exposed to an acetone HDO stream. The direct correlation of acetone HDO reaction pathways with different catalytic sites serves as a complementary tool to investigate the catalyst surface. Comprehensive textural, structural, and electronic characterization, coupled with catalytic data, enabled us to elucidate the formation and nature of active sites in $\text{MoO}_x/\text{MoO}_x\text{C}_y$ catalysts and their dependence on reaction conditions.

For the $\text{MoO}_x/\text{MoO}_x\text{C}_y$ phases, we show that the most active catalysts do not only present the more usual Mo^{6+} oxidation state, but greater amounts of lower oxidation states. Thus, it is possible that using transition-metal molybdates (MMo) would be beneficial to lower and stabilize the oxidation state of the molybdenum sites due to their enhanced redox properties under the reaction conditions, making these materials good candidates as HDO catalysts. Therefore, we also evaluated first-row transition-metal molybdates (Mn^{2+} , Fe^{3+} , Co^{2+} , Cu^{2+} , Zn^{2+}), additionally motivated by the abundance and affordability of such metals.

Finally, in an effort to enhance the accessibility of active sites within $\text{MoO}_x/\text{MoO}_x\text{C}_y$ and to combine them with other functionalities, supported zeolite catalysts were also investigated. ZSM-5 zeolite with varying Si/Al molar ratios (11.5, 40, and 140), resulting in different concentrations of acid sites, served as supports for MoO_x (Mo/zeolite) and the first-row transition metals (M/zeolite) previously studied as mixed molybdates. In addition to the primary goal of achieving bifunctionality, zeolites offer a high surface area due to their intricate framework of channels and cavities, thereby introducing a confinement effect that can significantly influence catalytic activity.

Chapter 3. Experimental section

3.1. Materials

All the employed reagents were purchased in high purity. Molybdenum oxide (MoO_3 , nanopowder/ MoO_2 , 99 %), copper oxide (CuO , nanopowder/ Cu_2O , 97 %), manganese(II) nitrate tetrahydrate ($\text{Mn}(\text{NO}_3)_2 \cdot 4\text{H}_2\text{O}$, ≥ 97.0 %), cobalt(II) nitrate hexahydrate ($\text{Co}(\text{NO}_3)_2 \cdot 6\text{H}_2\text{O}$, 98 %), nickel(II) nitrate hexahydrate ($\text{Ni}(\text{NO}_3)_2 \cdot 6\text{H}_2\text{O}$, ≥ 98.5 %), copper(II) nitrate (hemi)pentahydrate ($\text{Cu}(\text{NO}_3)_2 \cdot 2.5\text{H}_2\text{O}$, 98 %), zinc(II) nitrate hexahydrate ($\text{Zn}(\text{NO}_3)_2 \cdot 6\text{H}_2\text{O}$, 98 %), acetone (HPLC Plus Grade, ≥ 99.9 %), and isopropanol (anhydrous, 99.5%) were obtained from Sigma-Aldrich. Ammonium heptamolybdate tetrahydrate ($(\text{NH}_4)_6\text{MoO}_7 \cdot 4\text{H}_2\text{O}$) and iron(III) nitrate nonahydrate ($\text{Fe}(\text{NO}_3)_3 \cdot 9\text{H}_2\text{O}$, ≥ 99.0 %) were supplied by Supelco. Dichloromethane (CH_2Cl_2), Nitric (HNO_3 , 65-67 %), and hydrochloric (HCl , 37 %) acids were purchased from Synth. Trimethylphosphine oxide (TMPO) (≥ 95.0 %) was obtained from Alfa Aesar. Boric acid (H_3BO_3 , 99.5 %) was provided by ECIBRA. Hydrofluoric acid (HF , 40 %) was purchased from Merck. Commercial ZSM-5 zeolites ($\text{Si}/\text{Al} = 11.5$, CBV2314/ $\text{Si}/\text{Al} = 40$, CBV8014/ $\text{Si}/\text{Al} = 140$, CBV28014) were supplied by Zeolyst.

3.2. Methods

3.2.1 Bulk Mo-based catalysts

The bulk metal oxide catalysts were commercially obtained, while the first-row transition metal molybdate catalysts (Mn, Fe, Co, Cu, and Zn) were prepared following a standard synthesis describe elsewhere [212]. The general procedure involved the dissolution of 2.0 mmol of ammonium heptamolybdate tetrahydrate ($(\text{NH}_4)_6\text{MoO}_7 \cdot 4\text{H}_2\text{O}$) in 200 mL of water at 40 °C. Separately, the appropriate amount of each transition metal nitrate (2.0 mmol for Mn, Co, Cu, and Zn, and 1.3 mmol for Fe) was dissolved in 100 mL of water at room temperature. The transition metal solution was added to the molybdate one dropwise with the help of an autotitrator (5 mL min^{-1}). After the addition, the precipitated mixture was aged for 2 h under vigorous stirring at room temperature, washed with water, dried at 120 °C overnight, and calcined under air

atmosphere ($5\text{ }^{\circ}\text{C min}^{-1}$ until $500\text{ }^{\circ}\text{C}$, 4 h). The catalysts were called MMo, where M corresponds to the first-row transition metal (Mn, Fe, Co, Cu, or Zn).

3.2.2 Supported Mo/zeolite and M/zeolite catalysts

The metal/zeolite supported catalysts were prepared using a conventional wet impregnation method. Pristine ZSM-5 zeolites with Si/Al molar ratios equal to 11.5, 40, and 140, respectively called Z11.5, Z40, and Z140, were tested in the acetone HDO reaction. Only the Z140 sample was used to prepare the metal/zeolite catalysts. To achieve 5 at.% (metal atoms to zeolite silicon atoms) supported catalysts, 0.79 mmol of each transition metal salt (Mo, Fe, Co, Ni, and Cu) was dissolved in 40 mL of water under vigorous stirring. 1.0 g of zeolite was then added to the system that was sonicated at $\sim 60\text{ }^{\circ}\text{C}$ until dryness. The final solid was dried at $120\text{ }^{\circ}\text{C}$ overnight and calcined under air atmosphere ($5\text{ }^{\circ}\text{C min}^{-1}$ until $500\text{ }^{\circ}\text{C}$, 4 h). The catalysts were called M/Z140, where M denotes the dispersed metal (Mo, Fe, Co, Ni, or Cu), Z140 corresponds to the ZSM-5 zeolite with Si/Al molar ratio of 140.

3.3. Characterization

Powder X-ray diffractograms (XRD) were obtained in a Bruker D8 Advance Eco diffractometer, operating with $\text{CuK}\alpha 1$ radiation source ($\lambda = 1.5406\text{ \AA}$), 30 kV voltage, 10 mA filament current, and a Ni filter. The measurements were collected in the 20 to $60^{\circ} 2\theta$ range, with a step of 0.05° and speed of $3^{\circ}\text{ min}^{-1}$.

X-ray photoelectron spectroscopy (XPS) measurements were carried out using a monochromatic Al $\text{K}\alpha$ source on a K-alpha spectrometer (Thermo Fisher Scientific) equipped with a 180° double-focusing hemispherical analyzer with a 128-channel detector. Survey and selected atomic signals were obtained with a pass energy of 50 eV and a step of 0.02 eV. Casa XPS software package was used to analyze the spectra, and the XPS peaks were fitted using a mixed Gauss-Lorentz function and Shirley background. All the measured spectra were corrected by setting the reference binding energy (BE) of carbon (C 1s) at 285 eV. Mo 3d spectra were fitted based on a previously reported work [213] considering a spin-orbit splitting of 3.1 eV ($3d_{5/2} - d_{3/2}$) for Mo^{5+} and Mo^{6+} . Mo^{4+} species was fitted considering both screened and unscreened contributions, with $3d_{5/2}$ peaks around 230.3 eV and 231.2 eV, respectively, and spin-

orbit splitting of 3.2 eV [73,213]. Even though the Mo 3d fittings were carefully conducted following the work by Baltrusaitis *et al.* [213], the co-existence of mixed Mo oxidation states can still lead to uncertainties.

The acid sites in the samples were probed by ^{31}P MAS-NMR analysis of adsorbed TMPO in a 400 MHz (9.4 T) Bruker Avance-II+ equipped with a 4 mm MAS 4BL CP BB probe. The spectra were collected at 161.97 MHz, using a 10 KHz spinning rate and a $\pi/12$ pulse (1.93 μs), with a 3 s delay, using $(\text{NH}_4)_2\text{HPO}_4$ as the reference at 1.33 ppm. The procedure followed for sample preparation can be found elsewhere [214]. Firstly, 400 mg of the sample was subjected to a dehydration treatment at 120 °C for 2 h under vacuum. Subsequently, 40 mg of solid TMPO was dissolved in anhydrous CH_2Cl_2 , and then introduced into the vessel containing the dehydrated sample under N_2 atmosphere inside a glove box to avoid the TMPO decomposition. The system was left equilibrating for 1 h, allowing the TMPO diffusion and complete adsorption over the acid sites. The removal of CH_2Cl_2 was performed at 50 °C under vacuum. To remove the physisorbed TMPO, the sample was further subjected to thermal treatment at 150 °C for 1 h, once more under vacuum. Finally, the TMPO-loaded sample was transferred into a MAS rotor and sealed by a gas-tight Kel-F cap inside an N_2 glovebox. The ^{31}P MAS-NMR experiment was performed subsequently, using an HPDEC single pulse sequence with 5 s recycle delay and 10 kHz sample spinning with the accumulation of 1000 free-induction-decay signals. The spectra contributions were fitted using Gaussian functions, in which the chemical shift and FWHM were fixed with ± 0.3 ppm and ± 1.0 ppm constraints, respectively. The acid site strength and type were determined based on the work of Wiper *et al.* [215].

The TMPO-loaded samples were subjected to phosphorus (P) elemental analysis by Inductively Coupled Plasma Optical Emission Spectrometry (ICP-OES) to quantify the acid sites. The amount of phosphorus obtained was directly related to the total available acid sites since each TMPO molecule adsorbs just at one acid site. The samples were digested overnight using a combination of acids: 2 mL HF: 4 mL HNO_3 : 4 mL HCl. Then, a saturated solution of H_3BO_3 was used to reduce the free fluoride ion concentration. The analysis was performed in an ICP-OES Analytik Jena apparatus, Model Quanta Elite, using a power of 1200 W. The calibration curve obtained using an external standard calibration method is presented in Figure A2.

N₂ physisorption was carried out in a NOVA 4200e Quantachrome Equipment to determine the specific surface area using the Brunauer–Emmett–Teller (BET) model. The samples were degassed by pretreatment at 120 °C for 2 h before analysis.

The thermogravimetric analysis (TGA) was performed in a TA equipment model SDT Q600 with N₂/synthetic air gas flow of 100 mL min⁻¹, with a heating rate of 10 °C min⁻¹ up to 1000 °C.

Temperature-programmed desorption of acetone (acetone-TPD) was also carried out using a triple filter quadrupole HPR-20 Hiden Analytical Mass Spectrometer. 500 mg of sample were placed in a quartz reactor and treated under He flow (30 mL min⁻¹) for 1 h at 200 °C. After cooling down to room temperature, acetone vapor was adsorbed over the sample by pressurizing the reactor up to 1.5 bar absolute (~20 mmol of acetone; 0.15:0.85 acetone:helium) for 10 min; the weakly physisorbed acetone was removed using a He flow (30 mL min⁻¹) for 2 h, also at room temperature. Finally, the sample was heated up to 500 °C (5 °C min⁻¹) under He flow (30 mL min⁻¹), and the acetone desorption was monitored, as well as the formation of propene, methane, and carbon dioxide.

Temperature programmed reduction under H₂ atmosphere (H₂-TPR) was performed in a triple filter quadrupole HPR-20 Hiden Analytical Mass Spectrometer. A quartz reactor was loaded with 100 mg of sample and treated under He flow (30 mL min⁻¹) for 1 h at 200 °C. After cooling to room temperature, the sample was reduced under 10% H₂/He flow (30 mL min⁻¹) at a heating rate of 5 °C min⁻¹ up to 800 °C.

Scanning electron microscopy (SEM) was performed using a Quanta 250 emission field scanning electron microscope (FESEM), operated at an acceleration voltage of 10 kV. It was equipped with an Oxford X-MAX50 dispersive energy spectrometer to perform elemental analysis (EDX). Before the analyses, the samples were deposited on a brass support over a carbon tape.

X-ray fluorescence (XRF) analyses to determine the commercial zeolites Si/Al molar ratios were carried out in a Shimadzu-XRF1800 fluorescence spectrometer. A 40 kV rhodium source was used with 95 mA current. Analyses were performed under vacuum, with continuous rotation of the sample, 8 ° min⁻¹, 0.1 ° steps. The fundamental parameters protocol was used to determine the elements concentration.

The aluminum environments on the commercial zeolites were probed by ²⁷Al MAS-NMR analysis in a 400 MHz (9.4 T) Bruker Avance-II+ equipped with a 4 mm MAS 4BL CP BB probe. The spectra were collected at 104.26 MHz, using a 10 KHz

spinning rate and a $\pi/12$ pulse (0.35 μ s), with a 2 s delay, using an acid solution of $\text{Al}(\text{NO}_3)_3$ as the reference at 0 ppm.

3.4. Catalytic Evaluation

3.4.1. Acetone HDO set up and main products

Gas-phase acetone HDO reaction was conducted in a plug-flow tubular reactor equipped with a quartz tube (inner diameter of 8.1 mm) with a catalytic bed composed of 50 mg of catalyst and 150 mg of diluent (quartz powder; <100 mesh). Acetone was introduced into the reactor using a saturation flask (2.4 mL min⁻¹ of acetone) and He as the carrier gas. H₂ was also fed to the reactor (51 mL min⁻¹; 21 mol H₂:mol acetone), using He for balance, achieving a total feed flow of 100 mL min⁻¹. Isopropanol HDO was also performed, maintaining similar conditions (2.4 mL min⁻¹ of isopropanol, 51 mL min⁻¹ of H₂, 21 mol H₂:mol isopropanol, 100 mL min⁻¹ total). Two different catalytic tests were carried out: temperature ramps, to map the catalytic activity of the samples as a function of temperature, and isothermal tests, to analyze the effect of time on stream (TOS). In each test, a new load of catalyst was always used. The sample was heated under H₂ to the target temperature (10 °C min⁻¹), and the substrate (acetone or isopropanol) was introduced. For some post-reaction characterization, the catalysts were submitted to the same reaction conditions without diluent and using higher loadings.

The reaction products were analyzed by an online gas chromatograph (GC; Agilent Technologies, model 7890A) equipped with two columns, HP-1 and HP-MOLESIEVE, with FID and TCD detectors. Substrate conversion (acetone or isopropanol), products' distribution, yield, and carbon balance were calculated as follows in Equations 1–4.

Equation 1.

$$\text{Conversion (C - mol \%)} = \frac{\text{carbon moles of consumed reactant}}{\text{carbon moles in reactant feed}} \cdot 100\%$$

Equation 2.

$$\text{Product distribution (C – mol \%)} = \frac{\text{carbon moles of product}}{\text{carbon moles of all products}} \cdot 100\%$$

Equation 3.

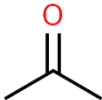
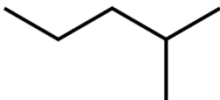
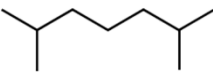
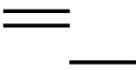

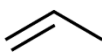
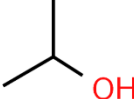
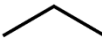
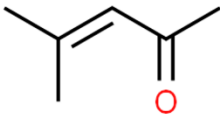
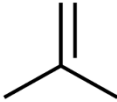
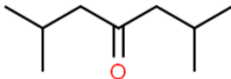
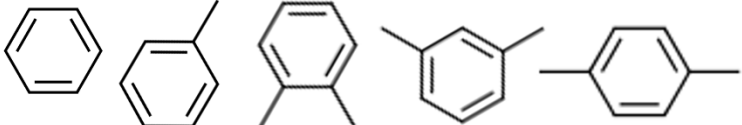
$$\text{Yield (C – mol \%)} = \frac{\text{Conversion (C – mol \%)} \cdot \text{Product distribution (C – mol \%)}}{100}$$

Equation 4.

$$\text{Carbon balance} = \frac{\text{carbon moles of all products}}{\text{carbon moles in reactant feed}}$$

The main products detected in acetone HDO were methane (C₁), ethene/ethane (C₂), propane (C_{3A}), propene (C_{3E}), isobutene/isobutane and isomers (C₄), hexene/hexane and isomers (C₆), nonene/nonane and isomers (C₉), carbon dioxide (CO₂), isopropanol (IPA), methyl isobutyl ketone and isomers (C_{6O}), diisobutyl ketone and isomers (C_{9O}), and aromatics, such as benzene, toluene, and xylenes (BTX). In Chapter 4, alkanes and alkanes other than C_{3E} and C_{3A} (C₁, C₂, C₄, C₆, and C₉) will be summarized as C_n products. In Chapters 5 and 6, hydrogenation/hydrogenolysis products (C₁, C₂, C_{3A}, IPA = HHP), coupling deoxygenated products (C₄, C₆, C₉ = CDP), direct deoxygenation products (C_{3E} = DDP), and oxygenated products (CO₂, C₂HO, C_{6O}, C_{9O} = OP), will be referred together using these nomenclatures. The structural formulas of acetone and the main products are depicted in Table 4. Carbon balances were commonly close to ideal, slightly dropping with TOS and/or depending on the temperature (still > 85 %).

Table 4. Structural formula of acetone and main products obtained through acetone HDO reaction.

Acetone (ACE)		hexene/hexane and isomers (C ₆)	
methane (C ₁)	CH ₄	nonane/nonene and isomers (C ₉)	
ethene/ethane (C ₂)		carbon dioxide (CO ₂)	
propene (C ₃ E)		isopropanol (IPA)	
propane (C ₃ A)		methyl isobutyl ketone and isomers (C ₆ O)	
isobutene/isobutane and isomers (C ₄)		diisobutyl ketone and isomers (C ₉ O)	
benzene, toluene, and xylenes (BTX)			

3.4.2. Effect of diffusive transport phenomena

This section is based on experimental data presented in Chapter 10, Section 10.1, focusing on the evaluation of two transfer steps: diffusion from the fluid bulk to the external surface of the catalytic particle (external diffusion), and diffusion within the particle to the catalytic site (internal diffusion) [216]. The catalysts under analysis correspond to the systems outlined in Chapters 4, 5, and 6: commercial MoO₃ nanopowder, FeMo mixed oxide, and Z140 pristine zeolite, respectively. The pores are considered as the unstructured void fraction within the aggregate of particles constituting the catalyst powder.

For the assessment of external mass and heat transfer, the Mears criterion was employed as a quick method to estimate limitations [216]. Regarding mass transfer, the Mears number, defined in Equation 5, was calculated. Thermophysical properties of the fluid were estimated using the Fuller-Schetter-Giddings correlation for binary and mixture diffusivities, Chapman-Enskog theory for dynamic viscosity, and Ranz correlation for the Sherwood number, under the condition of Reynolds number $\ll 1$ [216]. A value of $MR < 0.15$ indicates the absence of external mass transfer limitations.

Equation 5.

$$MR = \frac{-r'_A(obs) \rho_b R_n}{K_c C_{AB}}$$

where:

$r'_A(obs)$ = observed reaction rate, kmol/kg cat.s.

ρ_b = catalyst bed bulk density, kg/m³.

R = catalyst particle radius, m.

n = reaction order – assumed as one.

k_c = mass transfer coefficient, m/s, calculated from the Ranz correlation.

C_{Ab} = bulk concentration of acetone, mol/dm³.

On the other hand, for heat transfer, the corresponding Mears number is calculated as shown in Equation 6. Activation energies were determined also using the experimental data presented in Chapter 9, Section 9.1, with conversions not exceeding 10%, assuming a first-order reaction with acetone. Thermal conductivities for the gases were acquired from the DWSIM software.

Equation 6.

$$MR = \frac{|\Delta H_r| - r'_A(obs) R E_{at} \rho_b}{h R_g T_0^2}$$

where:

R_g = 8.314 J/(K.mol).

E_{at} = activation energy, J/mol.

T_0 = reaction temperature, K.

ΔH_r = reaction enthalpy at T_0 , J/mol.

h = heat transfer coefficient, calculated from $Nu = 2,0$ as $Re \ll 1$.

Internal mass transfer was assessed using the Weisz-Prater criterion, with the assumption of first-order reaction kinetics [216]. In this context, a Weisz-Prater coefficient, defined in Equation 7, less than one indicates the absence of internal concentration gradients.

Equation 7.

$$C_{WP} = \frac{-r'_A(obs) \rho_c R^2}{D_{Ae} C_{AS}}$$

where:

ρ_c = catalyst density, kg/m³.

D_{Ae} = effective diffusion coefficient, considering porous catalyst parameters, such as catalyst tortuosity, porosity and constriction factor, m²/s.

C_{AS} = external surface concentration of acetone, mol/dm³.

Lastly, internal heat transfer was evaluated using the Weisz-Hicks criterion [217]. Similar to the previous scenario, a Weisz-Hicks coefficient, as defined in Equation 8, must be significantly less than one to indicate the absence of internal heat transfer limitations.

Equation 8.

$$C_{WH} = C_{WP} \exp\left(\frac{\gamma \beta}{1 + \beta}\right)$$

where:

γ = Arrhenius number = $\frac{E_{at}}{R_g T_S}$

T_S = surface reaction temperature, K.

β = maximum particle temperature difference = $\frac{C_{AS} (-AH_r) D_{Ae}}{\lambda_m T_S}$, K.

λ_m = fluid thermal conductivity, W/(m.K).

Chapter 4. MoO_x properties evaluated during acetone HDO reaction: The impact of strong Brønsted acid sites and Mo⁵⁺ species generated on stream

* A significant portion of this chapter (text, figures, and tables) is part of a scientific paper published in *ChemCatChem*, referenced as [107] in this work, and entitled “Enhanced Brønsted Acidity and Hydrogenating Sites Generated on MoO₃ during Acetone Hydrodeoxygenation”. The appropriate permissions for reuse and reprint have been provided by *John Wiley and Sons* and can be found at the Appendix (Chapter 10, section 10.3, subsection 10.3.1).

4.1. Contextualization

As already mentioned, when MoO₃ is exposed to a reducing atmosphere in combination with oxygenated or alkane streams, in addition to MoO₂, molybdenum oxyhydride (MoO_xH_y) and oxycarbohydride (MoO_xC_yH_z) phases are also formed [61,62,106], with molybdenum oxidation states spanning from +6 to +2 [61,62]. MoO_xH_y and MoO_xC_yH_z are isostructural to the MoO_xC_y phase, the difference being a matter of genesis for the former, i.e., H vs. C/H incorporation, and nomenclature for the latter. Incorporating hydrogen is more difficult to follow up; in this sense, the MoO_xC_y phase could also be described as MoO_xC_yH_z, avoided herein for the sake simplicity.

The intermediary molybdenum oxides and/or oxycarbide phases that are formed under typical HDO reaction conditions have shown the ability to catalyze different reaction pathways that require acid (Brønsted or Lewis), metallic, or the combination of more than one site, in bifunctional mechanisms [22]. Figure 15 shows a general reaction network for acetone HDO using Mo-based catalysts that could be extended to MoO_x/MoO_xC_y. Acetone is the simpler ketone representative, but still, the acetone HDO reaction network is extensive, leading to different products according to the nature of the catalytic sites. While dehydration and condensation steps are typically catalyzed by Brønsted/Lewis acid sites (AS) alone, oxygen vacancies (OVS) can participate in direct deoxygenation routes following the reverse Mars-van-Krevelen mechanism [39]. Hydrogenation/hydrogenolysis sites (HS) are commonly represented by metallic sites, and in the case of oxides and/or oxycarbide phases, they are not straightforwardly defined.

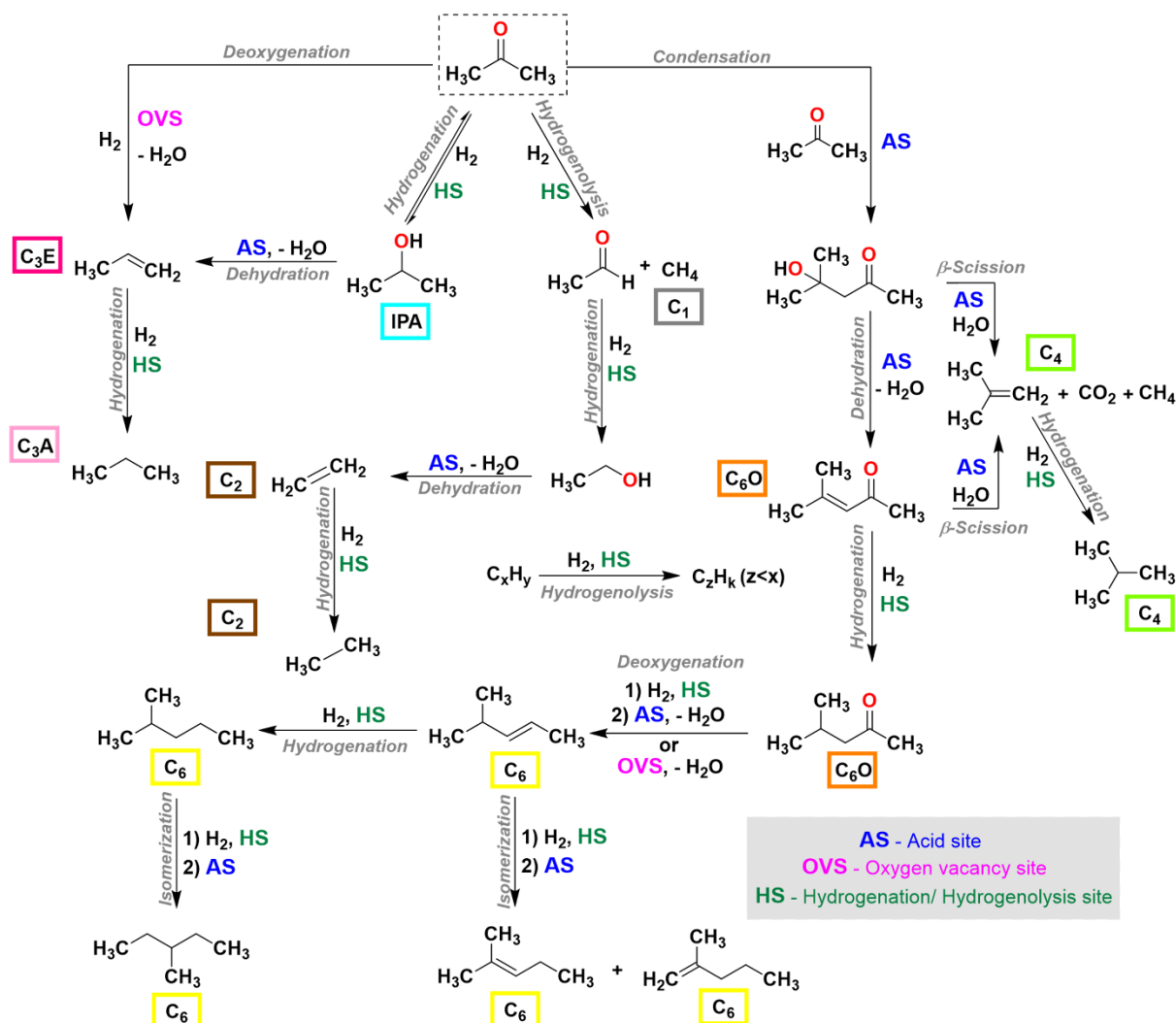


Figure 15. Reaction network for acetone HDO over Mo-based catalysts. Extracted from [107].

The reduction/carburization process of MoO₃ is believed to enhance the AS, OVS, and HS active sites. Beyond the Lewis-type cationic Mo^{δ+} sites and related OVS, Brønsted acid sites occur as surface hydroxyl groups generated from the hydrogen activation process [218]. The origin of the HS, on the other hand, has been ambiguously attributed to the formation of either the reduced MoO₂ phase [219,220], or the MoO_xC_y itself [221]. In the case of the MoO₂ phase, theoretical calculations and experimental data have confirmed a metallic character by the density of states at the Fermi level [218,222]. Catalytic results, such as the reversible acetone hydrogenation [219,223], the bifunctional alkane and alkene isomerizations [220] and the acid-catalyzed formation of isobutene *via* the β-scission of the condensation products in the presence of water [224] agree with the co-existence of HS.

Several catalytic reports involving bulk and supported MoO_3 in HDO reactions have proposed the main reaction pathways and the catalytic sites involved in each step [55–60,68]. However, the influence of the new phases formed under reaction conditions due to surface modifications is much less understood. In a pioneer work, Prasomsri *et al.* [39] studied the HDO reaction of different model biomass-derived oxygenated compounds over MoO_3 , including acetone. Theoretical calculations were used to elucidate the reaction mechanisms, proposing the role of OVS in the direct deoxygenation of acetone to propene. Later, the formation of reduced phases under m-cresol HDO was experimentally verified, and the MoO_xC_y phase was assigned as the actual active phase under HDO reaction [64]. Shetty *et al.* [67] detailed how the creation of the OVS in MoO_3 under acetone HDO atmosphere makes the surface approach a metallic behavior. However, despite acknowledging the phase transition that occurred under reaction generating MoO_2 and MoO_xC_y , these phases were not analyzed. The formation of a MoO_xC_y phase was found to be dependent on the reaction temperature and showed greater stability under reaction; it stabilized Mo^{5+} species and prevented overreduction to Mo^{4+} and Mo^{3+} , which are present in the less active MoO_2 phase [63,64]. From a different perspective, Mortensen *et al.* [225] studied the performance of Mo_2C and related the oxidation of Mo_2C to MoO_2 under HDO conditions to catalyst deactivation. Sullivan *et al.* [66] showed that partially oxidized Mo_2C could hydrodeoxygenate biomass-derived compounds with high selectivity, with almost no subsequent hydrogenation. In an insightful work, Murugappan *et al.* [63] used NAP-XPS (near ambient pressure - X-ray photoelectron spectroscopy) to unveil the *in situ* formation of MoO_xC_y under HDO conditions on both MoO_3 and Mo_2C catalysts. However, the nature and amount of oxygen in the MoO_xC_y phase in each case were different and directly impacted the catalytic performance. Putting these studies together, the crucial role of MoO_x and MoO_xC_y phases on the general HDO catalytic activity and their dependence on reaction conditions becomes clear.

In this chapter, we aim to shed new light on the properties of the active sites formed when MoO_3 nanopowder was exposed to acetone HDO stream. As shown in Figure 15, the direct dependence of the acetone HDO reaction pathways with the different catalytic sites can be used as a complementary probe to address the catalyst surface. Textural, structural, and electronic characterization associated with the catalytic data allowed us to elucidate the formation and nature of the active sites in the Mo-based catalysts and their dependence on the reaction conditions.

4.2. Results

The evolution of MoO₃ nanopowder (MoO₃_comm) under acetone HDO reaction was evaluated as a function of temperature, by heating from 300 °C to 400 °C or cooling from 400 °C to 300 °C (300→400 and 400→300 tests, respectively), or under isothermal conditions, at 350 °C or 400 °C for 6 h (named 350C and 400C, respectively). The results are presented below and summarized in Table 5.

Table 5. Summary of the catalytic data obtained for acetone HDO reaction as a function of temperature (300→400 and 400→300 tests) and under isothermal conditions (350C and 400C tests) for the MoO_x catalysts.

Catalytic test		Parameter	Acetone conversion (%)	Products' distribution (%)				
				C ₆ O	IPA	C ₃ E	C ₃ A	C _n
Temperature ramp	300→400	300 °C	4	9	12	79	-	-
		400 °C	13	19	1	60	9	11
	400→300	400 °C	31	4	1	69	15	11
		300 °C	4	34	10	28	28	-
Isothermal (MoO ₃ _comm)	350C	1h	7	14	29	57	-	-
		6h	12	17	3	34	37	9
	400C	1h	39	4	1	70	15	10
		6h	22	14	1	57	19	9
Isothermal (MoO ₂ _comm)	350C	1h	6	28	54	13	5	-
		6h	7	15	70	9	6	-
	400C	1h	10	44	30	21	5	-
		6h	9	43	40	12	5	-

Impact of the temperature profile: The first set of experiments was performed to evaluate in detail the catalytic performance of the MoO₃_comm between 300 and 400 °C, considering that MoO_xC_y formation was previously observed in this temperature range [58,64]. Figure 4.1. shows the results for the 300→400 (Figure 4.1.A) and 400→300 (Figure 4.1.B) tests, also summarized in Table 7. At 300 °C, the initial conversion was around 5%, and the main products were C₃E, IPA, and C₆O. From 300

°C to about 340 °C, the conversion remained around 5%, but the formation of condensation products, C₆O, increased (50%). The conversion practically doubled between 340 and 360 °C, reaching 10%. This increase was followed by a significant change in the products' distribution, with a drop in C₆O formation (28%) and an increase in the catalyst hydrogenation capability, favoring C₃A (36%) at 350 °C (see Figure 15). Other C_n products also appear (i.e., C₁, C₂, C₄, and C₆) but add up to less than 10% of the total products. From 360 °C to 400 °C, the conversion slowly increases to 13%, with products' distribution almost constant but with an increase in the C₃E/C₃A ratio, which points to a lower hydrogenating capability at higher temperatures. In the 400→300 test (Figure 4.1.B), the initial conversion at 400 °C was much higher than the final conversion in the 300→400 test, about 31% against 13%, respectively. The same products were formed in both tests, but a smaller amount of C₆O was detected when starting at 400 °C. With the temperature decreasing to 300 °C, the conversion gradually drops to 4%, with an increase in C₆O, IPA, and C₃A and a gradual decrease in C₃E. Below 340 °C, C_n products were no longer observed.

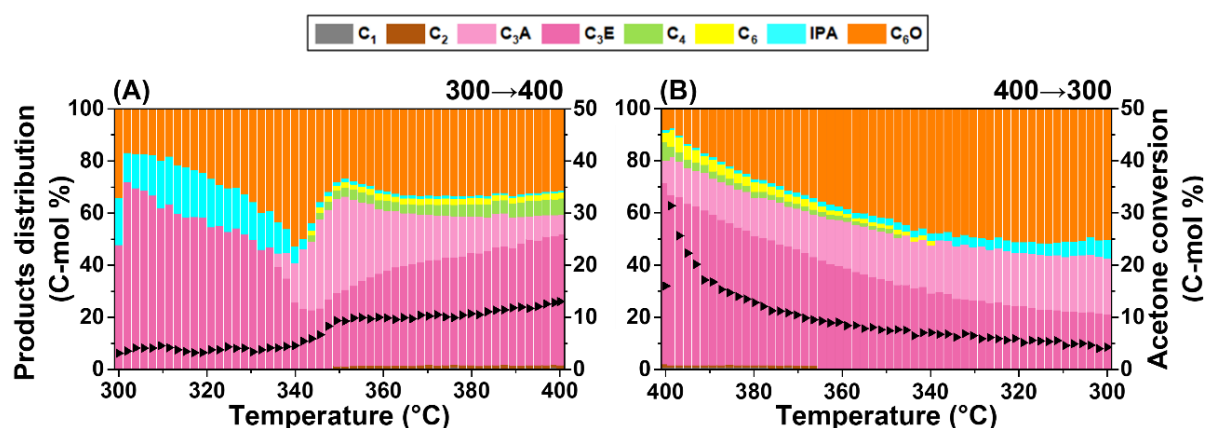


Figure 16. Products' distribution (colored) and conversion (black triangles) for acetone HDO reaction over MoO₃_comm: (A) 300→400, from 300 to 400 °C, and (B) 400→300, from 400 to 300 °C. total TOS: 18 h (0.1 °C min⁻¹). WHSV = 7.32 g_{acetone} g_{catalyst}⁻¹ h⁻¹. Feed: 2.4 mL min⁻¹ acetone, 51 mL min⁻¹ H₂, balance He. Total flow: 100 mL min⁻¹.

To shed light on the structural modifications over MoO₃_comm under HDO conditions, XRD measurements were conducted on the post-reaction catalysts (Figure A3). The MoO₃_comm initial phase matches the orthorhombic crystal structure (ICSD CollCode 166363), whereas the post-reaction patterns showed that the MoO₃ phase was fully converted to a mixture of MoO₂ (ICSD CollCode 244050) and MoO_xC_y phases [221,226] in both tests. In the 300→400 test, the change around 350 °C in

acetone conversion and product' distribution may be associated with this phase transition. The slow increase in temperature up to 400 °C seems to have favored the formation of an ordered MoO_xC_y phase, detected by XRD, even though it has been previously reported that this phase would not withstand temperatures close to 400 °C and above [64]. By starting at 400 °C (400→300 test), this phase could still be detected but in a smaller amount.

According to the experimental temperature profile, the different proportions of the final phases, MoO_xC_y and MoO_2 , impacted the final products' distribution. The more carburized catalyst obtained in the 300→400 test favored C_3E , whereas the predominance of MoO_2 in the 400→300 test favored hydrogenation products (C_3A and IPA), besides C_6O (Table 5).

Impact of the temperature under isothermal conditions: To further evaluate the contribution of MoO_xC_y and MoO_2 phases to the catalyst results, acetone HDO reaction was carried out over $\text{MoO}_3_{\text{comm}}$ and $\text{MoO}_2_{\text{comm}}$ as a function of TOS at two temperatures (isothermal tests): 350 °C (350C), in which a step in the acetone conversion and products' distribution occurred (Figure 16 A); and at 400 °C (400C), in which the highest acetone conversion was achieved (Figure 16 B). Figure 17 presents the results as a function of TOS during 6 h, also summarized in Table 5. The catalytic performance of $\text{MoO}_3_{\text{comm}}$ was similar to the previous results shown in Figure 1. At 350 °C (350C, Figure 17 A), it is possible to visualize the change in the conversion and products' distribution after about 2-3 h on stream. Acetone conversion started at around 6% and ended at about 12%. Products' distribution was similar to the 300→400 test; however, under isothermal conditions at 350 °C, the catalyst seemed to retain its maximum hydrogenating/hydrogenolysis capability since C_3A (~35%) and C_n (~9%) production remained constant to the end of 350C. Under isothermal conditions at 400 °C (400C, Figure 17 B), acetone conversion reached almost 50% but gradually dropped to about 20%. Again, a parallel can be drawn with the catalytic profile of the 400→300 test, but unlike that experiment, the C_6O production did not increase as much, ending at 24% after 6 h on stream. Figure 17 A shows that a similar phase transformation towards the MoO_xC_y and MoO_2 phases occurred under isothermal conditions and will be discussed in more detail later.

For MoO₂_comm at 350 °C (350C, Figure 17 C), the conversion varied between 5% and 8%, while IPA increased (38-61%) and C₃E, C₃A, and C₆O decreased on TOS (Table 7). At 400 °C (400C, Figure 17 D), the acetone conversion (9%), as well as C₆O (60%), remained constant on TOS, and once more, IPA increased, and C₃E and C₃A decreased (Table 5). No C_n product was observed in either of the situations. The post-reaction XRD patterns of the MoO₂_comm catalysts (Figure A4) showed an unchanged crystalline structure, indicating that an ordered MoO_xC_y phase was not formed even at 350 °C starting from MoO₂. Interestingly, despite the entirely different catalytic profiles of MoO₂_comm and MoO₃_comm at 400 °C (400C), the MoO₂ phase was the only crystalline phase observed for both (Figures 18 A and A3). MoO₂_comm presented a similar catalytic profile at 350 and 400 °C (350C and 400C), with C₆O as the primary product. Nonetheless, MoO₃_comm (400C) showed significantly higher conversions at 400 °C and C₃E as the main product. A deeper structural and surface investigation was then performed to better understand the catalytic results.

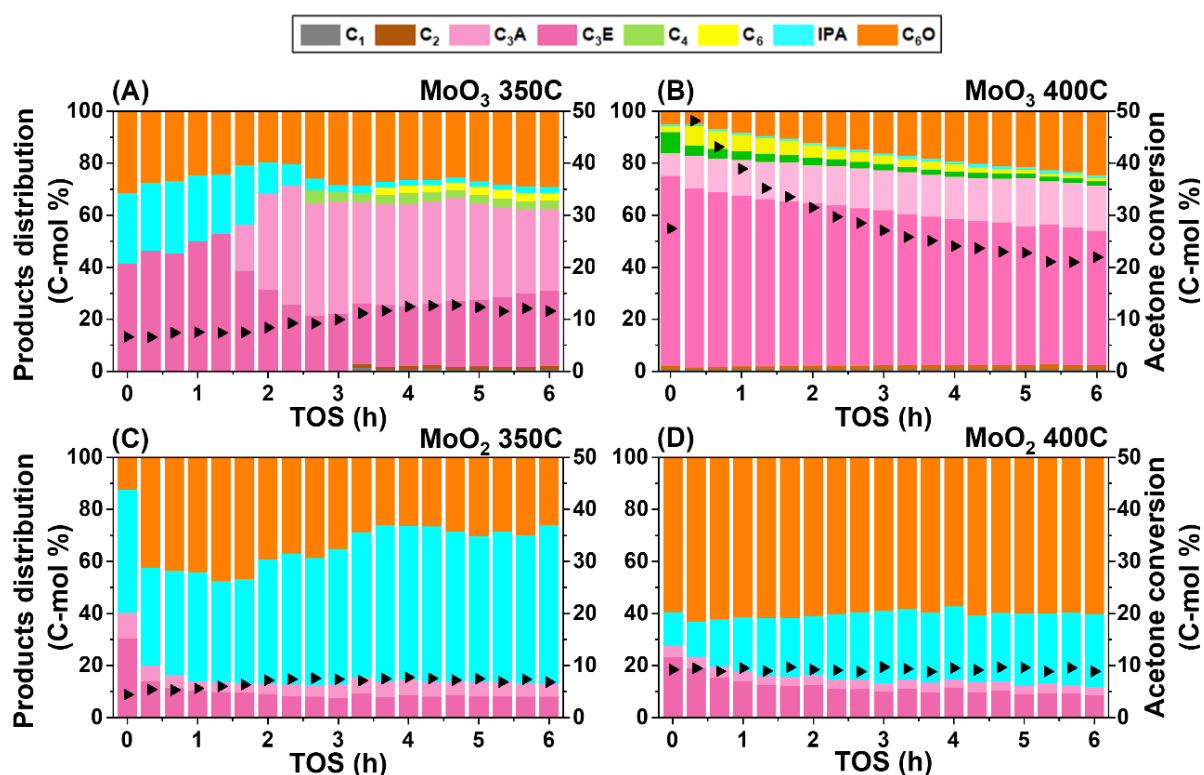


Figure 17. Products' distribution (colored bars) and conversion (black triangles) of acetone HDO reactions for MoO₃_comm (A, B) and MoO₂_comm (C, D): 350C, isothermal at 350 °C (A, C), and 400C, isothermal at 400 °C (B, D). TOS: 6 h. WHSV = 7.14 g_{acetone} g_{catalyst}⁻¹ h⁻¹. Feed: 2.4 mL min⁻¹ acetone, 51 mL min⁻¹ H₂, balance He. Total flow: 100 mL min⁻¹.

Structural and electronic evolution of MoO₃ under acetone HDO isothermal

conditions: Figure 18 A shows the XRD structural characterization of the initial MoO₃_comm and the post-reaction catalysts (isothermal tests). The partial/total reduction of MoO₃ forming MoO₂ and MoO_xC_y phases under acetone HDO was confirmed, in which their ratio depended on the reaction temperature and TOS. When MoO₃_comm was submitted to acetone HDO reaction at 350 °C for 1h, there were no significant structural modifications, and the MoO₃ phase was maintained (350C1h catalyst); on the other hand, after 6 h (350C6h catalyst), pronounced changes occurred, resulting in the complete transition of MoO₃ crystalline phase to MoO₂ and MoO_xC_y phases.

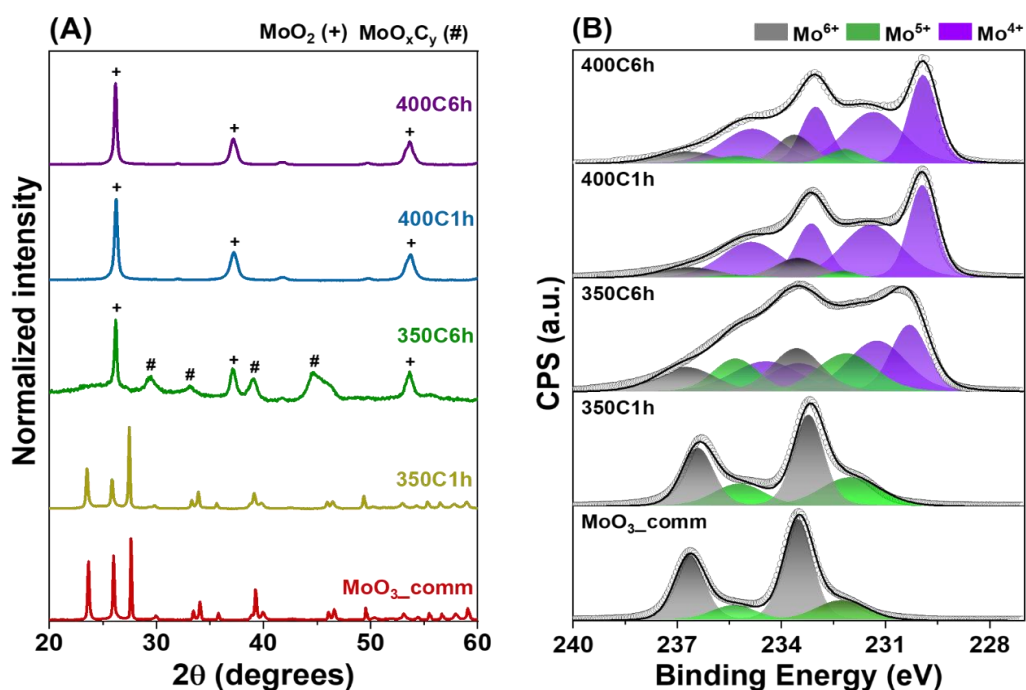


Figure 18. (A) XRD patterns and (B) XPS spectra of Mo 3d region of post-reaction samples: MoO₃_comm (as received) and 350C1h, 350C6h, 400C1h, and 400C6h catalysts after acetone HDO reaction. The spin-orbit splitting of 3.1 eV was considered for each Mo species. Reaction conditions of pre-treated samples: WHSV = 7.14 g_{acetone} g_{catalyst}⁻¹ h⁻¹. Feed: 2.4 mL min⁻¹ acetone, 51 mL min⁻¹ H₂, balance He. Total flow: 100 mL min⁻¹.

When submitted to a higher reaction temperature, i.e., 400 °C, the MoO₃ phase transforms into the MoO₂ crystalline phase before 1 h on stream (400C1h catalyst). After 6 h on stream, no further modification could be identified by XRD (400C6h catalyst). For comparison, MoO₃_comm was also submitted to the H₂ stream at 400

°C for 1 h (without acetone feeding). The XRD pattern (Figure A5) demonstrated that the MoO_3 to MoO_2 phase transition was delayed in the absence of acetone. It is worth mentioning that diffraction peaks related to the crystalline MoO_xC_y phase did not appear for both 400C1h and 400C6h catalysts.

Electronic characterization of the catalysts' surface was analyzed by XPS, as shown in Figure 18 B. Tables A1 and A2 summarized the XPS results. The spectra of the Mo 3d region demonstrated that several Mo species were formed depending on the reaction temperature and TOS, in agreement with XRD data (Figure 18 A). $\text{MoO}_3_{\text{comm}}$ 3d_{5/2} peaks at 233.5 eV and 232.3 eV (and the corresponding 3d_{3/2} peaks at 236.6 eV and 235.4 eV) were attributed to Mo^{6+} (75.6 %) and Mo^{5+} (24.4%) species, respectively. The formation of Mo^{5+} species has been related to the MoO_3 surface reduction induced by the X-ray probe [213]. The spectrum of the 350C1h catalyst presented a similar profile to that observed for $\text{MoO}_3_{\text{comm}}$, with Mo^{6+} (62.6 %) and Mo^{5+} (37.4 %) species. On the other hand, the 350C6h catalyst was partially reduced, presenting a mixture of Mo species composed of Mo^{6+} (21.8 %), Mo^{5+} (22.6 %), and Mo^{4+} (55.6 %). The temperature favored the reduction, and the 400C1h catalyst was composed of Mo^{6+} (12.4 %), Mo^{5+} (3.0 %), and Mo^{4+} (84.6 %). No significant changes in the ratio of these species were observed for the 400C6h catalyst, which presented the same Mo^{6+} (14.8 %), Mo^{5+} (6.9 %), and Mo^{4+} (78.3 %) species. Whereas the presence of Mo^{6+} species can be attributed to a surface layer of MoO_3 [73,213], the Mo^{5+} species can be majorly related to MoO_xC_y phase and Mo^{4+} to MoO_2 and/or MoO_xC_y phases with higher carbon content.

The quantitative surface analysis of Mo, C, and O based on XPS data is presented in Table A9. A 2.3-fold increase in the C at.% content was observed when comparing the $\text{MoO}_3_{\text{comm}}$ and 350C1h catalyst; after 6h on stream, 350C6h catalyst, the C at.% content had no significant changes. Although the C at.% content almost did not vary with TOS, more reduced Mo species (Figure 18 B and Table A8), a decrease of the Mo/O ratio (Table A9), and new contributions at higher BE in the O1s region (Figure A6) were observed. These results agree with forming a MoO_xC_y phase [65]. Similar trends were found for 400C1h and 400C6h catalysts; the C at.% content increased by about 2.2-fold compared to the $\text{MoO}_3_{\text{comm}}$, and the overall Mo/O and Mo/C ratios decreased on TOS, which is consistent with the formation of a disordered MoO_xC_y phase at this temperature. O 1s spectra of 400C1h and 400C6h also presented contributions at higher BE (Figure A7).

The results indicate that the 400C1h catalyst was formed not only by MoO_2 but also by a disordered MoO_xC_y phase. Even though the only crystalline phase detected by XRD in the 400C1h catalyst was MoO_2 , when $\text{MoO}_2_{\text{comm}}$ was submitted to acetone HDO reaction, it presented inferior results in terms of conversion and distribution of deoxygenated products compared to 400C1h catalyst (Figure 17). The formation of other carbon phases, such as coke, should also be considered.

The thermogravimetric results obtained under N_2 and O_2 atmospheres are shown in Figure A8 and Table A10. Under oxidizing conditions, the 350C1h catalyst did not present significant weight loss or gain events, in line with the more oxidized MoO_3 structure [64]. The 350C6h, 400C1h, and 400C6h catalysts showed weight losses that varied between 2.7 and 3.3 % below 350°C that were attributed to H_2O loss [106]. Above this temperature, two different weight gain events were observed. The first one, between 330 and 400 °C, varied from 1.0 to 1.3 % and could be associated with the oxidation of MoO_xC_y into MoO_3 ; the second one, between 400 and 500 °C, ranged from 7.0 to 7.5 % and could be related to the oxidation of MoO_2 into MoO_3 [106]. Considering the weight gains under O_2 and the losses under N_2 from 330 to 500 °C, an average 10.4% weight gain was found for these catalysts, in good agreement with the 12.4 % theoretical weight gain associated with the complete oxidation of MoO_2 into MoO_3 . The weight loss for the MoO_xC_y phase is difficult to estimate since this phase can present different compositions depending on the H_2 /carbon stream, temperature, and TOS. No expressive formation of soft coke could be detected [106].

Evaluation of acid sites and evolution under acetone HDO reaction: Since the AS also play an essential role in the acetone HDO reaction pathways (Figure 15), $\text{MoO}_3_{\text{comm}}$, 350C6h, and 400C1h samples had their acid properties probed by TMPO adsorption monitored by ^{31}P NMR spectroscopy. These catalysts were mainly chosen because they are structurally and electronically distinct, as already discussed. While $\text{MoO}_3_{\text{comm}}$ matches the MoO_3 phase, 350C6h catalyst was formed by a mixture of $\text{MoO}_2/\text{MoO}_x\text{C}_y$ crystalline phases and 400C1h by a single MoO_2 crystalline phase. Despite not much explored for metal oxides, TMPO adsorption monitored by ^{31}P NMR spectroscopy is a reliable technique for determining the nature, strength, and concentration of AS in many solid catalysts [227]. The main advantage of this approach is the linear correlation that exists between the chemical shift of the adsorbed TMPO and the deprotonation energy of the TMPOH^+ species formed over Brønsted acid sites

(BAS); the higher the spectral chemical shift, the stronger the adsorption of TMPO [214]. On the other hand, this technique is less sensitive to Lewis acid sites (LAS) of different strengths [214].

It is worth mentioning that most reports on MoO_x and MoO_xC_y acid properties end up not converging in terms of AS quantification, nature, and strength [194,228–232]. Classic techniques, such as thermoprogrammed desorption of ammonia (NH_3 -TPD) and pyridine adsorption, monitored by FTIR (Py-FTIR) [229–231], are essential in the study of the acidity of catalysts but have some limitations. NH_3 -TPD helps determine the AS strength [194,228], but it cannot differentiate between the type and strength of BAS versus LAS [233] and may overestimate AS concentrations due to the formation of complexes such as $\text{NH}_4^+ \cdot n\text{NH}_3$ [234]. Py-FTIR can differentiate BAS and LAS through specific bands but fails to determine the strength of the sites and their quantification due to overlapping bands. Thus, the phosphine oxide adsorption monitored by ^{31}P NMR, combined with P elemental analysis, seems to be a good compromise.

Figure 19 shows the ^{31}P NMR spectra for the three selected samples, where a broad multi-contribution signal could be detected in the region of ~ 30 to ~ 90 ppm. Signal deconvolution allowed addressing and quantifying each of the five distinguished contributions [215] (see the Experimental Section, Chapter 3, for details). The signal around 40 ppm (Phys), present to a greater extent in the $\text{MoO}_3_{\text{comm}}$ and 400C1h catalyst (Table A11), can be associated with physisorbed TMPO. The signal centered in 60 ppm is often attributed to LAS, presenting this sole contribution on metal oxides [235,236]. BAS can be found from nearly 50 ppm to over 80 ppm, encompassing four possible contributions, B1 to B4, increasing in acid strength [215]. The analyzed samples showed all these contributions (Table A11); however, the 350C6h catalyst presented a more significant percentage of stronger BAS (B2-B4), followed by the 400C1h sample.

The P elemental analysis of the TMPO adsorbed samples allowed estimating the total AS concentration (LAS + BAS) since each TMPO molecule anchors in a single site. The physisorbed TMPO contribution obtained from the deconvolution of the ^{31}P NMR spectra was subtracted for each case. The total amount of AS (per gram of catalyst) followed the order $\text{MoO}_3_{\text{comm}} < 400\text{C1h} < 350\text{C6h}$, as shown in Table 6. When normalizing the total AS by the corresponding SSA (Table A12), the total AS per nm^2 was similar for $\text{MoO}_3_{\text{comm}}$ and 350C6h catalyst and smaller for the 400C1h

catalyst due to the increase in SSA (Table 6). Moreover, the BAS/LAS ratio increased twice for 350C6h but was similar for MoO₃_comm and 400C1h. These results confirm the different nature of the surface of MoO₃ when exposed to different reaction conditions.

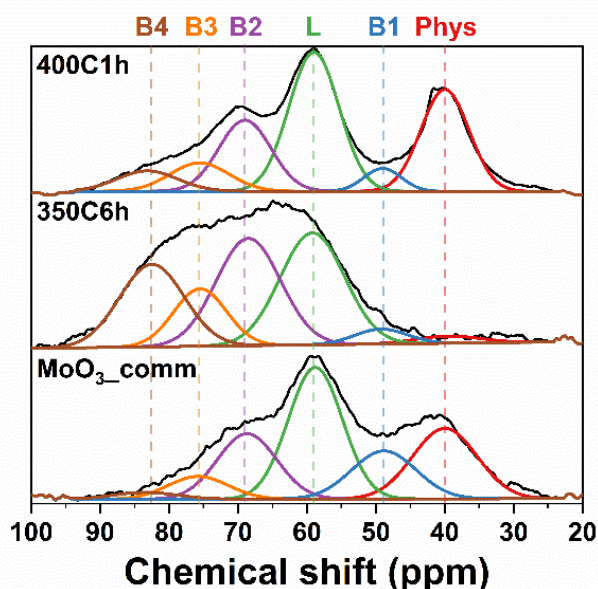


Figure 19. ³¹P NMR spectra of adsorbed TMPO on (bottom) MoO₃_comm (as received) and (middle) 350C6h and (top) 400C1h catalysts. Reaction conditions of pre-treated samples: WHSV = 7.14 g_{acetone} g_{catalyst}⁻¹ h⁻¹. Feed: 2.4 mL min⁻¹ acetone, 51 mL min⁻¹ H₂, balance He. Total flow: 100 mL min⁻¹. Phys. - physisorbed TMPO, L - LAS, B1 to B4 - BAS, where the higher the number, the stronger the site.

Table 6. Acid and textural data of: MoO₃_comm, 350C6h and 400C1h catalysts after acetone HDO reaction. Reaction conditions of pre-treated samples: WHSV = 7.14 g_{acetone} g_{catalyst}⁻¹ h⁻¹. Feed: 2.4 mL min⁻¹ acetone, 51 mL min⁻¹ H₂, balance He. Total flow: 100 mL min⁻¹.

Sample	AS ^a	BAS ^a	LAS ^a	BAS/LAS ^a	(B2+B3+B4)/B1 ^a	AS nm ⁻² (x10 ⁻²) ^b
MoO ₃ _comm	19 ± 1	11 ± 1	9 ± 1	1.2	1.9	163 ± 10
350C6h	70 ± 5	48 ± 4	22 ± 2	2.2	19.5	173 ± 13
400C1h	56 ± 3	30 ± 2	26 ± 1	1.1	5.5	77 ± 4

^a obtained by ³¹P NMR of adsorbed TMPO. In μmol g⁻¹.

^b normalized by the SSA obtained by N₂ physisorption.

Probing acetone-surface interaction: So far, the performed characterizations encompassed some key properties of the $\text{MoO}_x/\text{MoO}_x\text{C}_y$ catalysts when subjected to the acetone HDO stream. In this sense, acetone-TPD experiments were carried out intending to better understand the substrate-surface interactions. Many reports on the acetone adsorption on metal oxides agree that most molecules adsorb in a η^1 -configuration, i.e., through the interaction of the lone-pair electrons on the carbonyl oxygen atom and the $\text{M}^{\delta+}$ sites [237–240]. However, other adsorption modes are possible, according to the nature of the surface sites and experimental conditions. Mesityl oxide, η^1 -enolate, η^2 -acetate, η^2 -diolate, and even poly-acetone species have also been proposed as adsorbed candidate structures [238]. Furthermore, the desorption is highly influenced by the coverage degree and the formation of multilayers, which can enhance acetone-acetone repulsion [238].

The acetone-TPD curves obtained for MoO_3 _comm, 350C6h, and 400C1h are displayed in Figure 20. The first two acetone desorption peaks are centered around 60 °C and 100 °C; they are common to all catalysts and can be related to physisorbed molecules. These contributions usually appear under high coverage rates, and the peaks maximum tend to be displaced to lower temperatures with increasing coverage [240]. Other desorption peaks can be found at higher temperatures, spanning from 150 to 400 °C, and are more likely attributed to chemisorbed η^1 -acetone on $\text{M}^{\delta+}$ sites, as observed in many studies on Al_2O_3 , TiO_2 , ZrO_2 , and CeO_2 [238,241,242]. BAS should also play an essential role in acetone desorption at this temperature range and the results are consistent with the ^{31}P NMR experiments. Despite not much studied in metal oxides, solid-state NMR experiments showed that ^{13}C carbonyl chemical shifts of acetone adsorbed on BAS in molecular sieves can provide a measure of their intrinsic site acidity [243,244].

Besides the acetone, C_3E , C_1 , and CO_2 formation were also monitored (Figure 20). All catalysts presented concomitant C_1 and CO_2 evolution after 400 °C, resulting from residual acetone decomposition given the elevated temperature. More interestingly, C_3E development was significantly different for each case. The more oxidized surface of MoO_3 _comm presented three discrete and localized desorption peaks, around 120, 280, and 430 °C, the latter showing a minor contribution (Figure 20 A). For the 350C6h catalyst, two broad C_3E desorption peaks were observed at ~ 280 and 430 °C (Figure 20 B), while for the 400C1h catalyst, the first peak was shifted to a higher temperature, 350 °C (Figure 20 C). The results showed that acetone was

more strongly bound and reactive to deoxygenation in these two catalysts, which present more reduced surfaces than MoO₃_comm.

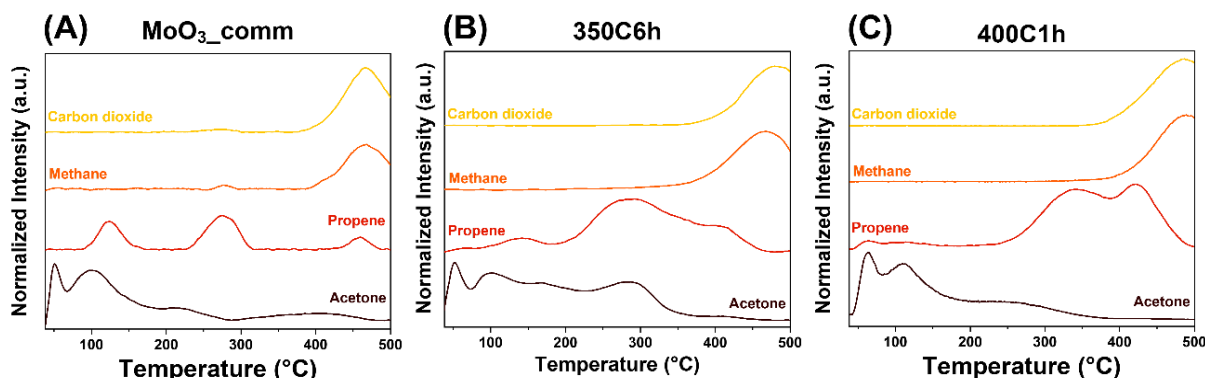


Figure 20. Acetone-TPD curves of (A) MoO₃_comm, (B) 350C6h, and (C) 400C1h catalysts after acetone HDO reaction. Acetone, propene, methane, and carbon dioxide were monitored from room temperature to 500 °C. Reaction conditions of pre-treated samples: WHSV = 7.14 g_{acetone} g_{catalyst}⁻¹ h⁻¹. Feed: 2.4 mL min⁻¹ acetone, 51 mL min⁻¹ H₂, balance He. Total flow: 100 mL min⁻¹.

Isopropanol “HDO” reaction: To further evaluate the contribution of the different pathways in the acetone HDO reaction, direct IPA formation and consumption was monitored, by changing inlet stream from acetone/H₂ to IPA/H₂. Figure A11 shows the change in the catalytic profile when acetone was substitute by IPA, under isothermal conditions. Differently from the acetone HDO experiments, the catalytic profile obtained for IPA HDO conditions did not present any significant modification in the products’ distribution over TOS, even though the post-reaction XRD patterns confirmed the formation of MoO₂ and MoO_xC_y phases under TOS also in this case (Figure A12). The main product was C₃E, and the IPA conversion was significantly higher (> 80 %) than acetone under similar conditions. Since there was no competition with acetone adsorption, as in acetone HDO, all catalytic sites were available to IPA, and the dehydration over AS forming C₃E was promoted (see Figure 15).

4.3. Discussion

MoO₃ usually crystallizes as an orthorhombic phase with Mo nominal oxidation state of 6+, while MoO₂ presents a monoclinic structure and Mo nominal oxidation state of 4+. On the other hand, the most accepted structure for the MoO_xC_y is a face-centered cubic cell, in which the lattice nodes are occupied by the Mo atoms and the

octahedral voids by the lighter atoms (C and O) [221]. It has been shown, however, that a higher O content favors the amorphization of the MoO_xC_y phase [61]. When $\text{MoO}_3_{\text{comm}}$ was submitted to acetone HDO reaction, the MoO_3 crystalline phase was converted to MoO_2 and MoO_xC_y phases, the ratio among these phases and the nature of the MoO_xC_y phase were dependent on the temperature and TOS. At 350 °C, the reduction of $\text{MoO}_3_{\text{comm}}$ and transformation to MoO_2 and MoO_xC_y crystalline phases was slow, with an induction period of about 3 h (Figures 17 A and 18 A). At 400 °C, the reduction was faster and the MoO_xC_y crystalline phase was not formed (Figures 17 B and 18 B).

The partial reduction of the orthorhombic MoO_3 that takes place under an H_2 /oxygenate atmosphere and heating, generates oxygen vacancies randomly distributed over the surface. As oxygen is removed, it leads to atomic rearrangement to eliminate the vacancies through local collapses. Once the structure of MoO_3 is formed by double lamellae of side-sharing octahedra, this condensation process can lead to the concurrent formation of the monoclinic MoO_2 and MoO_xC_y phases [106,126]. The delay in the $\text{MoO}_3 \rightarrow \text{MoO}_2$ phase transition when the $\text{MoO}_3_{\text{comm}}$ was submitted to reduction under H_2 stream (Figure A5) confirms that the presence of the oxygenate facilitated this process. The coexistence of MoO_2 and MoO_xC_y phases under acetone HDO is in good agreement with previous theoretical and experimental studies, considering both the formation of MoO_xC_y crystalline or amorphous phase. Kurlov *et al.* [106] submitted a carbon-supported MoO_3 catalyst to *in situ* carburization followed by XRD and XANES analyses. The XRD patterns show that MoO_3 transitioned to MoO_2 around 400 °C and then fully converted into Mo_2C at 750 °C; no other crystalline phases were observed during heating. On the other hand, XANES data presented a C-component pointing to a different contribution between MoO_2 and Mo_2C . The formation of an oxycarbide phase was proposed due to carbon incorporation during annealing, matching the bulk MoO_2 structure. These findings agree with other studies: Delporte *et al.* [126] showed the coexistence of MoO_2 and an amorphous oxycarbide phase after carburization through high-resolution transmission electron microscopy; Likith *et al.* [245] undertook a detailed theoretical investigation showing the thermodynamic stability of different oxycarbide polymorphs coexisting with MoO_2 . The thermogravimetric data (Figure A8 and Table A10) provided additional evidence for the coexistence of an amorphous oxycarbide phase and MoO_2 at 400 °C.

Concerning the textural properties, previous works have shown that the

evolution of MoO_3 to MoO_xC_y phase is commonly accompanied by an increase in SSA [106,226] in which the development of micropores and/or small mesopores reflects the topotaxy of the transition between phases [226]. While the final crystalline phases differed according to the reaction temperature and TOS, the surface analysis also indicated that both catalysts contained MoO_xC_y phases that were different in nature.

It has been shown that the Mo oxidation state of the MoO_xC_y phase can vary depending on the C and O content. *In situ* and *operando* NAP-XPS studies in the presence of an anisole/ H_2 stream demonstrated that the Mo oxidation states observed for the MoO_xC_y phase transitioned between +6 and +5 during the reaction [63]. Other works showed that oxycarbide phases with higher C content are characterized by more reduced Mo oxidation states, +4 and +3. [61,246]. In our case, the reaction at 400 °C led to more reduced $\text{Mo}^{\delta+}$ species, mainly +4, that were more stable during TOS, whereas a progressive reduction occurred when the reaction temperature was 350 °C, from +6 to +4 (Figure 18 B). The higher degree of reduction exhibited by 400C1h catalyst was associated with a larger shift of C_3E desorption towards high temperature over acetone-TPD experiments (Figure 20). King *et al.* [240] verified that C_3E was the primary product (>80%) during acetone-TPD over UO_2 and attributed this high deoxygenation degree to the oxophilic nature of the metal oxide. Senanayake *et al.* [239] reported that fully oxidized CeO_2 showed a weak interaction with acetone. However, the acetone chemisorbed strongly on reduced CeO_{2-x} with molecular acetone desorbing at higher temperatures, followed mainly by C_3E . Kräuter *et al.* [247] prepared $\text{Ti}^{2+}/\text{Ti}^{3+}$ -rich TiO_2 surfaces through argon ion bombardment and verified strong acetone binding over the reduced surface, with C_3E formation in a wide range of temperatures (100 to 400 °C).

Looking in more detail at the acid properties of the catalysts, the total AS per gram of catalyst significantly increased under reaction conditions (Table 6). Although both BAS and LAS increased under reaction conditions, the creation of stronger BAS sites was favored at lower temperature. In a sequence of works on Mo_2C under acetone and IPA HDO reactions [66,174,175], Bhan *et al.* attributed the origin and activity of AS to the oxycarbide phase generated *in situ* on the catalyst surface. Unlike the formation of MoO_xC_y from MoO_3 _comm exposed to an H_2 /acetone stream, in those works, the Mo_2C catalyst was treated in an oxidizing atmosphere, adding oxygen to the surface after hydrogen activation, and ended up forming BAS. The BAS was probed *in situ* during the reactions by titration of 2,6-di-tert-butylpyridine (DTBP) and

monitoring the IPA dehydration to C₃E. It is accepted that the AS nature and strength in crystalline solids are highly influenced by the lattice strain and electronic properties of the atoms [248,249]. In zeolites, for example, which present well-defined and understood BAS, the different frameworks, sites concentration, proximity, and the presence of heteroatoms greatly influence the BAS strength [250]. The reduction/carburization that MoO₃_comm went under reaction conditions altered the surface properties, as seen by the changes in SSA and the C/O ratio (Table A9). As shown, the formation of MoO_xC_y phases, combined with the less polarized Mo-C bonds, increased the concentration and strength of the BAS.

In summary, the detailed structural, electronic, textural, and acid characterization results showed the transformation suffered by MoO₃_comm under acetone HDO stream, and how the balance of different catalytic sites was dependent on temperature and TOS. This balance directly impacted the acetone interaction and can now be associated to the main reaction pathways that determine the final products' distribution (Figure 15).

The main products obtained in the acetone HDO on MoO₃_comm and MoO₂_comm at 350 and 400 °C (isothermal conditions, Figure 17) were C₆O, IPA, C₃E, C₃A, and C_n, summarized in terms of yield on Figure 21. Figure 15 shows that although subsequent dehydration and hydrogenation steps are also involved in the overall C₆O production, the first step to form C₆O is acetone condensation mediated by AS. The formation of IPA requires HS sites, whereas the formation of C₃E can be derived from direct deoxygenation of acetone mediated by OVS or through hydrogenation/dehydration steps *via* IPA and HS/AS sites. For the sake of simplicity, we chose to sum the contributions of C₁, C₂, C₄, and C₆ products as C_n. Although they can be obtained through various pathways, AS and HS mediate all of them. The smaller products can be formed through the hydrogenolysis of the larger ones (C-C cleavage), while alkenes' hydrogenation could also occur. C₁ can appear together with acetaldehyde through the hydrogenolysis of acetone (HS); then acetaldehyde could be hydrogenated to ethanol (HS), which could dehydrate into C₂ products (AS). In turn, C₆O can be deoxygenated, giving rise to C₆ (HS+AS), but can also suffer the acid-catalyzed β -scission forming C₄ (AS). The dependence of each product with the different catalytic sites allows us to follow the reaction network.

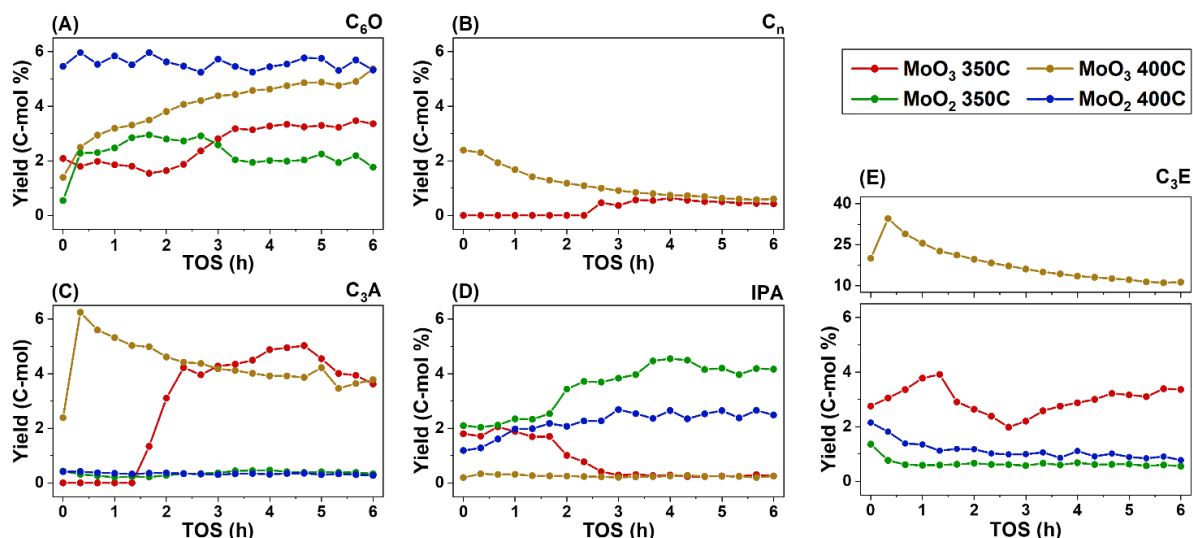


Figure 21. Yields of (A) C_6O , (B) C_n , (C) C_3A , (D) IPA, and (E) C_3E of acetone HDO reactions for MoO_3_comm and MoO_2_comm : 350C, isothermal at 350 °C, and 400C, isothermal at 400 °C. TOS: 6 h. WHSV = $7.14 \text{ g}_{acetone} \text{ g}_{catalyst}^{-1} \text{ h}^{-1}$. Feed: 2.4 mL min^{-1} acetone, $51 \text{ mL min}^{-1} \text{ H}_2$, balance He. Total flow: 100 mL min^{-1} . In (B), C_n was not detected for MoO_2_comm at both temperatures.

At 350 °C, there was a step in C_6O yield after 2-3 h on stream (Figure 21 A) for MoO_3_comm , following the phase transition to MoO_2/MoO_xC_y and the increase in AS. At 400 °C, the C_6O yield steadily increased to the end of the experiment. The increasing C_6O yield with TOS at both temperatures could be associated with the increasing overall AS concentration with the progress of the reduction/carburization process. The formation of the disordered MoO_xC_y phase found in the 400C1h catalyst led to AS concentration slightly smaller than 350C6h and LAS comparable (Table 6). At the studied temperatures, both LAS and BAS should contribute to acetone condensation [251], so even the fact that 350C6h had significantly stronger BAS (Table 6), they should not drive significant changes. On the other hand, MoO_2_comm presented constant C_6O yields during the reaction showing that the AS did not change significantly when the formation of the MoO_xC_y phase was not favored.

C_n was also detected in MoO_3_comm after the phase transition at 2-3 h on TOS (Figure 21 B). At 400 °C, a maximum yield was achieved at 1 h and then slowly reduced with TOS. As mentioned, the continuous reduction/carburization process of MoO_3_comm led to a gradual increase in the C_6O yield associated with the generation of AS. At 400 °C, the C_n yield seems to follow the opposite trend, reflecting the evolution of AS and HS on TOS. Even though not straightforwardly defined for

MoO_x/MoO_xC_y catalysts, the HS nature and activity originate from their electronic characteristics. The better C_n yields were verified when the Mo^{δ+} species were halfway between more oxidized and more reduced oxidation states, near +5, as shown by the XPS data (Figure 18 B). We can infer that HS activity should lie near Mo⁵⁺, in agreement with the lack of C_n production by MoO₂_comm, weakening the proposal that this phase should be a source of hydrogenolysis sites [219,220].

For MoO₃_comm, C₃A presents a similar behavior to C_n in both temperatures (Figure 21 C), an expected result since these products are all mediated by HS; in the case of C₃A, it is obtained from hydrogenation C₃E. At 350 °C, the C₃A production matched the phase transition after 2-3 h, reaching its maximum As for C_n, this suggests that the MoO₃ phase was not active in C₃A production. At 400 °C, a maximum was achieved at 1 h and then slowly decreased with TOS. Interestingly, the C₃A/C₃E ratio at 350 °C (Figure A10) could be up to eight times greater in the presence of the MoO_xC_y phase, showing that the Mo^{δ+} oxidation state close to +5 is indeed related to HS activity. The higher yield to C₃A compared to C_n can be explained by the larger quantity of C₃E produced by these catalysts than any C_n possible precursor. Nevertheless, a significant difference between C_n and C₃A yield trend appears for MoO₂_comm; while C_n was not detected, the C₃A yield was small, regardless of the temperature. This shows that MoO₂ presents HS with hydrogenating characteristics, even to a lesser extent. On the other hand, the results corroborated that the MoO_xC_y presents both hydrogenation and hydrogenolysis HS.

IPA is another product obtained by HS through the hydrogenation of acetone; however, it does not follow a similar behavior found for C_n and C₃A in any condition (Figure 21 D). For MoO₃_comm, at 350 °C, the IPA yield dropped drastically after the phase transition in 2-3 h. Contrary to what was seen for C_n and C₃A, the initial MoO₃ presented active HS for acetone hydrogenation forming IPA. Furthermore, the abrupt decrease in IPA yield is accompanied by an increase in C₃E (Figure 21 E), which can be related to the rise of AS favoring the dehydration step. At 400 °C, IPA presented low yield, indicating a strong AS performance, corroborated by the high C₃E production. However, the descending profile of C₃E along TOS is not compatible with the increase in the AS verified in the formation of C₆O at this temperature. This apparent independence between the behavior of IPA and C₃E suggests that another pathway might be concurrently operating, for example, the direct deoxygenation *via* OVS. Another vital result to support this hypothesis is the significantly high yield to C₃E

at the beginning of the reaction. At 400 °C, the accelerated transition to $\text{MoO}_2/\text{MoO}_x\text{C}_y$, giving rise to the disordered oxycarbide phase, produced a more defective surface with high SSA (Table A12), which could be related to a more significant OVS concentration. As the acetone-TPD experiments show, acetone appears more strongly bound to the surface in this situation, being majorly deoxygenated to C_3E at higher temperatures (Figure 20). For the MoO_2 _comm, the C_3E and IPA behaviors at both temperatures were similar (Figure 6D and 6E); as the C_3E yield decreased, the IPA yield increased. As mentioned, MoO_2 presents HS that were inactive for hydrogenolysis and little active for hydrogenation due to its over-reduced nature. However, the small and descending production of C_3E , even with the presence of IPA, does not agree with the high C_6O yield. At the studied temperatures, acetone condensation seemed to be synergistically catalyzed by both LAS and BAS [251], while IPA dehydration to C_3E was more dependent on BAS, especially the stronger ones [252,253].

When IPA was fed to the reaction, substituting acetone (IPA “HDO” test), the high C_3E yield showed that the AS dominates against the HS at 350 °C. On the other hand, at 400 °C, the HS became more important once acetone and C_3A were also formed. It is worth noting that, in this case, the formation of C_6O from acetone was not detected and likely related to the low acetone/high IPA concentration on the stream, even with the prevalence of AS. The high selectivity to C_3E under different conditions shows that the dehydration pathway was privileged over the $\text{MoO}_2/\text{MoO}_x\text{C}_y$ phase. Even though the acetone HDO reactions impose some site competition, the high rate of IPA consumption reiterates the extent of AS activity, especially the stronger BAS [252,253]. As already discussed, the phase transition from MoO_3 to $\text{MoO}_2/\text{MoO}_x\text{C}_y$ was accelerated in the presence of acetone, and IPA could cause a similar effect. Given the differences in activation, adsorption, and activity between IPA and acetone, it is possible that the formation of the $\text{MoO}_2/\text{MoO}_x\text{C}_y$ was faster under IPA HDO conditions, which would justify the constant activity observed.

4.4. Considerations

Figure 22 summarizes the active sites and related reaction pathways from the observed systems under different conditions, emphasizing the two oxycarbide phases, ordered and amorphous. It is worth noting, however, that this might represent a simplified picture of this complex system since we cannot rule out the co-existence of

MoO_xC_y disordered phase with the ordered one at 350 °C contributing to the average properties of what we call ordered phase. Initially, MoO₃ was concomitantly reduced and carburized under acetone HDO stream. At 350 °C, there was an induction period in the first hours of the reaction, with the progress of surface reduction and the creation of OVS. The catalyst's surface was characterized by active HS favoring acetone hydrogenation and the lowest AS concentration. At some point, about 2-3 h on TOS at this temperature, the formation of an ordered MoO_xC_y phase became favored, presenting the highest AS concentration, with the predominance of stronger BAS. This phase was significantly active for both hydrogenation and hydrogenolysis steps, a behavior attributed to its singular electronic characteristics, which comprise Mo^{δ+} species halfway between more oxidized and more reduced oxidation states, close to +5. The disordered MoO_xC_y phase, formed at 400 °C, was the trickiest to unravel due to its amorphous nature and, for this reason, was carefully analyzed. This phase showed moderate HS activity for hydrogenolysis but less HS activity for hydrogenation than its ordered counterpart. There were also few AS, but still in a more significant number and stronger when compared to MoO₃. The differential properties of the disordered MoO_xC_y phase seem to be the higher SSA related to its more defective structure.

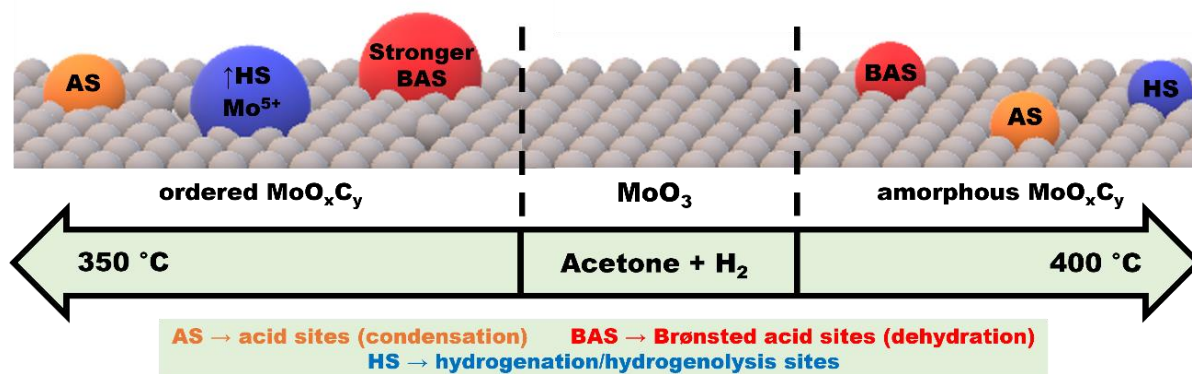


Figure 22. Active sites and related reaction pathways showed by the ordered and amorphous oxycarbide phases, both formed during acetone HDO reaction over MoO₃ catalyst at 350 and 400 °C, respectively.

Chapter 5. First-row transition metal molybdates (MMo) as candidates for acetone HDO reaction: Promoting C-C coupling products and high deoxygenation degrees

5.1. Contextualization

Unsupported mixed metal oxide phases containing two or more metals, commonly referred to as bulk mixed metal oxides, have applications in various fields, including photo-, electro-, and thermocatalysis [254–256]. However, they are primarily employed as selective oxidation catalysts [257–259]. While these oxides typically manifest as stoichiometric crystalline phases, their intricate structures and diverse compositions offer a range of properties that are often overlooked and underestimated, particularly in catalytic applications [260,261]. These bulk mixed metal oxides exhibit variable oxidation states, leading to variable coordination sites, diverse chemical characteristics of surface sites (including redox, basic, and acid functionalities), oxygen mobility reactivity, and the presence of vacancies and defects [259].

Within bulk mixed metal oxides, metal molybdates (MMo) have garnered considerable interest from both researchers and industry due to their versatility and straightforward synthesis [212]. Notably, FeMo has found widespread commercial use as a catalyst for the selective oxidation of methanol to formaldehyde [262]. The intense scrutiny of FeMo catalysts has helped to challenge a major paradigm in heterogeneous catalysis: the notion that catalyst surfaces merely represent terminations of bulk crystalline planes [259]. Given that heterogeneous catalysis primarily occurs at the surface, it is crucial to closely consider the relationship between catalytic performance and surface characteristics [263,264].

Numerous studies have revealed that the outermost surface layer of bulk MMo tends to be enriched with amorphous MoO_x species [265–269]. Specifically, for FeMo catalysts, it has been demonstrated that expanding this MoO_x contribution to crystalline MoO_3 domains enhances the overall methanol oxidation performance through synergy effects from the oxide phases [270,271]. Furthermore, this process promotes the formation of stoichiometric FeMo (with a Mo/Fe ratio of 1.5) at the catalyst surface, which is believed to be the most active phase for selective methanol oxidation [272]. Many reports have investigated the correlation between FeMo structural and surface characteristics with its catalytic performance [273–276]. Interestingly, it has been found

that other bulk MMo, including MnMo, CoMo, and NiMo, also show enhanced catalytic activity when surface MoO₃ domains are present [277–279].

Considering the different applications of MMo, they have been successfully and systematically employed as oxidation catalysts, enabling the same scientific approach employed for the use of MoO_x systems in HDO reactions, based primarily on the aforementioned reverse Mars-van-Krevelen mechanism. [280]. Despite the many reports on different metal molybdates, such as Ti³⁺, Fe³⁺, Co²⁺, V⁴⁺, V⁵⁺, Cr³⁺, Mn²⁺, Mn⁴⁺, Cu²⁺, Ni²⁺, and Zn²⁺ [212,281], to the best of our knowledge, there are few dedicated studies in the literature exploring their use as HDO catalysts [282]. There may be some confusion, as many works on HDO use the term "metal molybdates" to refer to catalysts combining molybdenum with other transition metals. These catalysts may not necessarily comprise the so-called bulk mixed metal oxides. Among these reports there are molybdenum bimetallic sulfides [283–285], phosphides [286,287], and also supported catalysts [131,132,283,284,288].

In contrast to oxidation reactions, the HDO atmosphere is not only reducing but also carburizing, given the combined presence of H₂ and carbon substrates in the reaction flow. In Chapter 4, we showed that under these conditions and with increasing temperature, MoO₃ undergoes a severe phase transition to MoO₂ and oxycarbide phases (MoO_xC_y) [107]. At higher temperatures, carbides are then obtained (Mo_xC_y) [180]. It was not until recently that this type of phase transition was reported for MMo. In an insightful work, Xu *et al.* [289] prepared CoMo, NiMo, and CuMo samples, which were subsequently treated under a H₂/methane atmosphere before employed as CO₂ hydrogenation catalysts. Through *in situ* time-resolved X-ray diffraction, the authors demonstrated an intricate phase transition from the MMo phases, progressing through a mixture of crystalline MoO_xC_y, α-MoC_{1-x}, and finally β-Mo₂C, with the corresponding metallic phase (Co, Ni, or Cu) at temperatures above 600 °C. All the final systems, M/Mo₂C, exhibited superior activities in CO₂ conversion, especially Cu/Mo₂C, which was highly selective towards methanol, as verified by subsequent studies [289,290].

Similar M/Mo₂C systems were proposed as potential catalysts for HDO reactions. Co- and Cu-modified Mo₂C were theoretically studied for furfural, glycerol, and propanediols HDO [170,207,291,292]. The promising features of these catalysts were systematically attributed to electronic modifications of the surface metallic atoms by the Mo₂C support. This leads to enhanced adsorption strength of intermediates and

reduced activation barrier for C-O cleavage reactions [291]. Despite interesting, these studies lack subsequent experimental investigations and, more than that, they propose and analyze bare supported systems, where the phase transitions related to mixed MMo structures are not present.

In Chapter 4, we showed that the intermediary $\text{MoO}_x/\text{MoO}_x\text{C}_y$ phases that are formed from MoO_3 under typical HDO reaction conditions have the ability to catalyze different reaction pathways that require acid (Brønsted or Lewis), metallic, or the combination of more than one site, in bifunctional mechanisms [107]. The most active catalysts do not only present the more usual Mo^{6+} oxidation state, but greater amounts of lower oxidation states [107]. Thus, it is possible that using MMo catalysts would be beneficial to stabilize these oxidation states due to their enhanced redox properties under the reaction conditions, besides the additional functionalities that may arise from the unexplored phase transitions under HDO stream.

Figure 23 shows an adapted reaction network for acetone HDO using MMo catalysts. The main differences regarding the scheme of Figure 15 rely on the additional production of higher condensation products (C_9O) and its deoxygenated counterparts (C_9), respectively obtained through the action of acid sites (AS) and the so-called hydrogenation/hydrogenolysis sites (HS).

Therefore, in this chapter, we prepared and explored first-row transition-metal molybdates (MMo, where $\text{M} = \text{Mn}^{2+}, \text{Fe}^{3+}, \text{Co}^{2+}, \text{Cu}^{2+}, \text{Zn}^{2+}$) in the acetone HDO reaction, additionally motivated by the abundance and affordability of such metals. Our main objective was to shed new light on the properties of these bulk mixed metal oxides, with new metallic functionalities, and to understand the phase transitions they undergo under reaction conditions. As shown in Figure 23, the direct dependence of the acetone HDO reaction pathways on the different catalytic sites can be used as a complementary probe to address the catalyst surface.

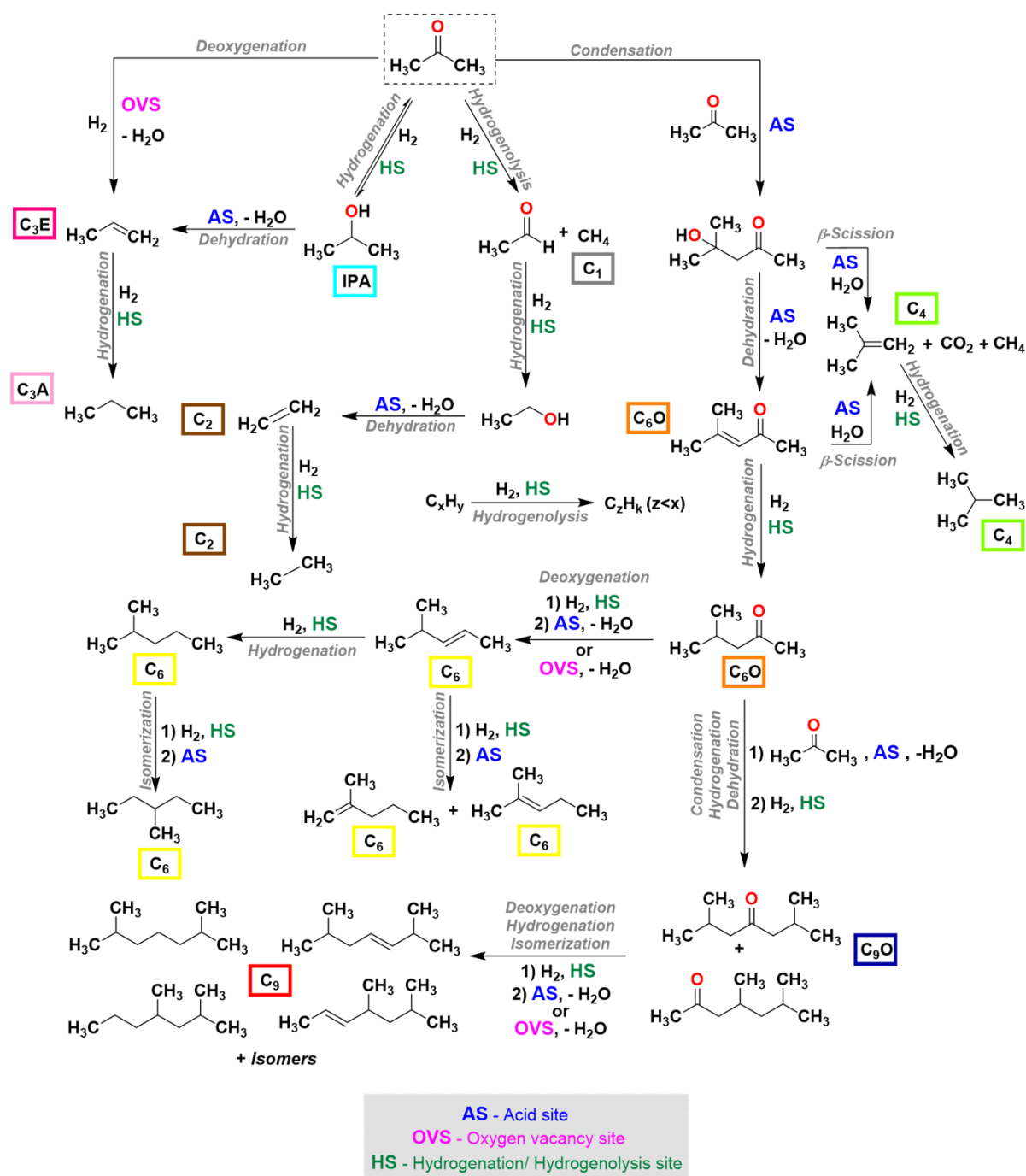


Figure 23. Reaction network for acetone HDO over MMo catalysts. Adapted from [107].

5.2. Results

Synthesis and characterization of MMo catalysts: The crystalline structures of the MMo catalysts were examined by powder XRD of the calcined samples and the results are shown in Figure 24. All the collected patterns show the successful preparation of the bulk mixed oxide structures. The diffraction peaks of the MnMo pattern can be

indexed to the monoclinic MnMoO_4 phase (ICSD CollCode 15615). The synthesized FeMo and CoMo structures also correspond to monoclinic systems, $\text{Fe}_2(\text{MoO}_4)_3$ (ICSD CollCode 16402) and CoMoO_4 (ICSD CollCode 118340), respectively. CuMo catalyst pattern matches the orthorhombic $\text{Cu}_3\text{Mo}_2\text{O}_9$ phase (ICSD CollCode 2836), while ZnMo can be attributed to the triclinic ZnMoO_4 structure (ICSD CollCode 17030).

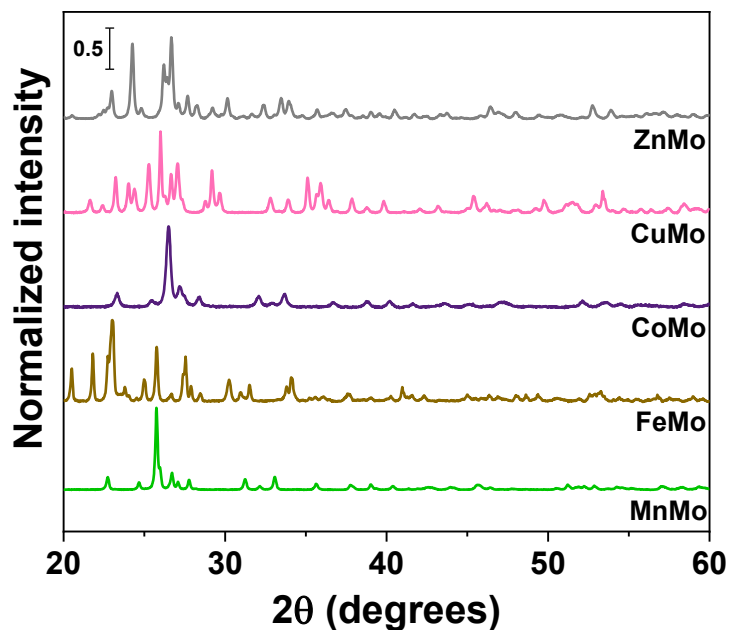


Figure 24. XRD patterns of the first-row transition metal molybdate catalysts (MMo): MnMo, FeMo, CoMo, CuMo, and ZnMo.

In general, the MMo catalysts presented low surface areas, ranging from around 4 to 22 $\text{m}^2 \text{g}^{-1}$ (Table A13), coherent with most bulk mixed oxides [259]. There is a clear correlation between the surface areas and the size of the MMo crystals observed by SEM analysis (Figure 25). Once they could only exhibit aggregation-derived porosity, the larger the crystal, the smaller the surface area. MnMo presented larger rod-like crystals (Figure 25 A), with at least 2 μm of length [212,293]. FeMo, CoMo, and CuMo, despite the different sizes, presented an aggregation of smaller irregular particles (Figure 25 B, C, and D) [212,294–297]. On the other hand, ZnMo crystallized as interpenetrated plates of up to 1 μm , but usually smaller (Figure 25 E) [212].

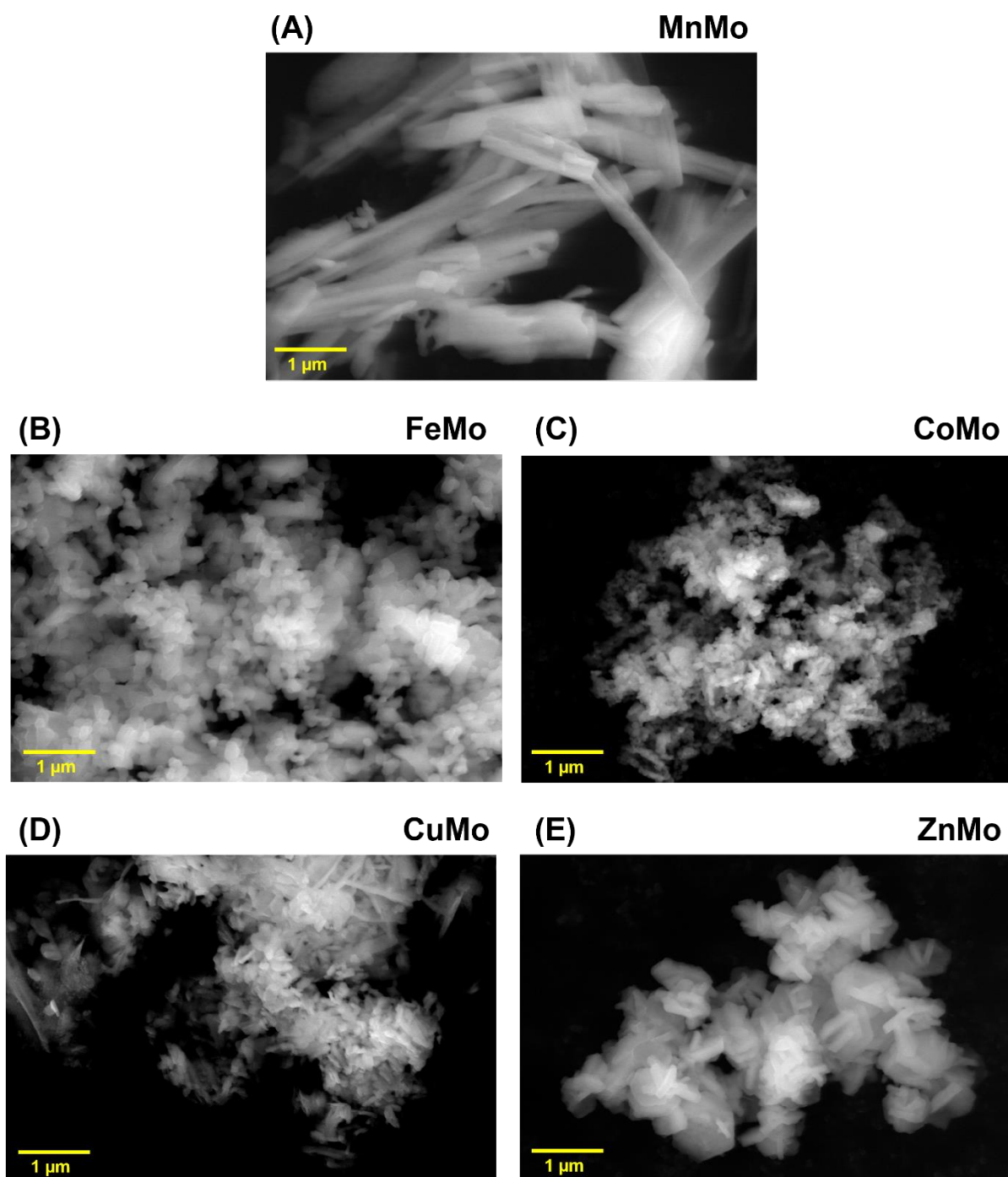


Figure 25. SEM images of the first-row transition metal molybdate catalysts (MnMo): (A) MnMo, (B) FeMo, (C) CoMo, (D) CuMo, and (E) ZnMo.

In terms of composition, as shown in Table 7, SEM-EDS (detailed in Figure A13) analysis provided coherent Mo/M atomic ratios when compared to the nominal values calculated based on the chemical formula of the corresponding crystalline structures. On the other hand, the XPS atomic surface analysis (detailed in Table A14), also

shown in Table 7, revealed molybdenum enrichment in the surface of all MMo catalysts, presenting Mo/M atomic ratios 1.5- to 2.0-fold higher. Numerous studies shown that the outermost surface layer of bulk MMo tends to present an extensive concentration of amorphous MoO_x domains [265–269], especially FeMo [270,271].

Table 7. Nominal and experimental atomic ratios (Mo/M, where M = Mn, Fe, Co, Cu, Zn) of the first-row transition metal molybdate catalysts (MMo). The experimental data was obtained through SEM-EDX and XPS measurements.

Sample	Atomic ratios		
	Nominal Mo/M	Experimental Mo/M (SEM-EDX) ^a	Experimental Mo/M (XPS) ^b
MnMo	1.0	1.0	2.0
FeMo	1.5	1.9	3.0
CoMo	1.0	1.0	1.7
CuMo	0.7	0.6	1.2
ZnMo	1.0	0.8	1.4

^a more details in Figure A13

^b more details in Table A14

The H₂-TPR curves (Figure A14) showed that, under diluted H₂ atmosphere, all the MMo catalysts went through major reduction events with increasing temperature. The reduction of molybdenum was not fully observed in any of the cases, as under the analysis conditions, it starts to reduce only at higher temperatures, above 700 °C [107]. The other events can be attributed to the reduction of the first-row transition metal atoms, all above 500 °C, except for copper. The MoCu catalyst exhibits two major reduction events centered at 327 and 394 °C, likely related to Cu²⁺→Cu¹⁺ and Cu¹⁺→Cu⁰ transitions, respectively.

Impact of the temperature profile: Following the preliminary experiments employed for the MoO₃ nanopowder (Figure 16), the synthesized MMo catalysts were exploratory tested in the acetone HDO reaction as a function of temperature, by heating from 300 to 400 °C. The acetone conversions and products' distributions are shown in Figure 26 and summarized in Table 8. The MoO₃ data obtained under similar conditions are shown for comparison purposes.

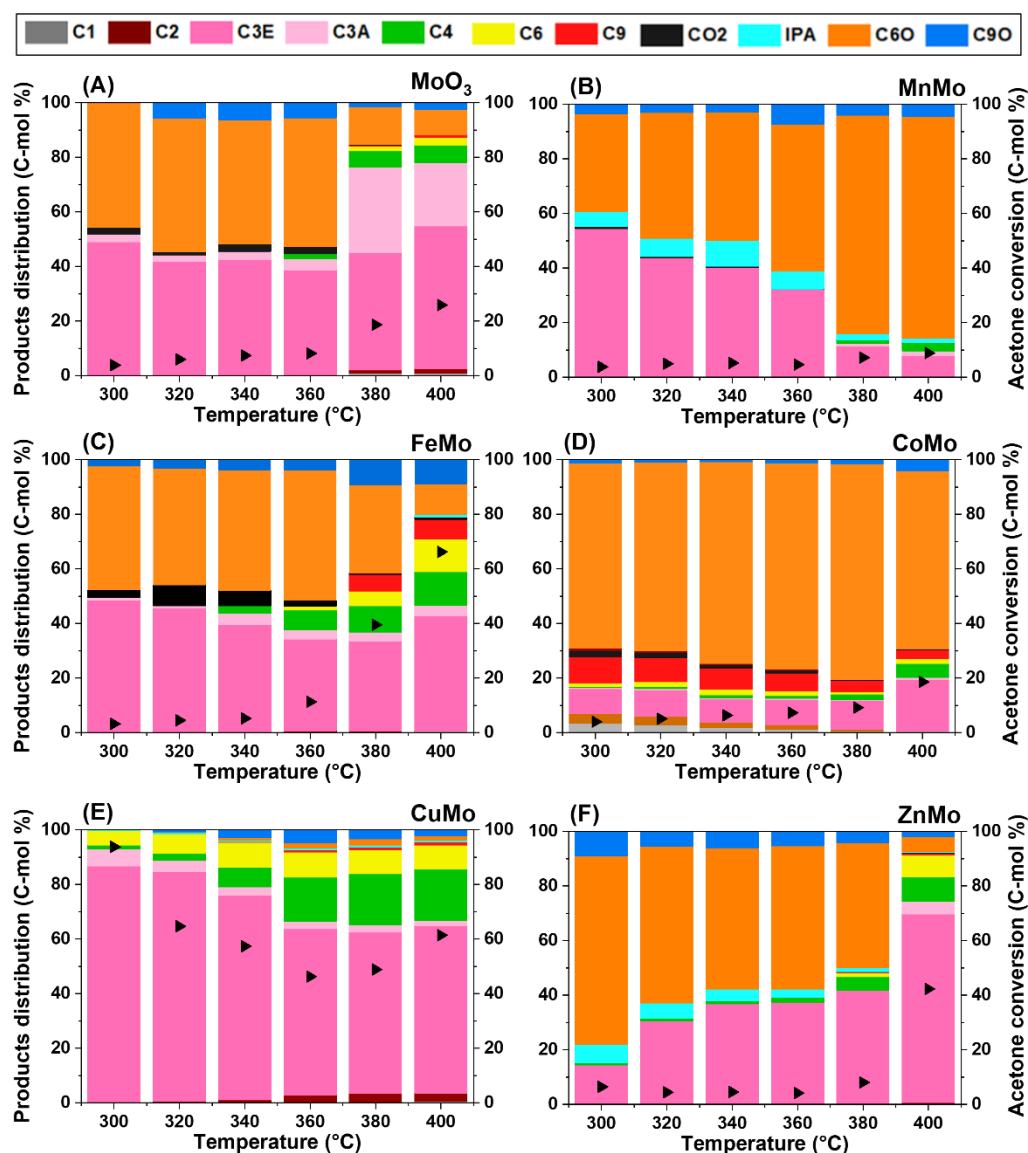


Figure 26. Products' distribution (colored) and conversion (black triangles) for acetone HDO reaction over MoO₃_comm (A) and first-row transition metal molybdate catalysts (MMo): MnMo (B), FeMo (C), CoMo (D), CuMo (E), and ZnMo (F). 300→400 tests were carried out from 300 to 400 °C, isothermal every 20 °C, total TOS: 3 h. WHSV = 7.32 g_{acetone} g_{catalyst}⁻¹ h⁻¹. Feed: 2.4 mL min⁻¹ acetone, 51 mL min⁻¹ H₂, balance He. Total flow: 100 mL min⁻¹.

Table 8. Summary of the catalytic data obtained for acetone HDO reaction as a function of temperature (300→400 tests) for the first-row transition metal molybdate catalysts (MMo): MnMo, FeMo, CoMo, CuMo, and ZnMo. Also, MoO₃ for comparison purposes.

Sample	Temperature (°C)	Acetone conversion (%)	Products' distribution (%)			
			HHP*	DDP*	CDP*	OP*
MoO ₃	300	4	3	49	-	48
	400	26	26	52	10	12
MnMo	300	4	6	54	-	40
	400	9	4	8	3	85
FeMo	300	3	1	49	-	50
	400	66	5	42	31	22
CoMo	300	4	8	9	11	72
	400	19	2	19	10	69
CuMo	300	94	6	87	7	-
	400	61	6	61	29	4
ZnMo	300	7	7	14	1	78
	400	42	6	69	18	7

* HHP (hydrogenation/hydrogenation products): C₁, C₂, C₃A, IPA

* DDP (direct deoxygenation products): C₃E

* CDP (coupling deoxygenated products): C₄, C₆, C₉

* OP (oxygenated products): CO₂, C₂HO, C₆O, C₉O

In general, the MMo catalysts behaved similarly to MoO₃, showing the highest acetone conversion at 400 °C. However, the temperature profile and the final products' distribution proved to be quite different. An important thing to note is that the MMo catalysts, especially FeMo and CuMo at 400 °C, promoted the formation of higher hydrocarbons (C₄, C₆, C₉), originated from the deoxygenation and cleavage of condensation oxygenated products (C₆O, C₉O). In this sense, differently from Chapter 4, where these products were minor ones and thus summarized as C_n together with hydrogenation products (C₁, C₂), here we employed a different nomenclature for the sake of clarity. Hydrogenation/hydrogenolysis products (C₁, C₂, C₃A, IPA) were called

HHP; coupling deoxygenated products (C_4 , C_6 , C_9), CDP; direct deoxygenation products (C_3E), DDP; and oxygenated products (CO_2 , C_2HO , C_6O , C_9O), OP.

MnMo and CoMo exhibited the least favorable outcomes, displaying low conversion rates (9 and 19 % at 400 °C, respectively) and a pronounced selectivity for undesired OP products across all temperature ranges. Interestingly, at 400 °C, MoO_3 , despite exhibiting a lower overall conversion (26 %) compared to the other MMo catalysts, favored the production of DDP and HHP products (52 and 26 %, respectively). At this same temperature, FeMo, CuMo, and ZnMo presented higher conversions (66, 61, and 42 %, respectively), with significant deoxygenation degree (HHP + DDP + CDP), especially regarding CDP products (42, 61, and 69 %, respectively), as already stated.

The catalysts, ranked by acetone conversion at 400 °C, followed the order MnMo < CoMo < MoO_3 < ZnMo < CuMo < FeMo. Similarly, in terms of deoxygenation degree at 400 °C, the order was MnMo < CoMo < FeMo < MoO_3 < ZnMo < CuMo. Thus, the catalytic evaluation as a function of TOS at 400 °C for all catalyst were carried out, as well as the investigation of the structural characteristics of the post-reaction catalysts.

Impact of temperature under isothermal conditions: The acetone conversions and products' distributions related to the acetone HDO reaction over MMo catalysts under isothermal conditions at 400 °C are shown in Figure 27 and summarized in Table 9. Again, the MoO₃ data was displayed for comparison.

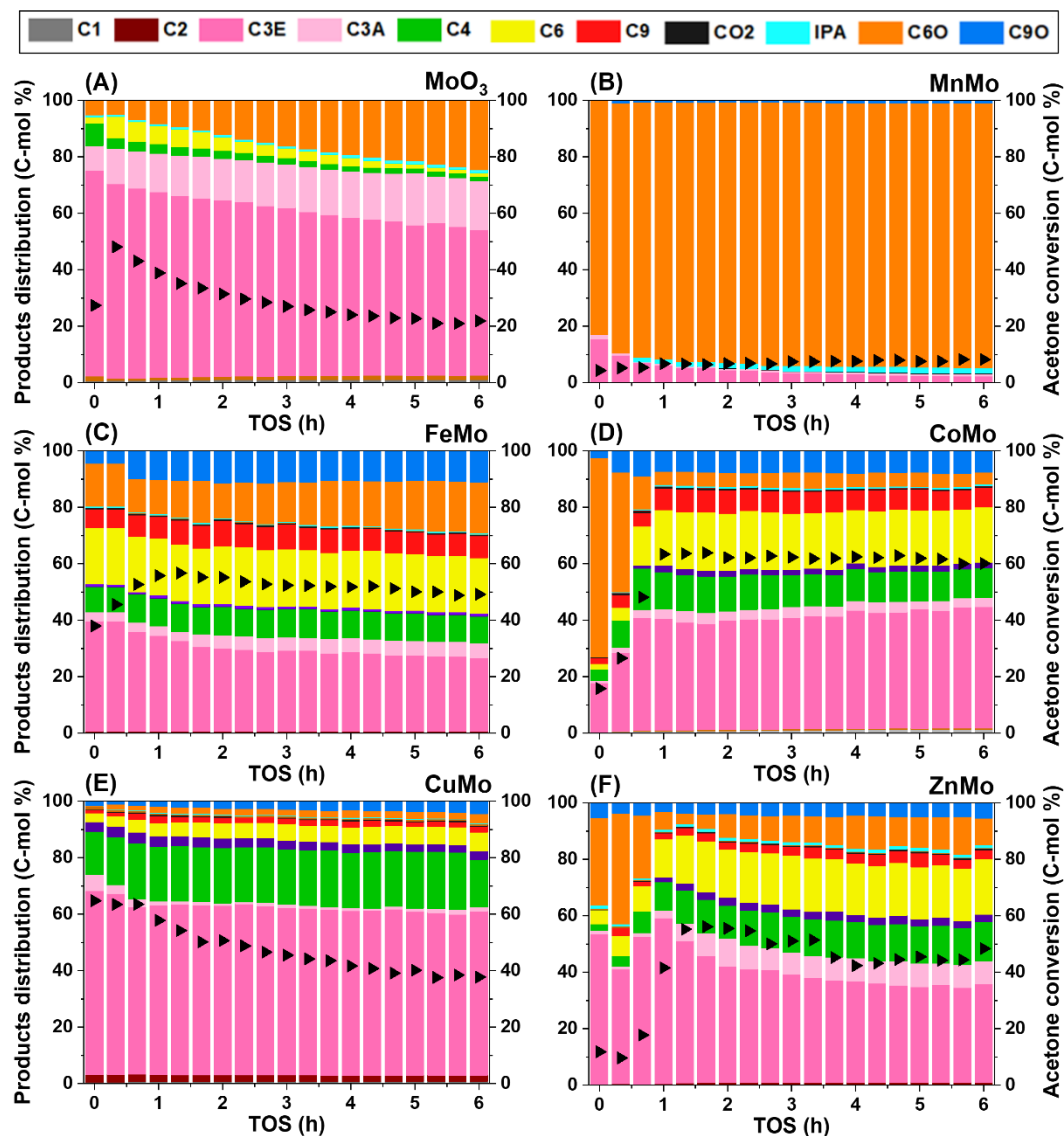


Figure 27. Products' distribution (colored) and conversion (black triangles) for acetone HDO reaction over MoO₃ (A) and first-row transition metal molybdate catalysts (MMo): MnMo (B), FeMo (C), CoMo (D), CuMo (E), and ZnMo (F). 400C tests were carried out at 400 °C, isothermal, TOS: 6 h. WHSV = 7.32 g_{acetone} g_{catalyst}⁻¹ h⁻¹. Feed: 2.4 mL min⁻¹ acetone, 51 mL min⁻¹ H₂, balance He. Total flow: 100 mL min⁻¹.

Table 9. Summary of the catalytic data obtained under acetone HDO isothermal conditions (400C tests) for the first-row transition metal molybdate catalysts (MMo): MnMo, FeMo, CoMo, CuMo, and ZnMo. Also, MoO₃ is shown.

Sample	TOS (h)	Acetone conversion (%)	Products' distribution (%)			
			HHP*	DDP*	CDP*	OP*
MoO ₃	1	39	16	66	10	8
	6	22	21	51	3	25
MnMo	1	7	2	6	-	92
	6	8	3	3	-	94
FeMo	1	56	4	34	39	23
	6	49	7	26	38	29
CoMo	1	63	5	39	43	13
	6	60	6	42	40	12
CuMo	1	58	5	60	30	5
	6	38	5	58	29	8
ZnMo	1	55	8	50	34	8
	6	48	11	35	39	15

* HHP (hydrogenation/hydrogenation products): C₁, C₂, C₃A, IPA

* DDP (direct deoxygenation products): C₃E

* CDP (coupling deoxygenated products): C₄, C₆, C₉

* OP (oxygenated products): CO₂, C₂HO, C₆O, C₉O

The activity of MoO₃ has already been extensively discussed in the first part of this work, Chapter 4, but it is worth emphasizing that a phase transition to MoO₂ and to a disordered MoO_xC_y phase takes place at 400 °C (Figure A15 A), accompanied by a slow deactivation along the 6 h on stream (from 39 to 22 % conversion) and an increase in OP (8 to 25 %) in detriment to DDP products (66 to 51 %). Among the MMo catalysts, MnMo showed the poorest results, with low conversion (~8 %) and high selectivity towards undesired condensation products (OP > 90 %) independent of TOS. In this case, there was no changes in the catalyst structure, as showed by the post-reaction XRD pattern (Figure A15 B), indicating that the presence of manganese in the lattice made the material resistant to the effects caused by the reaction conditions.

FeMo, CoMo, and ZnMo showed similar catalytic behaviors (Figure 27 C, D, and F) with an activation step prior to more stabilized acetone conversions and products' distributions. Both FeMo and CoMo took about 1 h to reach approximately 60 % conversion, while ZnMo took twice the time to achieve the same activity. Despite presenting different products' distributions during this activation period, once stabilized, these molybdates presented around 80 % degree of deoxygenation, producing mostly DDP products, i.e., C₃E. It is interesting to note that they also showed significant selectivity to CDP products, a very distinct behavior compared to MoO₃. During TOS, differently from their manganese counterpart, FeMo and CoMo underwent a phase transition to MoO₂ and an α -MoC_{1-x} phase, with no indication of crystalline phases containing the related first-row transition metals, while ZnMo additionally formed a segregated ZnO phase (Figure A15 F).

The CuMo catalyst did not exhibit an activation pattern at 400 °C, unlike the other metal molybdates (Figure 27 E). At the beginning of the reaction, it presented around 65 % acetone conversion, slightly deactivating during TOS, while the products' distribution remained essentially the same. The degree of deoxygenation was the highest among the studied molybdates, consisting of DDP and CDP, the latter in minor proportion. OP products like C₆O and C₉O represent less than 10 % of the products' distribution, increasing as the deactivation advanced. The XRD pattern of the post-reaction catalyst (Figure A15) showed that the structure was fully converted to Cu⁰, which is in accordance with the H₂-TPR profile of the CuMo (Figure A14). Copper exsolution and aggregation capability when transitioning from Cu²⁺ to Cu⁰ under reducing conditions is well known [298,299], however molybdenum crystalline structures are intriguingly absent.

Due to its high deoxygenation degree and high conversion already at 300°C (Figure 26), the CuMo catalyst was explored at lower temperatures, starting at 100 °C. Other copper/molybdenum systems were also tested, in an attempt to understand the CuMo severe structural modifications observed under reaction conditions.

Investigating CuMo and related catalysts: The CuMo catalyst was tested in the acetone HDO reaction from 100 to 300 °C. Other copper/molybdenum systems were studied to elucidate the high catalytic activity exhibited by CuMo, concurrent with the observed phase transitions under acetone HDO atmosphere. Pure molybdenum and copper oxides were tested (MoO₃, CuO, and Cu₂O), as well as a MoO₃/CuO physical

mixture (PM) and a 10 wt.% impregnated CuO@MoO_3 sample. The acetone conversions and products' distributions are shown in Figure 28. and the results at 300 °C are summarized in Table 10.

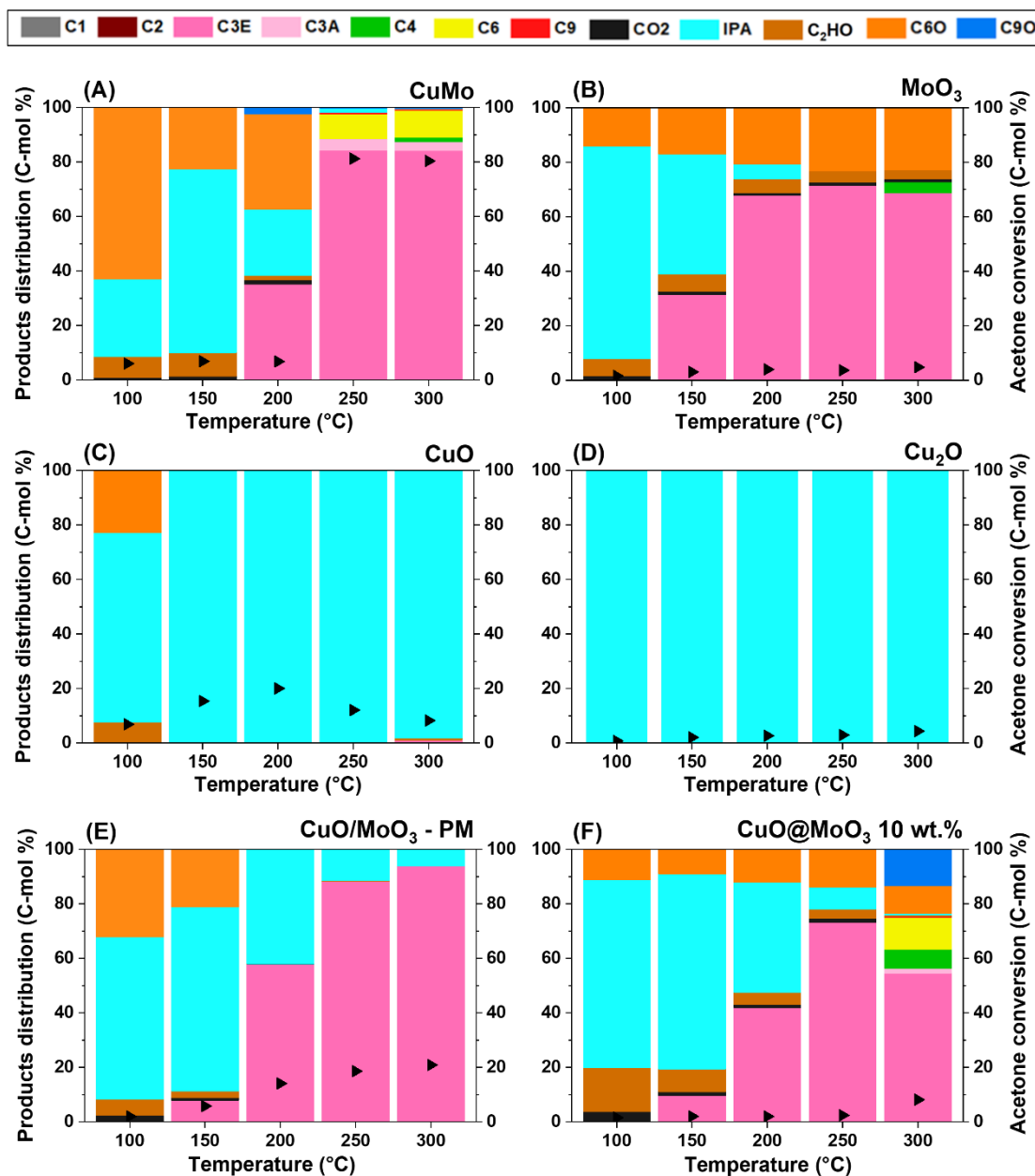


Figure 28. Products' distribution (colored) and conversion (black triangles) for acetone HDO reaction over CuMo (A) and related catalysts: MoO₃_comm (B), CuO (C), Cu₂O (D), CuO/MoO₃ – PM (physical mixture) (E), CuO@MoO₃ 10 wt.% (impregnated) (F). The 100→300 tests were carried out from 100 to 300 °C, isothermal every 50 °C, total TOS: 2.5 h. WHSV = 7.32 g_{acetone} g_{catalyst}⁻¹ h⁻¹. Feed: 2.4 mL min⁻¹ acetone, 51 mL min⁻¹ H₂, balance He. Total flow: 100 mL min⁻¹.

Table 10. Summary of the catalytic data obtained for acetone HDO reaction as a function of temperature (100→300 tests), at 300 °C, for CuMo and related catalysts: MoO₃_comm, CuO, Cu₂O, CuO/MoO₃ – PM (physical mixture), CuO@MoO₃ 10 wt.% (impregnated).

Sample	Acetone conversion (%)	Products' distribution (%)			
		HHP*	DDP*	CDP*	OP*
CuMo	80	4	84	12	-
MoO ₃	5	-	69	4	27
CuO	8	98	1	-	1
Cu ₂ O	4	100	-	-	-
CuO/MoO ₃ – PM	21	6	93	-	1
CuO@MoO ₃ 10 wt.%	8	2	55	19	24

* HHP (hydrogenation/hydrogenation products): C₁, C₂, C₃A, IPA

* DDP (direct deoxygenation products): C₃E

* CDP (coupling deoxygenated products): C₄, C₆, C₉

* OP (oxygenated products): CO₂, C₂HO, C₆O, C₉O

When submitted to acetone HDO reaction from 100 to 200 °C (Figure 28), all the studied catalysts presented poor catalytic activity (conversion < 15 %), producing predominantly condensation and hydrogenation products. Only the catalysts containing molybdenum (CuMo, MoO₃, CuO/MoO₃ – PM, and 10 wt.% CuO@MoO₃) started promoting DDP at 200 °C and continue to do so at higher temperatures. It is interesting to note that, at 250 and 300 °C, these same catalysts presented all high deoxygenation degrees (above 75 %). However, excepting CuMo, the acetone conversions were still low (< 20 %). At 300 °C, CuMo presented 100 % deoxygenation degree, with an 80 % conversion and 84 % selectivity to DDP, which are interesting results in the acetone HDO context, especially given the reaction temperature. Finally, the catalysts containing only copper (CuO and Cu₂O) displayed low conversions (< 20 %) and undesired products' distributions, largely promoting acetone hydrogenation to IPA, part of the HHP products. Thus, no related catalyst, containing molybdenum, copper, or both, exhibited catalytic activity close to or superior to CuMo.

As seen at 400 °C, under HDO conditions, CuMo transitioned to Cu⁰. However, at 300 °C, a Cu₂O phase was obtained, as observed in the post-reaction XRD pattern

(Figure A16). It is important to highlight that none of the other related catalysts reached this crystalline phase (Figure A16). At 300 °C, the CuMo catalyst presented superior activity, promoting DDP products (87 % against 61 % at 400 °C) with higher acetone conversion too (94 % against 61 % at 400 °C), which seems to be related to the stabilized Cu₂O phase. Once more, there is no indication of molybdenum crystalline structures and, across the phase transition, the crystallite mean size decreased from 77 nm (CuMo) to 54 nm (Cu₂O, at 300 °C) and 58 nm (Cu⁰, at 400 °C).

5.3. Discussion

Bulk mixed metal oxides typically crystallize in the form of perovskites (ABO₃) or spinels (AB₂O₄) [259], where A cation has AO₁₂ and AO₄ coordination, respectively, and B cations contain BO₆ coordination for both structures. That is the case of some well-known applicable mixed oxide materials such as BaZrO₃ and SmCoO₃ perovskites [300,301], also being possible doubly substitute ones, as (La_{0.6}Sr_{0.4})(Co_{0.2}Fe_{0.8})O₃ [302], as well as CoAl₂O₄ and ZnAl₂O₄ spinels [303,304]. For molybdates (MMoO₄) and vanadates (M₂V₂O₇), whether they present transition, alkaline, or alkaline earth metals, molybdenum and vanadium play a fundamental role in the crystalline arrangement, once exhibiting higher oxidation states (commonly +6 for Mo and +5 for V) and occupying octahedral sites regardless of the structure [259].

The first-row transition metal molybdates (MMo, where M = Mn²⁺, Fe³⁺, Co²⁺, Cu²⁺, Zn²⁺) explored here were prepared by a simple co-precipitation approach using ammonium heptamolybdate tetrahydrate and the correspondent metal nitrates [212]. The calcined materials presented crystalline XRD patterns (Figure 24) that could be assigned to existent crystallographic data regarding their composition. As seen, MnMo, FeMo, and CoMo were crystallized as monoclinic structures, while ZnMo was triclinic and CuMo was orthorhombic. The CuMo orthorhombic phase presents the Cu₃Mo₂O₉ formula, showing that part of the molybdenum precursor probably remained unreacted and that a different structure was then promoted.

Despite the correlation between the nominal Mo/M atomic ratios and the experimental ones obtained through SEM-EDS analysis (Table 7), the XPS atomic analysis data (Table 7) show a higher molybdenum concentration on the surface. As seen, the experimental Mo/M molar ratios were 1.5- to 2.0-fold higher than the nominal one, calculated based on the formula of the corresponding crystalline structures.

Besides XPS measurements, Low Energy Ion Scattering (LEIS), which determines quantitatively the composition of the outermost layers of solid samples [305], also proved surface molybdenum enrichment for metal molybdates samples [267]. Recent advances in electron microscopy techniques with enhanced resolution indicated an amorphous layer of MoO_x domains ($\sim 1\text{-}2\text{ nm}$) in the surface of bulk mixed metal oxides [268,269]. From another perspective, *in situ* methanol chemisorption monitored by infrared spectroscopy showed that only Mo-OCH_3 species are present on the surface of the $\text{Fe}_2(\text{MoO}_4)_3$ phase [306], confirming extensive surface coverage by MoO_x species.

Despite the widely reported surface coating of bulk mixed metal oxides by amorphous MoO_x domains, which could shield access to active metallic sites and affect the expected catalytic activity, under acetone HDO reaction conditions, there is a complete restructuring of MMo catalysts. XRD analyzes of the post-reaction catalysts after 6 h on stream at $400\text{ }^\circ\text{C}$ (Figure A15) showed severe phase transitions for all the molybdates, excepting MnMo, which resisted conversion and maintained the monoclinic MnMoO_4 structure. FeMo, CoMo, and ZnMo mixed oxide structures were transformed in a mixture of $\beta\text{-MoO}_2$ and $\alpha\text{-MoC}_{1-x}$, with no detectable crystalline phases related to the corresponding first-row transition metals. Only ZnMo led to a fraction of ZnO in the phase mixture. In turn, CuMo took the opposite way, with a resultant crystalline Cu^0 pattern and absence of molybdenum related structures.

There are few studies in the literature exploring the structural behavior of metal molybdates under a reducing atmosphere [307], and even fewer under a carburizing atmosphere [289]. Despite the extensive literature on $\text{Fe}_2(\text{MoO}_4)_3$, most studies deal with its structural properties under oxidizing environments. Nevertheless, a possible $\text{Fe}_2(\text{MoO}_4)_3 \leftrightarrow \text{FeMoO}_4$ redox cycle during methanol oxidation reaction was proposed [308,309]. Contrary to expectations, studies involving *in situ* bulk characterization by XRD showed that the FeMoO_4 phase does not appear under the studied conditions [310]. Cycles involving reducing and oxidizing atmospheres were conducted at $472\text{ }^\circ\text{C}$ [310]. Additionally, it was reported that $\text{Fe}_2(\text{MoO}_4)_3$ maintains its fully oxidized and intact structure even in the presence of various reducing gases for prolonged periods at temperatures up to $350\text{ }^\circ\text{C}$ [311].

Rodriguez *et al.* [307] showed that from room temperature until $500\text{ }^\circ\text{C}$, under a 5 % H_2 flow, CoMoO_4 transitioned to $\text{Co}_2\text{Mo}_3\text{O}_8$ and then to CoMoO_3 . CoMoO_4 was also evaluated under a CH_4/H_2 carburizing atmosphere by the same research group,

together with other metal molybdates [289]. *In situ* time-resolved XRD measurements showed the formation of CoO at 490 °C, a mixture of α -MoC_{1-x} and Co⁰ at 720 °C, finally reaching the β -Mo₂C and Co⁰ phases at 760 °C. For CuMoO₄, the same work reported the presence of Cu⁰ in all XRD patterns above 240 °C, accompanied by MoO_xC_y at this same temperature, Mo⁰ at 520 °C onwards, and β -Mo₂C at 620 °C. The final materials, M/Mo₂C, were subsequently evaluated in the CO₂ hydrogenation reaction, presenting exciting results, especially Cu/Mo₂C, which was highly selective towards methanol.

Despite interesting, none of these studies reflect the acetone HDO conditions employed here, and they also do not reach the same crystalline phases observed for the post-reaction MMo catalysts. Even carburization with CH₄ led to different results than using acetone. At 400 °C, MnMo did not change at all, while FeMo, CoMo, and ZnMo transformed into a mixture of β -MoO₂ and α -MoC_{1-x} (with ZnO for the ZnMo). In turn, CuMo phase transition resulted in Cu₂O at 300°C and Cu⁰ at 400°C.

The main products obtained in the acetone HDO using the MMo catalysts at any reaction conditions were C₁, C₂, C₃A, C₃E, C₄, C₆, C₉, IPA, C₆O, and C₉O (Figures 26 and 27, Tables 8 and 9). Figure 23 shows that although subsequent dehydration and hydrogenation steps are also involved in the overall C₆O and C₉O production (OP), the first step to form them is acetone condensation mediated by AS. The formation of IPA (HHP) requires HS sites, whereas the formation of C₃E (DDP) can be derived from direct deoxygenation of acetone mediated by OVS or through hydrogenation/dehydration steps via IPA and HS/AS sites. C₁, C₂, C₃A (HHP) were produced through hydrogenation or hydrogenolysis steps using HS sites. C₆O and C₉O can be deoxygenated, giving rise to C₆ and C₉ (CDP), respectively, using HS and AS sites. Additionally, C₆O can suffer the acid-catalyzed β -scission forming C₄ (CDP), also using AS. The dependence of each product with the different catalytic sites allows us to follow the reaction network and try to establish correlations with the post-reaction structures obtained.

At 400 °C (Figure 27 and Table 9), the MMo catalysts presented different catalytic activities. MnMo showed a reduced acetone conversion (< 8 %), producing mainly OP products (> 90 %), independent of TOS. This result may be related to its very low surface area (3.6 m² g⁻¹) and also to its static structural nature under reaction conditions. Manganese does not reduce and possibly does not assist molybdenum in achieving stabilized lower oxidation states. The few available sites on the surface are

likely hydroxyl groups formed on stream, that could act as BAS, thus promoting acetone condensation to C_6O .

In turn, FeMo, CoMo, and ZnMo presented similar catalytic behaviors, all of them required an activation period of around 1-2 h to reach maximum acetone conversion and then remained essentially stable until the end of the reaction. After 6 h on stream, they exhibited the following order of conversion: CoMo (60 %) > FeMo (49 %) > ZnMo (48 %), which corresponds to the same order of surface areas (Table A13). In terms of products' distribution, they presented a high selectivity to CDP products (around 40 %), also promoting DDP products (from 26 to 42 %). As already mentioned, both CDP and DDP are proposedly produced through a bifunctional mechanism involving HS and AS sites (Figure 23). It is important to highlight that the deoxygenation degree was always higher than 70 % for these catalysts, reaching almost 90 % for CoMo. Furthermore, a significant portion of these deoxygenated products is CDP, highlighting not only the ability of these catalysts to fulfill their role in the HDO context but also to promote carbon chain growth.

Despite the many works using molybdenum carbides as catalysts in HDO processes [312], the majority of the literature employs β - Mo_2C over the less stable α - MoC_{1-x} . The same is valid for molybdenum oxide catalysts, in which MoO_3 is preferred to MoO_2 , extensively considered a less active phase [63,64]. After acetone HDO reaction at 400 °C, FeMo, CoMo, and ZnMo catalysts convert precisely into a mixture of these two undesired phases and an eventual amorphous contribution from the corresponding first-row transition metals as more oxidized species. In Chapter 4 we saw that MoO_2 promoted essentially IPA and C_6O products, with very low conversion (Figure 16 and Table 5). Reports on β - Mo_2C being used as acetone HDO catalysts showed a high selectivity to IPA, evidencing the molybdenum carbides hydrogenating capability [66]. It was only with the enrichment of its surface with oxygen, leading to the formation of hydroxyl groups (BAS) on stream, that the material began to exhibit selectivity towards C_3E and C_3A , reinforcing the hypothesis of a bifunctional mechanism [66]. In this case, acetone is hydrogenated to IPA (HS), which is then dehydrated to generate C_3E (AS), which can be finally hydrogenated to C_3A (HS).

CuMo presented the most interesting catalytic activity among the MMo catalysts. It showed a relatively high initial conversion at 400 °C (58 %), which slightly drops to the end of the reaction (38 %). Nevertheless, the products' distribution remained practically the same along TOS, promoting DDP and CDP products (~ 60

and 30 %, respectively), with the highest deoxygenation degree (> 90 %). As mentioned earlier, this catalyst is intriguing for following the opposite path compared to the other MMo catalysts, presenting only a copper crystalline phase at the end of the reaction, Cu^0 , and neither MoO_2 nor $\alpha\text{-MoC}_{1-x}$. The molybdenum must be amorphized, however, at the studied temperature, it could be found as the disordered MoO_xC_y phase, as previously proposed at Chapter 4. This hypothesis is further supported by the fact that the presence of intermediate MoO_xC_y phases has already been reported in this temperature range during the carburization of CuMoO_4 [289].

At 300°C (Figure 28 and Table 10), CuMo HDO capability is even more prominent, showing 80 % acetone conversion and 100 % deoxygenation degree (4 % HHP, 84 % DDP, and 12 %CDP). In this case, the CuMo structure was converted to a Cu_2O phase (Figure A14), with molybdenum crystalline phases being once more absent. Although MoO_xC_y phases, whether crystalline or amorphous, are not commonly found in this temperature range, the presence of a metal with increased reducibility can be paramount. It is reported that Pt/ MoO_3 systems under reducing/carburizing conditions converts to molybdenum bronze even at room temperature [313,314]. The hydrogen produced on Pt surface spillover to the oxide surface, further diffusing into the lattice. Upon heating, the carbon on stream is consumed and starts incorporating into the structure to form oxycarbide intermediates. For the Pt/ MoO_3 system, using a H_2/CH_4 flow, it can occur in temperatures as low as 250°C . Considering the differences between Pt and Cu as potential sites for hydrogen adsorption, dissociation, and spillover, a parallel mechanism could be proposed for the formation of amorphous MoO_xC_y phases.

The other copper/molybdenum related catalysts tested for comparison purposes did not present the same promising results as CuMo. MoO_3 , as expected, presented good deoxygenation degree (73 %) but poor acetone conversion (5 %), being unable to convert to reduced and/or oxycarbide phases alone below 350°C [107]. Both copper oxides, CuO and Cu_2O , showed low conversions (< 8 %) and basically promoted acetone hydrogenation to IPA (HHP). The physical mixture between MoO_3 and CuO presented better results (21 % conversion and 99 % deoxygenation degree), but still inferior to CuMo. The existence of two segregated phases from the beginning may not promote the synergistic effect expected between the copper and molybdenum atoms. Finally, the impregnated 10 wt.% $\text{CuO}@ \text{MoO}_3$, as the MoO_3 , presented low conversion (8 %), despite a reasonable deoxygenation

degree (76 %), the difference being the significant production of CDP and OP. Despite creating an interface between the copper and molybdenum phases, it would be difficult to achieve the intended Mo/M molar ratio without promoting extensive segregation.

5.4. Considerations

Despite some remaining questions regarding the activity of MMo catalysts, especially concerning their surface and structural modifications under reaction conditions, this class of materials has shown potentiality as HDO catalysts. Except for MnMo, the molybdates exhibited high acetone conversion and high selectivity to deoxygenated products at 400 °C. Compared to MoO₃, they showed significantly superior conversion and greater stability over TOS. FeMo, CoMo, and ZnMo particularly promoted C-C coupling products, CDP. Their production starts with acetone condensation to C₆O and C₉O mediated by AS, followed by their deoxygenation giving rise to C₆ and C₉, respectively, using HS and AS sites thorough a bifunctional mechanism. C₆O can also suffer the acid-catalyzed β -scission forming C₄, also using AS. This interesting selectivity should be related to β -MoO₂ and α -MoC_{1-x} phases, common to all these post-reaction catalysts, or even to molybdenum amorphous phases. On the other hand, CuMo transitioned to copper crystalline phases, Cu₂O at 300 °C and Cu⁰ at 400 °C. In both situations, acetone conversion and deoxygenation degree are high, promoting desired C₃E. This high HDO activity was proposedly attributed to a combination of copper catalytic sites and amorphous MoO_xC_y over it, and makes CuMo a potential catalyst for more appealing HDO applications.

Chapter 6. Evaluating Mo/zeolite and M/zeolite catalysts over acetone HDO reaction: The effect of combining zeolites acidity and abundant metals

6.1. Contextualization

Zeolites form a crucial class of crystalline microporous materials featuring a three-dimensional framework formed through the interconnection of TO_4 tetrahedra, where T denotes atoms like silicon, aluminum, or other heteroatoms. The varied configurations of TO_4 tetrahedra connections lead to a diverse array of microporous structures within zeolites, comprising more than 250 acknowledged families according to the International Zeolite Association [315]. Zeolites are also recognized for their thermal stability and regulable acidity [316]. Therefore, they play a pivotal role in industrial applications as adsorbents, ion exchangers, molecular sieves, and specially as catalysts, being an important part of many economic and environmental challenging processes [317–319]. It is worth mentioning that zeolites make up over 40 % of all solid catalysts employed in oil refining, petrochemical processing, and fine chemicals [320].

In conventional aluminosilicate zeolites, the overall negative charge is determined by the number of framework AlO_4^- units. When this charge is neutralized by a proton, it gives rise to Brønsted acid sites (BAS) within the zeolite framework, serving as active sites in acid-catalyzed reactions [321]. Additionally, it is known that during zeolite activation and catalysis, some bridging hydroxyl groups undergo dihydroxylation. This process leads to the formation of extra-framework species, which act as electron acceptor sites, namely Lewis acid sites (LAS). These centers have been shown to enhance the acidity of BAS, contributing to various important processes such as light paraffin isomerization and fluid catalytic cracking [322]. Nevertheless, the understanding of LAS in zeolites remains limited compared to BAS literature [323].

In addition to zeolites well-known intrinsic acidity and stability, they also possess a high surface area related to an intricate framework of channels and cavities. Such characteristics make these materials particularly useful for constructing robust bifunctional catalysts, exhibiting both acid and metallic sites. The latter can be incorporated through a variety of simple and effective procedures: impregnation, ion exchange, deposition-precipitation, or even encapsulation during crystallization [324]. Optimizing the ratio between active sites with different catalytic functions is vital for achieving specific products' distributions. Synergistic effects are expected if the acid

and metallic functionalities are in close proximity and probably under cavity confinement [325,326]. This type of site engineering in metal/zeolite systems has been widely explored in recent years [327].

Among the processes that can take advantage of metal/zeolite bifunctional properties is the hydrodeoxygenation (HDO) reaction, one of the main routes studied for biomass valorization, which has emerged as an alternative to current energy matrices due to its non-fossil origin and abundant raw material [328]. Naturally, most studies involving zeolites as acid matrices for HDO catalysis have predominantly employed ZSM-5 [324], which has been extensively applied in the petroleum industry for many years, combining it with highly active noble metals, such as platinum, ruthenium, rhodium, and palladium [329–333]. More recently, alternative metal catalytic sites have been sought and evaluated, particularly the abundant and affordable metals from the first-row transition series [324], with special attention to nickel [334–337].

Considering the reactions involved in HDO processes, using catalysts that approximate and combine acid and metallic functionalities in a single material, such as the metal/zeolite systems, appears to be economically and energetically advantageous. Most studies in the HDO literature use large aromatic molecules as model compounds, such as phenol, guaiacol, anisole, cresol, furan, and benzophenone [338], many of which present diffusion limitations depending on the zeolite structure and pore opening. Smaller molecules, such as acetone, are less employed, even though ketones represent up to 15 % of the bio-oil matrix.

When submitted to HDO reaction of biomass-derived compounds, metal/zeolite catalysts have presented exciting results. Some main concepts are still under intense scrutiny such as the correct combination of metal and acid sites, site-ratio balancing, the proximity between such functions, the already mentioned confinement effect, among others [324]. Many studies have focused on reactions in the liquid phase, aiming to convert phenol [329,339,340], catechol [329], anisole [44], guaiacol [329,341,342], cresol [342], levulinic acid [343–345], as well as phenolic dimers [329,336,341] and triglycerides [337,346], which are more appealing given the biomass upgrading context. Most of them have dedicated themselves to evaluate metal/zeolite catalysts employing noble metals, but very few on abundant transition metals, which are not only more accessible and cheaper, but can be significantly active under reaction conditions promoting desired products.

Figure 29 shows an adapted reaction network for acetone HDO using metal/zeolite catalysts [107]. The main differences regarding the scheme of Figure 15 rely on the production of higher condensation products (C_9O) and aromatics (BTX) involving acid-catalyzed steps. Reportedly, in an acid environment, BTX can be promoted under pore confinement through the well-known hydrocarbon pool mechanism [347,348].

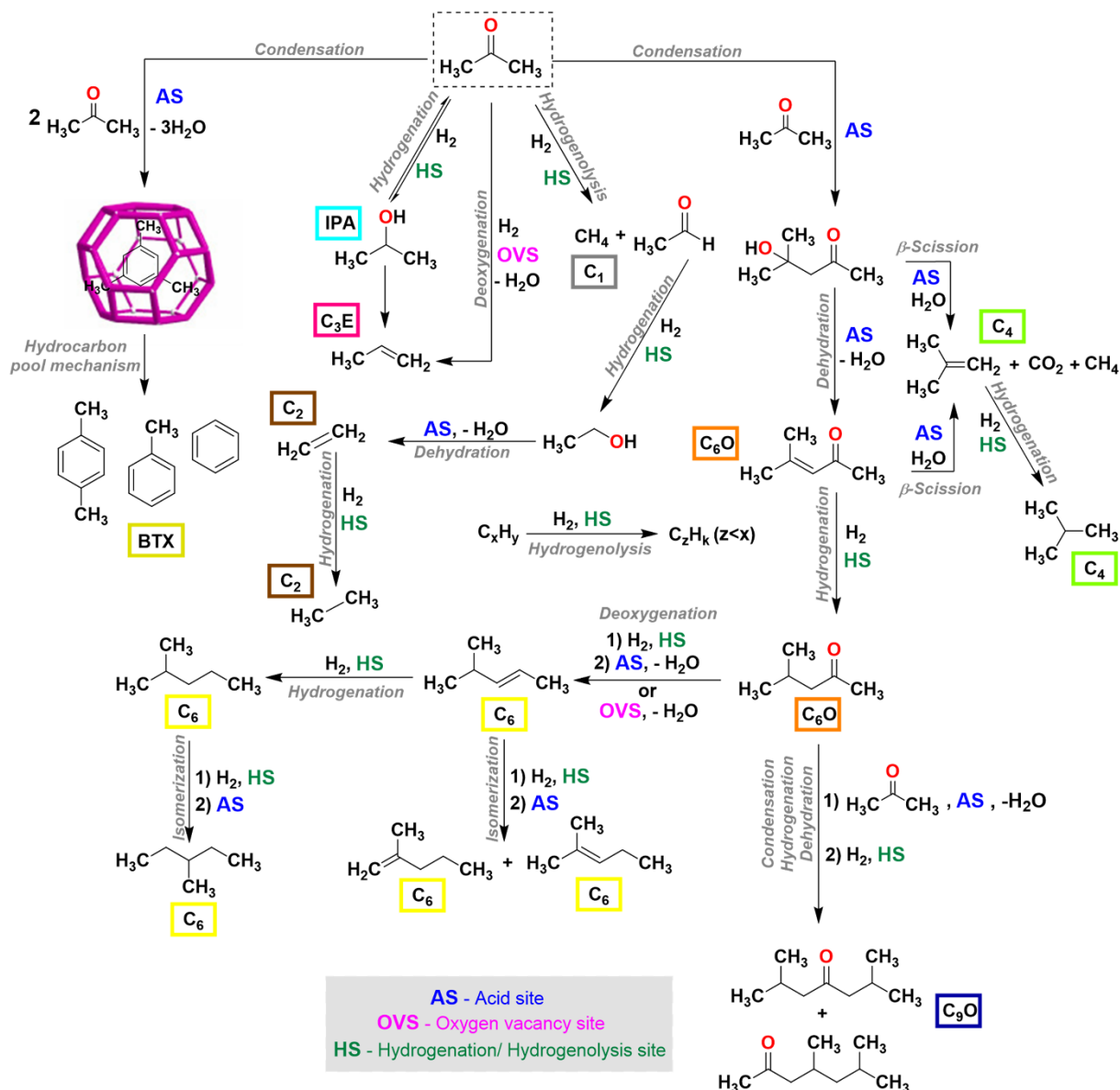


Figure 29. Reaction network for acetone HDO over metal/zeolite catalysts. Adapted from [107].

As reported in Chapter 4, our group highlighted the importance of undercoordinated $\text{Mo}^{\delta+}$ active species generated on MoO_3 under HDO reaction conditions as HS sites [107]. Murugappan *et al.* [349] studied MoO_3 catalysts supported on various matrices and demonstrated that TiO_2 and ZrO_2 were able to stabilize these active species.

Therefore, in an effort to enhance the accessibility and stability of the undercoordinated $\text{Mo}^{\delta+}$ active sites, that presented hydrogenating/hydrogenolysis capability approaching metallic behavior (Chapter 4), and to combine them with acid functionalities, supported zeolite catalysts were also investigated in the acetone HDO reaction. ZSM-5 zeolite with different concentrations of acid sites served as supports for molybdenum (Mo/zeolite) and other metals from the first-row transition series (M/zeolite), some of them previously studied in the form of the bulk mixed oxide structures (Chapter 5). In addition to the primary goal of achieving bifunctionality, as already mentioned, zeolites offer a high surface area due to their intricate framework of channels and cavities, thereby introducing a confinement effect that can significantly influence catalytic activity. As shown in Figure 29, the direct dependence of the acetone HDO reaction pathways on the different catalytic sites and combinations among them can be used to unveil the characteristics of the metal/zeolite catalysts.

6.2. Results

The influence of zeolite acid sites concentration on acetone HDO: ZSM-5 zeolites with different Si/Al molar ratios, referred to as Z11.5, Z40, and Z140, were commercially obtained and exploratively tested in the acetone HDO reaction as a function of temperature (200→400 tests) before metal impregnation. The catalytic results are presented in Figure 30 and summarized in Table 11.

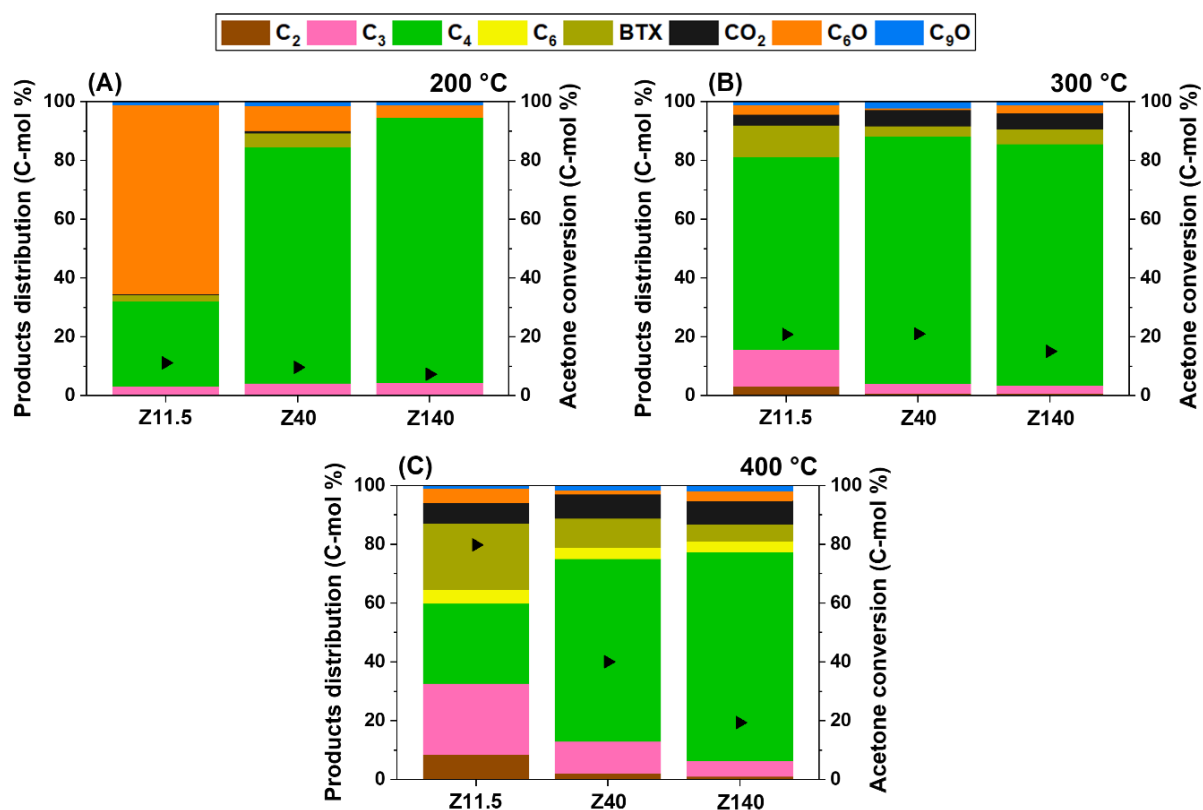


Figure 30. Products' distribution (colored) and conversion (black triangles) for acetone HDO reaction over pristine ZSM-5 zeolites (Z11.5, Z40, and Z140) at (A) 200 °C, (B) 300 °C, and (C) 400 °C. 200→400 tests were carried out from 200 to 400 °C, isothermal every 100 °C, total TOS: 1.5 h. WHSV = $7.32 \text{ g}_{\text{acetone}} \text{ g}_{\text{catalyst}}^{-1} \text{ h}^{-1}$. Feed: 2.4 mL min^{-1} acetone, $51 \text{ mL min}^{-1} \text{ H}_2$, balance He. Total flow: 100 mL min^{-1} .

Table 11. Summary of the catalytic data obtained for acetone HDO reaction as a function of temperature (200→400 tests), for pristine ZSM-5 zeolites (Z11.5, Z40, and Z140) at 200 °C, 300 °C, and 400 °C.

Sample	Temperature (°C)	Acetone conversion (%)	Products' distribution (%)				
			HHP*	DDP*	CDP*	BTX*	OP*
Z11.5	200	11	-	3	29	2	66
	300	21	3	13	66	11	7
	400	80	9	24	32	23	12
Z40	200	10	-	4	80	5	11
	300	21	1	3	84	4	8
	400	40	2	11	66	10	11
Z140	200	7	-	4	90	-	6
	300	15	1	3	82	5	9
	400	18	1	6	75	6	12

* HHP (hydrogenation/hydrogenation products): C₁, C₂, C₃A, IPA

* DDP (direct deoxygenation products): C₃E

* CDP (coupling deoxygenated products): C₄, C₆, C₉

* BTX (aromatic products): benzene, toluene, xylenes

* OP (oxygenated products): CO₂, C₂HO, C₆O, C₉O

In general, the ZSM-5 catalysts promoted the same products regardless of the reaction conditions. Acetone conversions initially began at low levels, around 10 % at 200 °C, and then increased with temperature, showing a direct correlation with the different Si/Al molar ratios (Figure A18 and Table A15). For the Z11.5 catalyst, conversion reached 80 % at 400°C, followed by Z40 with 40 %, and Z140 with 18 %.

In terms of products' distribution, CDP products (C₄, C₆, C₉) were mainly promoted, especially C₄. HHP (C₁, C₂) and OP (CO₂, C₂HO, C₆O, C₉O) were hardly produced (> 10 %), while DDP (C₃E) and BTX (benzene, toluene, xylenes) were promoted at higher temperatures (400 °C).

At 200 °C, excepting Z11.5, which privileged OP products (66 %), CDP were extensively promoted. The same trend regarding CDP was observed at 300 °C, however DDP and BTX started to become important, especially for Z11.5. At 400 °C,

these two groups of products achieve their maximum production for all the catalysts, but Z40 and Z140 still presented a higher selectivity to CDP, 66 and 75 %, respectively. At this temperature, Z11.5 exhibited the most diversified products' distribution profile, with 9 % HHP, 24 % DDP, 32 % CDP, 23 % BTX, and 12 % OP.

When evaluated over TOS, the ZSM-5 catalysts exhibited different catalytic activity, particularly concerning acetone conversion and overall deactivation, as shown in Figure 31 and Table 12.

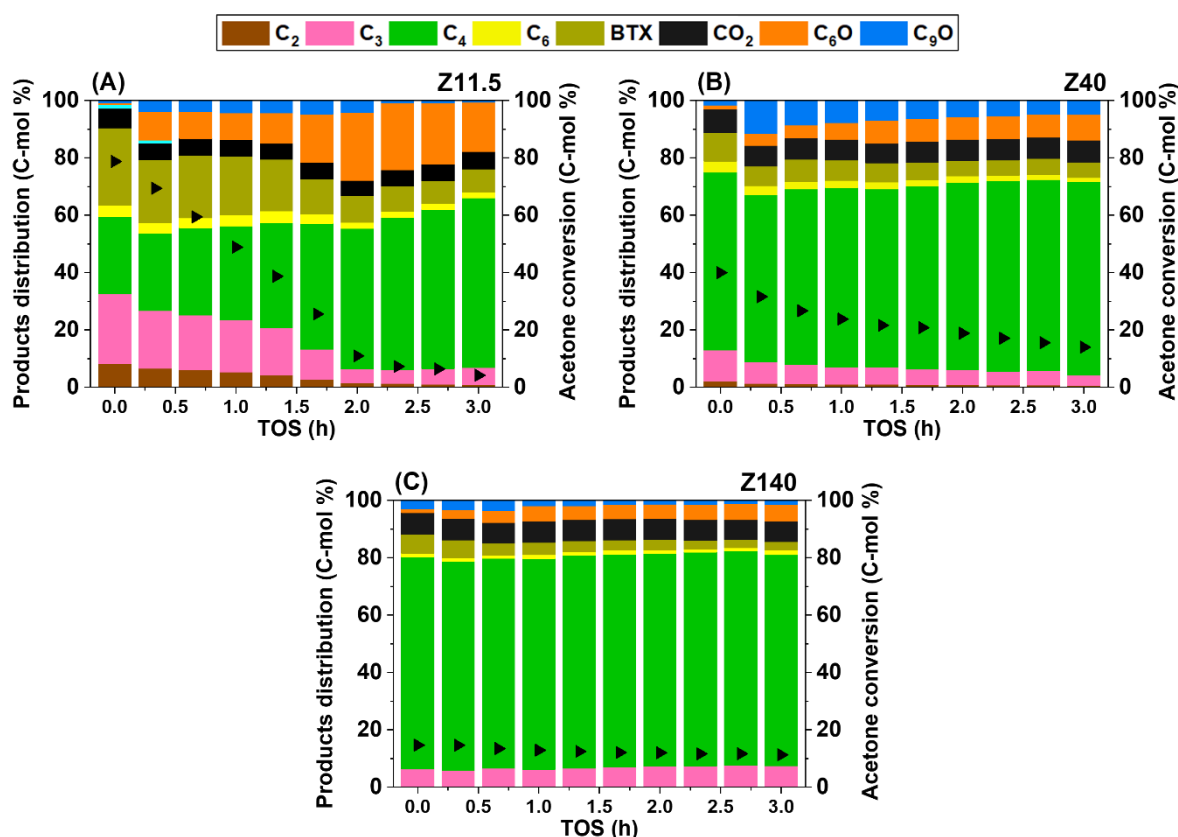


Figure 31. Products' distribution (colored) and conversion (black triangles) for acetone HDO reaction over pristine ZSM-5 zeolites: (A) Z11.5, (B) Z40, (C) and Z140, isothermal at 400 °C, TOS: 3 h. WHSV = 7.32 g_{acetone} g_{catalyst}⁻¹ h⁻¹. Feed: 2.4 mL min⁻¹ acetone, 51 mL min⁻¹ H₂, balance He. Total flow: 100 mL min⁻¹.

Table 12. Summary of the catalytic data obtained for acetone HDO reaction as a function of TOS (isothermal tests), for pristine ZSM-5 zeolites (Z11.5, Z40, and Z140) at 400 °C.

Sample	TOS (h)	Acetone conversion (%)	Products' distribution (%)				
			HHP*	DDP*	CDP*	BTX*	OP*
Z11.5	0	80	9	24	32	23	12
	3	4	1	6	62	8	23
Z40	0	40	2	11	66	10	11
	3	14	1	4	69	5	21
Z140	0	18	1	6	75	6	12
	3	15	-	8	75	3	14

* HHP (hydrogenation/hydrogenation products): C₁, C₂, C₃A, IPA

* DDP (direct deoxygenation products): C₃E

* CDP (coupling deoxygenated products): C₄, C₆, C₉

* BTX (aromatic products): benzene, toluene, xylenes

* OP (oxygenated products): CO₂, C₂HO, C₆O, C₉O

At the beginning of TOS, the catalysts presented the same conversions and products' distributions seen for acetone HDO at 400 °C as a function of temperature (Figure 30 and Table 11). Notably, the Z140 catalyst was very stable throughout the 3 h on stream, while Z40 went through some deactivation (40→14% acetone conversion), resulting in decreased DDP selectivity (11→4%) and a doubling of OP products (11→21%). In turn, Z11.5 experienced nearly complete deactivation (80→4% conversion) and a drastic decrease in HHP (9→1%), DDP (24→6%), and BTX (23→8%) products, while showing an increase in CDP (32→62%) and OP (12→23%).

The correlation between the catalysts Si/Al molar ratios and the observed products' distributions is evident, and it will be discussed in more detail later, as well as the pronounced deactivation exhibited by samples with higher concentrations of structural aluminum, namely Z11.5 and Z40. Thus, the Z140 zeolite was chosen as the acid support for molybdenum and the first-row transition metals (Fe, Co, Ni, and Cu), in order to avoid undesired effects on catalytic activity.

Mo/zeolite and M/zeolite catalysts prepared via wet impregnation: The crystalline structures of the metal/zeolite catalysts prepared via wet impregnation were examined via powder XRD of the calcined samples (Figure A19). All the collected patterns match the profile of pure Z140 zeolite (ZSM-5 structure) [315], with no indication of other crystalline phases related to the supported metals. The same samples were evaluated through SEM and presented similar spherical zeolite crystals measuring approximately 1 to 3 μm , as shown by Figure 32. Small crystals with undefined shapes and varying sizes depending on the sample could also be observed. On average, they ranged between 0.1 and 1 μm , reaching up to 2 μm for the Cu/Z140 sample, which generally exhibited larger crystals regarding this particular type. SEM-EDS measurements (Figure A20) showed that these crystals have a higher concentration of the respective supported metals in each case. While the spectra collected in the central regions of the zeolite crystals showed loadings more consistent with the expected (5 at.%), focusing on the smaller crystals revealed metal enrichment.

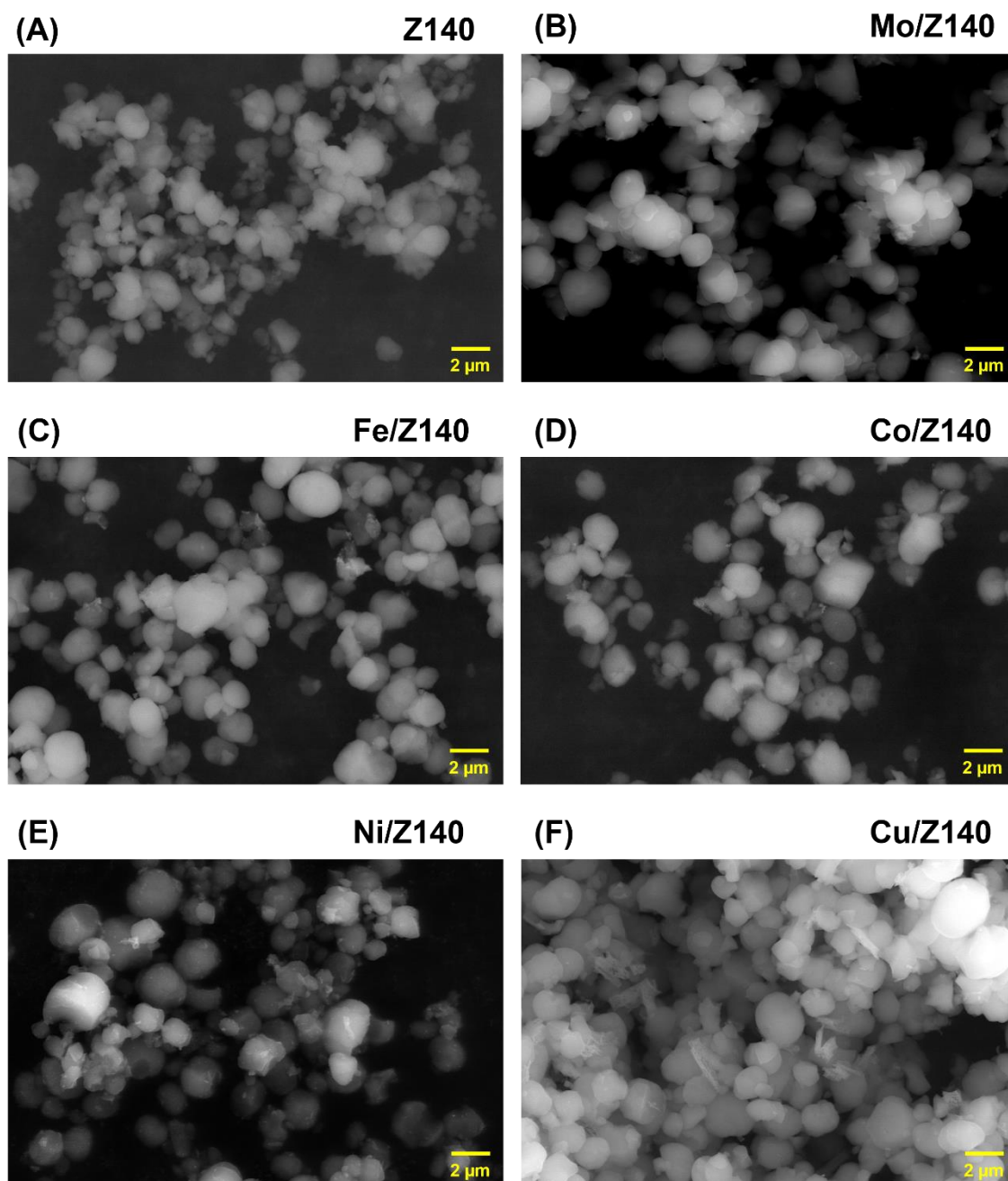


Figure 32. SEM images of the metal/zeolite catalysts: (A) Z140, (B) Mo/Z140, (C) Fe/Z140, (D) Co/Z140, (E) Ni/Z140, (F) Cu/Z140.

The impact of temperature on Mo/zeolite and M/zeolite catalysts: The metal/zeolite catalysts prepared through wet impregnation were evaluated in the acetone HDO reaction as a function of temperature (200→400 tests). The catalytic results are presented in Figure 33 and summarized in Table 13.

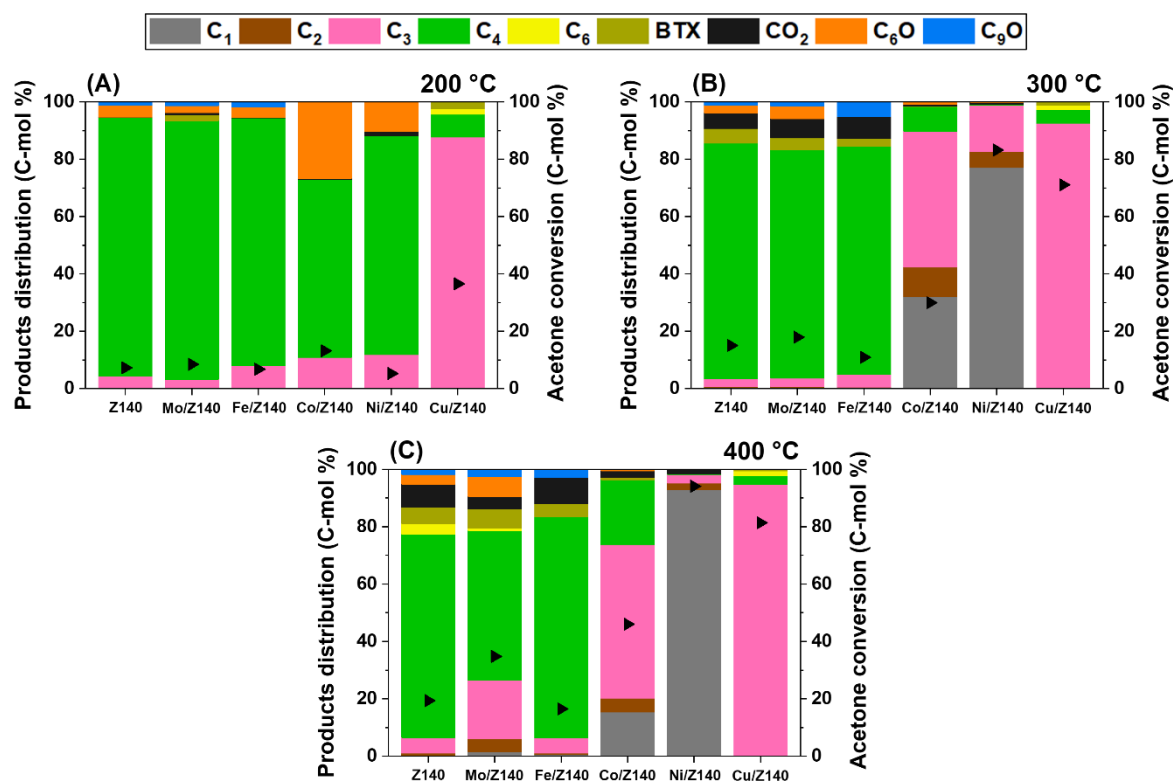


Figure 33. Products' distribution (colored) and conversion (black triangles) for acetone HDO reaction over Z140 and metal/zeolite catalysts (Mo/Z140, Fe/Z140, Co/Z140, Ni/Z140, and Cu/Z140) at (A) 200 °C, (B) 300 °C, and (C) 400 °C. 200→400 tests were carried out from 200 to 400 °C, isothermal every 100 °C, total TOS: 1.5 h. WHSV = 7.32 g_{acetone} g_{catalyst}⁻¹ h⁻¹. Feed: 2.4 mL min⁻¹ acetone, 51 mL min⁻¹ H₂, balance He. Total flow: 100 mL min⁻¹.

Table 13. Summary of the catalytic data obtained for acetone HDO reaction as a function of temperature (200→400 tests), for Z140 and metal/zeolite catalysts (Mo/Z140, Fe/Z140, Co/Z140, Ni/Z140, and Cu/Z140) at 200 °C, 300 °C, and 400 °C.

Sample	Temperature (°C)	Acetone conversion (%)	Products' distribution (%)				
			HHP*	DDP*	CDP*	BTX*	OP*
Z140	200	7	-	4	90	-	6
	300	15	1	3	82	5	9
	400	20	1	6	75	6	12
Mo/Z140	200	8	-	3	90	2	5
	300	18	1	3	80	4	12
	400	35	6	20	53	7	14
Fe/Z140	200	7	-	8	86	-	6
	300	11	1	4	80	3	12
	400	16	1	5	77	5	12
Co/Z140	200	13	-	11	62	-	17
	300	30	43	47	9	-	1
	400	46	20	54	23	1	2
Ni/Z140	200	5	-	12	76	-	12
	300	83	83	16	-	-	1
	400	94	95	3	-	-	2
Cu/Z140	200	37	-	88	10	2	-
	300	71	-	93	6	1	-
	400	81	-	95	5	-	-

* HHP (hydrogenation/hydrogenation products): C₁, C₂, C₃A, IPA

* DDP (direct deoxygenation products): C₃E

* CDP (coupling deoxygenated products): C₄, C₆, C₉

* BTX (aromatic products): benzene, toluene, xylenes

* OP (oxygenated products): CO₂, C₂HO, C₆O, C₉O

It is important to highlight that irrespective of the reaction conditions, all catalysts exhibited high deoxygenation degrees (>85 %), with significant variations in acetone conversion and distribution of deoxygenated products, which depended on reaction temperature and the nature of the supported metals. At 200°C, except for Cu/Z140, the other metal/zeolite catalysts showed similar performances compared to pure Z140, with low acetone conversions (~10 %) and extensive CDP production, particularly C₄. Conversely, Cu/Z140 demonstrated a 37 % conversion and a high direct deoxygenation degree, with 88 % of DDP.

At 300 °C, Mo/Z140 and Fe/Z140 presented no significant changes in catalytic activity, still mirroring the pure Z140 zeolite. Cu/Z140 practically doubled acetone conversion, reaching 71 % activity, and maintaining the high selectivity to DDP products around 93 %. In turn, Co/Z140 and Ni/140 started promoting HHP products (43 and 86 %, respectively), especially C₁ in both cases, demonstrating high hydrogenating capability. Notably, Ni/Z140 catalyst reached 83 % acetone conversion, being mostly active towards C-C cleavage, leading to extensive methanation.

At 400 °C, Fe/Z140 catalyst was still very similar to pure Z140, with low acetone conversions (~20 %) and promotion of CDP products (~75 % of products' distribution). On the other hand, Mo/Z140 presented some performance improvement, reaching 35 % conversion and balancing between DDP (20 %) and CDP (53 %) products. Co/Z140 became slightly more active, with 46 % conversion, decreasing the production of HHP (20 %) and increasing the selectivity to DDP (54 %). Ni/Z140 achieved its maximum hydrogenating capability, presenting 95 % of HHP within the products' distribution, besides a high conversion of 94 %. Once more, Cu/Z140 maintained high catalytic performances, with 81 % acetone conversion, leading to 95 % of DDP products.

Within the context of acetone HDO, the Cu/Z140 catalyst yielded the best results, as it selectively cleaved the acetone C-O bond, predominantly leading to DDP products, namely, C₃E. Thus, this system was more extensively studied through the preparation of other Cu/Z140 samples employing different methods. The catalysts were then evaluated in the acetone HDO reaction.

6.3. Discussion

As already stated, ZSM-5 zeolite, from the MFI topological family, is undoubtedly the most well-known, studied, and employed zeolite. It has been extensively applied in the petroleum industry as a heterogeneous catalyst for hydrocarbon isomerization reactions and many other important processes [350]. Over the years, the knowledge developed around ZSM-5 has led to a broader understanding of its versatility. The MFI topological structure can be obtained through various synthetic procedures, employing a wide range of structure directing agents (SDA's), both organic and inorganic, compositions of the synthesis gel, temperatures, and crystallization periods. The combinations of these variables have led to a high tunability of ZSM-5 characteristics. Materials with a wide range of Si/Al molar ratios (and therefore acidity), crystal shapes, and sizes can be easily prepared.

The ZSM-5 framework comprises parallel and straight 10-membered ring (10-MR) channels intersected by sinusoidal 10-MR channels [315]. Due to the smaller pore size of the straight 10-MR channels (5.3 x 5.6) and sinusoidal 10-MR channels (5.5 x 5.1) compared to the voids formed at the intersections (around 6.4), steric hindrance on products or the transition state is expected to be more pronounced within the 10-MR channels than at the intersections. This type of phenomenon, in this particular case concerning the ZSM-5 structure, has a strong influence on the catalytic properties of zeolites and can be considered one of the many possible confinement effects. In addition to the zeolite structure itself, the presence of trapped species or extra-framework cations, as well as the concentration, distribution, and nature of acid sites, can generate spatial and electronic effects that are quite significant to the zeolite activity [351].

In the case of the commercial ZSM-5 zeolites explored here, the only characteristics provided by the supplier (Zeolyst) are related to their estimated specific surface areas ($\sim 400 \text{ m}^2 \text{ g}^{-1}$) and the Si/Al molar ratios equal to 11.5, 40, and 140. Since they were purchased in their ammonium forms, meaning ammonium ions were counterbalancing the AlO_4^- sites of the zeolite framework, the samples were primarily calcined to obtain their protonic forms (more acidic) before any characterization or catalytic application in the acetone HDO reaction. The powder XRD patterns (Figure A17) confirmed the ZSM-5 crystalline structure [315], while XRF elemental analysis showed that the Si/Al ratios of 11.5, 40, and 140, were actually 16, 58, and 121,

respectively. In addition, the ^{27}Al MAS-NMR spectra (Figure A18) unveiled that Z40 and Z140 presented solely tetrahedrally coordinated aluminum sites (Al_{Td}), while Z11.5 also showed a significant amount (12 %) of extra-framework octahedral aluminum (Al_{Oh}) (Table A15). In principle, Brønsted acid sites (BAS) can be directly correlated with accessible Al_{Td} within the zeolite framework, while Lewis acid sites (LAS) are trickiest to unravel, being usually associated with presence of undercoordinated T atoms [352–354]. Thus, taking into account the Al_{Td} atoms present in the studied ZSM-5 zeolites, the acidity order is $\text{Z11.5} > \text{Z40} > \text{Z140}$, as expected. Considering the actual Si/Al molar ratios (Table A15), Z11.5 would have around 3 times more acid sites than Z40, which would be 2 times more acidic than Z140.

When employed in the acetone HDO reaction as a function of temperature (Figure 30 and Table 11), the ZSM-5 catalysts showed a dependence on catalytic activity and Si/Al molar ratios, correlated to active acid sites. The more acidic the zeolite, the greater the conversion increase and the overall activity with the rise in temperature, reaching its maximum at 400 °C. In general, the catalysts proved to be highly selective towards CDP products, especially C_4 , also producing BTX, i.e. aromatics. Both groups of products were not yet observed for the other oxide and mixed oxide catalysts explored in the previous chapters of this study. Their formation seems to be related to the zeolites intricate microporous framework and recognizable Brønsted acidity. C_4 , as isobutene, is produced from the acid-catalyzed β -scission of C_6O , the latter being also generated through an acid-catalyzed pathway, the condensation of acetone (Figure 29). It is reasonable to suggest that the confinement imposed by the zeolitic cages and cavities promotes the breakdown of the C_6O formed, hindering its diffusion. The formation of BTX products from acetone, although not extensively reported [40,355], was primarily attributed to further aldol condensation between acetone and C_6O . In parallel with other well-known processes in zeolite catalysis, such as the methanol-to-olefins (MTO) reaction, the formation of aromatics may arise from the hydrocarbon pool mechanism [348]. Through this pathway, acetone should access the acidic environment within the zeolite pores, where it reacts directly with active species confined therein. Paraffins, olefins, and small aromatics capable of diffusing out of the pores can be identified in the product mixture, while substances unable to escape undergo conversion into coke [347]. Many works involving biomass conversion and zeolite systems deal with aromatics processing and promotion [324].

In any case, the need for acid sites is evident, justifying the higher selectivity to BTX following the order $Z11.5 > Z40 > Z140$.

Finally, when employed in the acetone HDO reaction as a function of TOS (Figure 31 and Table 12), the ZSM-5 catalysts also exhibited a behavior dependent on their Si/Al molar ratio. The Z11.5 catalyst, more acidic, despite showing high acetone conversion at the beginning of the reaction, around 80 %, suffered rapid and extensive deactivation over the 3 hours on stream, reaching 4 % conversion. This decrease in activity is likely related to the formation of coke inside the zeolitic microporous structure, blocking the pores and rendering the acid sites inaccessible [356,357]. The production of BTX and smaller hydrocarbons, the latter possibly generated through cracking, also decrease. On the other hand, condensation OP products are promoted, probably catalyzed by the external, unconfined acid sites. Z40 also suffered some deactivation, but less significative, and Z140 essentially maintained its initial activity unchanged. Z140 low concentration of acid sites should not allow extensive coke formation, preserving its activity, albeit low (~15 %), over TOS.

Based on these preliminary data regarding pure ZSM-5 zeolites in the acetone HDO reaction, Z140 was chosen as the support for molybdenum and the first-row transition metals in order to provide a porous matrix with high surface area but low acidity, so as not to mask the activity of the supported phases. For example, Z11.5 exhibited high conversion and a highly diversified products' distribution that could be potentially deleterious to a comprehensive study on metal/zeolite catalysts.

The 5 at.% metal/zeolite samples were prepared using a conventional wet impregnation method, which is one of the simplest and most widely employed impregnation techniques. This procedure consists of mixing the zeolite support with the required metal precursor solution. Here we used iron, cobalt, nickel, and copper nitrates as the first-row transition metal precursors and ammonium heptamolybdate tetrahydrate as the molybdenum precursor. It is important to highlight that the diffusion of the solution into the extensive microporous framework of zeolites is difficult, particularly if residual gas is trapped when the support is poorly wetted [324].

Nevertheless, SEM analysis (Figure 32) revealed the presence of small needle-like crystals (from 0.1 to 1.0 μm) in all metal/zeolite samples, alongside larger zeolite crystals with a spherical habit (1.0 to 3.0 μm). Subsequent SEM-EDS analysis (Figure A20) indicated a high metal loading on these needle-like crystals, suggesting the formation of surface metal oxide particles. Conversely, EDS spectra collected over the

zeolite crystals (Figure A20) showed metal loadings much closer to the expected value of 5 at.%. These findings indicate that, despite the presence of metal oxide particles on the zeolite surface, a portion of the supported phase is well dispersed.

Despite molybdenum presented some promising results as a bulk oxide (Chapter 4), Mo/Z140 did not prove to be an efficient catalyst for acetone HDO reaction (Figure 33 and Table 13). At intermediate temperatures (200 and 300 °C) it presented the same activity seen for the pure Z140 zeolite, with increased production of DDP at 400 °C (3→20 %), but still considerably inferior to MoO₃ and its oxycarbide phases at the same conditions [107]. This poor performance may be related to the molybdenum loading.

Once employed in the acetone HDO reaction, Fe/Z140 presented the poorest performance among the studied metal/zeolite catalysts (Figure 33 and Table 13), with little improvement compared to the pure Z140 zeolite. It showed low conversions (< 15 %) across all studied temperatures and essentially promoted C₄. Iron is indeed the less active of the first-row transition metals explored here, needing higher loadings and severe reducing pre-treatments to achieve better catalytic active at the employed conditions [358].

On the other hand, Co/Z140 presented promising catalytic activity (Figure 33 and Table 13). Despite cobalt well-known reduction at low temperatures and significant methanation capability [41], once supported on Z140, it balanced between HHP (20 %) and DDP (54 %) products, presenting 46 % acetone conversion at 400 °C. In turn, Ni/Z140 failed in promoting appealing HDO products other than HHP, which represented 94 % of the products' distribution at 400 °C (Figure 33 and Table 13). Nickel methanation capability is remarkable [359–361] and, despite the low loading, it still privileged this reaction pathway.

Finally, Cu/Z140 was by far the better acetone HDO catalyst among the studied metal/zeolite systems (Figure 33 and Table 13). Since 200 °C until 400 °C, it presented high conversions and high selectivity to DDP products. Even though all catalysts showed good deoxygenation degree, considering the HDO context, DDP products are ultimately desired, once they represent the promotion of selective C-O bond cleavage in detriment of parallel scissions or coupling reactions. The best result was achieved at 400 °C, with 81 % acetone conversion and 95 % selectivity to DDP. The literature lacks reports on Cu/zeolite catalysts for HDO processes, however, we observed that

bulk copper molybdate catalysts also presented promising HDO results, while bulk copper oxides (Cu_2O and CuO) were not promising at all (Chapter 5).

6.4. Considerations

Despite some remaining questions regarding the characterization of the metal/zeolite catalysts, they presented interesting results within the acetone HDO context, leading to high deoxygenation degrees. The pure ZSM-5 catalysts promoted mainly C_4 and BTX products, likely arising from acid-catalyzed pathways within the microporous zeolite structure. Once supporting molybdenum and the first-row transition metals, the activity significantly changed. Mo/Z140 and Fe/Z140 did not present promising results, while Co/Z140 balanced between hydrogenation and deoxygenation products, and Ni/Z140 led to extensive methanation. In turn, Cu/Z140 presented high activity and high deoxygenation degree, promoting mainly C_3E since 200 °C, consolidating copper as an attractive component for efficient acetone HDO.

Chapter 7. Final considerations

In the first part of this study, we demonstrate that acetone HDO on MoO_3 nanopowder induces partial reduction/carburization, forming MoO_xC_y with varied catalytic sites depending on reaction conditions. The MoO_xC_y characteristics are influenced by temperature and TOS, impacting catalytic site balance and products' distribution. At 350 °C, an ordered MoO_xC_y phase coexists with MoO_2 , while at 400 °C, MoO_3 fully converts into crystalline MoO_2 and a disordered MoO_xC_y phase. A 3-4-fold increase in total AS occurs between MoO_3 and MoO_xC_y phases, with 3- to 10-fold stronger BAS concentration. MoO_xC_y , especially the ordered phase, favors intermediary Mo^{5+} oxidation states around +5, which significantly influences selectivity, exhibiting greater hydrogenation/hydrogenolysis capability. MoO_3 proved to be a good catalyst for the acetone HDO reaction, presenting good selectivity to direct deoxygenation products, C_3E .

With the MoO_3 study, we contributed to the understanding of the properties of the complex oxycarbide phases, invariably recurrent in Mo-based catalysts under reducing/carburizing conditions, as is the case of HDO reactions employing different substrates. We addressed the electronic and acidic characteristics still underexplored for MoO_xC_y : the hydrogenating behavior associated with Mo^{5+} species and the strong Brønsted acidity, unusual for metal oxides. Furthermore, given its extensive ramifications, the acetone HDO reaction proved valuable in probing different functionalities.

Following this path, we prepared and screened through the acetone HDO reaction a family of bulk metal molybdates (MMo , where $\text{M} = \text{Mn}, \text{Fe}, \text{Co}, \text{Cu}, \text{and Zn}$). These MMo catalysts presented unique activities depending on the associated first-row transition metal and also on the temperature and TOS. FeMo , CoMo , and ZnMo showed similar catalytic activities with high deoxygenation capability, extensively promoting coupling deoxygenated products (C_4 , C_6 , C_9). Differently from MoO_3 , these catalysts transitioned to a mixture of MoO_2 and an $\alpha\text{-MoC}_{1-x}$ phase at 400 °C. The CuMo was the most intriguing catalyst among the proposed set, showing high acetone conversion and C_3E selectivity since 300 °C. At this point, the CuMo structure (Cu^{2+}) converted to Cu_2O (Cu^{1+}), while heating up to 400 °C led to metallic copper (Cu^0).

With the MoM study, we showed the potential application of mixed metal oxides on HDO processes. FeMo , CoMo , and ZnMo promoted cascade reactions, leading to

chain growth, which could be a promising feature for certain emerging valorization reactions, such as the CO₂ hydrogenation to ethanol and higher alcohols and methanol upgrading to fuel-range hydrocarbons. In turn, CuMo showed itself as a potent HDO catalyst, promoting high conversion and high deoxygenation degree, selectively cleaving acetone C-O bonds.

Finally, we also prepared and tested on the acetone HDO reaction 5 wt.% supported metal/zeolite catalysts. Based on our previous findings, we employed Mo and also some first-row transition metals (Fe, Co, Ni, and Cu). We saw that the pristine ZSM-5 zeolites promoted still unseen acid-catalyzed products: BTX, through aldol condensation and hydrocarbon pool mechanisms, and C₄, through the scission of C₆O inside the zeolitic pores. Their catalytic activity was directly correlated to their acid sites content, being chosen the material with Si/Al molar ratio of 140 to support the metals. Mo/Z140 and Fe/Z140 did not present promising results, while Co/Z140 balanced between hydrogenation and deoxygenation products, and Ni/Z140 led to extensive methanation. In turn, Cu/Z140 presented high activity and high deoxygenation degree, promoting mainly C₃E since 200 °C.

Despite the poor performance of the Mo/zeolite catalyst, the study involving abundant first-row transition metals supported on zeolites generated some interesting results, all of them promoting high deoxygenation degrees. Co/Z140 showed promising results, with good acetone conversion and balanced products' distribution, while Cu/Z140 consolidated the potential of copper catalysts for acetone HDO reaction.

Chapter 8. Perspectives

Although we have made substantial progress in determining the properties of the $\text{MoO}_x/\text{MoO}_x\text{C}_y$ system, highlighting the promotion of strong Brønsted acid sites and the hydrogenation/hydrogenolysis capacity *via* undercoordinated $\text{Mo}^{\delta+}$ species, we have not sought to understand how to stabilize and maximize the performance of these functionalities. Different thermal pretreatments under reaction, reducing or oxidizing conditions, could shed new light on this understanding, especially regarding the formation of core-shell systems and their impact on HDO conversion and selectivity.

In turn, the mixed MMo catalysts showed unique activities in the acetone HDO reaction. Advancement in the post-reaction characterization of the FeMo, CoMo, and ZnMo systems would bring greater understanding of the $\alpha\text{-MoC}_{1-x}$ phase amidst the amorphous metallic phases activity, which compose the mixture obtained under reaction conditions. These catalysts promoted interesting C-C coupling pathways. On the other hand, the CuMo system exhibited high conversion and selective C-O bond cleavage, being the most attractive material among the studied catalysts. It also undergoes severe phase transitions, segregating into amorphous molybdenum phases and crystalline copper phases. Although not part of this work, XPS and XAS post-reaction analyses are being conducted in partnership with the Cardiff Catalysis Institute and the Rutherford Appleton Laboratory. At the latter institution, insightful *in situ* DRIFTS analyses under acetone HDO conditions have been also carried out, attempting to track the evolution of the CuMo catalyst.

Finally, the Mo/zeolite and M/zeolite catalysts showed good results, especially in terms of deoxygenation degree, promoting C_4 products, referring to isobutene and isomers. In this work, we present a general screening of these systems. Advances could be made regarding the preparation of these catalysts, aiming to better understand the balance between metallic sites and zeolitic acid sites, especially for the promising Cu/Z140 system. More fundamental studies, seeking to correlate the concentration, proximity, type, and strength of the acid functionalities with condensation and dehydration steps, recurrent in HDO, would also be very welcome.

It is important to note that the possibilities are “almost” endless. The purpose of the work presented here is not to cover all these perspectives, but rather to serve as a foundational piece within its proposal and the related research area. In doing so, it aims to provide support for further studies both within and beyond our research group.

Chapter 9. References

- [1] D. Guban, I.K. Muritala, M. Roeb, C. Sattler, *Int J Hydrogen Energy* 45 (2020) 26156–26165.
- [2] T. Cordero-Lanzac, J. Rodríguez-Mirasol, T. Cordero, J. Bilbao, *Energy & Fuels* 35 (2021) 17008–17031.
- [3] J. Zhang, J. Sun, Y. Wang, *Green Chemistry* 22 (2020) 1072–1098.
- [4] Y. Yang, X. Xu, H. He, D. Huo, X. Li, L. Dai, C. Si, *Int J Biol Macromol* 242 (2023) 124773.
- [5] A.O. Ojo, *Fermentation* 9(11) (2023) 990.
- [6] S. Al Arni, *Ind Crops Prod* 115 (2018) 330–339.
- [7] F.-X. Collard, J. Blin, *Renewable and Sustainable Energy Reviews* 38 (2014) 594–608.
- [8] T.A. Khan, A.S. Saud, S.S. Jamari, M.H.A. Rahim, J.-W. Park, H.-J. Kim, *Biomass Bioenergy* 130 (2019) 105384.
- [9] Z.E. Zadeh, A. Abdulkhani, O. Aboelazayem, B. Saha, *Processes* 8 (2020) 799.
- [10] R.E. Guedes, A.S. Luna, A.R. Torres, *J Anal Appl Pyrolysis* 129 (2018) 134–149.
- [11] V. Strezov, M. Patterson, V. Zymala, K. Fisher, T.J. Evans, P.F. Nelson, *J Anal Appl Pyrolysis* 79 (2007) 91–100.
- [12] H. Marsh, F. Rodríguez-Reinoso, in: *Activated Carbon*, Elsevier, 2006, pp. 13–86.
- [13] O. Konur, ed., *Bioenergy and Biofuels*, CRC Press, 2018.
- [14] D. Meier, B. van de Beld, A. V. Bridgwater, D.C. Elliott, A. Oasmaa, F. Preto, *Renewable and Sustainable Energy Reviews* 20 (2013) 619–641.
- [15] M. Patel, X. Zhang, A. Kumar, *Renewable and Sustainable Energy Reviews* 53 (2016) 1486–1499.
- [16] V. Dhyani, T. Bhaskar, *Renew Energy* 129 (2018) 695–716.
- [17] H.A. Baloch, S. Nizamuddin, M.T.H. Siddiqui, S. Riaz, A.S. Jatoti, D.K. Dumbre, N.M. Mubarak, M.P. Srinivasan, G.J. Griffin, *J Environ Chem Eng* 6 (2018) 5101–5118.
- [18] G.W. Huber, A. Corma, *Angewandte Chemie International Edition* 46 (2007) 7184–7201.
- [19] B. Valle, A. Remiro, N. García-Gómez, A.G. Gayubo, J. Bilbao, *Journal of Chemical Technology & Biotechnology* 94 (2019) 670–689.

- [20] G. López Juste, J.J. Salvá Monfort, *Biomass Bioenergy* 19 (2000) 119–128.
- [21] A. Oasmaa, S. Czernik, *Energy & Fuels* 13 (1999) 914–921.
- [22] L. Qu, X. Jiang, Z. Zhang, X. Zhang, G. Song, H. Wang, Y. Yuan, Y. Chang, *Green Chemistry* 23 (2021) 9348–9376.
- [23] Q. Zhang, J. Chang, T. Wang, Y. Xu, *Energy Convers Manag* 48 (2007) 87–92.
- [24] A. Oasmaa, J. Korhonen, E. Kuoppala, *Energy & Fuels* 25 (2011) 3307–3313.
- [25] A. Oasmaa, T. Sundqvist, E. Kuoppala, M. Garcia-Perez, Y. Solantausta, C. Lindfors, V. Paasikallio, *Energy & Fuels* 29 (2015) 4373–4381.
- [26] Y. Wang, S. Wang, F. Leng, J. Chen, L. Zhu, Z. Luo, *Sep Purif Technol* 152 (2015) 123–132.
- [27] M. Bertero, G. de la Puente, U. Sedran, *Energy & Fuels* 25 (2011) 1267–1275.
- [28] D. Chen, J. Zhou, Q. Zhang, X. Zhu, *Renewable and Sustainable Energy Reviews* 40 (2014) 69–79.
- [29] A.G. Gayubo, A.T. Aguayo, A. Atutxa, R. Aguado, J. Bilbao, *Ind Eng Chem Res* 43 (2004) 2610–2618.
- [30] A.G. Gayubo, A.T. Aguayo, A. Atutxa, R. Aguado, M. Olazar, J. Bilbao, *Ind Eng Chem Res* 43 (2004) 2619–2626.
- [31] K. Iisa, R.J. French, K.A. Orton, M.M. Yung, D.K. Johnson, J. ten Dam, M.J. Watson, M.R. Nimlos, *Energy & Fuels* 30 (2016) 2144–2157.
- [32] X. Chen, Y. Chen, H. Yang, X. Wang, Q. Che, W. Chen, H. Chen, *Bioresour Technol* 273 (2019) 153–158.
- [33] T. Lepage, M. Kammoun, Q. Schmetz, A. Richel, *Biomass Bioenergy* 144 (2021) 105920.
- [34] W. Nabgan, T.A. Tuan Abdullah, R. Mat, B. Nabgan, Y. Gambo, M. Ibrahim, A. Ahmad, A.A. Jalil, S. Triwahyono, I. Saeh, *Renewable and Sustainable Energy Reviews* 79 (2017) 347–357.
- [35] A. Ochoa, J. Bilbao, A.G. Gayubo, P. Castaño, *Renewable and Sustainable Energy Reviews* 119 (2020) 109600.
- [36] W.-H. Chen, W. Farooq, M. Shahbaz, S.R. Naqvi, I. Ali, T. Al-Ansari, N.A. Saidina Amin, *Energy* 226 (2021) 120433.
- [37] Z. Li, E. Jiang, X. Xu, Y. Sun, R. Tu, *Renew Energy* 146 (2020) 1991–2007.
- [38] T.P. Vispute, G.W. Huber, *Green Chemistry* 11 (2009) 1433.
- [39] T. Prasomsri, T. Nimmanwudipong, Y. Román-Leshkov, *Energy Environ Sci* 6 (2013) 1732.

- [40] J. Wang, M. Jabbour, L. Abdelouahed, S. Mezghich, L. Estel, K. Thomas, B. Taouk, *Can J Chem Eng* 99 (2021) 1082–1093.
- [41] D.S. Leite, G.B. Strapasson, D. Zanchet, *Molecular Catalysis* 530 (2022) 112623.
- [42] D. Liu, H. Du, in: *Advances in Biofuels Production, Optimization and Applications*, Elsevier, 2024, pp. 85–102.
- [43] T. Nimmanwudipong, C. Aydin, J. Lu, R.C. Runnebaum, K.C. Brodwater, N.D. Browning, D.E. Block, B.C. Gates, *Catal Letters* 142 (2012) 1190–1196.
- [44] H. Lee, H. Kim, M.J. Yu, C.H. Ko, J.-K. Jeon, J. Jae, S.H. Park, S.-C. Jung, Y.-K. Park, *Sci Rep* 6 (2016) 28765.
- [45] H. Ge, Y. Kuwahara, M. Okada, H. Yamashita, *ACS Sustain Chem Eng* 12 (2024) 2162–2171.
- [46] G. Mo, W. Wu, Y. Luo, M. Pan, W. Zhang, H. Zhang, K. Huang, *Fuel* 369 (2024) 131712.
- [47] A.M. Ruppert, M. Brzezińska, N. Keller, *Catal Today* 433 (2024) 114651.
- [48] Y.-C. Lin, C.-L. Li, H.-P. Wan, H.-T. Lee, C.-F. Liu, *Energy & Fuels* 25 (2011) 890–896.
- [49] Y. Romero, F. Richard, S. Brunet, *Appl Catal B* 98 (2010) 213–223.
- [50] D. Raikwar, M. Munagala, S. Majumdar, D. Shee, *Catal Today* 325 (2019) 117–130.
- [51] W. Jiang, J.-P. Cao, C. Zhu, M. Zhao, Z.-H. Ni, X.-Y. Zhao, J.-X. Xie, L. Zhao, Y.-P. Zhao, H.-C. Bai, *Appl Catal B* 307 (2022) 121137.
- [52] L. Nie, D.E. Resasco, *J Catal* 317 (2014) 22–29.
- [53] Z. JING, T. ZHANG, J. SHANG, M. ZHAI, H. YANG, C. QIAO, X. MA, *Journal of Fuel Chemistry and Technology* 46 (2018) 427–440.
- [54] C.-W. Lee, P.-Y. Lin, B.-H. Chen, R.G. Kukushkin, V.A. Yakovlev, *Catal Today* 379 (2021) 124–131.
- [55] M.W. Nolte, J. Zhang, B.H. Shanks, *Green Chemistry* 18 (2016) 134–138.
- [56] M.W. Nolte, A. Saraeian, B.H. Shanks, *Green Chemistry* 19 (2017) 3654–3664.
- [57] X. Zhang, J. Tang, Q. Zhang, Q. Liu, Y. Li, L. Chen, C. Wang, L. Ma, *Catal Today* 319 (2019) 41–47.
- [58] M. Shetty, K. Murugappan, T. Prasomsri, W.H. Green, Y. Román-Leshkov, *J Catal* 331 (2015) 86–97.

- [59] A. Saraeian, S.J. Burkhov, D. Jing, E.A. Smith, B.H. Shanks, *ACS Sustain Chem Eng* 9 (2021) 6685–6696.
- [60] W. Lv, X. Hu, Y. Zhu, Y. Xu, S. Liu, P. Chen, C. Wang, L. Ma, *Renew Energy* 188 (2022) 195–210.
- [61] A. Kurlov, X. Huang, E.B. Deeva, P.M. Abdala, A. Fedorov, C.R. Müller, *Nanoscale* 12 (2020) 13086–13094.
- [62] J. Fan, X. Wu, A. Piñeiro-García, N. Boulanger, Y. Panecatl-Bernal, A. Ashok, S. Koroidov, E. Gracia-Espino, *ACS Appl Nano Mater* 4 (2021) 12270–12277.
- [63] K. Murugappan, E.M. Anderson, D. Teschner, T.E. Jones, K. Skorupska, Y. Román-Leshkov, *Nat Catal* 1 (2018) 960–967.
- [64] T. Prasomsri, M. Shetty, K. Murugappan, Y. Román-Leshkov, *Energy Environ. Sci.* 7 (2014) 2660–2669.
- [65] W.-S. Lee, A. Kumar, Z. Wang, A. Bhan, *ACS Catal* 5 (2015) 4104–4114.
- [66] M.M. Sullivan, A. Bhan, *ACS Catal* 6 (2016) 1145–1152.
- [67] M. Shetty, B. Buesser, Y. Román-Leshkov, W.H. Green, *The Journal of Physical Chemistry C* 121 (2017) 17848–17855.
- [68] M. Shetty, K. Murugappan, W.H. Green, Y. Román-Leshkov, *ACS Sustain Chem Eng* 5 (2017) 5293–5301.
- [69] E. Furimsky, *Appl Catal* 6 (1983) 159–164.
- [70] P.M. Mortensen, J.-D. Grunwaldt, P.A. Jensen, K.G. Knudsen, A.D. Jensen, *Appl Catal A Gen* 407 (2011) 1–19.
- [71] D.A. Ruddy, J.A. Schaidle, J.R. Ferrell III, J. Wang, L. Moens, J.E. Hensley, *Green Chem.* 16 (2014) 454–490.
- [72] G. Andersson, A. Magnéli, L.G. Sillén, M. Rottenberg, *Acta Chem Scand* 4 (1950) 793–797.
- [73] D.O. Scanlon, G.W. Watson, D.J. Payne, G.R. Atkinson, R.G. Egdell, D.S.L. Law, *The Journal of Physical Chemistry C* 114 (2010) 4636–4645.
- [74] P.F. Carcia, E.M. McCarron, *Thin Solid Films* 155 (1987) 53–63.
- [75] I.A. de Castro, R.S. Datta, J.Z. Ou, A. Castellanos-Gomez, S. Sriram, T. Daeneke, K. Kalantar-zadeh, *Advanced Materials* 29 (2017).
- [76] A. Chithambararaj, N. Rajeswari Yogamalar, A.C. Bose, *Cryst Growth Des* 16 (2016) 1984–1995.
- [77] L. Zheng, Y. Xu, D. Jin, Y. Xie, *Chemistry of Materials* 21 (2009) 5681–5690.
- [78] M. Vosough, G.R. Khayati, S. Sharafi, *Thermochim Acta* 715 (2022) 179289.

- [79] Ø.S. Fjellvåg, A. Ruud, H.H. Sønsteby, O. Nilsen, H. Fjellvåg, *Cryst Growth Des* 20 (2020) 3861–3866.
- [80] Y. Liu, S. Yang, Y. Lu, N. V. Podval'naya, W. Chen, G.S. Zakharova, *Appl Surf Sci* 359 (2015) 114–119.
- [81] A. Magnéli, G. Andersson, G. Sundkvist, G. Sundkvist, *Acta Chem Scand* 9 (1955) 1378–1381.
- [82] R. Tokarz-Sobieraj, R. Gryboś, M. Witko, *Appl Catal A Gen* 391 (2011) 137–143.
- [83] T.L. Christiansen, E.D. Bøjesen, M. Juelsholt, J. Etheridge, K.M.Ø. Jensen, *ACS Nano* 13 (2019) 8725–8735.
- [84] G. Wulff, *Z Kristallogr Cryst Mater* 34 (1901) 449–530.
- [85] X.W. Lou, H.C. Zeng, *Chemistry of Materials* 14 (2002) 4781–4789.
- [86] Y. Du, J. He, G. Hou, F. Yuan, *Electrochim Acta* 334 (2020) 135593.
- [87] K. Trzciński, Z. Zarach, M. Szkoda, A.P. Nowak, K. Berent, M. Sawczak, *Sci Rep* 13 (2023) 16668.
- [88] C. Zhang, X. Zou, Z. Du, J. Gu, S. Li, B. Li, S. Yang, *Small* 14 (2018).
- [89] Y. Zhang, H. Guo, J. Ren, X. Li, W. Ren, R. Song, *Appl Catal B* 298 (2021) 120582.
- [90] J. Yang, X. Xiao, P. Chen, K. Zhu, K. Cheng, K. Ye, G. Wang, D. Cao, J. Yan, *Nano Energy* 58 (2019) 455–465.
- [91] H.-S. Kim, J.B. Cook, H. Lin, J.S. Ko, S.H. Tolbert, V. Ozolins, B. Dunn, *Nat Mater* 16 (2017) 454–460.
- [92] P.-R. Huang, Y. He, C. Cao, Z.-H. Lu, *Sci Rep* 4 (2014) 7131.
- [93] W.A. Sławiński, Ø.S. Fjellvåg, A. Ruud, H. Fjellvåg, *Acta Crystallogr B Struct Sci Cryst Eng Mater* 72 (2016) 201–208.
- [94] K.A. Goulas, A. V. Mironenko, G.R. Jenness, T. Mazal, D.G. Vlachos, *Nat Catal* 2 (2019) 269–276.
- [95] T. Ressler, A. Walter, J. Scholz, J.-P. Tessonnier, D.S. Su, *J Catal* 271 (2010) 305–314.
- [96] H. Al-Kandari, S. Al-Kandari, F. Al-Kharafi, A. Katrib, *Energy & Fuels* 23 (2009) 5737–5742.
- [97] D. Li, *Appl Catal B* 16 (1998) 255–260.
- [98] H.H. Kung, *Industrial & Engineering Chemistry Product Research and Development* 25 (1986) 171–178.

- [99] M. Chen, C.M. Friend, E. Kaxiras, *J Am Chem Soc* 123 (2001) 2224–2230.
- [100] R. Coquet, D.J. Willock, *Physical Chemistry Chemical Physics* 7 (2005) 3819.
- [101] M. Shetty, D. Zanchet, W.H. Green, Y. Román-Leshkov, *ChemSusChem* 12 (2019) 2171–2175.
- [102] L. Chen, A.C. Cooper, G.P. Pez, H. Cheng, *The Journal of Physical Chemistry C* 112 (2008) 1755–1758.
- [103] H. Cheng, L. Chen, A.C. Cooper, X. Sha, G.P. Pez, *Energy Environ Sci* 1 (2008) 338.
- [104] D.R. Moberg, T.J. Thibodeau, F.G. Amar, B.G. Frederick, *The Journal of Physical Chemistry C* 114 (2010) 13782–13795.
- [105] A. Lal Bose, V. Agarwal, *ChemPhysChem* 23 (2022).
- [106] C. Bouchy, C. Pham-Huu, B. Heinrich, E.G. Derouane, S.B. Derouane-Abd Hamid, M.J. Ledoux, *Appl Catal A Gen* 215 (2001) 175–184.
- [107] G.B. Báfero, G.B. Strapasson, D.S. Leite, D. Zanchet, *ChemCatChem* 15 (2023).
- [108] A. GERVASINI, *J Catal* 131 (1991) 190–198.
- [109] S. Li, D.A. Dixon, *J Phys Chem A* 110 (2006) 6231–6244.
- [110] G. Busca, *Catal Today* 41 (1998) 191–206.
- [111] S.K. Maity, M.S. Rana, B.N. Srinivas, S.K. Bej, G. Murali Dhar, T.S.R. Prasada Rao, *J Mol Catal A Chem* 153 (2000) 121–127.
- [112] S.K. Maity, M.S. Rana, S.K. Bej, J. Ancheyta-Juárez, G. Murali Dhar, T.S.R. Prasada Rao, *Appl Catal A Gen* 205 (2001) 215–225.
- [113] M. Ferrari, B. Delmon, P. Grange, *Microporous and Mesoporous Materials* 56 (2002) 279–290.
- [114] D. Duayne Whitehurst, T. Isoda, I. Mochida, in: 1998, pp. 345–471.
- [115] H. Chen, Q. Wang, X. Zhang, L. Wang, *Fuel* 159 (2015) 430–435.
- [116] Y. Huang, Y. Hu, F. Ye, Y. Fang, *Energy & Fuels* 31 (2017) 8356–8362.
- [117] M. Rana, M.N. Islam, A. Agarwal, G. Taki, S.-J. Park, S. Dong, Y.-T. Jo, J.-H. Park, *Energy & Fuels* 32 (2018) 11564–11575.
- [118] A. Afshar Taromi, S. Kaliaguine, *Fuel Processing Technology* 171 (2018) 20–30.
- [119] S. Fangkoch, S. Boonkum, S. Ratchahat, W. Koo-amornpattana, A. Eiad-Ua, W. Kiatkittipong, W. Klysubun, A. Srifa, K. Faungnawakij, S. Assabumrungrat, *ACS Omega* 5 (2020) 6956–6966.

- [120] A. Saraeian, A. Aui, Y. Gao, M.M. Wright, M. Foston, B.H. Shanks, *Green Chemistry* 22 (2020) 2513–2525.
- [121] G. Guo, D. Chen, T. Ahmed, X. Dou, K. Chen, W. Li, *Fuel* 306 (2021) 121599.
- [122] C. Wang, L. Guo, K. Wu, X. Li, Y. Huang, Z. Shen, H. Yang, Y. Yang, W. Wang, C. Li, *Journal of Energy Chemistry* 84 (2023) 122–130.
- [123] G.B. Strapasson, L.S. Sousa, G.B. Báfero, D.S. Leite, B.D. Moreno, C.B. Rodella, D. Zanchet, *Appl Catal B* 335 (2023) 122863.
- [124] *J Am Chem Soc* 126 (2004) 982–982.
- [125] T. Ressler, R.E. Jentoft, J. Wienold, M.M. Günter, O. Timpe, *J Phys Chem B* 104 (2000) 6360–6370.
- [126] P. Delporte, F. Meunier, C. Pham-Huu, P. Vennegues, M.J. Ledoux, J. Guille, *Catal Today* 23 (1995) 251–267.
- [127] P. Delporte, C. Pham-Huu, M.J. Ledoux, *Appl Catal A Gen* 149 (1997) 151–180.
- [128] Z. Huang, Y. Du, J. Zhang, X. Wu, H. Shen, G. Jing, *Environ Sci Technol* 53 (2019) 5309–5318.
- [129] V.O.O. Gonçalves, C. Ciotonea, S. Arrii-Clacens, N. Guignard, C. Roudaut, J. Rousseau, J.-M. Clacens, S. Royer, F. Richard, *Appl Catal B* 214 (2017) 57–66.
- [130] R. Lødeng, C. Ranga, T. Rajkhowa, V.I. Alexiadis, H. Bjørkan, S. Chytil, I.H. Svenum, J. Walmsley, J.W. Thybaut, *Biomass Convers Biorefin* 7 (2017) 343–359.
- [131] D.G.B. Dionizio, L. Forrer, G. Berhault, P.M. de Souza, C.A. Henriques, *Molecular Catalysis* 536 (2023) 112882.
- [132] V. Itthibenchapong, P. Chakthranont, C. Sattayanon, T. Butburee, K. Faungnawakij, S. Namuangruk, *Appl Surf Sci* 547 (2021) 149170.
- [133] X. Diao, N. Ji, T. Li, Z. Jia, S. Jiang, Z. Wang, C. Song, C. Liu, X. Lu, Q. Liu, *J Catal* 401 (2021) 234–251.
- [134] M. Selvaraj, K. Shanthi, R. Maheswari, A. Ramanathan, *Energy & Fuels* 28 (2014) 2598–2607.
- [135] C. Ranga, R. Lødeng, V.I. Alexiadis, T. Rajkhowa, H. Bjørkan, S. Chytil, I.H. Svenum, J. Walmsley, C. Detavernier, H. Poelman, P. Van Der Voort, J.W. Thybaut, *Chemical Engineering Journal* 335 (2018) 120–132.
- [136] M. Shetty, E.M. Anderson, W.H. Green, Y. Román-Leshkov, *J Catal* 376 (2019) 248–257.

- [137] S. Haida, S. Löbner, H. Lund, S. Bartling, C. Kreyenschulte, H. Atia, A.M. Abdel-Mageed, C. Kubis, A. Brückner, *Catal Sci Technol* 14 (2024) 2201–2217.
- [138] Y. Yang, C. Ochoa-Hernández, V.A. de la Peña O'Shea, P. Pizarro, J.M. Coronado, D.P. Serrano, *Appl Catal B* 145 (2014) 91–100.
- [139] W.-S. Lee, Z. Wang, R.J. Wu, A. Bhan, *J Catal* 319 (2014) 44–53.
- [140] Y. Li, J. Fu, B. Chen, *RSC Adv* 7 (2017) 15272–15277.
- [141] S. Wang, D. Xu, Y. Chen, S. Zhou, D. Zhu, X. Wen, Y. Yang, Y. Li, *Catal Sci Technol* 10 (2020) 3015–3023.
- [142] D. Valencia, L. Díaz, L.F. Ramírez-Verduzco, M.A. Amezcua-Allieri, J. Aburto, *Mater Lett* 251 (2019) 226–229.
- [143] D. Valencia, L. Díaz-García, L.F. Ramírez-Verduzco, A. Qamar, A. Moewes, J. Aburto, *RSC Adv* 9 (2019) 18292–18301.
- [144] T.K. Vo, D.T. Quang, J. Kim, *Catal Commun* 169 (2022) 106478.
- [145] Y. Shi, Y. Cao, Y. Duan, H. Chen, Y. Chen, M. Yang, Y. Wu, *Green Chemistry* 18 (2016) 4633–4648.
- [146] S. Albarracin-Suazo, L. Freitas de Lima e Freitas, B. MacQueen, A. Heyden, J.A. Lauterbach, E. Nikolla, Y.J. Pagán-Torres, *ACS Sustain Chem Eng* 10 (2022) 5719–5727.
- [147] J. Zhang, C. Zhao, C. Li, S. Li, C.-W. Tsang, C. Liang, *Catal Sci Technol* 10 (2020) 2948–2960.
- [148] J.G. Chen, *Chem Rev* 96 (1996) 1477–1498.
- [149] J.-L. Calais, *Adv Phys* 26 (1977) 847–885.
- [150] A. Neckel, *Int J Quantum Chem* 23 (1983) 1317–1353.
- [151] H.H. Hwu, J.G. Chen, *Chem Rev* 105 (2005) 185–212.
- [152] J.R. dos S. Politi, F. Viñes, J.A. Rodriguez, F. Illas, *Physical Chemistry Chemical Physics* 15 (2013) 12617.
- [153] X.-R. Shi, S.-G. Wang, H. Wang, C.-M. Deng, Z. Qin, J. Wang, *Surf Sci* 603 (2009) 852–859.
- [154] M.I. Naher, S.H. Naqib, *Results Phys* 37 (2022) 105505.
- [155] T. Qin, Z. Wang, Y. Wang, F. Besenbacher, M. Otyepka, M. Dong, *Nanomicro Lett* 13 (2021) 183.
- [156] Q. Zhu, Q. Chen, X. Yang, D. Ke, *Mater Lett* 61 (2007) 5173–5174.
- [157] G. Vitale, M.L. Frauwallner, E. Hernandez, C.E. Scott, P. Pereira-Almao, *Appl Catal A Gen* 400 (2011) 221–229.

- [158] J. Han, J. Duan, P. Chen, H. Lou, X. Zheng, H. Hong, *Green Chemistry* 13 (2011) 2561.
- [159] C. Giordano, C. Erpen, W. Yao, M. Antonietti, *Nano Lett* 8 (2008) 4659–4663.
- [160] Z. Lin, L. Cai, W. Lu, Y. Chai, *Small* 13 (2017).
- [161] J.A. Schaidle, L.T. Thompson, *J Catal* 329 (2015) 325–334.
- [162] F. Solymosi, R. Németh, L. Óvári, L. Egri, *J Catal* 195 (2000) 316–325.
- [163] R. BARTHOS, F. SOLYMOSI, *J Catal* 249 (2007) 289–299.
- [164] G. Adamski, K. Dyrek, A. Kotarba, Z. Sojka, C. Sayag, G. Djéga-Mariadassou, *Catal Today* 90 (2004) 115–119.
- [165] M. Grilc, G. Veryasov, B. Likozar, A. Jesih, J. Levec, *Appl Catal B* 163 (2015) 467–477.
- [166] X. Ye, J. Ma, W. Yu, X. Pan, C. Yang, C. Wang, Q. Liu, Y. Huang, *Journal of Energy Chemistry* 67 (2022) 184–192.
- [167] J.R. Kitchin, J.K. Nørskov, M.A. Barteau, J.G. Chen, *Catal Today* 105 (2005) 66–73.
- [168] J.A. Schaidle, J. Blackburn, C.A. Farberow, C. Nash, K.X. Steirer, J. Clark, D.J. Robichaud, D.A. Ruddy, *ACS Catal* 6 (2016) 1181–1197.
- [169] W. Liu, B. Chen, X. Duan, K.-H. Wu, W. Qi, X. Guo, B. Zhang, D. Su, *ACS Catal* 7 (2017) 5820–5827.
- [170] Y. Shi, Y. Yang, Y.-W. Li, H. Jiao, *ACS Catal* 6 (2016) 6790–6803.
- [171] Y. Shi, Y. Yang, Y.-W. Li, H. Jiao, *Catal Sci Technol* 6 (2016) 4923–4936.
- [172] M.M. Sullivan, C.-J. Chen, A. Bhan, *Catal Sci Technol* 6 (2016) 602–616.
- [173] H. Guo, Z. Qi, Y. Liu, H. Xia, L. Li, Q. Huang, A. Wang, C. Li, *Catal Sci Technol* 9 (2019) 2144–2151.
- [174] M.M. Sullivan, A. Bhan, *J Catal* 344 (2016) 53–58.
- [175] M.M. Sullivan, J.T. Held, A. Bhan, *J Catal* 326 (2015) 82–91.
- [176] F.G. Baddour, C.P. Nash, J.A. Schaidle, D.A. Ruddy, *Angewandte Chemie* 128 (2016) 9172–9175.
- [177] S. Ramanathan, S.T. Oyama, *J Phys Chem* 99 (1995) 16365–16372.
- [178] B. Dhandapani, T. St. Clair, S.T. Oyama, *Appl Catal A Gen* 168 (1998) 219–228.
- [179] K.J. Smith, *Curr Opin Green Sustain Chem* 22 (2020) 47–53.
- [180] X. Du, R. Zhang, D. Li, C. Hu, H. Garcia, *Journal of Energy Chemistry* 73 (2022) 68–87.

- [181] J. Han, J. Duan, P. Chen, H. Lou, X. Zheng, H. Hong, *ChemSusChem* 5 (2012) 727–733.
- [182] A.L. Jongerius, P.C.A. Bruijninx, B.M. Weckhuysen, *Green Chemistry* 15 (2013) 3049.
- [183] H. Guo, Y. Song, P. Chen, H. Lou, X. Zheng, *Catal Sci Technol* 8 (2018) 4199–4208.
- [184] C.-C. Tran, D. Akmach, S. Kaliaguine, *Green Chemistry* 22 (2020) 6424–6436.
- [185] J. Remón, M. Casales, J. Gracia, M.S. Callén, J.L. Pinilla, I. Suelves, *Chemical Engineering Journal* 405 (2021) 126705.
- [186] A. Ayala-Cortés, D. Torres, E. Frecha, P. Arcelus-Arrillaga, H.I. Villafán-Vidales, A. Longoria, J.L. Pinilla, I. Suelves, *J Environ Chem Eng* 11 (2023) 111395.
- [187] H. Wang, S. Liu, Y. Dai, C.S. Kim, K.J. Smith, *Energy & Fuels* 38 (2024) 647–658.
- [188] A.L. Jongerius, R.W. Gosselink, J. Dijkstra, J.H. Bitter, P.C.A. Bruijninx, B.M. Weckhuysen, *ChemCatChem* 5 (2013) 2964–2972.
- [189] J. Chang, T. Danuthai, S. Dewiyanti, C. Wang, A. Borgna, *ChemCatChem* 5 (2013) 3041–3049.
- [190] R. Moreira, E. Ochoa, J. Pinilla, A. Portugal, I. Suelves, *Catalysts* 8 (2018) 127.
- [191] Z. Cai, F. Wang, X. Zhang, R. Ahishakiye, Y. Xie, Y. Shen, *Molecular Catalysis* 441 (2017) 28–34.
- [192] J. Remón, E. Ochoa, C. Foguet, J.L. Pinilla, I. Suelves, *Fuel Processing Technology* 191 (2019) 111–120.
- [193] E. Ochoa, D. Torres, J.L. Pinilla, I. Suelves, *Catal Today* 357 (2020) 240–247.
- [194] E. Blanco, D.A. Aguirre-Abarca, J.N. Díaz de León, N. Escalona, *New Journal of Chemistry* 44 (2020) 12027–12035.
- [195] L. Fei, S.M. Ng, W. Lu, M. Xu, L. Shu, W.-B. Zhang, Z. Yong, T. Sun, C.H. Lam, C.W. Leung, C.L. Mak, Y. Wang, *Nano Lett* 16 (2016) 7875–7881.
- [196] A. Sulman, P. Mäki-Arvela, L. Bomont, M. Alda-Onggar, V. Fedorov, V. Russo, K. Eränen, M. Peurla, U. Akhmetzyanova, L. Skuhrovcová, Z. Tišler, H. Grénman, J. Wärnå, D.Yu. Murzin, *Catal Letters* 149 (2019) 2453–2467.
- [197] J.F. Kurisingal, S. Lee, J.G. Lee, K. An, *Catalysts* 12 (2022) 1605.
- [198] Q. Lu, C.-J. Chen, W. Luc, J.G. Chen, A. Bhan, F. Jiao, *ACS Catal* 6 (2016) 3506–3514.

- [199] T. Iida, M. Shetty, K. Murugappan, Z. Wang, K. Ohara, T. Wakihara, Y. Román-Leshkov, *ACS Catal* 7 (2017) 8147–8151.
- [200] J. Zhu, E.A. Uslamin, N. Kosinov, E.J.M. Hensen, *Catal Sci Technol* 10 (2020) 3635–3645.
- [201] S. Boullosa-Eiras, R. Lødeng, H. Bergem, M. Stöcker, L. Hannevold, E.A. Blekkan, *Catal Today* 223 (2014) 44–53.
- [202] C.-J. Chen, W.-S. Lee, A. Bhan, *Appl Catal A Gen* 510 (2016) 42–48.
- [203] C.-J. Chen, A. Bhan, *ACS Catal* 7 (2017) 1113–1122.
- [204] X. Chen, X. Chen, J. Qi, C. Liang, *Molecular Catalysis* 492 (2020) 110972.
- [205] L.F. Sosa, P.M. de Souza, R.A. Rafael, R. Wojcieszak, V. Briois, L.R. Francisco, R.C. Rabelo-Neto, E. Marceau, S. Paul, F.S. Toniolo, F.B. Noronha, *Appl Catal B* 331 (2023) 122720.
- [206] W.-S. Lee, Z. Wang, W. Zheng, D.G. Vlachos, A. Bhan, *Catal Sci Technol* 4 (2014) 2340.
- [207] Z. Lin, W. Wan, S. Yao, J.G. Chen, *Appl Catal B* 233 (2018) 160–166.
- [208] L.F. Sosa, P.M. de Souza, R.A. Rafael, R. Wojcieszak, E. Marceau, S. Paul, V. Briois, F.B. Noronha, F.S. Toniolo, *ChemCatChem* 16 (2024).
- [209] H. Wang, S. Liu, M. Schmiß, C.S. Kim, K.J. Smith, *Ind Eng Chem Res* (2022).
- [210] S.A.W. Hollak, R.W. Gosselink, D.S. van Es, J.H. Bitter, *ACS Catal* 3 (2013) 2837–2844.
- [211] A.S. Rocha, L.A. Souza, R.R. Oliveira, A.B. Rocha, V. Teixeira da Silva, *Appl Catal A Gen* 531 (2017) 69–78.
- [212] C. Peng, L. Gao, S. Yang, J. Sun, *Chemical Communications* (2008) 5601.
- [213] J. Baltrusaitis, B. Mendoza-Sanchez, V. Fernandez, R. Veenstra, N. Dukstiene, A. Roberts, N. Fairley, *Appl Surf Sci* 326 (2015) 151–161.
- [214] X. Yi, H.-H. Ko, F. Deng, S.-B. Liu, A. Zheng, *Nat Protoc* 15 (2020) 3527–3555.
- [215] P. V. Wiper, J. Amelse, L. Mafrá, *J Catal* 316 (2014) 240–250.
- [216] M.A. Cremasco, *Fundamentos de Transferência de Massa*, 2a Edição, Editora da UNICAMP, Campinas, 2012.
- [217] P.B. Weisz, J.S. Hicks, *Chem Eng Sci* 17 (1962) 265–275.
- [218] A. Katrib, V. Logie, N. Saurel, P. Wehrer, L. Hilaire, G. Maire, *Surf Sci* 377–379 (1997) 754–758.
- [219] A. Benadda, A. Katrib, A. Barama, *Appl Catal A Gen* 251 (2003) 93–105.
- [220] P. Wehrer, S. Libs, L. Hilaire, *Appl Catal A Gen* 238 (2003) 69–84.

- [221] C. Bouchy, C. Pham-Huu, B. Heinrich, C. Chaumont, M.J. Ledoux, *J Catal* 190 (2000) 92–103.
- [222] V. Stoeberl, M. Abbate, L.M.S. Alves, C.A.M. dos Santos, R.J.O. Mossaneck, *J Alloys Compd* 691 (2017) 138–143.
- [223] T. Matsuda, Y. Hirata, S. Suga, H. Sakagami, N. Takahashi, *Appl Catal A Gen* 193 (2000) 185–193.
- [224] J. Sun, R.A.L. Baylon, C. Liu, D. Mei, K.J. Martin, P. Venkitasubramanian, Y. Wang, *J Am Chem Soc* 138 (2016) 507–517.
- [225] P.M. Mortensen, H.W.P. de Carvalho, J.-D. Grunwaldt, P.A. Jensen, A.D. Jensen, *J Catal* 328 (2015) 208–215.
- [226] C. Bouchy, C. Pham-huu, M.J. Ledoux, *J Mol Catal A Chem* 162 (2000) 317–334.
- [227] A. Zheng, S. Li, S.-B. Liu, F. Deng, *Acc Chem Res* 49 (2016) 655–663.
- [228] T. Ohno, Z. Li, N. Sakai, H. Sakagami, N. Takahashi, T. Matsuda, *Appl Catal A Gen* 389 (2010) 52–59.
- [229] S. Triwahyono, A.A. Jalil, N.N. Ruslan, H.D. Setiabudi, N.H.N. Kamarudin, *J Catal* 303 (2013) 50–59.
- [230] L.O. Alemán-Vázquez, F. Hernández-Pérez, J.L. Cano-Domínguez, A. Rodríguez-Hernández, J.L. García-Gutiérrez, *Fuel* 117 (2014) 463–469.
- [231] J. Harmel, T. Roberts, Z. Zhang, G. Sunley, P. de Jongh, K.P. de Jong, *J Catal* 390 (2020) 161–169.
- [232] M. Lewandowski, A. Szymańska-Kolasa, C. Sayag, G. Djéga-Mariadassou, *Appl Catal B* 261 (2020) 118239.
- [233] H. Knozinger, H. Krietenbrink, P. Ratnasamy, *J Catal* 48 (1977) 436–439.
- [234] M. Takeuchi, T. Tsukamoto, A. Kondo, M. Matsuoka, *Catal Sci Technol* 5 (2015) 4587–4593.
- [235] M. Kitano, E. Wada, K. Nakajima, S. Hayashi, S. Miyazaki, H. Kobayashi, M. Hara, *Chemistry of Materials* 25 (2013) 385–393.
- [236] S. Lang, M. Benz, U. Obenaus, R. Himmelmann, M. Hunger, *ChemCatChem* 8 (2016) 2031–2036.
- [237] J.M. Vohs, M.A. Barteau, *J Phys Chem* 95 (1991) 297–302.
- [238] M.A. Henderson, *J Phys Chem B* 108 (2004) 18932–18941.
- [239] S.D. Senanayake, W.O. Gordon, S.H. Overbury, D.R. Mullins, *The Journal of Physical Chemistry C* 113 (2009) 6208–6214.

- [240] R. King, H. Idriss, *Langmuir* 25 (2009) 4543–4555.
- [241] H. Idriss, C. Diagne, J.P. Hindermann, A. Kiennemann, M.A. Barteau, *J Catal* 155 (1995) 219–237.
- [242] A. Mattsson, M. Leideborg, K. Larsson, G. Westin, L. Österlund, *J Phys Chem B* 110 (2006) 1210–1220.
- [243] A.I. Biaglow, R.J. Gorte, G.T. Kokotailo, D. White, *J Catal* 148 (1994) 779–786.
- [244] H. Fang, A. Zheng, Y. Chu, F. Deng, *The Journal of Physical Chemistry C* 114 (2010) 12711–12718.
- [245] S.R.J. Likith, C.A. Farberow, S. Manna, A. Abdulslam, V. Stevanović, D.A. Ruddy, J.A. Schaidle, D.J. Robichaud, C. V. Ciobanu, *The Journal of Physical Chemistry C* 122 (2018) 1223–1233.
- [246] A. Kurlov, E.B. Deeva, P.M. Abdala, D. Lebedev, A. Tsoukalou, A. Comas-Vives, A. Fedorov, C.R. Müller, *Nat Commun* 11 (2020) 4920.
- [247] J. Kräuter, L. Mohrhusen, T. Thiedemann, M. Willms, K. Al-Shamery, *Zeitschrift Für Naturforschung A* 74 (2019) 697–707.
- [248] K. Nakajima, Y. Baba, R. Noma, M. Kitano, J.N. Kondo, S. Hayashi, M. Hara, *J Am Chem Soc* 133 (2011) 4224–4227.
- [249] M. Luisa Marin, G.L. Hallett-Tapley, S. Impellizzeri, C. Fasciani, S. Simoncelli, J.C. Netto-Ferreira, J.C. Scaiano, *Catal. Sci. Technol.* 4 (2014) 3044–3052.
- [250] N. Katada, K. Suzuki, T. Noda, G. Sastre, M. Niwa, *The Journal of Physical Chemistry C* 113 (2009) 19208–19217.
- [251] A.G. Panov, J.J. Fripiat, *J Catal* 178 (1998) 188–197.
- [252] C.P. Nash, A. Ramanathan, D.A. Ruddy, M. Behl, E. Gjersing, M. Griffin, H. Zhu, B. Subramaniam, J.A. Schaidle, J.E. Hensley, *Appl Catal A Gen* 510 (2016) 110–124.
- [253] S. Zhao, W.D. Wang, L. Wang, W. Wang, J. Huang, *J Catal* 389 (2020) 166–175.
- [254] G. Lee, S. Lee, J. Kim, D.W. Kim, Y. Kang, D. Kim, *Adv Energy Mater* 7 (2017).
- [255] C. Chen, H. Fan, J. Shaya, Y. Chang, V.B. Golovko, O. Toulemonde, C. Huang, Y. Song, C. Lu, *Appl Organomet Chem* 33 (2019).
- [256] S.K. Ray, J. Hur, *Journal of Industrial and Engineering Chemistry* 101 (2021) 28–50.
- [257] M. Misono, in: 2013, pp. 25–65.

- [258] A.S. Burange, M.B. Gawande, in: *Encyclopedia of Inorganic and Bioinorganic Chemistry*, Wiley, 2016, pp. 1–19.
- [259] I.E. Wachs, K. Routray, *ACS Catal* 2 (2012) 1235–1246.
- [260] I.E. Wachs, *Catal Today* 100 (2005) 79–94.
- [261] I.E. Wachs, *Catal Today* 423 (2023) 113883.
- [262] S. Chapman, C. Brookes, M. Bowker, E.K. Gibson, P.P. Wells, *Faraday Discuss* 188 (2016) 115–129.
- [263] M. Boudart, in: *Interactions on Metal Surfaces*, Springer-Verlag, Berlin/Heidelberg, n.d., pp. 275–298.
- [264] G.A. Somorjai, A.S. Mujumdar, *Drying Technology* 13 (1995) 507–508.
- [265] L.J. Burcham, L.E. Briand, I.E. Wachs, *Langmuir* 17 (2001) 6175–6184.
- [266] L.J. Burcham, M. Badlani, I.E. Wachs, *J Catal* 203 (2001) 104–121.
- [267] S. V. Merzlikin, N.N. Tolkachev, L.E. Briand, T. Strunskus, C. Wöll, I.E. Wachs, W. Grünert, *Angewandte Chemie International Edition* 49 (2010) 8037–8041.
- [268] K. Routray, W. Zhou, C.J. Kiely, W. Grünert, I.E. Wachs, *J Catal* 275 (2010) 84–98.
- [269] K. Routray, W. Zhou, C.J. Kiely, I.E. Wachs, *ACS Catal* 1 (2011) 54–66.
- [270] L.E. Cadus, Y.L. Xiong, F.J. Gotor, D. Acosta, J. Naud, P. Ruiz, B. Delmon, in: 1994, pp. 41–54.
- [271] E. Söderhjelm, M.P. House, N. Cruise, J. Holmberg, M. Bowker, J.-O. Bovin, A. Andersson, *Top Catal* 50 (2008) 145–155.
- [272] Y. Okamoto, F. Morikawa, K. Oh-Hiraki, T. Imanaka, S. Teranishi, *J. Chem. Soc., Chem. Commun.* (1981) 1018–1019.
- [273] G. Jin, W. Weng, Z. Lin, N.F. Dummer, S.H. Taylor, C.J. Kiely, J.K. Bartley, G.J. Hutchings, *J Catal* 296 (2012) 55–64.
- [274] C. Brookes, M. Bowker, E.K. Gibson, D. Gianolio, K.M.H. Mohammed, S. Parry, S.M. Rogers, I.P. Silverwood, P.P. Wells, *Catal Sci Technol* 6 (2016) 722–730.
- [275] A. Gaur, M. Stehle, K.V. Raun, J. Thrane, A.D. Jensen, J.-D. Grunwaldt, M. Høj, *Physical Chemistry Chemical Physics* 22 (2020) 11713–11723.
- [276] M. Dürl, K. Sowa, M. Panthöfer, N. Oefner, D. Stark, B.J.M. Etzold, A. Möller, *The Journal of Physical Chemistry C* 127 (2023) 7019–7026.
- [277] U. OZKAN, *J Catal* 116 (1989) 171–183.
- [278] U. Ozkan, G.L. Schrader, *Appl Catal* 23 (1986) 327–338.
- [279] U. OZKAN, *J Catal* 95 (1985) 120–136.

- [280] Z.-Z. Pan, Y. Li, Y. Zhao, C. Zhang, H. Chen, *Catal Today* 364 (2021) 2–6.
- [281] W.P. Doyle, G. McGuire, G.M. Clark, *Journal of Inorganic and Nuclear Chemistry* 28 (1966) 1185–1190.
- [282] F. Han, Y. Liu, G. Li, L. Yuan, A. Wang, F. Wang, T. Zhang, N. Li, *Green Chemistry* 25 (2023) 1056–1066.
- [283] E. Laurent, B. Delmon, *Appl Catal A Gen* 109 (1994) 77–96.
- [284] I.D. Mora-Vergara, L. Hernández Moscoso, E.M. Gaigneaux, S.A. Giraldo, V.G. Baldovino-Medrano, *Catal Today* 302 (2018) 125–135.
- [285] V.N. Bui, D. Laurenti, P. Afanasiev, C. Geantet, *Appl Catal B* 101 (2011) 239–245.
- [286] G.-N. Yun, S.-J. Ahn, A. Takagaki, R. Kikuchi, S.T. Oyama, *J Catal* 353 (2017) 141–151.
- [287] L.I. Al-Ali, O. Elmutasim, K. Al Ali, N. Singh, K. Polychronopoulou, *Nanomaterials* 12 (2022) 1435.
- [288] C. Ranga, V.I. Alexiadis, J. Lauwaert, R. Lødeng, J.W. Thybaut, *Appl Catal A Gen* 571 (2019) 61–70.
- [289] W. Xu, P.J. Ramírez, D. Stacchiola, J.L. Brito, J.A. Rodriguez, *Catal Letters* 145 (2015) 1365–1373.
- [290] S. Posada-Pérez, P.J. Ramírez, R.A. Gutiérrez, D.J. Stacchiola, F. Viñes, P. Liu, F. Illas, J.A. Rodriguez, *Catal Sci Technol* 6 (2016) 6766–6777.
- [291] K.-E. You, S.C. Ammal, Z. Lin, W. Wan, J.G. Chen, A. Heyden, *J Catal* 388 (2020) 141–153.
- [292] K.-E. You, S.C. Ammal, Z. Lin, A. Heyden, *ACS Catal* 12 (2022) 4581–4596.
- [293] Y. Zhang, Y. Teng, Y. Li, X. Du, L. Liu, Y. Wu, Y. Meng, Y. Hua, X. Zhao, X. Liu, *Ionics (Kiel)* 25 (2019) 4361–4370.
- [294] Z. Zhao, X. Qi, Y. He, N. Li, H. Lai, B. Liu, Y. Chen, T. Jin, *Microchimica Acta* 191 (2024) 159.
- [295] S. Hajebi, A. Abedini, *Journal of Materials Science: Materials in Electronics* 27 (2016) 4489–4493.
- [296] Y. Zhang, G. Zhao, Y. Jiang, W. Hong, Y. Zhang, M. Deng, H. Shuai, W. Xu, G. Zou, H. Hou, X. Ji, *ChemElectroChem* 6 (2019) 1688–1695.
- [297] N.F. Dummer, Z. Sodiq-Ajala, D.J. Morgan, T.E. Davies, *Catal Commun* 163 (2022) 106414.

- [298] J.A. Rodriguez, J.Y. Kim, J.C. Hanson, M. Pérez, A.I. Frenkel, *Catal Letters* 85 (2003) 247–254.
- [299] Y. Cai, H. Jia, C. Li, X. Si, J. Cao, W. Fei, J. Qi, *Chemical Engineering Journal* 418 (2021) 129495.
- [300] C.Y. Regalado Vera, H. Ding, D. Peterson, W.T. Gibbons, M. Zhou, D. Ding, *Journal of Physics: Energy* 3 (2021) 032019.
- [301] A. V. Gavrikov, A.B. Ilyukhin, E. V. Belova, A.D. Yapryntsev, Z. V. Dobrokhotova, A. V. Khrushcheva, N.N. Efimov, *Ceram Int* 46 (2020) 13014–13024.
- [302] M. Gao, E.Y. Konyshcheva, J. Yang, *Int J Hydrogen Energy* 47 (2022) 41336–41346.
- [303] P. Panda, R. Mishra, S. Panigrahy, S. Barman, *ACS Appl Nano Mater* 5 (2022) 5176–5186.
- [304] S. Gouadria, M. Abudllah, Z. Ahmad, P. John, M.U. Nisa, S. Manzoor, S. Aman, M.N. Ashiq, M.I. Ghor, *Ceram Int* 49 (2023) 4281–4289.
- [305] H. BRONGERSMA, M. DRAXLER, M. DERIDDER, P. BAUER, *Surf Sci Rep* 62 (2007) 63–109.
- [306] L.J. Burcham, L.E. Briand, I.E. Wachs, *Langmuir* 17 (2001) 6164–6174.
- [307] J.A. Rodriguez, J.Y. Kim, J.C. Hanson, J.L. Brito, *Catal Letters* 82 (2002) 103–109.
- [308] G. Alessandrini, L. Cairati, P. Forzatti, P.L. Villa, F. Trifirò, *Journal of the Less Common Metals* 54 (1977) 373–386.
- [309] N. Burriesci, F. Garbassi, M. Petrera, G. Petrini, N. Pernicone, in: 1980, pp. 115–126.
- [310] S.D.M. Jacques, O. Leynaud, D. Strusevich, A.M. Beale, G. Sankar, C.M. Martin, P. Barnes, *Angewandte Chemie International Edition* 45 (2006) 445–448.
- [311] M. HOUSE, A. CARLEY, M. BOWKER, *J Catal* 252 (2007) 88–96.
- [312] Z. Lin, R. Chen, Z. Qu, J.G. Chen, *Green Chemistry* 20 (2018) 2679–2696.
- [313] J. Lee, *J Catal* 112 (1988) 44–53.
- [314] J.J. Fripiat, in: *Surface Properties and Catalysis by Non-Metals*, Springer Netherlands, Dordrecht, 1983, pp. 477–491.
- [315] (n.d.).
- [316] C.S. Cundy, P.A. Cox, *Microporous and Mesoporous Materials* 82 (2005) 1–78.
- [317] M.E. Davis, *Nature* 417 (2002) 813–821.
- [318] B.M. Weckhuysen, J. Yu, *Chem Soc Rev* 44 (2015) 7022–7024.

- [319] Y. Li, J. Yu, *Nat Rev Mater* 6 (2021) 1156–1174.
- [320] R. Rinaldi, F. Schüth, *Energy Environ Sci* 2 (2009) 610–626.
- [321] J. Čejka, A. Corma, S. Zones, eds., *Zeolites and Catalysis*, Wiley, 2010.
- [322] E.T.C. Vogt, B.M. Weckhuysen, *Chem Soc Rev* 44 (2015) 7342–7370.
- [323] M. Ravi, V.L. Sushkevich, J.A. van Bokhoven, *Nat Mater* 19 (2020) 1047–1056.
- [324] W. Luo, W. Cao, P.C.A. Bruijninx, L. Lin, A. Wang, T. Zhang, *Green Chemistry* 21 (2019) 3744–3768.
- [325] N. Batalha, L. Pinard, C. Bouchy, E. Guillon, M. Guisnet, *J Catal* 307 (2013) 122–131.
- [326] W. Song, Y. Liu, E. Baráth, C. Zhao, J.A. Lercher, *Green Chemistry* 17 (2015) 1204–1218.
- [327] Q. Zhang, S. Gao, J. Yu, *Chem Rev* 123 (2023) 6039–6106.
- [328] J. Ethiraj, D. Wagh, H. Manyar, *Energy & Fuels* 36 (2022) 1189–1204.
- [329] W. Zhang, J. Chen, R. Liu, S. Wang, L. Chen, K. Li, *ACS Sustain Chem Eng* 2 (2014) 683–691.
- [330] D.-Y. Hong, S.J. Miller, P.K. Agrawal, C.W. Jones, *Chem. Commun.* 46 (2010) 1038–1040.
- [331] M. Hellinger, H.W.P. Carvalho, S. Baier, D. Wang, W. Kleist, J.-D. Grunwaldt, *Appl Catal A Gen* 490 (2015) 181–192.
- [332] H. Wang, H. Ruan, M. Feng, Y. Qin, H. Job, L. Luo, C. Wang, M.H. Engelhard, E. Kuhn, X. Chen, M.P. Tucker, B. Yang, *ChemSusChem* 10 (2017) 1846–1856.
- [333] H. Ohta, K. Yamamoto, M. Hayashi, G. Hamasaka, Y. Uozumi, Y. Watanabe, *Chemical Communications* 51 (2015) 17000–17003.
- [334] T.M. Huynh, U. Armbruster, M. Pohl, M. Schneider, J. Radnik, D. Hoang, B.M.Q. Phan, D.A. Nguyen, A. Martin, *ChemCatChem* 6 (2014) 1940–1951.
- [335] X. Zhang, T. Wang, L. Ma, Q. Zhang, T. Jiang, *Bioresour Technol* 127 (2013) 306–311.
- [336] C. Zhao, J.A. Lercher, *Angewandte Chemie* 124 (2012) 6037–6042.
- [337] B. Peng, Y. Yao, C. Zhao, J.A. Lercher, *Angewandte Chemie International Edition* 51 (2012) 2072–2075.
- [338] I. Barroso-Martín, D. Ballesteros-Plata, A. Infantes-Molina, M.O. Guerrero-Pérez, J. Santamaría-González, E. Rodríguez-Castellón, *IET Renewable Power Generation* 16 (2022) 3009–3022.
- [339] C. Zhao, D.M. Camaioni, J.A. Lercher, *J Catal* 288 (2012) 92–103.

- [340] C. Zhao, S. Kasakov, J. He, J.A. Lercher, *J Catal* 296 (2012) 12–23.
- [341] G. Yao, G. Wu, W. Dai, N. Guan, L. Li, *Fuel* 150 (2015) 175–183.
- [342] Y. Wang, J. Wu, S. Wang, *RSC Adv* 3 (2013) 12635.
- [343] W. Luo, P.C.A. Bruijninx, B.M. Weckhuysen, *J Catal* 320 (2014) 33–41.
- [344] X. GU, B. ZHANG, H. LIANG, H. GE, H. YANG, Y. QIN, *Journal of Fuel Chemistry and Technology* 45 (2017) 714–722.
- [345] B. Zhang, Q. Wu, C. Zhang, X. Su, R. Shi, W. Lin, Y. Li, F. Zhao, *ChemCatChem* 9 (2017) 3646–3654.
- [346] B. Ma, X. Yi, L. Chen, A. Zheng, C. Zhao, *J Mater Chem A Mater* 4 (2016) 11330–11341.
- [347] N.M. Eagan, M.D. Kumbhalkar, J.S. Buchanan, J.A. Dumesic, G.W. Huber, *Nat Rev Chem* 3 (2019) 223–249.
- [348] S. Wang, Z. Qin, M. Dong, J. Wang, W. Fan, *Chem Catalysis* 2 (2022) 1657–1685.
- [349] K. Murugappan, C. Mukarakate, S. Budhi, M. Shetty, M.R. Nimlos, Y. Román-Leshkov, *Green Chemistry* 18 (2016) 5548–5557.
- [350] T.F. Degnan, G.K. Chitnis, P.H. Schipper, *Microporous and Mesoporous Materials* 35–36 (2000) 245–252.
- [351] Y. Chai, W. Dai, G. Wu, N. Guan, L. Li, *Acc Chem Res* 54 (2021) 2894–2904.
- [352] L. Shirazi, E. Jamshidi, M.R. Ghasemi, *Crystal Research and Technology* 43 (2008) 1300–1306.
- [353] G.L. Woolery, G.H. Kuehl, H.C. Timken, A.W. Chester, J.C. Vartuli, *Zeolites* 19 (1997) 288–296.
- [354] J.A. Rabo, G.J. Gajda, *Catalysis Reviews* 31 (1989) 385–430.
- [355] X. Yang, R.W. Jenkins, J.H. Leal, C.M. Moore, E.J. Judge, T.A. Semelsberger, A.D. Sutton, *ACS Sustain Chem Eng* 7 (2019) 14521–14530.
- [356] M. Guisnet, P. Magnoux, *Appl Catal* 54 (1989) 1–27.
- [357] M. Guisnet, P. Magnoux, in: 1994, pp. 53–68.
- [358] Nunes PBM, Strapasson GB, Báfero GB, Zanchet D, *ChemRxiv* (2024).
- [359] L. Shen, J. Xu, M. Zhu, Y.-F. Han, *ACS Catal* 10 (2020) 14581–14591.
- [360] A.I. Tsiotsias, N.D. Charisiou, I. V. Yentekakis, M.A. Goula, *Nanomaterials* 11 (2020) 28.
- [361] D. Schmider, L. Maier, O. Deutschmann, *Ind Eng Chem Res* 60 (2021) 5792–5805.

Chapter 10. Appendix

10.1. Effect of mass and heat transport phenomena

In this section, we analyzed the effect of mass and heat transport phenomena concerning the three main classes of catalysts investigated in the acetone HDO reaction within this work, focusing on the evaluation of both external and internal diffusion. Figure A1 presents acetone conversion and products' distribution as a function of temperature (100–300 °C) for the commercial MoO₃ nanopowder, FeMo mixed oxide, and Z140 pristine zeolite – representing the catalysts discussed in Chapters 4, 5, and 6, respectively. Detailed assessments of their catalytic activity and other significant correlations are presented in their respective chapters, being not relevant here.

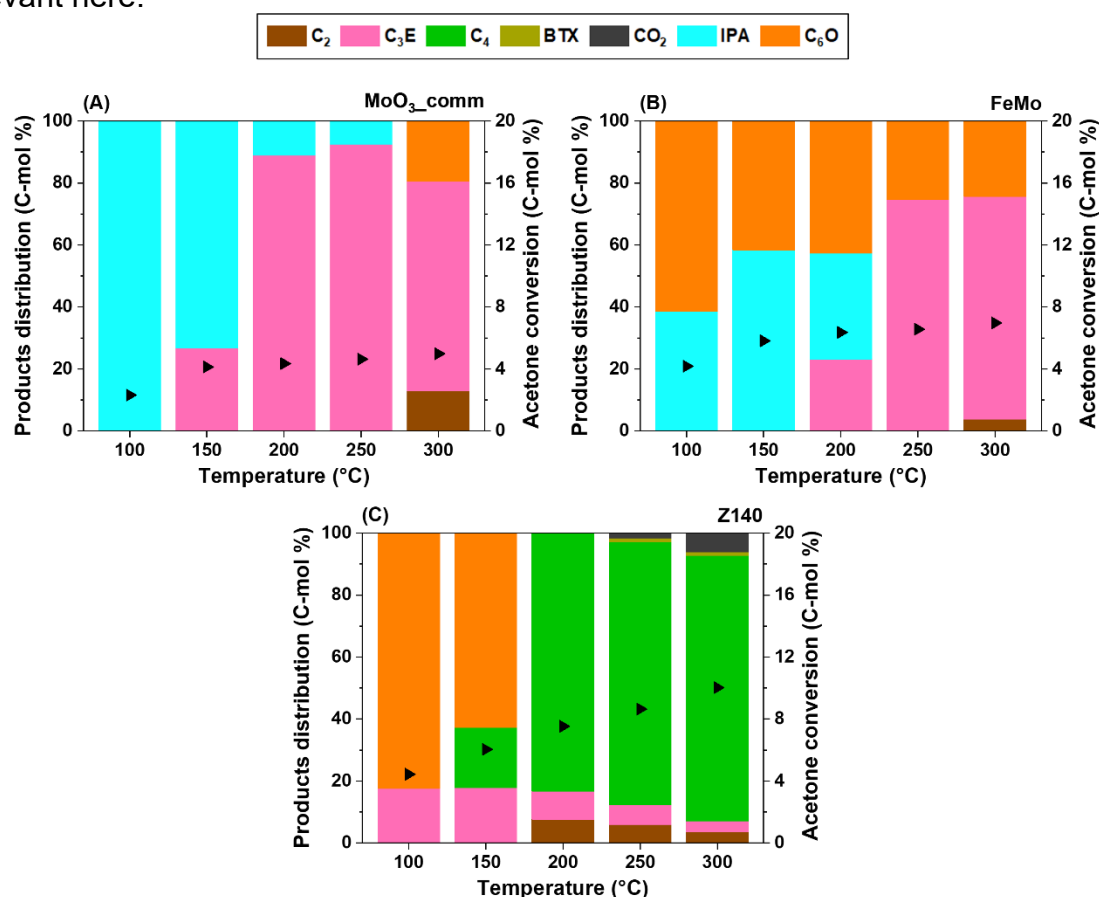


Figure A1. Products distribution (colored) and conversion (black triangles) for acetone HDO reaction over commercial MoO₃ nanopowder (A), FeMo mixed oxide (B), and Z140 pristine zeolite (C). 100→300 tests were carried out from 100 to 300 °C, isothermal every 50 °C, total TOS: 2 h. WHSV = 7.32 g_{acetone} g_{catalyst}⁻¹ h⁻¹. Feed: 2.4 mL min⁻¹ acetone, 51 mL min⁻¹ H₂, balance He. Total flow: 100 mL min⁻¹.

Tables A1 summarizes the necessary parameters measured for the catalytic beds to compute heat/mass transfer criteria, while Tables A2-A4 summarizes both internal and external mass transfer numbers for a typical catalytic test using each sample (Figure A1). The combination of $MR < 0.15$ (Mears criterion) and $C_{WP} \ll 1$ (Weisz-Prater criterion) suggests that any kind of diffusion phenomena limit the acetone HDO reaction in the conditions employed within this work.

Table A1. Measured catalytic bed parameters.

X	catalyst density, ρ_c (kg/m³)	catalyst bed bulk density, ρ_b (kg/m³)	catalyst particle radius, R (m)	bed porosity, ϕ
MoO₃_comm	978.13	998.64	5.58×10^{-5}	0.021
FeMo	629.77	740.38	5.58×10^{-5}	0.176
Z140	566.78	690.25	5.58×10^{-5}	0.218

Table A2. Mass transfer criteria for MoO₃_comm catalytic tests (see Figure 1).

Temperature (°C)	Conversion (%)	Rate (mol/g_{cat}.s)	MR	C_{WP}
100	2.31	7.58×10^{-7}	4.02×10^{-5}	7.50×10^{-7}
150	4.13	1.35×10^{-6}	5.74×10^{-5}	1.07×10^{-6}
200	4.35	1.42×10^{-6}	4.97×10^{-5}	9.29×10^{-7}
250	4.63	1.52×10^{-6}	4.44×10^{-5}	8.30×10^{-7}
300	4.99	1.63×10^{-6}	4.08×10^{-5}	7.62×10^{-7}

Table A3. Mass transfer criteria for FeMo catalytic tests (see Figure 1).

Temperature (°C)	Conversion (%)	Rate (mol/g_{cat}.s)	MR	C_{WP}
100	4.18	1.37×10^{-6}	5.37×10^{-5}	1.04×10^{-7}
150	5.82	1.90×10^{-6}	6.00×10^{-5}	1.16×10^{-7}
200	6.36	2.08×10^{-6}	5.39×10^{-5}	1.04×10^{-7}
250	6.57	2.15×10^{-6}	4.67×10^{-5}	9.04×10^{-8}
300	6.97	2.28×10^{-6}	4.22×10^{-5}	8.18×10^{-8}

Table A4. Mass transfer criteria for Z140 catalytic tests (see Figure 1).

Temperature (°C)	Conversion (%)	Rate (mol/g_{cat}.s)	MR	C_{WP}
100	4.44	1.45×10^{-6}	5.31×10^{-5}	4.24×10^{-5}
150	6.04	1.98×10^{-6}	5.80×10^{-5}	5.41×10^{-5}
200	7.53	2.46×10^{-6}	5.95×10^{-5}	6.39×10^{-5}
250	8.65	2.83×10^{-6}	5.73×10^{-5}	6.97×10^{-5}
300	10.03	3.28×10^{-6}	5.67×10^{-5}	7.72×10^{-5}

For heat transfer purposes, the catalytic data between 100–300 °C (Figure A1) is still used, as the phase transitions involving the Mo-based catalysts should occur only above 300 °C. Tables A5-A7 indicate that there was no significant temperature gradient observed from the bulk fluid to the catalytic site.

Table A5. Heat transfer criteria for MoO₃_comm catalytic tests (see Figure 1).

Temperature (°C)	Conversion (%)	Rate (mol/g _{cat} .s)	MR	C _{WH}
100	2.31	7.58×10^{-7}	9.62×10^{-12}	7.50×10^{-7}
150	4.13	1.35×10^{-6}	8.86×10^{-12}	1.07×10^{-6}
200	4.35	1.42×10^{-6}	9.59×10^{-13}	9.29×10^{-7}
250	4.63	1.52×10^{-6}	5.05×10^{-13}	8.30×10^{-7}
300	4.99	1.63×10^{-6}	1.40×10^{-12}	7.62×10^{-7}

Table A6. Heat transfer criteria for FeMo catalytic tests (see Figure 1).

Temperature (°C)	Conversion (%)	Rate (mol/g _{cat} .s)	MR	C _{WH}
100	4.18	1.37×10^{-6}	2.14×10^{-12}	1.04×10^{-7}
150	5.82	1.90×10^{-6}	4.97×10^{-12}	1.16×10^{-7}
200	6.36	2.08×10^{-6}	1.73×10^{-12}	1.04×10^{-7}
250	6.57	2.15×10^{-6}	4.88×10^{-14}	9.04×10^{-8}
300	6.97	2.28×10^{-6}	8.04×10^{-13}	8.18×10^{-8}

Table A7. Heat transfer criteria for Z140 catalytic tests (see Figure 1).

Temperature (°C)	Conversion (%)	Rate (mol/g _{cat} .s)	MR	C _{WH}
100	4.44	1.45×10^{-6}	3.60×10^{-12}	4.24×10^{-5}
150	6.04	1.98×10^{-6}	2.18×10^{-12}	5.41×10^{-5}
200	7.53	2.46×10^{-6}	1.83×10^{-11}	6.39×10^{-5}
250	8.65	2.83×10^{-6}	1.65×10^{-11}	6.97×10^{-5}
300	10.03	3.28×10^{-6}	1.53×10^{-11}	7.72×10^{-5}

As a result, catalytic activity measurements were conducted under conditions where neither heat nor mass transfer phenomena were constraining factors. Consequently, the obtained data accurately reflect the kinetics of the reactive process.

10.2. Supporting information

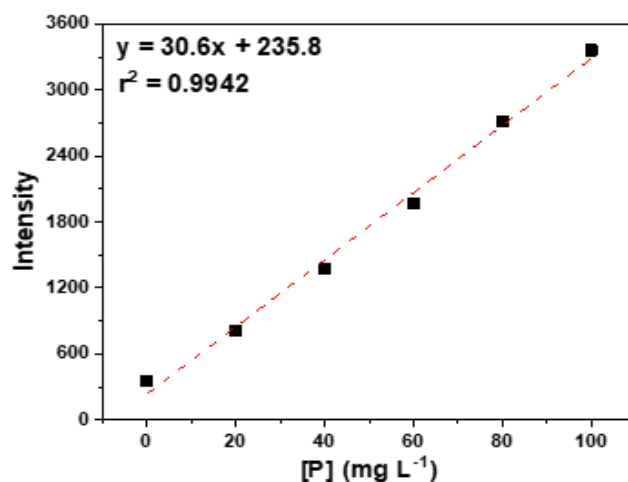


Figure A2. ICP-OES phosphorus external standard calibration curve.

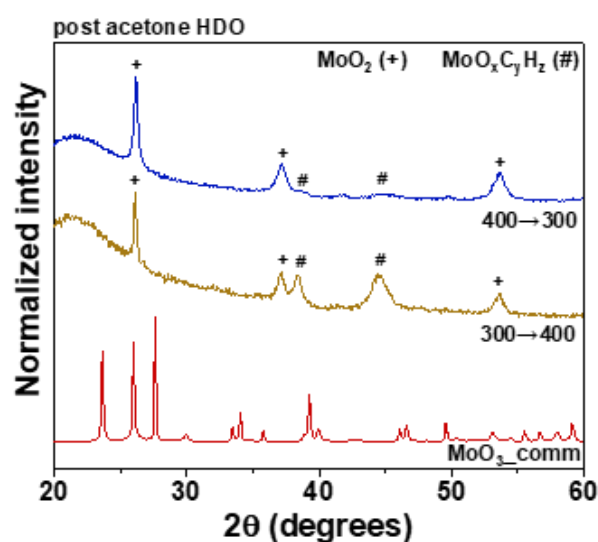


Figure A3. XRD patterns of the MoO₃_comm: as received and after acetone HDO reaction, 300→400 and 400→300 tests. TOS: 18 h (0.1 °C/min). The amorphous halo between 20 and 30 ° 2θ is related to quartz powder used as a diluent in the catalytic tests. Reaction conditions of post-run catalysts: WHSV = 7.14 g_{acetone} g_{catalyst}⁻¹ h⁻¹. Feed: 2.4 mL min⁻¹ acetone, 51 mL min⁻¹ H₂, balance He. Total flow: 100 mL min⁻¹.

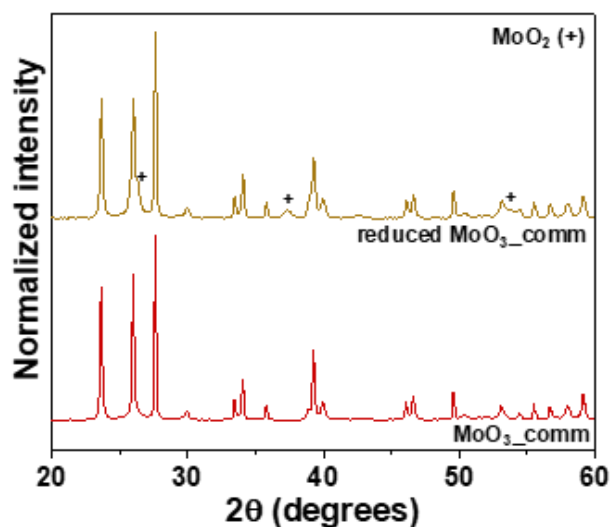


Figure A4. XRD patterns of $\text{MoO}_2_{\text{comm}}$: as received and after acetone HDO reaction at 350 °C and 400 °C for 6 h, 350C6h, and 400C6h, respectively. The amorphous halo between 20 and 30 ° 2θ is related to quartz powder used as a diluent in the catalytic tests. WHSV = 7.14 g_{acetone} g_{catalyst}⁻¹ h⁻¹. Feed: 2.4 mL min⁻¹ acetone, 51 mL min⁻¹ H₂, balance He. Total flow: 100 mL min⁻¹.

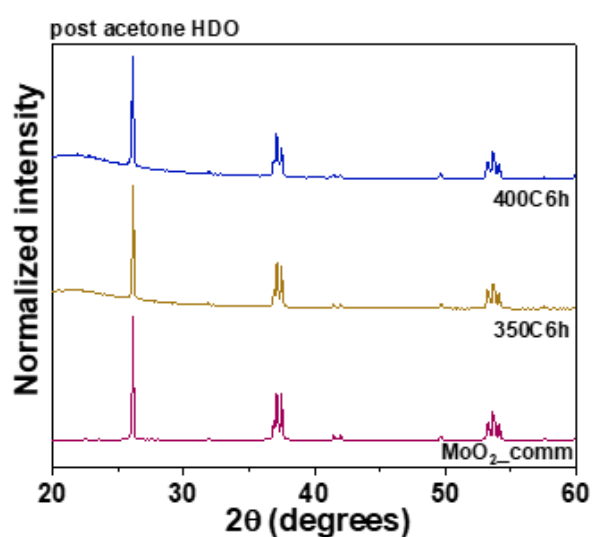


Figure A5. XRD patterns of the $\text{MoO}_3_{\text{comm}}$, as received, and after reduction under H₂ atmosphere at 400 °C for 1 h (51 mL min⁻¹ H₂).

Table A8. XPS fitting parameters for Mo 3d_{5/2} spectra, comprising binding energy and full width at half maximum of each Mo species observed.

Sample	Mo 3d _{5/2}					
	Binding Energy (eV)			FWHM (eV)		
	Mo ⁴⁺	Mo ⁵⁺	Mo ⁶⁺	Mo ⁴⁺	Mo ⁵⁺	Mo ⁶⁺
MoO ₃ _comm	-	232.2	233.5	-	1.7	1.0
350C1h	-	232.0	233.2	-	2.0	1.0
350C6h	230.3 (s); 231.2 (un)	232.1	233.5	1.3 (s); 2.0 (un)	2.0	1.7
400C1h	229.9 (s); 231.4 (un)	232.3	233.6	1.0 (s); 2.0 (un)	1.0	1.5
400C6h	229.9 (s); 231.3 (un)	232.2	233.6	1.0 (s); 2.0 (un)	1.2	1.3

s – screened; un – unscreened; spin-orbit splitting of 3.1 eV

Table A9. The atomic surface concentration of C, O, and Mo obtained through XPS measurements: MoO₃_comm (as received) and 350C1h, 350C6h, 400C1h, and 400C6h catalysts after acetone HDO reaction. Reaction conditions of pre-treated samples: WHSV = 7.14 g_{acetone} g_{catalyst}⁻¹ h⁻¹. Feed: 2.4 mL min⁻¹ acetone, 51 mL min⁻¹ H₂, balance He. Total flow: 100 mL min⁻¹.

Sample	Quantification (at.%)			Atomic ratios		
	C	O	Mo	Mo/O	Mo/C	Mo/(C+O)
MoO ₃ _comm	13.6	55.5	30.9	0.6	2.3	0.4
350C1h	31.1	44.3	24.6	0.6	0.8	0.3
350C6h	32.4	50.3	17.3	0.3	0.5	0.2
400C1h	29.8	42.1	28.1	0.7	0.9	0.4
400C6h	30.7	45.6	23.7	0.5	0.8	0.3

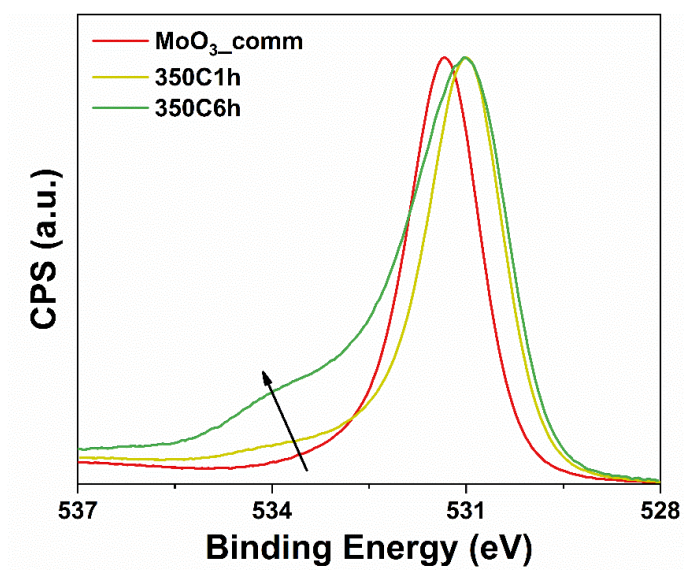


Figure A6. XPS spectra of O1s region for MoO₃_comm, 350C1h, and 350C6h catalysts.

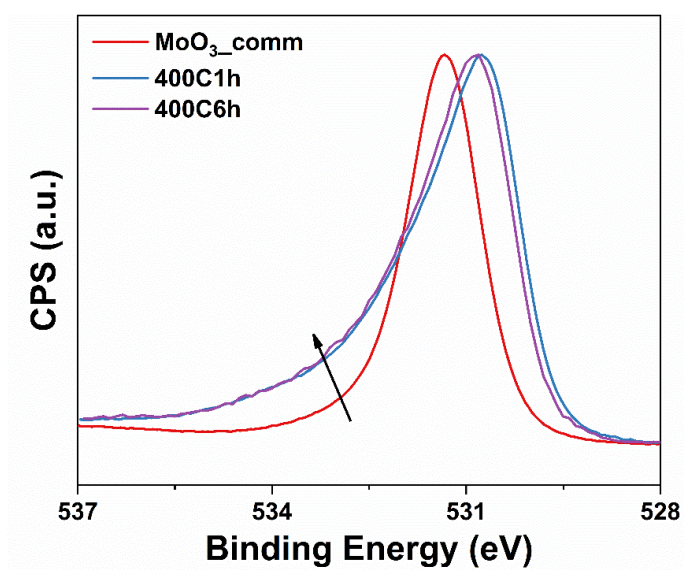


Figure A7. XPS spectra of O1s region for MoO₃_comm, 400C1h, and 400C6h catalysts.

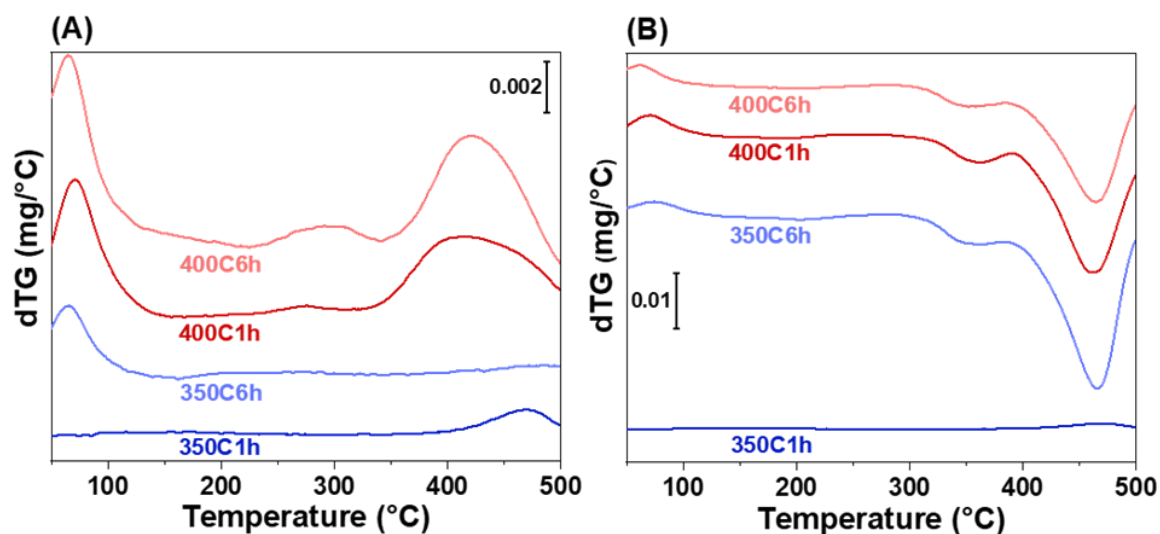


Figure A8. dTG curves obtained from the thermogravimetric analysis of 350C1h, 350C6h, 400C1h, and 400C6h catalysts after acetone HDO reaction under (A) N₂ and (B) synthetic air atmosphere. Reaction conditions of pre-treated samples: WHSV = 7.14 g_{acetone} g_{catalyst}⁻¹ h⁻¹. Feed: 2.4 mL min⁻¹ acetone, 51 mL min⁻¹ H₂, balance He. Total flow: 100 mL min⁻¹.

Table A10. Weight losses and gains obtained from the thermogravimetric analysis of 350C1h, 350C6h, 400C1h, and 400C6h catalysts after acetone HDO reaction under N₂ and synthetic air atmosphere. Reaction conditions of pre-treated samples: WHSV = 7.14 g_{acetone} g_{catalyst}⁻¹ h⁻¹. Feed: 2.4 mL min⁻¹ acetone, 51 mL min⁻¹ H₂, balance He. Total flow: 100 mL min⁻¹.

Atmosphere	Sample	Weight Loss (-) / Gain (+)			
		50-150 °C	150-330 °C	330-400 °C	400-500 °C
N ₂	350C1h	x	x	0.5 (-)	
	350C6h	1.4 (-)	1.4 (-)	2.5 (-)	
	400C1h	1.8 (-)	0.8 (-)	2.1 (-)	
	400C6h	2.8 (-)	0.7 (-)	1.5 (-)	
Air	350C1h	x	x	x	0.5 (-)
	350C6h	1.4 (-)	1.3 (-)	1.2 (+)	7.5 (+)
	400C1h	1.7 (-)	1.6 (-)	1.0 (+)	7.0 (+)
	400C6h	1.6 (-)	1.4 (-)	1.3 (+)	7.1 (+)

Table A11. Percentage distribution of Lewis (LAS) and Brønsted (BAS) acid sites of selected samples determined by ^{31}P NMR of TMPO: $\text{MoO}_3_{\text{comm}}$ (as received) and 350C6h and 400C1h catalysts after acetone HDO reaction. The concentration of physisorbed TMPO (Phys.) is also presented. B1-B4 stands for BAS, where the higher the number, the stronger the site. Reaction conditions of pre-treated samples: WHSV = $7.14 \text{ g}_{\text{acetone}} \text{ g}_{\text{catalyst}}^{-1} \text{ h}^{-1}$. Feed: 2.4 mL min^{-1} acetone, $51 \text{ mL min}^{-1} \text{ H}_2$, balance He. Total flow: 100 mL min^{-1} .

Sample	Percentage distribution (%)					
	Phys.	LAS	B1	B2	B3	B4
$\text{MoO}_3_{\text{comm}}$	22.2	34.8	15.1	19.0	6.7	2.2
350C6h	2.0	30.4	3.3	29.1	12.8	22.4
400C1h	24.4	35.4	6.2	18.7	8.8	6.5

Table A12. Specific surface areas (SSA) determined by N_2 physisorption experiments of $\text{MoO}_3_{\text{comm}}$ (as received) and selected samples after acetone HDO reaction. Reaction conditions of pre-treated samples: WHSV = $7.14 \text{ g}_{\text{acetone}} \text{ g}_{\text{catalyst}}^{-1} \text{ h}^{-1}$. Feed: 2.4 mL min^{-1} acetone, $51 \text{ mL min}^{-1} \text{ H}_2$, balance He. Total flow: 100 mL min^{-1} .

Sample	SSA ($\text{m}^2 \text{ g}^{-1}$)
$\text{MoO}_3_{\text{comm}}$	7.1
350C1h	19.4
350C6h	24.3
400C1h	44.2
400C6h	38.9

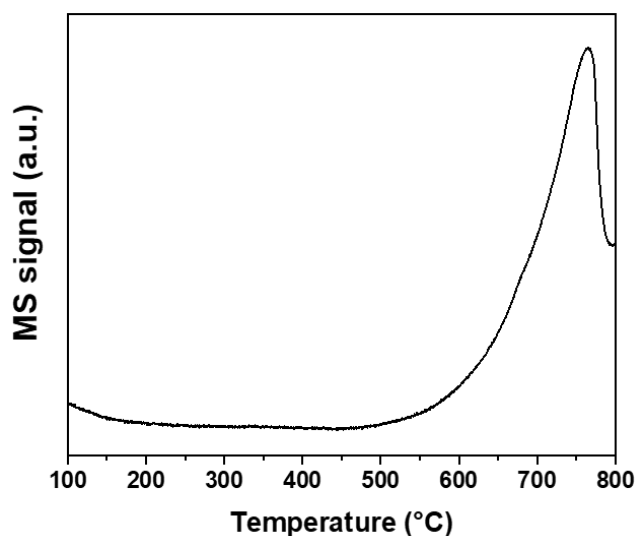


Figure A9. H₂-TPR curve of MoO₃_comm (as received).

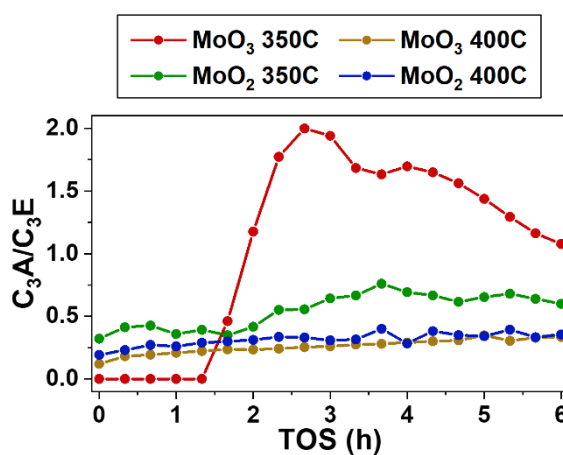


Figure A10. C₃A/C₃E ratio of acetone HDO reactions for MoO₃_comm and MoO₂_comm: 350C, isothermal at 350 °C, and 400C, isothermal at 400 °C. TOS: 6 h. WHSV = 7.14 g_{acetone} g_{catalyst}⁻¹ h⁻¹. Feed: 2.4 mL min⁻¹ acetone, 51 mL min⁻¹ H₂, balance He. Total flow: 100 mL min⁻¹.

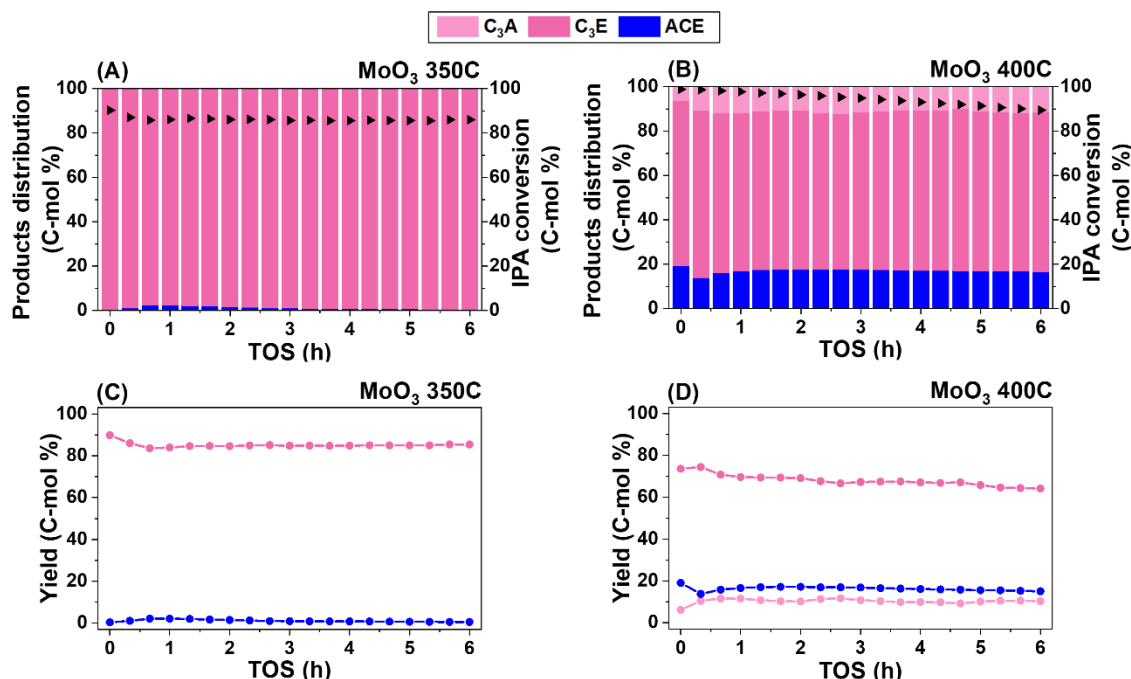


Figure A11. Products distribution (colored bars) and conversion (triangles) of isopropanol HDO reactions, and yields of C_3A , C_3E , and acetone (ACE) for MoO_3 _comm: 350C, isothermal at 350 °C (A, C), and 400C, isothermal at 400 °C (B, D). TOS: 6 h. WHSV = $7.32 \text{ g}_{\text{isopropanol}} \text{ g}_{\text{catalyst}}^{-1} \text{ h}^{-1}$. Feed: 2.4 mL min^{-1} isopropanol, $51 \text{ mL min}^{-1} \text{ H}_2$, balance He. Total flow: 100 mL min^{-1} .

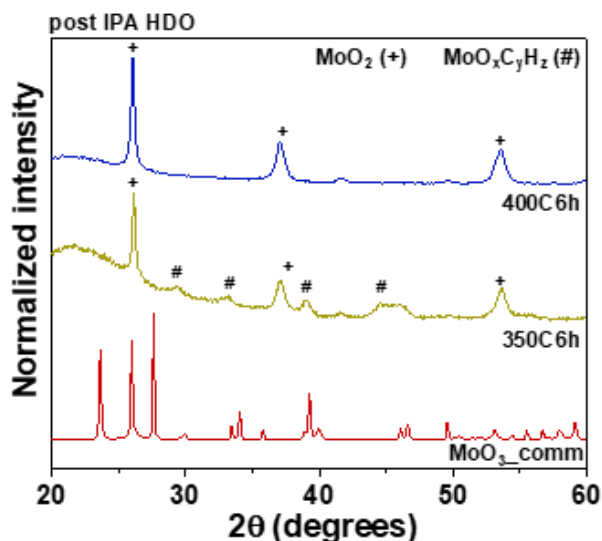


Figure A12. XRD patterns of MoO_3 _comm: as received and after IPA HDO reaction at 350 °C and 400 °C for 6 h, 350C6h, and 400C6h, respectively. The amorphous halo between 20 and 30 ° 2θ is related to quartz powder used as a diluent in the catalytic tests. WHSV = $7.32 \text{ g}_{\text{isopropanol}} \text{ g}_{\text{catalyst}}^{-1} \text{ h}^{-1}$. Feed: 2.4 mL min^{-1} acetone, $51 \text{ mL min}^{-1} \text{ H}_2$, balance He. Total flow: 100 mL min^{-1} .

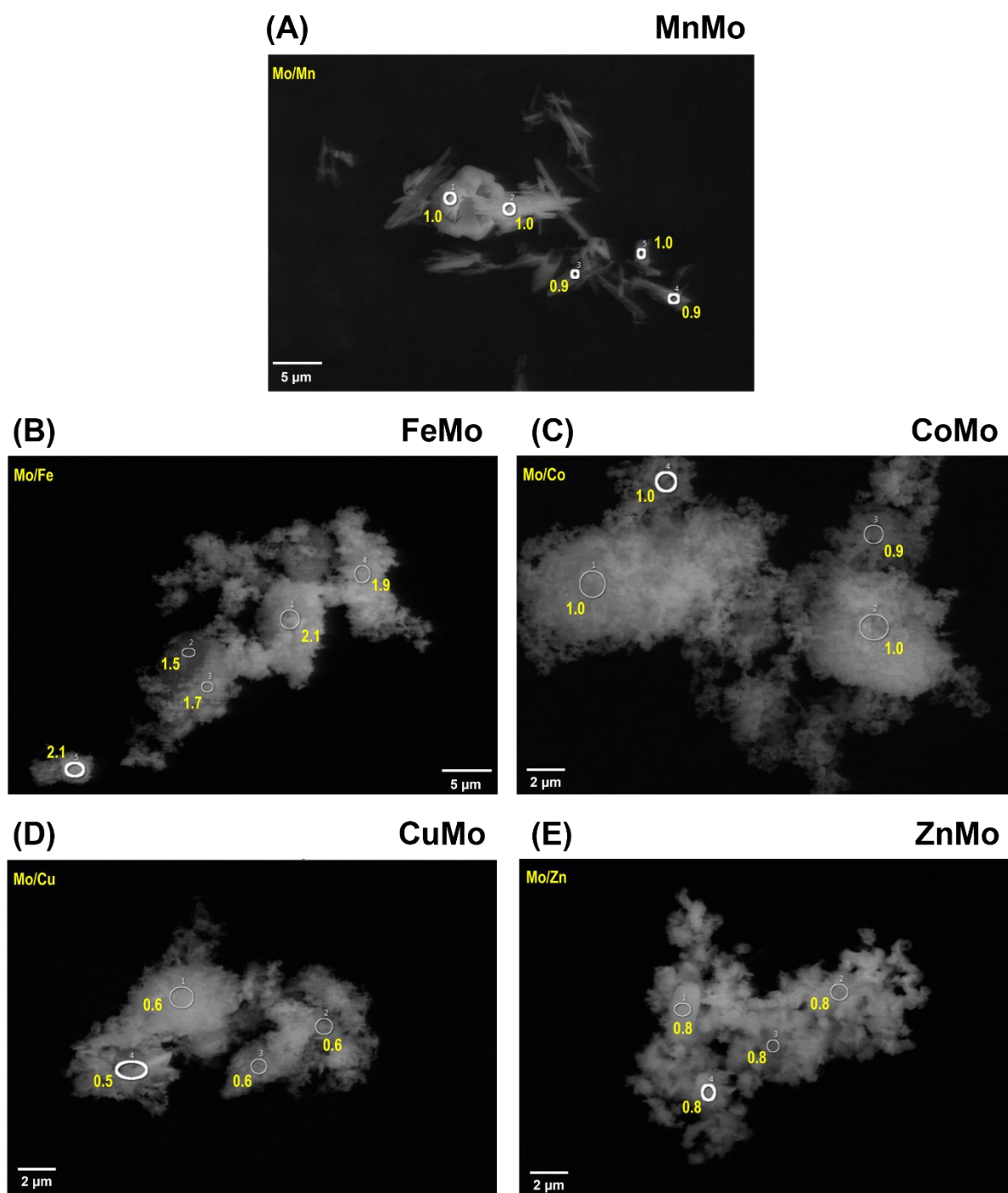


Figure A13. SEM images of the first-row transition metal molybdate catalysts highlighting the Mo/M atomic ratios obtained through EDX analysis: (A) MnMo, (B) FeMo, (C) CoMo, (D) CuMo, (E) ZnMo.

Table A13. Specific surface areas (SSA) determined by N₂ physisorption experiments of the first-row transition metal molybdate catalysts (MMo): MnMo, FeMo, CoMo, CuMo, and ZnMo

Sample	SSA (m ² g ⁻¹)
MnMo	3.6
FeMo	9.6
CoMo	21.6
CuMo	14.6
ZnMo	6.4

Table A14. The atomic surface concentration of C, O, Mo and M (M = Mn, Fe, Co, Cu, Zn) obtained through XPS measurements of the first-row transition metal molybdate catalysts (MMo).

Sample	Quantification (at.%)				Atomic ratios	
	C	O	Mo	M	Nominal Mo/M	Experimental Mo/M
MnMo	23.1	49.2	18.5	11.8 (Mn)	1.0	2.0
FeMo	19.9	53.9	19.7	6.6 (Fe)	1.5	3.0
CoMo	30.1	46.5	14.7	8.6 (Co)	1.0	1.7
CuMo	26.4	46.7	14.6	13.3 (Cu)	0.7	1.2
ZnMo	20.7	50.6	16.9	11.8 (Zn)	1.0	1.4

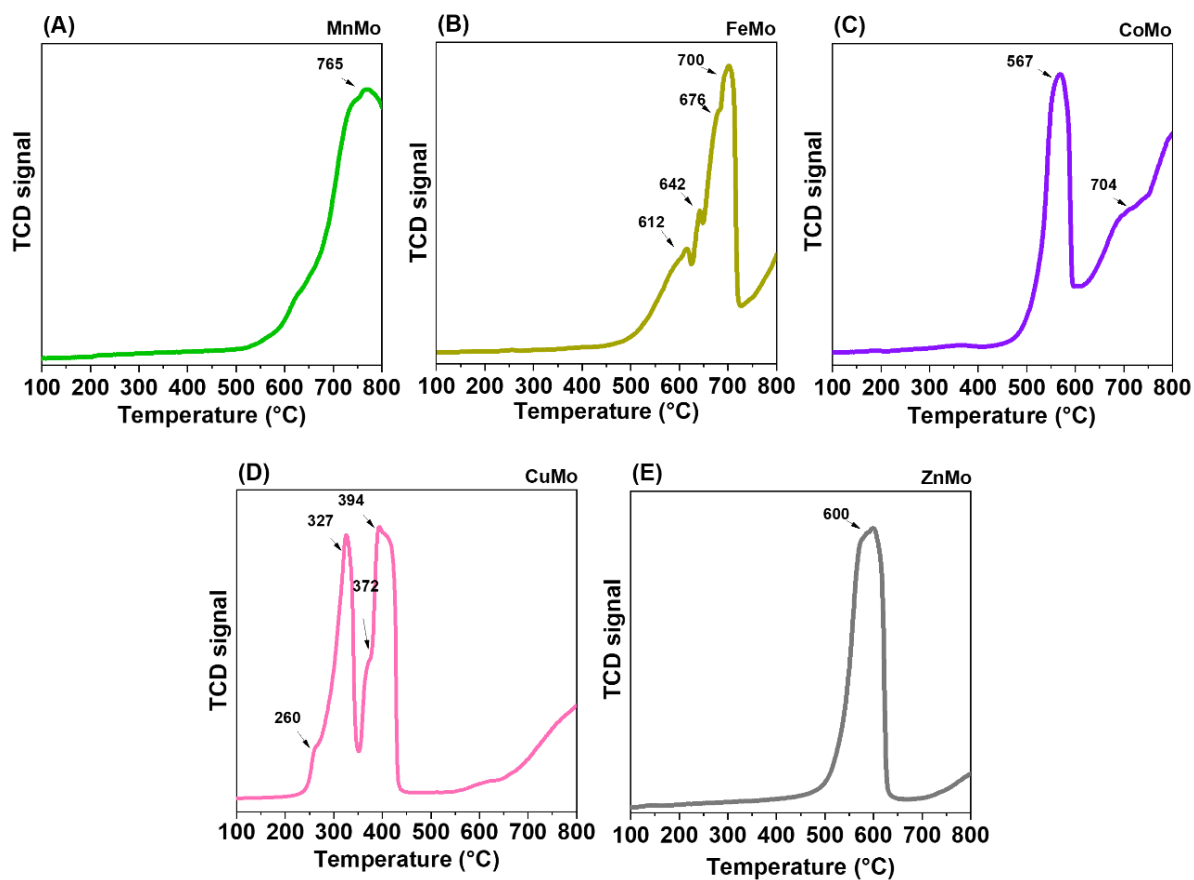


Figure A14. H₂-TPR curve of the first-row transition metal molybdate catalysts (MMo): MnMo (A), FeMo (B), CoMo (C), CuMo (D), and ZnMo (E).

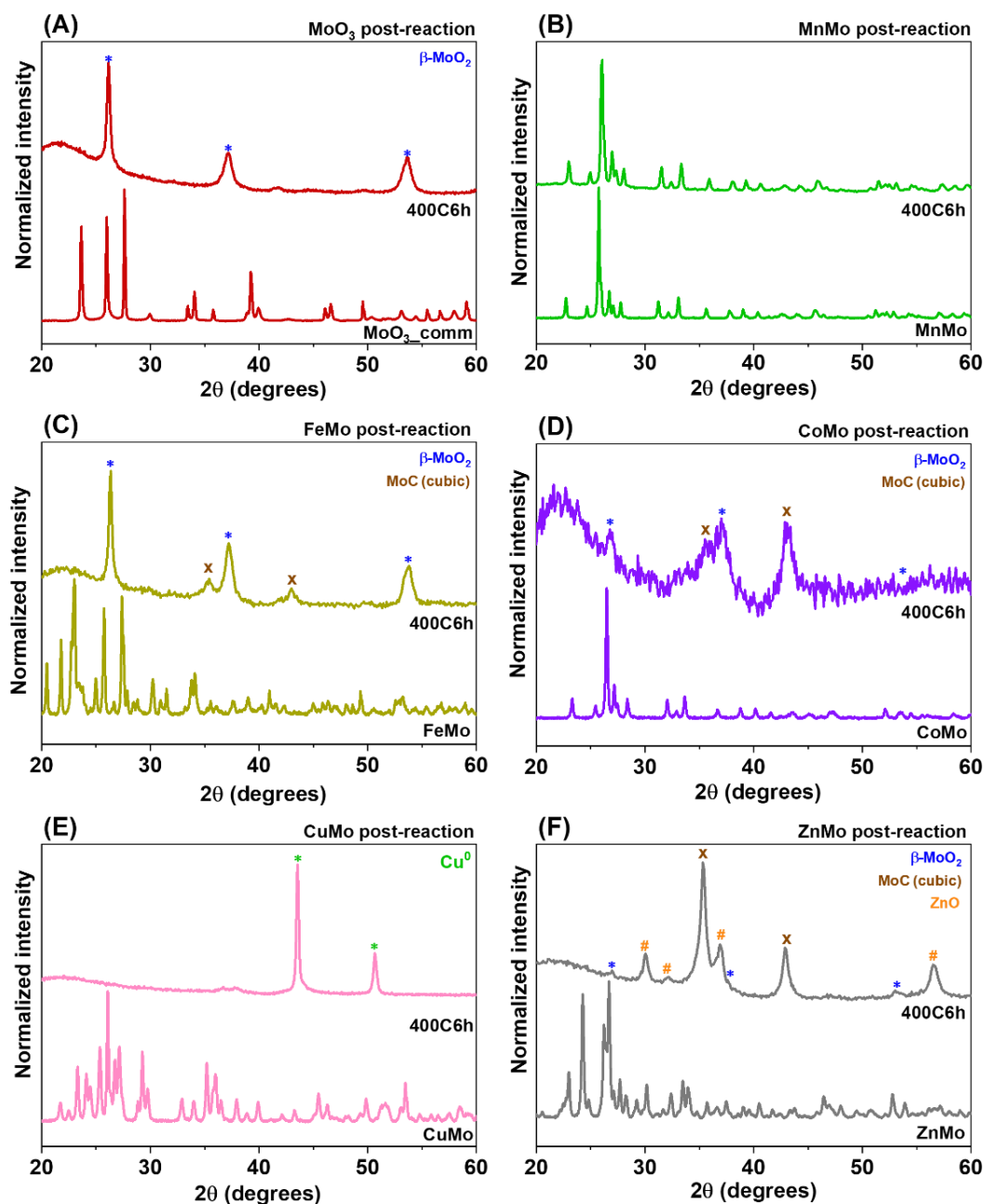


Figure A15. XRD patterns of MoO₃_comm (A) and the first-row transition metal molybdates catalysts (MMo): MnMo (B), FeMo (C), CoMo (D), CuMo (E), and ZnMo (F); before and after acetone HDO reaction at 400 °C for 6 h, 400C6h. The amorphous halo between 20 and 30 ° 2θ is related to quartz powder used as a diluent in the catalytic tests. WHSV = 7.14 g_{acetone} g_{catalyst}⁻¹ h⁻¹. Feed: 2.4 mL min⁻¹ acetone, 51 mL min⁻¹ H₂, balance He. Total flow: 100 mL min⁻¹.

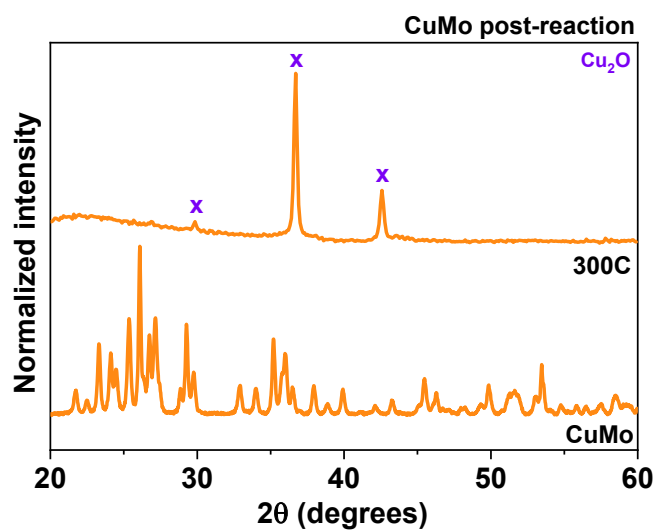


Figure A16. XRD patterns of the CuMo catalysts before and after acetone HDO reaction from 100 to 300 °C, 300C. The amorphous halo between 20 and 30 ° 2θ is related to quartz powder used as a diluent in the catalytic tests. WHSV = 7.14 g_{acetone} g_{catalyst}⁻¹ h⁻¹. Feed: 2.4 mL min⁻¹ acetone, 51 mL min⁻¹ H₂, balance He. Total flow: 100 mL min⁻¹.

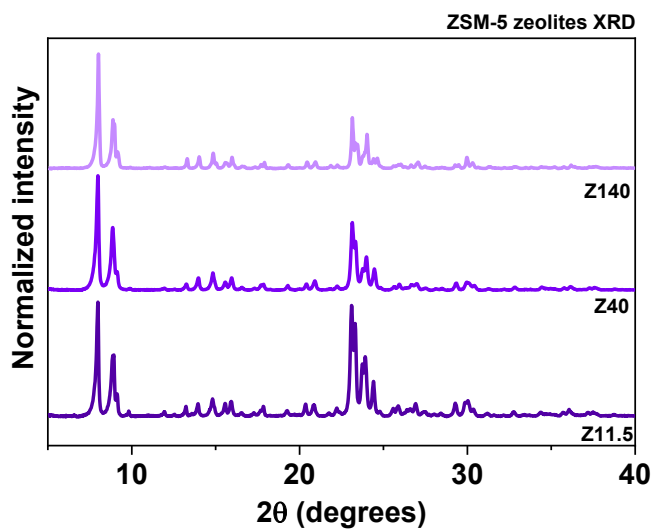


Figure A17. XRD patterns of the pristine ZSM-5 zeolites: Z11.5, Z40, and Z140.

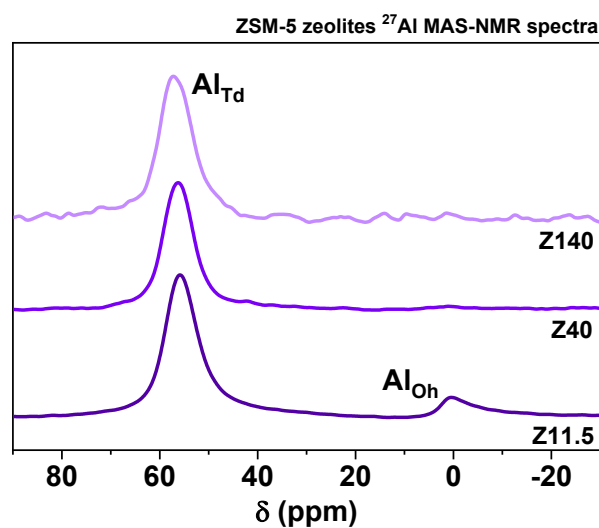


Figure A18. ^{27}Al MAS-NMR spectra of the pristine ZSM-5 zeolite catalysts: Z11.5, Z40, and Z140.

Table A15. Elemental analysis and Al-related data o of the pristine ZSM-5 zeolite catalysts: Z11.5, Z40, and Z140.

Zeolite	Si/Al _(nominal)	Si/Al _(real) ^a	% Al _{Td} ^a	% Al _{Oh} ^a	AS ($\mu\text{mol g}^{-1}$) ^b
Z11.5	11.5	16	88	12	841
Z40	40	58	100	-	271
Z140	140	121	100	0	131

^a obtained through XRF analysis

^b considering each Al_{Td} as an AS

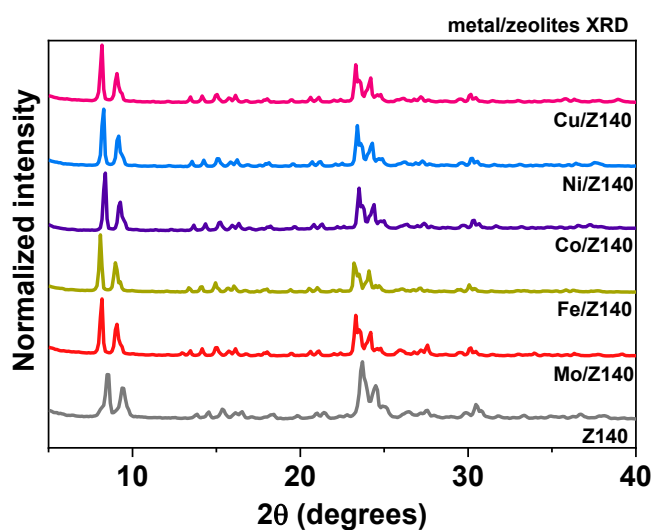


Figure A19. XRD patterns of the metal/zeolite catalysts: Z140 (for comparison purposes), Mo/Z140, Fe/Z140, Co/Z140, Ni/Z140, Cu/Z140.

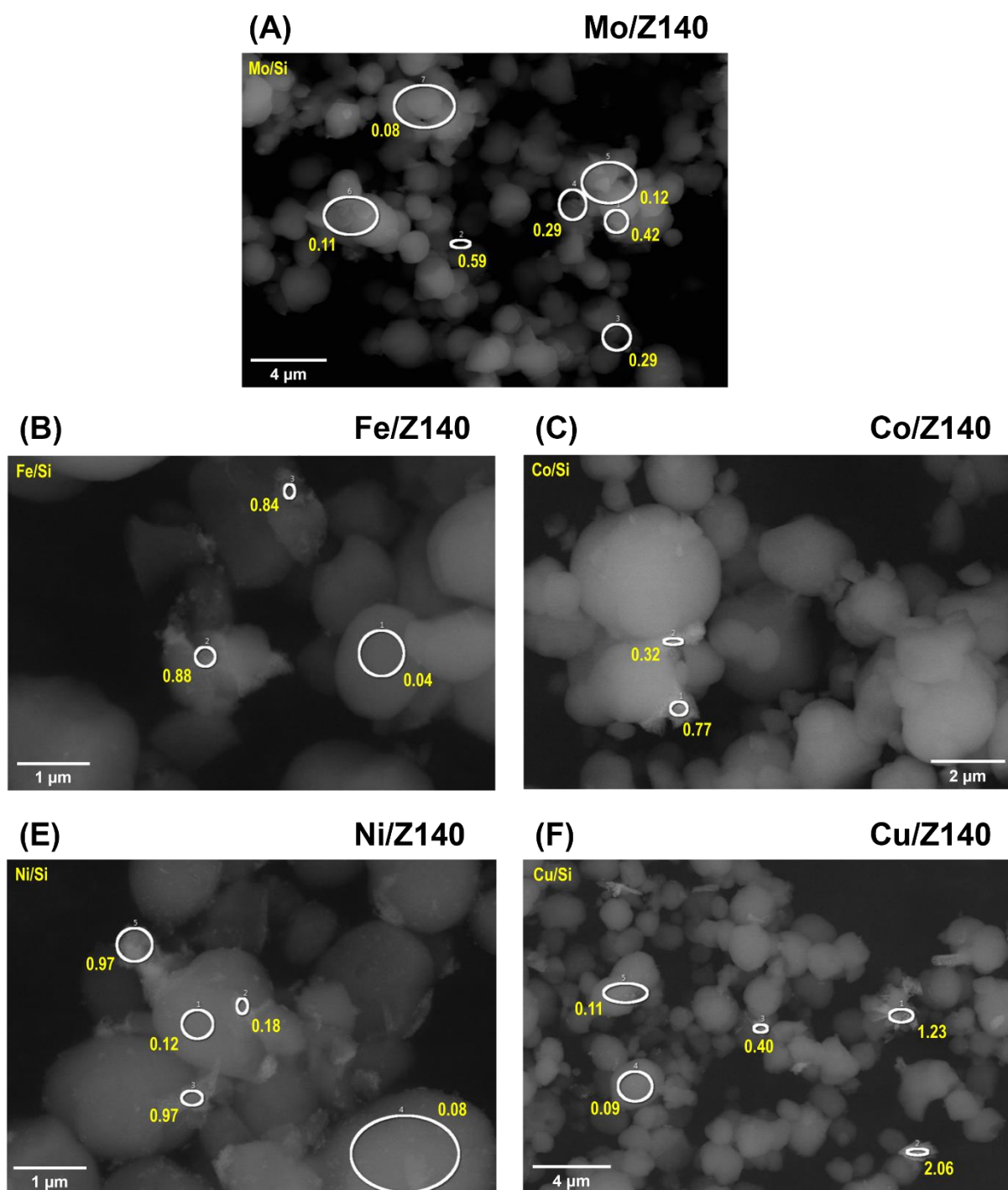


Figure A20. SEM images of the metal/zeolite catalysts highlighting the M/Si atomic ratios obtained through EDX analysis (A) Z140, (B) Mo/Z140, (C) Fe/Z140, (D) Co/Z140, (E) Ni/Z140, (F) Cu/Z140.

10.3. Permissions

10.3.1. Enhanced Brønsted Acidity and Hydrogenating Sites Generated on MoO₃ during Acetone Hydrodeoxygenation

JOHN WILEY AND SONS LICENSE TERMS AND CONDITIONS

Apr 30, 2024

This Agreement between Mr. Gabriel de Biasi Báfero ("You") and John Wiley and Sons ("John Wiley and Sons") consists of your license details and the terms and conditions provided by John Wiley and Sons and Copyright Clearance Center.

License Number	5778970721468
License date	Apr 30, 2024
Licensed Content Publisher	John Wiley and Sons
Licensed Content Publication	ChemCatChem
Licensed Content Title	Enhanced Brønsted Acidity and Hydrogenating Sites Generated on MoO ₃ during Acetone Hydrodeoxygenation
Licensed Content Author	Daniela Zanchet, Davi S. Leite, Guilherme B. Strapasson, et al
Licensed Content Date	Jul 18, 2023
Licensed Content Volume	15
Licensed Content Issue	16

Licensed Content Pages	13
Type of use	Dissertation/Thesis
Requestor type	Author of this Wiley article
Format	Electronic
Portion	Full article
Will you be translating?	No
Title of new work	Evaluation of molybdenum-based catalysts for the hydrodeoxygenation of biomass-derived model compounds
Institution name	University of Campinas
Expected presentation	Jun 2024
Requestor Location	Mr. Gabriel de Biasi Báfero General Osório St. 1661, 5 Campinas, São Paulo 13010-111 Brazil Attn: Mr. Gabriel de Biasi Báfero
Publisher Tax ID	EU826007151 Total0.00 USD
Terms and Conditions	

TERMS AND CONDITIONS

This copyrighted material is owned by or exclusively licensed to John Wiley & Sons, Inc. or one of its group companies (each a "Wiley Company") or handled on behalf of a

society with which a Wiley Company has exclusive publishing rights in relation to a particular work (collectively "WILEY"). By clicking "accept" in connection with completing this licensing transaction, you agree that the following terms and conditions apply to this transaction (along with the billing and payment terms and conditions established by the Copyright Clearance Center Inc., ("CCC's Billing and Payment terms and conditions"), at the time that you opened your RightsLink account (these are available at any time at <http://myaccount.copyright.com>).

Terms and Conditions

- The materials you have requested permission to reproduce or reuse (the "Wiley Materials") are protected by copyright.
- You are hereby granted a personal, non-exclusive, non-sub licensable (on a stand-alone basis), non-transferable, worldwide, limited license to reproduce the Wiley Materials for the purpose specified in the licensing process. This license, and any CONTENT (PDF or image file) purchased as part of your order, is for a one-time use only and limited to any maximum distribution number specified in the license. The first instance of republication or reuse granted by this license must be completed within two years of the date of the grant of this license (although copies prepared before the end date may be distributed thereafter). The Wiley Materials shall not be used in any other manner or for any other purpose, beyond what is granted in the license. Permission is granted subject to an appropriate acknowledgement given to the author, title of the material/book/journal and the publisher. You shall also duplicate the copyright notice that appears in the Wiley publication in your use of the Wiley Material. Permission is also granted on the understanding that nowhere in the text is a previously published source acknowledged for all or part of this Wiley Material. Any third party content is expressly excluded from this permission.
- With respect to the Wiley Materials, all rights are reserved. Except as expressly granted by the terms of the license, no part of the Wiley Materials may be copied, modified, adapted (except for minor reformatting required by the new Publication), translated, reproduced, transferred or distributed, in any form or by

any means, and no derivative works may be made based on the Wiley Materials without the prior permission of the respective copyright owner. For STM Signatory Publishers clearing permission under the terms of the STM Permissions Guidelines only, the terms of the license are extended to include subsequent editions and for editions in other languages, provided such editions are for the work as a whole in situ and does not involve the separate exploitation of the permitted figures or extracts, You may not alter, remove or suppress in any manner any copyright, trademark or other notices displayed by the Wiley Materials. You may not license, rent, sell, loan, lease, pledge, offer as security, transfer or assign the Wiley Materials on a stand-alone basis, or any of the rights granted to you hereunder to any other person.

- The Wiley Materials and all of the intellectual property rights therein shall at all times remain the exclusive property of John Wiley & Sons Inc, the Wiley Companies, or their respective licensors, and your interest therein is only that of having possession of and the right to reproduce the Wiley Materials pursuant to Section 2 herein during the continuance of this Agreement. You agree that you own no right, title or interest in or to the Wiley Materials or any of the intellectual property rights therein. You shall have no rights hereunder other than the license as provided for above in Section 2. No right, license or interest to any trademark, trade name, service mark or other branding ("Marks") of WILEY or its licensors is granted hereunder, and you agree that you shall not assert any such right, license or interest with respect thereto

- NEITHER WILEY NOR ITS LICENSORS MAKES ANY WARRANTY OR REPRESENTATION OF ANY KIND TO YOU OR ANY THIRD PARTY, EXPRESS, IMPLIED OR STATUTORY, WITH RESPECT TO THE MATERIALS OR THE ACCURACY OF ANY INFORMATION CONTAINED IN THE

- MATERIALS, INCLUDING, WITHOUT LIMITATION, ANY IMPLIED WARRANTY OF MERCHANTABILITY, ACCURACY, SATISFACTORY QUALITY, FITNESS FOR A PARTICULAR PURPOSE, USABILITY, INTEGRATION OR NON-INFRINGEMENT AND ALL SUCH WARRANTIES

ARE HEREBY EXCLUDED BY WILEY AND ITS LICENSORS AND WAIVED BY YOU.

- WILEY shall have the right to terminate this Agreement immediately upon breach of this Agreement by you.
- You shall indemnify, defend and hold harmless WILEY, its Licensors and their respective directors, officers, agents and employees, from and against any actual or threatened claims, demands, causes of action or proceedings arising from any breach of this Agreement by you.
- IN NO EVENT SHALL WILEY OR ITS LICENSORS BE LIABLE TO YOU OR ANY OTHER PARTY OR ANY OTHER PERSON OR ENTITY FOR ANY SPECIAL, CONSEQUENTIAL, INCIDENTAL, INDIRECT, EXEMPLARY OR PUNITIVE DAMAGES, HOWEVER CAUSED, ARISING OUT OF OR IN CONNECTION WITH THE DOWNLOADING, PROVISIONING, VIEWING OR USE OF THE MATERIALS REGARDLESS OF THE FORM OF ACTION, WHETHER FOR BREACH OF CONTRACT, BREACH OF WARRANTY, TORT, NEGLIGENCE, INFRINGEMENT OR OTHERWISE (INCLUDING, WITHOUT LIMITATION, DAMAGES BASED ON LOSS OF PROFITS, DATA, FILES, USE, BUSINESS OPPORTUNITY OR CLAIMS OF THIRD PARTIES), AND WHETHER OR NOT THE PARTY HAS BEEN ADVISED OF THE POSSIBILITY OF SUCH DAMAGES. THIS LIMITATION SHALL APPLY NOTWITHSTANDING ANY FAILURE OF ESSENTIAL PURPOSE OF ANY LIMITED REMEDY PROVIDED HEREIN.
- Should any provision of this Agreement be held by a court of competent jurisdiction to be illegal, invalid, or unenforceable, that provision shall be deemed amended to achieve as nearly as possible the same economic effect as the original provision, and the legality, validity and enforceability of the remaining provisions of this Agreement shall not be affected or impaired thereby.

- The failure of either party to enforce any term or condition of this Agreement shall not constitute a waiver of either party's right to enforce each and every term and condition of this Agreement. No breach under this agreement shall be deemed waived or excused by either party unless such waiver or consent is in writing signed by the party granting such waiver or consent. The waiver by or consent of a party to a breach of any provision of this Agreement shall not operate or be construed as a waiver of or consent to any other or subsequent breach by such other party.
- This Agreement may not be assigned (including by operation of law or otherwise) by you without WILEY's prior written consent.
- Any fee required for this permission shall be non-refundable after thirty (30) days from receipt by the CCC.
- These terms and conditions together with CCC's Billing and Payment terms and conditions (which are incorporated herein) form the entire agreement between you and WILEY concerning this licensing transaction and (in the absence of fraud) supersedes all prior agreements and representations of the parties, oral or written.
- This Agreement may not be amended except in writing signed by both parties. This Agreement shall be binding upon and inure to the benefit of the parties' successors, legal representatives, and authorized assigns.
- In the event of any conflict between your obligations established by these terms and conditions and those established by CCC's Billing and Payment terms and conditions, these terms and conditions shall prevail.
- WILEY expressly reserves all rights not specifically granted in the combination of
of

- the license details provided by you and accepted in the course of this licensing transaction, (ii) these terms and conditions and (iii) CCC's Billing and Payment terms and conditions.
- This Agreement will be void if the Type of Use, Format, Circulation, or Requestor Type was misrepresented during the licensing process.
- This Agreement shall be governed by and construed in accordance with the laws of the State of New York, USA, without regards to such state's conflict of law rules.
- Any legal action, suit or proceeding arising out of or relating to these Terms and Conditions or the breach thereof shall be instituted in a court of competent jurisdiction in New York County in the State of New York in the United States of America and each party hereby consents and submits to the personal jurisdiction of such court, waives any objection to venue in such court and consents to service of process by registered or certified mail, return receipt requested, at the last known address of such party.

WILEY OPEN ACCESS TERMS AND CONDITIONS

Wiley Publishes Open Access Articles in fully Open Access Journals and in Subscription journals offering Online Open. Although most of the fully Open Access journals publish open access articles under the terms of the Creative Commons Attribution (CC BY) License only, the subscription journals and a few of the Open Access Journals offer a choice of Creative Commons Licenses. The license type is clearly identified on the article.

The Creative Commons Attribution License

The Creative Commons Attribution License (CC-BY) allows users to copy, distribute and transmit an article, adapt the article and make commercial use of the article. The CC-BY license permits commercial and non-

Creative Commons Attribution Non-Commercial License

The Creative Commons Attribution Non-Commercial (CC-BY-NC) License permits use, distribution and reproduction in any medium, provided the original work is properly cited and is not used for commercial purposes. (see below)

Creative Commons Attribution-Non-Commercial-NoDerivs License

The Creative Commons Attribution Non-Commercial-NoDerivs License (CC-BY-NC-ND) permits use, distribution and reproduction in any medium, provided the original work is properly cited, is not used for commercial purposes and no modifications or adaptations are made. (see below)

Use by commercial "for-profit" organizations

Use of Wiley Open Access articles for commercial, promotional, or marketing purposes requires further explicit permission from Wiley and will be subject to a fee.

Further details can be found on Wiley Online Library <http://olabout.wiley.com/WileyCDA/Section/id-410895.html>

Other Terms and Conditions:

v1.10 Last updated September 2015

Questions? customercare@copyright.com.